Measurements of the complex refractive index of volcanic ash

Benjamin Edward Reed
St. Edmund Hall
University of Oxford

A thesis submitted for the degree of
Doctor of Philosophy
Trinity Term 2016

Abstract

This thesis describes laboratory measurements of the complex refractive index of volcanic ash particles. These measurements are needed to model the radiative impact of volcanic ash, vital for accurate satellite remote sensing. Three experimental methods have been developed, and the results for the complex refractive index and optical properties of a wide range of volcanic ash samples are presented.

Measurements were made of the spectral transmission of radiation through suspended volcanic ash particles inside an aerosol cell, using a Fourier transform spectrometer at infrared wavelengths and two diffraction grating spectrometers covering ultraviolet, visible, and near-infrared wavelengths. In addition to the optical measurements, a suite of sampling and sizing instruments were connected downstream of the aerosol cell to measure the particle size distribution. The method was calibrated using two quartz samples. Mass extinction coefficients for nine volcanic ash samples, at $0.3 - 14\,\mu$m, are presented and show considerable variation. These variations are linked to the composition of the samples, measured using X-ray fluorescence (XRF) analysis.

The complex refractive index, at $0.3 - 14\,\mu$m, of the two quartz samples and two samples of volcanic ash from the 2010 Eyjafjallajökull eruption were retrieved from the extinction measurements. The forward model used Mie theory and a classical damped harmonic oscillator (CDHO) model to represent the complex refractive index of the samples in terms of a finite set of band parameters, as well as the real refractive index of the sample in the small wavelength limit. Previous studies have shown that there is a redundancy in the retrievals between the band strength parameters and the real refractive index in the small wavelength limit, which can lead to spurious values for the retrieved complex refractive index. This problem was overcome by using an independent measurement of the real refractive index at a visible wavelength, to constrain the model parameter of the real refractive index in the short wavelength limit. Independent measurements of the complex refractive index at visible wavelengths are also important because the extinction produced at these wavelengths is highly sensitive to the particle size distribution, and any uncertainty in the measured size distribution will contribute to significant systematic error in the refractive index retrieved from extinction.

The retrieved spectral complex refractive index of Eyjafjallajökull ash was applied using the ORAC retrieval scheme to measurements of the 2010 Eyjafjallajökull eruption made by the MODIS instrument aboard NASA's Terra satellite. Significant difference were found in the retrieved plume parameters of optical path, effective radius, and plume altitude, compared to assuming a literature measurement for the refractive index of pumice.

For three discrete visible wavelengths (450, 546.7, and $650\,$nm) an optical microscope was used to make measurements of the complex refractive index of the volcanic ash samples. The long-established Becke line method was used to measure the real refractive index of the samples. For the imaginary refractive index, a new and novel method was developed involving measurements of the attenuation of light in individual particles. A strong linear correlation was found between the SiO_2 content of the samples and both their real and imaginary refractive indices at the visible wavelengths investigated. Furthermore, from the XRF compositional analysis of the samples values were calculated for the ratio of non-bridging oxygen atoms per tetrahedral cation (NBO/T), and it was found that NBO/T was an even stronger predictor of real refractive index at visible wavelengths.

The optical microscope measurements could only be applied to particles with a radius larger than $10\,\mu$m. A new refractometer method was investigated for retrieving the real refractive index of submicron particles from colloidal reflectance measurements close to the critical angle in an internal reflection configuration. A coherent scattering model (CSM) was used to model the coherent reflection from a half-space of monodisperse or polydisperse particles, and a simple extension of the model is presented to properly account for the modified size distribution at the interface in an internal reflection set-up. A rigorous sensitivity analysis was performed to determine how experimental uncertainties propagate into uncertainty associated with the retrieved real refractive index, and the uncertainty due to non-spherical effects was estimated using T-matrix methods. Experimental reflectance data at a wavelength of $635\,$nm were obtained for spherical monodisperse polystyrene calibration particles, a polydisperse sand sample, and a polydisperse volcanic ash sample. The retrieved values for the real refractive index agreed, within propagated uncertainties, with values measured using other techniques. The method is shown to be a viable technique for measuring the real refractive index of small quantities of submicron particles, and can also retrieve the concentration and size of particles.

Acknowledgements

I would like to thank Don Grainger for his help navigating the choppy seas of doctoral research. His advice, support, and patience shined bright through treacherous storms, allowing me to steer clear of shallow waters and perilous rocks.

I sincerely thank Dan Peters for his indispensable technical expertise and help, particularly during the aerosol cell experiments, but also throughout the rest of my thesis research. I must thank Robert McPheat and Gary Williams, at Rutherford Appleton Laboratory's Molecular Spectroscopy Facility, for their invaluable support and for keeping the FTS in check. Within the Earth Observation Data Group, I thank Greg McGarragh for running the ORAC retrievals presented in this thesis.

I would also like to thank Grace Holtkamp. Her support and care over the last two years is hugely appreciated, and has helped me immensely.

Contents

List of Figures

List of Tables

List of acronyms and abbreviations

APS	Aerodynamic particle sizer
CAA	The Civil Aviation Authority
CCN	Cloud condensation nuclei
CDHO	Classical damped harmonic oscillator
CPC	Condensation particle counter
CSM	Coherent scattering model
DMA	Differential mobility analyser
FTS	Fourier transform spectrometer
GB	Globar
HL	Halogen lamp
ICAO	The International Civil Aviation Authority
IPCC	The Intergovernmental Panel on Climate Change
IR	Infrared
MEC	Mass extinction coefficient
MODIS	Moderate Resolution Imaging Spectroradiometer
NBO/T	The ratio of non-bridging oxygen atoms to tetrahedral cations
NERC	The National Environmental Research Council
NIR	Near infrared
ORAC	Oxford – RAL Aerosol and Cloud
PMT	Photo-multiplier tube
RAL	Rutherford Appleton Laboratory
SMPS	Scanning mobility particle sizer
UV	Ultraviolet
VAAC	Volcanic ash advisory centre
VEI	Volcanic explosivity index
XRF	X-ray fluorescence

Chapter 1

Introduction

1.1 The importance of volcanic ash

Explosive volcanic eruptions inject significant fragmented silica material (tephra) and other aerosols into the atmosphere, as well as mixtures of gas. Smaller solid particles (with a radius less than 2 mm) are classified as volcanic ash [*Schmid*, 1981]. Larger particles tend to deposit proximal to the volcanic vent. Many millions of tonnes of volcanic ash can be injected high into the atmosphere, at which point atmospheric circulation can transport the plume hundereds to thousands of kilometers. Airborne volcanic ash has a number of important effects.

1.1.1 Aviation

The 2010 Eyjafjallajökull volcanic eruption is estimated to have cost the global economy US$ 5 bn [*Oxford Economics*, 2010; *European Union*, 2010], resulting from European airspace closure for six days as the ash cloud propagated downwind. Figure 1.1 shows an image of the Eyjafjallajökull ash plume captured by the Moderate Resolution Imaging Spectrometer (MODIS) on NASA's Terra satellite on 7 May 2010. Volcanic ash is a risk to aviation, primarily because of its impact on aircraft engines [*Dunn and Wade*, 1994; *Haiyan et al.*, 2015], and because damaging concentrations of particles, even in good conditions, may not be visible to the eye. The Civil Aviation Authority (CAA) had a zero-tolerance approach to civil aviation in the presence of volcanic ash, but following the 2010 Eyjafjallajökull eruption this was changed to permit flights within ash concentrations below 2×10^{-3} g cm^{-3} [*CAA*, 2010].

Following the 1991 eruption of Pinatubo, Philippines, the International Civil Aviation Organisation (ICAO) established nine volcanic ash advisory centres

Figure 1.1: The volcanic ash plume from the 2010 Eyjafjallajökull eruption. The image was captured by the MODIS instrument on NASA's Terra satellite on 11 May 2010, when the ash was streaming almost directly Southwards. The image width is 650 km.

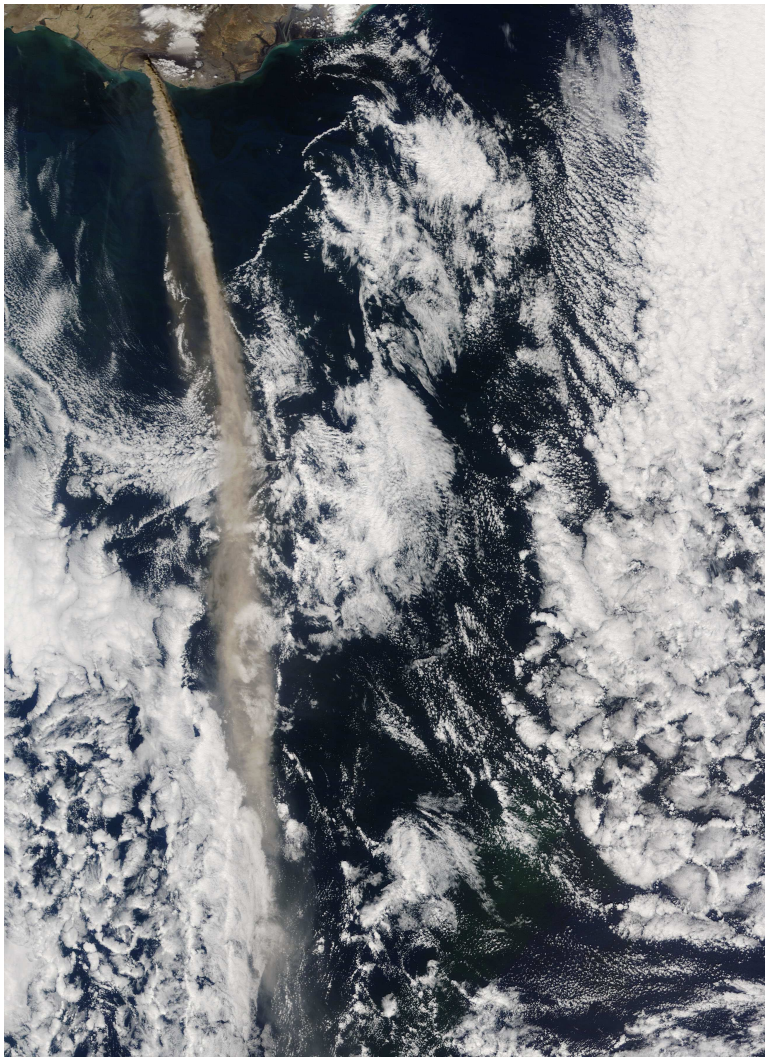

(VAACs) across the globe. The VAACs are responsible for issuing advisories to aviation authorities to inform decision making on whether airspace is safe. VAACs use volcanic data, satellite and ground based measurements, along with weather forecast and ash plume dispersion models to provide real-time data on ash concentrations as well as forecasts about ash cloud propagation [*Wallace et al.*, 2015].

Between 1953 – 2009 there were 94 confirmed encounters between aeroplanes and volcanic ash, 79 of which resulted in various degrees of damage, and nine of which resulted in engine shutdown during flight [*Guffanti et al.*, 2010]. At least two incidents have resulted in the shutdown of all engines [*Hanstrum and Watson*,

Figure 1.2: Damage to aeroplane engines caused by volcanic ash: **(a)** Ash deposition on engine components (Photo: Eric Moody, British Airways); **(b)** Abrasive damage [*Delapasse*, 2011].

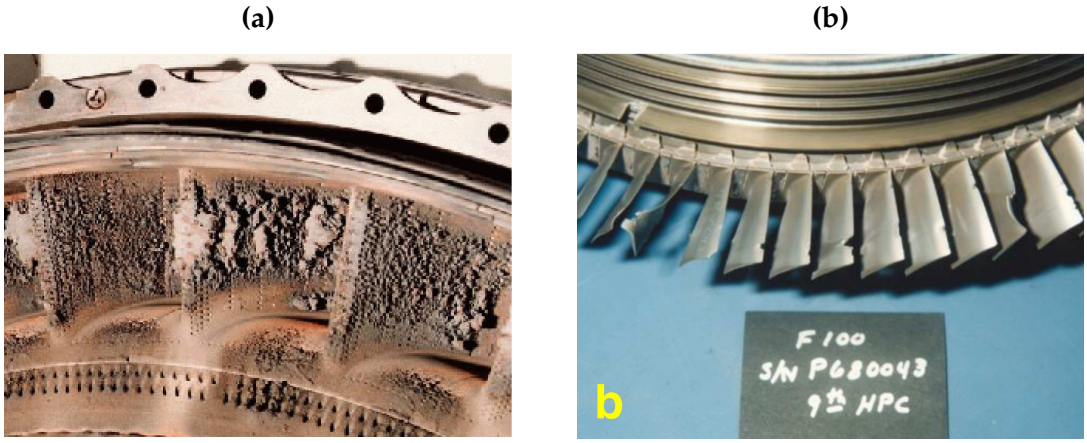

1983; *Przedpelski and Casadevall*, 1994], but there have been no crashes attributed to volcanic ash. Figure 1.2 shows examples of aeroplane engine damage caused by volcanic ash. The glassy component of volcanic ash undergoes a phase transition in jet engines, becoming plastic at temperatures between 700 and 1000 °C [*Przedpelski and Casadevall*, 1994]. The resulting liquid sticks to engine surfaces altering the engine's highly tuned aerodynamic performance. This sort of deposition is visible in Fig. 1.2a. Abrasive damage to turbine blades is shown in Fig. 1.2b.

1.1.2 The Earth's radiation balance

Injection of volcanic aerosol into the troposphere and stratosphere directly affects the Earth's radiation balance by scattering and absorbing shortwave solar radiation as well as absorbing and emitting infrared radiation [*Grainger et al.*, 2013]. The scattering and absorption produced varies as a function of the size, shape and complex refractive index of the ash, as well as depending on the incident wavelength of light. The primary direct effect is the scattering of solar radiation causing an increase in the Earth's albedo and therefore resulting in a negative radiative forcing, i.e. a cooling effect [*IPCC*, 2013].

Volcanic aerosol also affects the Earth's radiation balance indirectly by acting as cloud condensation nuclei (CCN) in the troposphere and altering the properties of clouds. Increased concentrations of volcanic aerosol lead to higher number densities of CCN, and for a parcel of dry air with a fixed water content, result in a higher concentration of smaller droplets and therefore a higher albedo — the Twomey or

first indirect effect [*Twomey*, 1977]. Additionally, smaller droplets may result in the suppression of precipitation and longer cloud lifetimes — the second indirect effect [*Albrecht*, 1989]. Another secondary indirect effect results because the presence of aerosol in the cloud may increase evaporation of cloud droplets because of absorption of solar radiation, as well as other less well understood effects [*Rosenfeld et al.*, 2014]. The impact of secondary indirect aerosol effects are generally not well understood or observed [*Boucher et al.*, 2013].

The direct and indirect impacts on the Earth's radiation balance are known to occur over the full range of volcanic activity from quiescent degassing to large explosive volcanic eruptions [*Yuan et al.*, 2011], but with varying impacts. Large volcanic eruptions, particularly when the plume height is high enough to inject sulphate aerosols into the stratosphere, can have a significant impact on climate lasting several years. The significant radiative forcing from large eruptions occurs because of sulphate aerosols injected into the stratosphere, formed predominantly from precursor SO_2 gas, which have long lifetimes and because their small size makes them effective scatterers of solar radiation [*Boucher et al.*, 2013]. The last major event was the 1991 eruption of Pinatubo, Philippines, which reduced global surface temperatures by $0.5\,^{\circ}$C for some months in 1992 [*Parker et al.*, 1996]. Uncertainties associated with the radiative impact of atmospheric aerosols remain the largest contribution to uncertainties in predictions of future climate change, and quantifying the anthropogenic contribution to climate change [*IPCC*, 2013].

1.1.3 Human health

Volcanic eruptions pose obvious risks to anyone in the immediate vicinity. Heavy ash fall can result in the collapse of building roofs under the weight of ash. However, the acute effects of respirable ash (particles with a radius $< 5\,\mu$m) can be much more widespread depending on the propagation of the ash plume. High levels of respirable ash can result in acute respiratory symptoms such as irritation of the chest, nose, and throat, as well as posing a more significant risk to people with pre-existing conditions such as asthma or bronchitis [*Gudmundsson*, 2011]. However, no link has so far been found between volcanic ash inhalation and long-term disease or injury.

1.2 Volcanoes and volcanic ash

1.2.1 Plate tectonics and the global distribution of volcanoes

The Earth's internal heat, accumulated during the Earth's formation by accretion 4.5 bn years ago and further generated by the decay of radioactive isotopes, drives the convective processes in the Earth's mantle that lead to the large-scale motion of the Earth's lithosphere[1] and the processes of plate tectonics [*LaFemina*, 2015]. This motion leads to the formation of volcanoes at diverging or converging plate boundaries, and when these boundaries involve continental plates land volcanoes form with the potential to inject volcanic ash into the atmosphere. Figure 1.3 shows the global distribution of active volcanoes and tectonic plate boundaries. It can be seen that the majority of volcanoes form a circle around the Pacific, the so called "Ring of Fire", along narrow paths on plate boundaries.

Figure 1.3: The global distribution of active volcanoes and plate boundaries. Image produced by the U.S. Geological Survey.

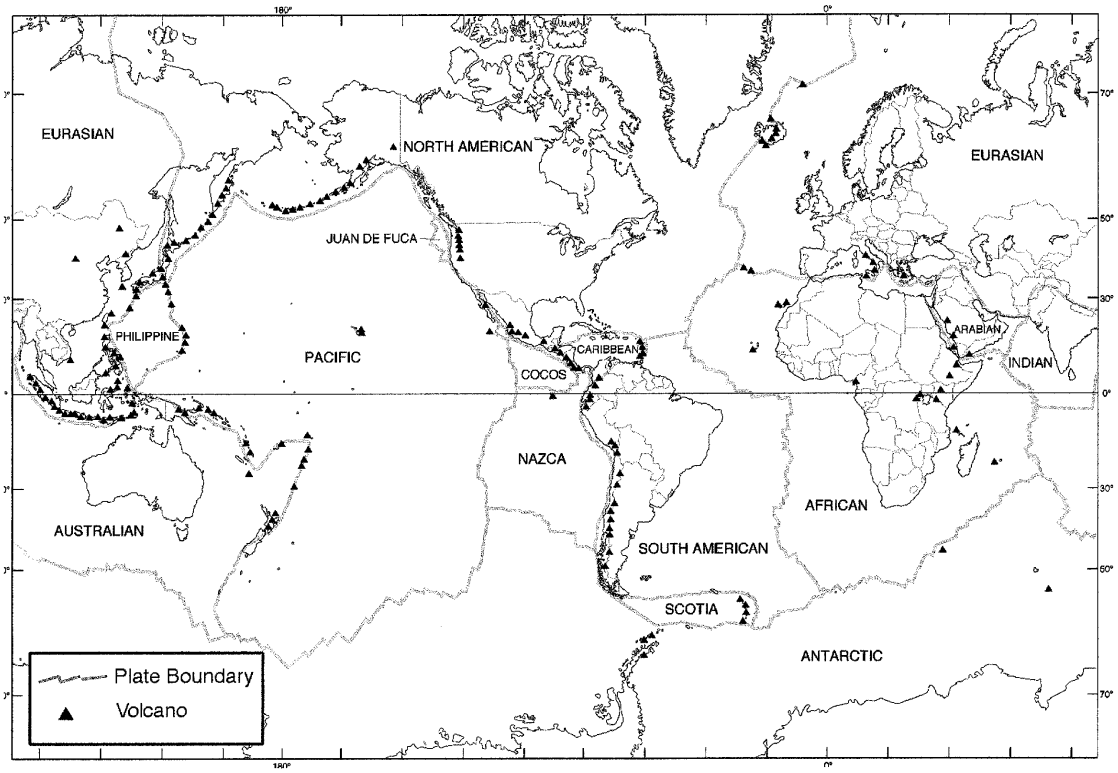

[1]The lithosphere is composed of the crust and the brittle uppermost part of the mantle.

1.2.2 Magma formation and eruptions types

The Earth's mantle is predominantly solid, although it acts as a highly viscous fluid on geological timescales. At diverging or converging plate boundaries, the Earth's upper mantle transitions to a fluid or semi-fluid state, expanding and rising and leading to the formation of volcanoes. This rising mixture of molten or semi-molten rock, dissolved gases and crystalline solids is referred to as magma. Rising magma can result from simple decompression of mantle (typical at a diverging boundary) or because the addition of volatiles, particularly H_2O, lowers the melting temperature (for example in the subduction zone at a converging boundary). It is this second mechanism of magma formation, associated with changes in the composition of the mantle, that is most significant for ash formation because it can result in highly explosive island-arc volcanism [*Sigurdsson*, 2015].

Volcanic eruptions that result solely from the rapid expansion and ascent of magma, accelerated by the rapid expansion of dissolved gases, are referred to as *magmatic*. However, eruptions can also be produced when magma interacts with external water, commonly supplied by the sea or a lake, and are referred to as *phreatomagmatic*. When water comes in contact with magma above a critical temperature a high heat transfer rate occurs and an explosion results as a consequence of the brittle reaction of the contracting melt driven by a rapid thermal expansion of water [*Büttner et al.*, 2002]. Another type of eruption can occur when magma provides heat, without direct contact, to water, causing groundwater or surface water to flash to steam. These eruptions are referred to as *phreatic*. Volcanic eruptions can involve magmatic, phreatomagmatic, and phreatic components or transition between phases dominated by one. For example, the 2010 Eyjafjallajökull eruption transitioned from a phreatomagmatic to a purely magmatic eruption [*Dellino et al.*, 2012].

1.2.3 Ash formation by fragmentation

Volcanic ash is abundantly produced when magma fragments during explosive eruptions, but silica particles are also known to be produced with relatively non-explosive (effusive degassing) volcanic activity [*Mather*, 2008]. During fragmentation the magma transitions from a continuous liquid phase containing gas bubbles and crystalline solids to a gas phase containing solid fragmented particles.

Primary fragmentation can occur as a result of rapid expansion, decompression or quenching. In magmatic eruptions, as the magma ascends the pressure drops

below the saturation pressure of dissolved gases, predominantly H_2O, CO_2, and SO_2, causing the magma to become super-saturated. The volatile species can no longer remain in solution and nucleate into gas bubbles, which grow and coalesce. Gas nucleation and the growth of gas bubbles provides the primary driving force accelerating the magma's ascent and resulting in high strain levels through the magma. The high strain causes fragmentation to occur by fluid instabilities in low viscosity magma and by brittle fracture when the tensile strength of the magma is exceeded in high viscosity magma [*Cashman and Rust*, 2016]. Fragmentation by decompression occurs when there is a sudden reduction of pressure, for example when the structural integrity of the volcano's dome fails or the plug in a volcanic conduit is suddenly released. Fragmentation by quenching occurs in phreatomagmatic eruptions when the magma is rapidly cooled by contact with water. Both the shape and size of the ash particles produced depend on the type of fragmentation, with fragmentation by quenching tending to produce the finest ash particles [*Liu et al.*, 2015a]. *Secondary* fragmentation refers to the breaking of particles under collision as well as the rounding of particles by abrasion, processes which alter the shape and size distributions of particles in the plume.

1.2.4 Eruption explosivity and size

Volcanic eruptions vary greatly in terms of the volume of material ejected, their eruption style and the hazards they pose. The two most useful measures to quantify the size of volcanic eruptions are their *magnitude* and *intensity* [*Pyle*, 2015]. The magnitude of a volcanic eruption is defined as:

$$\text{magnitude} = \log_{10}\left(\text{total erupted mass, kg}\right) - 7, \tag{1.1}$$

and the intensity is defined as:

$$\text{intensity} = \log_{10}\left(\text{mass eruption rate, kg/s}\right) + 3. \tag{1.2}$$

The intensity of a volcanic eruption is an important factor in determining the height of the volcanic plume. Volcanic plumes can be characterised as being either *weak* or *strong*. In weak plumes the wind advection dominates over buoyant plume rise; whereas for strong plumes the buoyancy dominates. Strong plumes tend to rise vertically, with the maximum plume height being a well defined function of

intensity (which determines the momentum of the buoyant column). If the momentum flux is sufficiently large the maximum plume height may exceed the natural buoyancy height of the plume, resulting in a radial gravity current and an umbrella-shaped volcanic plume [*Bursik et al.*, 1992]. Wind direction and strength then determine the lateral propagation of the plume.

Volcanic explosivity refers to the conversion of the potential energy of the magma into the kinetic energy of the eruption products (gas and tephra). The *volcanic explosivity index* (VEI), first introduced by *Newhall and Self* [1982], is an integer scale from 0 to 8 that is commonly used to characterise volcanic eruptions based on both the plume height (which depends on intensity) and the magnitude of the eruption. The VEI can be useful for comparing modern eruptions to historical eruptions, but it relies on the assumption that magnitude and intensity are related.

As an example, the 39 day eruption of Eyjafjallajökull in April – May 2010 erupted $4.8 \pm 1.2 \times 10^{11}$ kg of material [*Gudmundsson et al.*, 2012] giving it a magnitude of 4.7, and was estimated to have an average mass discharge rate of 9×10^5 kg/s during the most explosive phase [*Ripepe et al.*, 2013] corresponding to an intensity of 8.6. Based on plume height and magnitude the Eyjafjallajökull eruption corresponds to $\mathrm{VEI} = 3$. In contrast, the 1991 Pinatubo eruption, the most recent major eruption, ejected 1.1×10^{13} kg of material giving it a magnitude of 6.0, and had a peak mass eruption rate of 4×10^8 kg/s corresponding to an intensity of 11.6 [*Pyle*, 2015]. The 1991 Pinatubo eruption corresponded to $\mathrm{VEI} = 6$.

1.2.4.1 The relation between viscosity, NBO/T, and explosive fragmentation

The viscosity of the magma and the type of volcanic eruption (for example the interaction with water in phreatomagmatic eruptions) are the important factors in determining the explosivity and intensity of volcanic eruptions. In purely magmatic eruptions, the viscosity of the magma is the crucial factor. The viscosity of magmas can vary by a factor of 10^{14} [*Daines and Pec*, 2015], and is primarily determined by the SiO_2 content of the magma, its dissolved water content, and its temperature.

Silicate melts consist of a disordered network of SiO_4 tetrahedra in dynamic equilibrium resulting from the constant forming and breaking of Si — O bonds. The degree of polymerisation or the level of cross-linking in the melt is characterised by the ratio of non-bridging oxygen atoms to tetrahedral cations (NBO/T), where the tetrahedral cations are predominately Si, and is closely related to the

viscosity of the melt — a greater level of cross-linking between atoms, and hence higher NBO/T, leads to higher viscosity [*Wang et al.*, 2014]. Water reduces NBO/T and hence viscosity by reacting with bridging oxygen to form non-bridging oxygen and hydroxl molecules.

Magma fragmentation can be understood in terms of the glass transition between a viscous or ductile behaviour to an elastic or brittle behaviour [*Gonnermann*, 2015]. The silica melt can be considered a Maxwell material, having both properties of elasticity and viscosity. The relaxation time of a Maxwell material is given by $\tau_{\mathrm{r}} = \frac{\mu_{\mathrm{r}}}{G}$ where μ_{r} is the material's viscosity at low strain rates and G is the shear modulus of the elastic component of the material. It has been found that the glass transition between viscous or ductile and elastic or brittle occurs for strain rates approximately two orders of magnitude below τ_{r}^{-1} [*Dingwell*, 1996]. The temperature of the melt affects its viscosity, with higher temperatures resulting in a lower viscosity and therefore a shorter relaxation time.

Figure 1.4: The glass transition shown as a function of reciprocal temperature and the deformation timescale (the reciprocal of the strain rate). Image produced by *Dingwell* [1996].

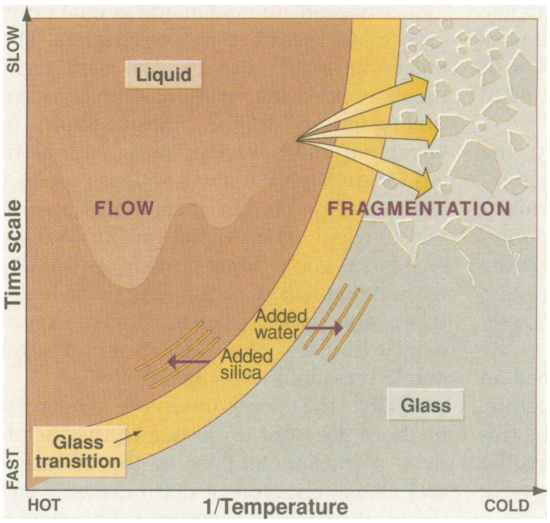

Figure 1.4, produced by *Dingwell* [1996], shows the glass transition curve as a function of reciprocal temperature and the deformation time scale (the reciprocal of the deformation strain rate). For deformation rates slower than the relaxation response of the material, the melt responds as a viscous fluid. For strain rates greater than the relaxation speed, the melt responds as an elastic material. For relatively low strains the elastic response is to store strain energy as elastic potential energy. However, larger strains result in fragmentation and the explosive conversion of

strain energy into the kinetic energy of fragments. Whether or not an eruption crosses the glass transition to explosive fragmentation therefore depends on the viscosity of the melt (which determines the relaxation time and varies depending on the composition, water content, and temperature) and the strain rates present in the eruption.

The strain rates are driven by the gas bubble nucleation and decompression. The stresses generated tend to be higher in more viscous (higher silica content) magmatic eruptions because buoyant bubble rise is resisted by viscous drag of the melt (preventing effusive losses and causing bubbles to ascend with the melt) and because higher viscosity results in greater bubble overpressure [*Gonnermann*, 2015] — the pressure difference between the gas bubble and the melt. Furthermore, viscous stresses with the wall of the conduit scale with the viscosity of the melt [*Massol and Jaupart*, 1999]. Interaction with water causes rapid heat transfer across the water-magma boundary. The rapid vapourisation of the water and quenching of the magma generates dynamic stresses, which are high enough to produce strains that cross the glass transition to fragmentation.

1.2.5 Ash composition

1.2.5.1 Ash components

Volcanic ash particles include *juvenile* particles formed from fragmented new magma, and *lithic* particles formed from abrasion of older volcanic rocks (e.g. from along the volcanic conduit). Lithic particles therefore tend to be more abundant in explosive eruptions. Since magma is a silica melt containing gas bubbles and crystals, the juvenile particles formed from magma during fragmentation and rapid solidification have properties that reflect the magma composition and the fragmentation process. The juvenile particles are predominantly glassy but can have a varying crystaline component (forming as individual crystal particles or included in larger glassy particles). The juvenile particles can also be dense or vesticular (containing gas bubbles).

1.2.5.2 Compositional classification of igneous material

Igneous materials (e.g. igneous rock formed from solidified magma or volcanic ash) are classified according to their composition. The most important classification is based on the mass percentage of SiO_2:

- *Felsic* materials contain greater than 63 % SiO_2.
- *Intermediate* materials contain 52 – 63 % SiO_2.
- *Mafic* materials contain 45 – 52 % SiO_2.
- *Ultramafic* materials contain less than 45 % SiO_2.

Igneous materials can also be classified according to their SiO_2 and alkali (NaO_2 + K_2O) content. Figure 1.5 shows the Total Alkaline Silica (TAS) diagram, first introduced by *Maitre et al.* [2002], for the classification of igneous materials.

Figure 1.5: TAS classification of igneous material by percentage mass SiO_2 content and alkali (NaO_2 + K_2O) content. From *Maitre et al.* [2002].

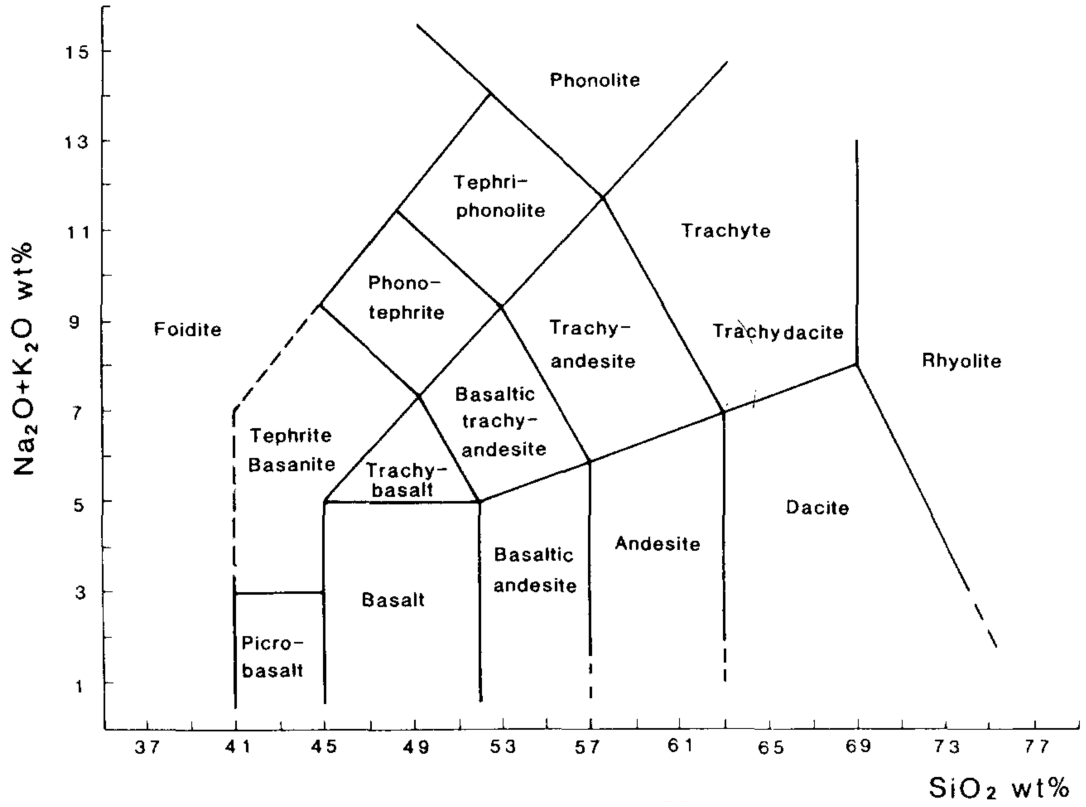

1.2.5.3 Magma composition versus ash composition

The SiO_2 content of volcanic ash is not always the same as that of the parental magma, and differences result from the crystal content of the magma and the crystallization process [*Cashman and Rust*, 2016]. As the magma ascends, crystallization is driven by the exsolution of H_2O from the melt lowering the solidification

temperature. The melt therefore evolves in composition, and because the crystals are silica-poor the silica content of the residual melt increases. The melt therefore fragments into ash particles with a higher silica content than the parental magma. The result is that crystal-poor magmas tend to produce volcanic ash with a similar SiO_2 content to the parental magma, and crystal-rich magmas produce ash with a significantly higher SiO_2 content than the parental magma. If the crystallization occurred sufficiently prior to the eruption then ash particles tend to have a narrow range of SiO_2 compositions, whereas if the crystallization is ascent-driven then the variation in SiO_2 content of particles is much larger. The increase in the SiO_2 of the ash compared to the parental magma, for crystal-rich magmas, can be 10 % or greater [*Wright et al.*, 2012].

1.2.6 Size, shape, density and settling velocities

Both the size and shape of ash particles vary depending on the fragmentation process, its explosivity, and the composition of the magma. Ash particles formed from explosive and viscous magmatic eruptions tend to form highly angular-shaped and vesticular glass particles; particles formed from low-viscosity magmatic eruptions tend to form droplet-shaped glass particles, with near-spherical or ellipsoid shapes; and particles formed from phreatomagmatic eruptions form blocky or pyramidal glass particles [*Heiken*, 1972].

The size distribution of ash particles is also determined by the fragmentation process. More explosive eruptions tend to produce *very fine* ash particles (radius $< 30\,\mu$m) more abundantly, and therefore higher silica content magmatic eruptions tend to be associated with finer ash [*Rose and Durant*, 2009]. Phreatomagmatic fragmentation is particularly explosive and efficient at producing fine ash. For example, phreatomagmatic fragmentation generated large quantities of fine ash during the 2010 Eyjafjallajökull and the 2011 Grímsvötn eruptions, contributing to the widespread transport of the ash due to the slower settling velocities of fine particles [*Liu et al.*, 2015b].

The size distribution of atmospheric volcanic ash evolves with distance from the volcanic source because larger particles have higher settling velocities and tend to be lost by sedimentation first. Figure 1.6 shows the fallout times for spherical particles of density $2.4\,\mathrm{g/cm^3}$ as a function of particle radius and altitude, calculated assuming the US Standard Atmosphere [*National Oceanic and Atmospheric Administration et al.*, 1976] and the drag formula presented in *Ganser* [1993]. The drag

Figure 1.6: Fallout time as a function of particle radius and plume injection height. The particles were assumed to be spherical with a density of $2.4\,\mathrm{g/cm^3}$, the US Standard Atmosphere was assumed, and the drag formula presented in *Ganser* [1993] was used.

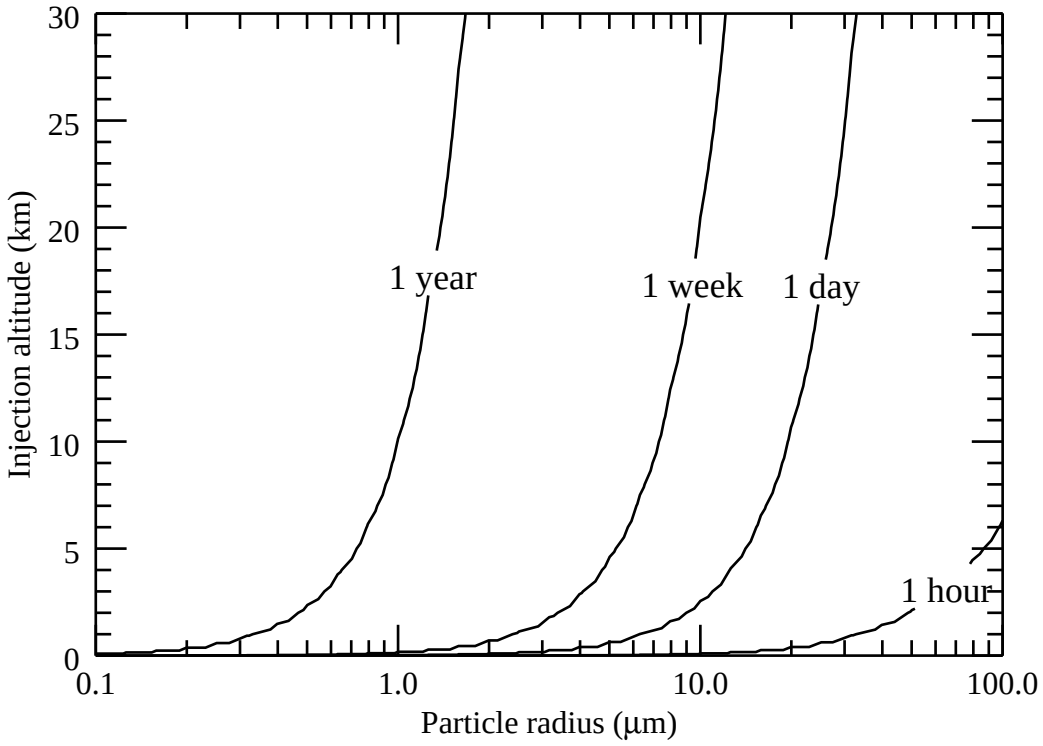

force experienced by irregularly shaped particles is higher than their volume equivalent spheres, and so their settling times tend to be greater [*Bagheri and Bonadonna*, 2016]. Particle agglomeration also plays an important role, acting to reduce the proportion of fine particles, and must be taken into account for accurate ash dispersion modelling [*Brown et al.*, 2012].

Figure 1.7 shows in-situ size distributions of the ash cloud from the 2010 eruption of Eyjafjallajökull measured by the UK Facility for Airborne Atmospheric Measurements (FAAM) BAe-146 aircraft [*Johnson et al.*, 2012]. The distribution is for all volcanic aerosol and so includes sulphate aerosol and volcanic ash. It can be seen that the distribution is bimodal with a fine mode (radius 0.05 – 0.3 μm) and a coarse mode (radius 0.3 – 20 μm). The fine mode was associated with sulphate aerosol although will also contain a component from ash, whereas the coarse mode was associated with volcanic ash. Noting that the graph shows diameter on the x-axis, it can be seen that by mass there is a significant proportion of the total aerosol and the volcanic ash mode that has a volume equivalent radius below 1.0 μm.

Figure 1.7: In-situ size distribution measurements of the volcanic ash cloud measured by the FAAM aircraft during the 2010 Eyjafjallajökull eruption as presented in *Johnson et al.* [2012]. The different coloured curves indicate different routes of the aircraft through the plume.

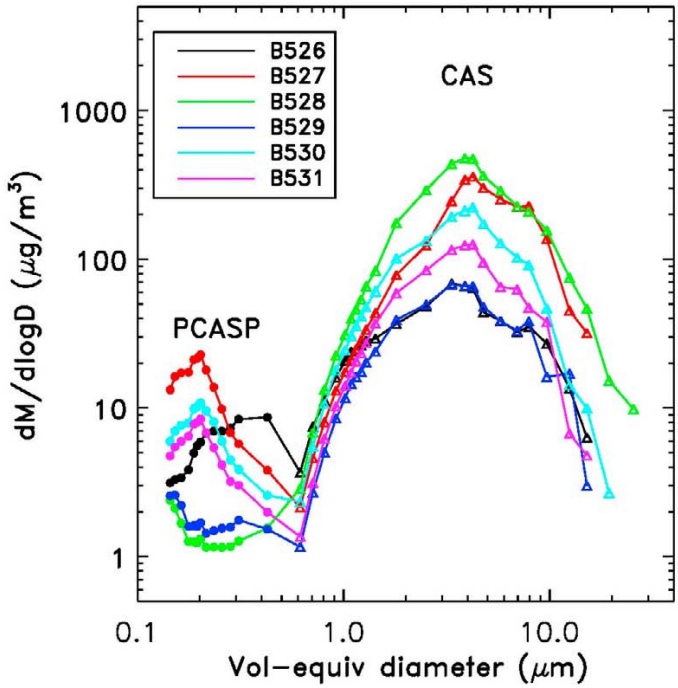

Furthermore, by number these particles will dominate.

The density of ash particles also varies considerably between eruptions and as a function of particle size, affecting settling velocities. Larger particles tend to be more vesicular depending on the level of eruption degassing and bubble formation, and therefore have a lower density. The density of juvenile ash particles has been found to decrease linearly with the logarithm of particle radius, tending to approach the glass density for radii less than $8\,\mu$m, whereas lithic particles uniformly have high densities similar to the glass density [*Cashman and Rust*, 2016].

Figure 1.8 shows scanning electron microscope (SEM) images of volcanic ash from the 21 – 28 May 2011 eruption of Grímsvötn, Iceland. The explosive basaltic eruption resulted in a 15–20 km high plume [*Stevenson et al.*, 2013], and ash was transported downwind to Northern Europe causing civil aviation disruption. The image shown in Fig. 1.8a was taken of a sample collected only 200 m from the volcanic vent (sample code VA4, detailed in Table 1.3). The proximity of the collection point to the vent means the sample contains a large proportion of coarser particles (radius $> 100\,\mu$m), but a large range of particle sizes are present. Gas bubble walls are clearly visible in some of the glassy fragments. The particles have highly angu-

Figure 1.8: SEM images of volcanic ash from the 21 – 28 May 2011 eruption of Grímsvötn, Iceland. The image in **(a)** was taken by Gemma Prata (Department of Earth Sciences, University of Oxford) of a sample collected 200 m from the volcanic vent; the sample has a code number, VA4, and is described in more detail in Table 1.3. The image in **(b)** shows a single glass particle deposited in Orkney, Scotland, 964 km from the volcanic vent — image credit: British Geological Survey/NERC.

(a)

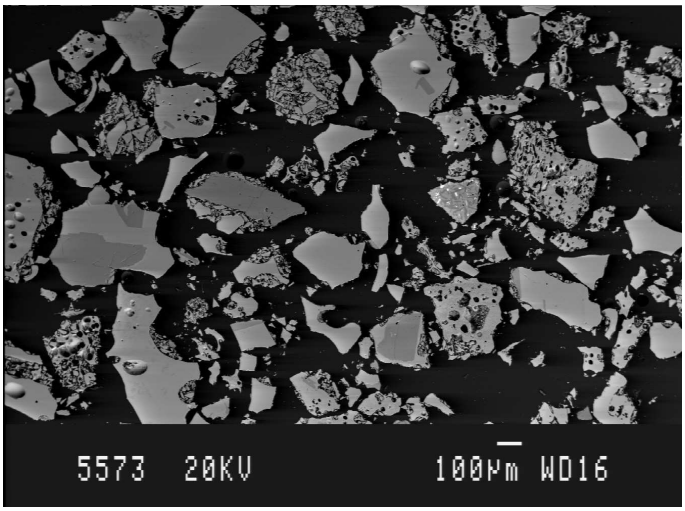

(b)

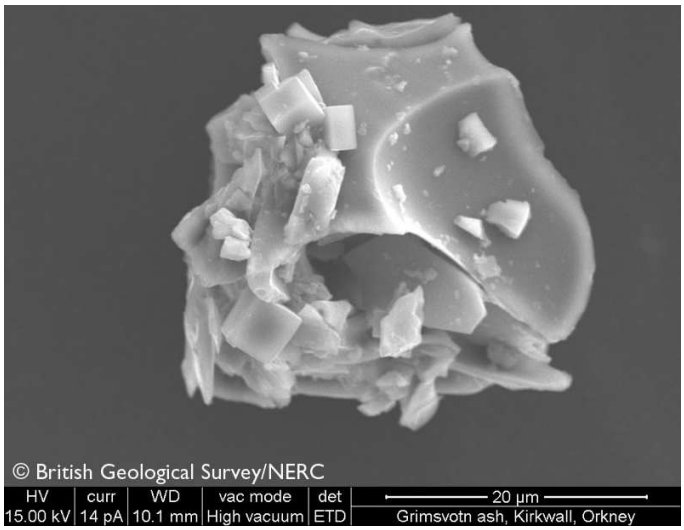

lar shapes, characteristic of explosive fragmentation. Fig. 1.8b shows a single glass particle with a diameter of $\sim 20\,\mu$m from a sample deposited in Orkney, Scotland, 964 km from the volcanic source. The small cubic structures stuck to the surface of the particle are likely to be halite crystals and probably formed when the particle

came into contact with ocean spray in the atmosphere. The wall of a gas bubble is visible on the particle, indicating it was formed by gas ascent and expansion driven fragmentation.

1.3 Remote sensing of volcanic ash

The remote sensing of volcanic ash can be broadly split into two categories: methods for rapid ash identification and methods that involve detailed radiative transfer modelling to retrieve the optical depth of the ash cloud as well as other properties such as the cloud top height and effective radius. The radiative transfer equation encapsulates the physics of radiative processes in the atmosphere and is required to interpret satellite measurements of volcanic clouds.

1.3.1 Radiometric basics and the radiative transfer (RT) equation

1.3.1.1 General RT equation

The *radiance*, $L(\mathbf{r}, \mathbf{s})$, is defined as the power per unit area, per unit solid angle at position $\mathbf{r}$ in the direction of the unit vector $\mathbf{s}$. An electromagnetic wave travelling through a scattering, absorbing and emitting elemental volume, dV, of length dl is attenuated by scattering and absorption and enhanced by scattering into the beam direction and thermal emission:

$$\frac{dL(\mathbf{r}, \mathbf{s}, \lambda)}{dl} = -\beta^{\text{ext}} L(\mathbf{r}, \mathbf{s}, \lambda) + \beta^{\text{sca}} L^{\text{s}}(\mathbf{r}, \mathbf{s}, \lambda) + \beta^{\text{abs}} L^{\text{b}}(\mathbf{r}, \mathbf{s}, \lambda, T), \tag{1.3}$$

where β^{ext}, β^{sca}, and β^{abs} are the volume extinction, scattering, and absorption coefficients, respectively. The extinction includes losses from scattering and absorption:

$$\beta^{\text{ext}} = \beta^{\text{sca}} + \beta^{\text{abs}}. \tag{1.4}$$

Providing the elemental volume is in thermal equilibrium with its surroundings then:

$$L^{\text{b}}(\mathbf{r}, \mathbf{s}, \lambda, T) = B(T(\mathbf{r}), \lambda), \tag{1.5}$$

where $B(T, \lambda)$ is the isotropic black-body radiance. The component of Eq. (1.8) due to scattering into the direction s can be expressed in terms of the ambient radiant field, $L^{\text{ambient}}(\mathbf{r}, \mathbf{s}')$, at the elemental volume:

$$L^{\text{s}}(\mathbf{r}, \mathbf{s}) = \int_0^{4\pi} \frac{P(\mathbf{s}', \mathbf{s})}{4\pi} L^{\text{ambient}}(\mathbf{r}, \mathbf{s}')\, d\Omega', \tag{1.6}$$

where $P(\mathbf{s}', \mathbf{s})$ is the phase function for the elemental scattering volume at $\mathbf{r}$, and $d\Omega'$ is the elemental solid angle centred on $\mathbf{s}'$. The phase function is the ratio of incident radiance from direction $\mathbf{s}'$ scattered into the direction $\mathbf{s}$ divided by the radiance that would be scattered into the same direction by an isotropic scatterer. $L^{\text{ambient}}(\mathbf{r}, \mathbf{s}') = L(\mathbf{r}, \mathbf{s}')$ providing there are no external sources. Typically the two enhancing terms in Eq. (1.8) are combined to form the *source function*, $J(\mathbf{r}, \mathbf{s}, T)$, such that:

$$J(\mathbf{r}, \mathbf{s}, T) = \tilde{\omega} L(\mathbf{r}, \mathbf{s}, \lambda) + (1 - \tilde{\omega}) L^{\text{b}}(\mathbf{r}, \mathbf{s}, \lambda, T), \tag{1.7}$$

and,

$$\frac{dL(\mathbf{r}, \mathbf{s}, \lambda)}{dl\beta^{\text{ext}}} = -L(\mathbf{r}, \mathbf{s}, \lambda) + J(\mathbf{r}, \mathbf{s}, T), \tag{1.8}$$

where $\tilde{\omega}$ is the single scattering albedo, defined as:

$$\tilde{\omega} = \frac{\beta^{\text{sca}}}{\beta^{\text{ext}}}. \tag{1.9}$$

1.3.1.2 Plane parallel atmosphere

In the plane parallel approximation curvature associated with the sphericity of the Earth is ignored, the atmosphere is assumed to be horizontally homogeneous, and the radiation field is assumed to be horizontally isotropic. In the plane parallel approximation, light paths are defined by $\mu = |\cos\theta|$ or $\mu' = \cos\theta$ where θ is the zenith angle.

In radiative transfer problems assuming a plane parallel atmosphere it is convenient to measure distance vertically in units of normal optical path or *optical depth*, τ, defined relative to the top of the atmosphere (TOA):

$$\tau(z) = \int_z^{z_{\text{TOA}}} \beta^{\text{ext}}(z')\, dz', \tag{1.10}$$

The optical depth, defined in this way, decreases with height to $\tau = 0$ at the TOA, such that:

$$d\tau = -\beta^{\text{ext}} \cos(\theta)\, dl. \tag{1.11}$$

The aerosol optical depth, τ_{a}, is defined as the optical depth from the TOA to the Earth's surface, and so includes extinction from the entire vertical aerosol column:

$$\tau_{\text{a}} = \tau(0) = \int_0^{z_{\text{TOA}}} \beta^{\text{ext}}(z')\, dz'. \tag{1.12}$$

The value of τ_{a} is the primary quantity retrieved from satellite TOA radiance measurements using detailed radiative transfer modelling, for example the Oxford – RAL Aerosol and Cloud (ORAC) retrieval scheme [*Kokhanovsky and de Leeuw*, 2009].

The radiative transfer equation in the plane parallel approximation can be expressed as:

$$\mu' \frac{dL(\tau, \mathbf{s}, \lambda)}{d\tau} = L(\tau, \mathbf{s}, \lambda) - J(\tau, \mathbf{s}, T, \lambda), \tag{1.13}$$

which can be separated into upward and downward components:

$$\mu \frac{dL^{\uparrow}(\tau, \mathbf{s}, \lambda)}{d\tau} = L^{\uparrow}(\tau, \mathbf{s}, \lambda) - J(\tau, \mathbf{s}, T, \lambda) \quad \text{for} \quad 0 < \theta < \frac{\pi}{2}, \tag{1.14}$$

and,

$$-\mu \frac{dL^{\downarrow}(\tau, \mathbf{s}, \lambda)}{d\tau} = L^{\downarrow}(\tau, \mathbf{s}, \lambda) - J(\tau, \mathbf{s}, T, \lambda) \quad \text{for} \quad \frac{\pi}{2} > \theta > \pi. \tag{1.15}$$

Solving Eq. (1.14) for the TOA upward radiance (the quantity measured by nadir viewing satellite), making use of the integrating factor $e^{-\tau/\mu}$, yields:

$$L^{\uparrow}(0, \mathbf{s}, \lambda) = L^{\uparrow}(\tau_0, \mathbf{s}, \lambda)\, e^{-\tau_0/\mu} + \frac{1}{\mu} \int_o^{\tau_0} J(\tau, \mathbf{s}, T, \lambda)\, e^{-\tau/\mu} d\tau, \tag{1.16}$$

where $\tau_0 = \tau_{\text{a}} + \tau_{\text{R}} + \tau_{\text{g}}$ is the total optical depth made up from the following components: the aerosol optical depth, τ_{a}, the optical depth due to Rayleigh scattering, τ_{R}, and the optical depth due to gaseous absorption, τ_{g}. The first term of Eq. (1.16) represents the upward radiance at the surface attenuated by the extinction through the atmosphere, whilst the second term represents the total light scattered or emitted into the beam direction at each layer in the atmosphere and then attenuated by the path from the layer to the TOA.

1.3.1.3 The source function

For treatments of the radiative transfer in the Earth's atmosphere, three components of the source function are considered: the diffuse field, $J^{\text{diffuse}}(\tau, \mathbf{s}, \lambda)$, the solar source, $J^{\text{solar}}(\tau, \mathbf{s}, \lambda)$, and the thermal source, $J^{\text{thermal}}(\tau, T, \lambda)$. The source function is then the sum of the three components:

$$J(\tau, \mathbf{s}, T, \lambda) = J^{\text{diffuse}}(\tau, \mathbf{s}, \lambda) + J^{\text{solar}}(\tau, \mathbf{s}, \lambda) + J^{\text{thermal}}(\tau, T, \lambda), \tag{1.17}$$

and the individual components can be expressed as:

$$J^{\text{diffuse}}(\tau, \mathbf{s}, \lambda) = \tilde{\omega} \int_o^{4\pi} L(\tau, \mathbf{s}', \lambda) \frac{P(\mathbf{s}', \mathbf{s})}{4\pi} d\Omega', \tag{1.18}$$

$$J^{\text{solar}}(\tau, \mathbf{s}, \lambda) = \tilde{\omega} E^0(\mathbf{s}_0) \frac{P(\tau, \mathbf{s}_0, \mathbf{s})}{4\pi} e^{\tau/\mu_0}, \tag{1.19}$$

$$J^{\text{thermal}}(\tau, T, \lambda) = (1 - \tilde{\omega}) B(T, \lambda), \tag{1.20}$$

where $E^0(\mathbf{s}_0)$ is the solar irradiance, $\mathbf{s}_0$ is the incident solar direction, and μ_0 is the magnitude of the cosine of the solar zenith angle. For typical atmospheric problems the dominance of each source component will vary with λ, and in some regimes components can be safely ignored. Generally three approximate regimes are considered: for $\lambda < 3.5\,\mu$m the solar and diffuse components dominate and the thermal component can be neglected; for $\lambda > 8.9\,\mu$m the solar term can be neglected; and in the intermediate regime, $3.5 < \lambda < 8.9\,\mu$m, care is required and all source components may be needed.

1.3.1.4 Aerosol extinction, the log-normal distribution, and the effective radius

Equation (1.12) describes the total optical path of aerosol in the atmosphere which is the primary quantity retrieved from satellite measurements. The extinction coefficient, β^{ext}, appearing in Eq. (1.12) is calculated according to:

$$\beta^{\text{ext}} = \int_0^{\infty} Q^{\text{ext}}(r, m(\lambda), \lambda) \pi r^2 N(r) dr, \tag{1.21}$$

where $Q^{\text{ext}}(r, m(\lambda), \lambda)$ is the extinction efficiency for a single particle, r is the particle radius, and $N(r)$ is the number of particles per unit volume with radii between r and $r + dr$. Extinction efficiencies must be computed with an appropriate scattering model: for spherical particles Mie theory is used, whereas for

non-spherical particles T-matrix methods can be used [*Bohren and Huffman*, 1983; *Mishchenko et al.*, 2000]. Interpretation of satellite measurements of aerosols requires *a priori* information about the complex refractive index, $m(\lambda)$, of particles, as well as their shape and size, because of the dependence of the extinction efficiency on these parameters. In most cases spherical particles, and therefore Mie theory, are assumed and so the dependence reduces to $m(\lambda)$ and $N(r)$.

In many instances the size distribution of atmospheric aerosols is well represented by a log-normal distribution:

$$n(r) = \frac{N_0}{\sqrt{2\pi}\ln(S)\,r}\exp\left\{\frac{[\ln(r)-\ln(r_{\mathrm{m}})]^2}{2\ln^2(S)}\right\}, \tag{1.22}$$

where N_0 is the total number of particles per unit volume, r_{m} is the median radius, and S controls the spread of the distribution. The effective radius, r_{e}, is an important parameter describing the distribution and is a retrieved quantity in the ORAC retrieval scheme. It is defined as the ratio of the third distribution moment, m_3, to the second, m_2:

$$r_{\mathrm{e}} = \frac{m_3}{m_2} = \frac{\int_0^\infty r^3 N(r)\,dr}{\int_0^\infty r^2 N(r)\,dr}. \tag{1.23}$$

For a log-normal distribution the effective radius can be expressed as:

$$r_{\mathrm{e}} = r_{\mathrm{m}}\exp\left(\frac{5}{2}\ln^2 S\right). \tag{1.24}$$

1.3.2 Ash flagging: Radiance (or brightness temperature) difference methods

Ash flagging methods allow the qualitative location of ash to be determined rapidly from satellite measurements and can provide a filter for detailed and computationally expensive retrievals such as the ORAC retrieval scheme. At infrared wavelengths with $\lambda > 8.9\,\mu$m the solar component of the source wavelength can be neglected. Furthermore, in the infrared extinction by atmospheric aerosols is dominated by absorption ($\tilde{\omega} \to 0$), and so the diffuse component of the source function can also be neglected. The equation for the TOA radiance, Eq. (1.16), therefore reduces to:

$$L^{\uparrow}(0,\mathbf{s},\lambda) = L^{\uparrow}(\tau_0,\mathbf{s},\lambda)\,e^{-\tau_0/\mu} + \frac{1}{\mu}\int_o^{\tau_0}(1-\tilde{\omega})\,B(T,\lambda)\,e^{\tau/\mu}d\tau, \tag{1.25}$$

If we further assume: a thin ash cloud with uniform temperature, T_c, in thermal equilibrium with its surroundings; that the atmosphere is perfectly clear apart from the ash cloud; and that the Earth can be assumed to be acting as a black body at T_s, then Eq. (1.25) at wavelength λ_1 becomes [*Prata*, 1989a]:

$$L^{\uparrow}(0, \mathbf{s}, \lambda_1) = B(T_s, \lambda_1)\, e^{-\tau_1/\mu} + \left(1 - e^{-\tau_1/\mu}\right) B(T_c, \lambda_1)\,, \tag{1.26}$$

and at a second wavelength λ_1:

$$L^{\uparrow}(0, \mathbf{s}, \lambda_2) = B(T_s, \lambda_2)\, e^{-\tau_2/\mu} + \left(1 - e^{-\tau_2/\mu}\right) B(T_c, \lambda_2)\,, \tag{1.27}$$

where τ_1 and τ_2 are the optical paths through the cloud at λ_1 and λ_2, respectively.

Figure 1.9: Optical thickness for 100 m aerosol plumes, calculated by *Grainger et al.* [2013]. Calculated assuming a log-normal distribution with $N_0 = 200\,\mathrm{cm}^{-3}$, $r_\mathrm{m} = 1\,\mu$m, and $S = 1.7$. Literature values for complex refractive indices were assumed. The plot also shows satellite wavelength channels for three instruments used for ash measurements.

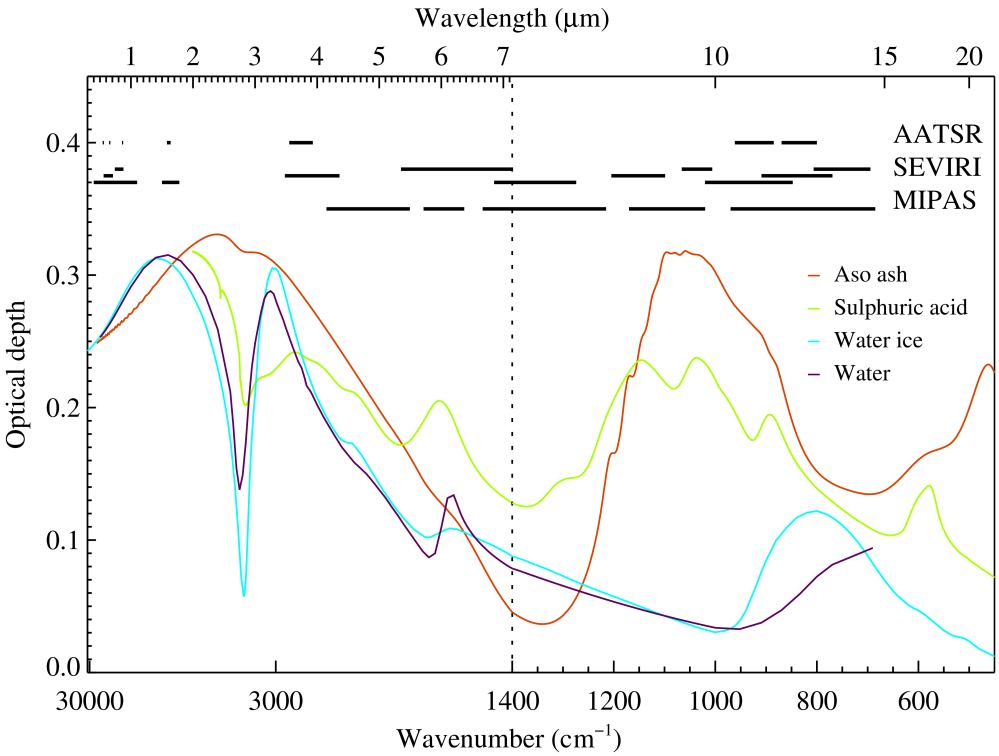

Figure 1.9, from *Grainger et al.* [2013], shows simulated optical paths through a 100 m ash cloud, as a function of wavelength, for four types of aerosol: Aso ash, sulphuric acid, ice, and water. Literature values for the complex refractive

index of the aerosols were assumed as well as a log-normal size distribution with $N_0 = 200\,\mathrm{cm}^{-3}$, $r_\mathrm{m} = 1\,\mu$m, and $S = 1.7$. It can be seen that from 11 to 12 μm the optical path of the ash and sulphuric acid (both present in ash plumes) decreases, whilst the optical path of water and ice increases. These differences in optical depth at different wavelengths relate to differences in TOA radiance (often expressed as brightness temperature, T_λ), via Eq. (1.26) and Eq. (1.27), and are widely exploited for ash flagging, e.g. *Prata* [1989b]; *Prata and Grant* [2001]; *Rose et al.* [2000]; *Corradini et al.* [2008]. Measurement channels at 11 and 12 μm are common on satellite imaging instruments, and negative values of $T_{11} - T_{12}$ are linked to ash. Various flagging schemes have been adopted for different instruments by investigating radiance differences. For example, *Lean* [2009] used $T_{11} - T_{12} < -0.1$ amongst other thresholds to flag for ash using measurements from the Advanced Along Track Scanning Radiometer (AATSR).

Brightness temperature methods can be used in some cases to estimate aerosol optical depth and effective radius. For example, *Prata and Prata* [2012] used a simple model involving the linearisation of Eq. (1.26) and Eq. (1.27), to retrieve estimates of τ_a and effective radius for the 2010 Eyjafjallajökull ash cloud from Spin Enhanced Visible and Infrared Imager measurements. However, although useful in many cases, temperature difference methods have problems when other atmospheric or surface conditions contribute to a negative $T_{11} - T_{12}$: for example strong temperature inversions near the surface, or areas containing Si-bearing minerals, such as deserts or wind blown dust, which can produce a negative $T_{11} - T_{12}$ for the same reasons as volcanic ash [*Grainger et al.*, 2013].

1.3.3 Detailed radiative transfer retrievals: ORAC

The ORAC forward model makes use of radiative transfer code to model the TOA radiance observed by a satellite as a function of aerosol microphysical properties (size and complex refractive index), using assumptions about the reflectance from the Earth's surface and the atmospheric state [*Kokhanovsky and de Leeuw*, 2009]. The radiative transfer code used in the ORAC forward model is the Discrete Ordinates Radiative Transfer (DISORT) software [*Stamnes et al.*, 1988], which solves Eq. (1.13) for a plane parallel atmosphere. The DISORT code is used within the ORAC forward model to calculate the reflectance and transmission of the amtosphere only for both the direct beam and diffuse radiation sources. There are three implementations: for the shortwave (thermal sources neglected), there is Lambertian fast forward model and the bidirectional reflectance distribution function (BRDF) fast for-

ward model; and there is the thermal infrared forward model for infrared channels which ignores the solar source function.

Within the Lamberian fast forward model the reflectance (the ratio of the incident solar radiance to the reflected TOA radiance) can be expressed as [*Kokhanovsky and de Leeuw*, 2009]:

$$R\left(\theta_0, \mathbf{s}\right) = R_{\mathrm{BD}}\left(\theta_0, \mathbf{s}\right) + \frac{T^{\downarrow}\left(\theta_0\right) T^{\uparrow}\left(\mathbf{s}\right) R_{\mathrm{L}}}{1 - R_{\mathrm{L}} R_{\mathrm{FD}}}, \tag{1.28}$$

where $R_{\mathrm{BD}}\left(\theta_0, \mathbf{s}\right)$ is the bi-directional reflectance of the atmosphere, $T^{\downarrow}\left(\theta_0\right)$ is the total transmission of the incident beam, $T^{\uparrow}\left(\mathbf{s}\right)$ is the total transmission in the viewing direction, R_{L} is the Lambertian (isotropic) reflectance of the surface, and R_{FD} is the diffuse reflectance of the atmosphere to diffuse radiance. $R_{\mathrm{BD}}\left(\theta_0, \mathbf{s}\right)$, $T^{\uparrow}\left(\mathbf{s}\right)$, and $T^{\uparrow}\left(\mathbf{s}\right)$ are computed using DISORT to generate look up tables for different aerosol properties and satellite viewing geometries. The BRDF forward model is more complicated because the surface reflectance is no longer isotropic and the diffuse and direct components of the radiance must be separated.

The ORAC model has been used to determine ash cloud properties by assuming particles have a log-normal size distribution (with S=1.77 fixed but with r_{m} a retrieved paramemter) and assuming the complex refractive index measured for Aso ash [*Grainger et al.*, 2013]. The primary retrieved parameter is the optical path of the ash cloud, which if the cloud is homogeneous can be expressed as: $\tau = \beta^{\mathrm{ext}} L$. The ash loading ($\mathrm{g\,m^{-2}}$) can then be claculated as:

$$m = \frac{\tau}{\beta^{\mathrm{ext}}} \rho \int_0^{\infty} \frac{4}{3} \pi r^3 n\left(r\right) dr \tag{1.29}$$

where ρ is the ash density. For a log-normal distribution this can be expressed as:

$$m = \frac{4}{3} \frac{N_0 \rho \tau}{\beta^{\mathrm{ext}}} \pi r_{\mathrm{e}}^3 \exp\left(2 \ln^2 S\right) \tag{1.30}$$

and N_0/β^{ext} is the average extinction per particle. Therefore if the ash optical path and the effective radius have been retrieved, m can readily be calculated. The CAA restriction on aviation in the presence of volcanic ash is a mass density less than $2 \times 10^{-3}\,\mathrm{g\,cm^{-3}}$ [*CAA*, 2010]. To convert m to a mass density requires knowledge of the ash cloud thickness, which could be provided by an independent measurement (e.g. balloon or lidar), or could be determined by assuming a typical value for β^{ext}. Alternatively, assuming the ash cloud height (a typical retrieved parameter) as the ash cloud thickens gives a minimum value for the ash density.

1.4 Volcanic ash complex refractive index

1.4.1 Definition of the complex refractive index

The complex refractive index of a material, m, is defined as the ratio of the speed of light in vacuum, c, to the phase velocity, $v_{\mathrm{p}} = \omega/k$, of light in the material [*Bohren and Huffman*, 1983]:

$$m = \frac{c}{v_{\mathrm{p}}} = \frac{ck}{\omega} = \sqrt{\frac{\epsilon\mu}{\epsilon_0\mu_0}}, \tag{1.31}$$

where ϵ and μ are the permittivity and permeability of the material. In general m, ϵ, and μ are functions of ω (i.e. the material is dispersive) and are complex. The complex refractive index can be expressed in terms of its real and imaginary parts as:

$$m = n + ik, \tag{1.32}$$

where n and k are real and positive. A plane wave, $\mathbf{E} = \mathbf{E}_0 \exp(i\mathbf{k}\cdot\mathbf{r} - i\omega t)$, travelling along the x-axis inside a material of complex refractive index, m, has the form:

$$\mathbf{E} = \mathbf{E}_0 \exp\left(-\frac{2\pi kx}{\lambda}\right) \exp\left(\frac{i2\pi nx}{\lambda} - i\omega t\right). \tag{1.33}$$

The imaginary part of the refractive index, k, causes the wave amplitude to decay, corresponding to the absorption of the wave energy by the material.

1.4.2 The complex refractive index of volcanic ash and modelling radiative transfer processes

The complex refractive index, $m(\lambda)$, of volcanic ash particles determines their scattering and absorption properties. For example, the Mie single particle extinction efficiency, $Q^{\mathrm{ext}}(r, m(\lambda), \lambda)$, depends only on the particle's size, complex refractive index, and the wavelength of the incident beam. If values of $m(\lambda)$ are assumed when modelling radiative transfer processes and they differ from the true complex refractive index of particles, then systematic modelling errors will be introduced propagating to modelling error associated with retrieved quantities. The composition of volcanic ash is known to vary considerably between different volcanic eruptions, and the composition of the volcanic ash may also differ significantly from the composition of the remnant magma and igneous rock of the volcano [*Wright et al.*,

2012; *Cashman and Rust*, 2016]. It is therefore important to have measurements of the complex refractive index for a range of volcanic eruptions and volcanic ash compositions. Ideally, eruption specific complex refractive index data would be used for analysing remote sensing data.

Figure 1.10 shows the variation in complex refractive index between various igneous rocks as well as a Mt Aso sample using some of the very limited available literature values (the references are detailed in Table 1.1). The plot on the bottom row of Fig. 1.10 shows the corresponding optical path, τ, for particles with these refractive indices, assuming a homogeneous ash cloud and a log-normal size distribution with parameters: $N_0 = 200\,\mathrm{cm}^{-3}$, $r_\mathrm{m} = 1\,\mu$m, and $S = 1.7$. It can be seen that there is considerable variation in the complex refractive indices, and that this translates to variation in the optical path of the ash cloud.

1.4.3 Existing measurements of volcanic ash complex refractive index

Despite the importance of knowing the complex refractive indices of volcanic ashes, existing measurements are very limited. Table 1.1 summarises the existing measurements of volcanic ashes, as well as the available data for various igneous rocks. The data for igneous rocks can be useful, but only ever provide an approximation to real ash particles which may differ considerably in composition from remnant volcanic rock from the same eruption. Table 1.2 summarises the experimental methods that have been applied to determine the complex refractive index of volcanic ash; references that detail the theoretical underpinning and experimental applications are given.

Measurements of the imaginary refractive index of volcanic ashes have been made using *diffuse reflectance* measurements. The measurements were made at UV-visible wavelengths [*Patterson*, 1981; *Patterson et al.*, 1983; *Krotkov et al.*, 1999] as well as NIR–IR wavelengths [*Patterson*, 1994]. The method involves preparing pellets of the sample combined with known quantities of a matrix medium such as barium sulphate, and then making total diffuse reflectance measurements of the sample employing an integrating sphere, as well as reflectance measurements of the background medium on which the pellet is mounted. The diffuse reflectance from the sample can then be modelled using a 2-stream approximations to the radiative transfer equation; a commonly used formulation being Kubelka-Munk theory [*Munk*, 1931]. The method requires knowledge of the real refractive index of the sample, which must be measured separately by another method, as well

Figure 1.10: The plots in the first two rows show the real and imaginary parts of the refractive index of various igneous rocks and Mt Aso ash particles. The references from which these values are taken are given in Table 1.1. The plot on the bottom row shows the corresponding optical path of 100 m thick homogeneous ash cloud, assuming a log-normal size distribution with parameters: $N_0 = 200\,\mathrm{cm}^{-3}$, $r_\mathrm{m} = 1\,\mu$m, and $S = 1.7$.

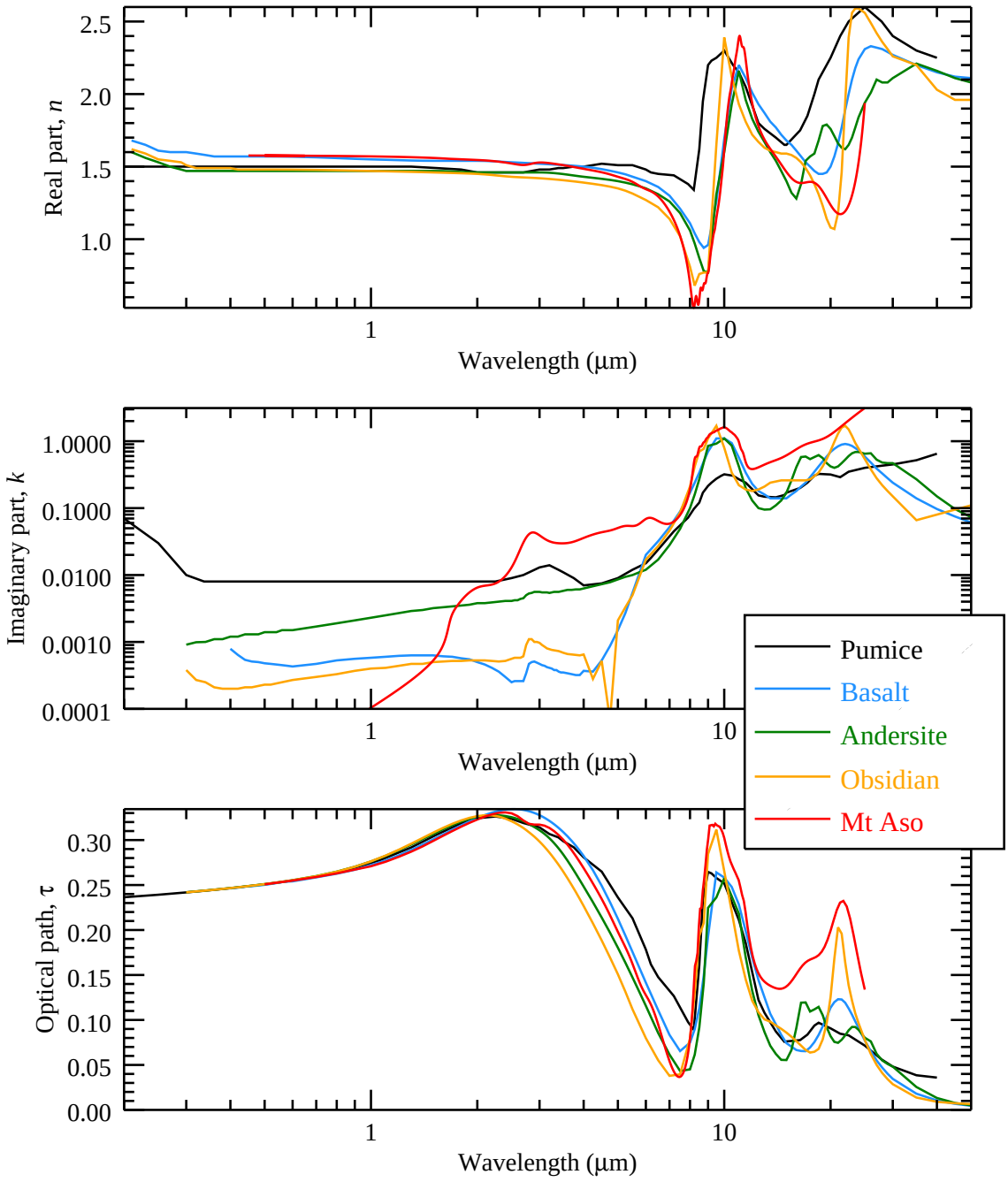

Table 1.1: Previous measurements of refractive indices of volcanic ash samples and igneous rocks.

Sample	Refractive index component	Spectral range (μm)	Reference
Volcanic ashes			
Mt St Helens	k only	0.3—0.7	*Patterson* [1981]
El Chichón	k only	0.3—0.7	*Patterson et al.* [1983]
Mayon	k only	1—20	*Patterson* [1994]
Mt Spurr	n and k	0.34, 0.36, 0.38	*Krotkov et al.* [1999]
Mt Aso	n and k	1—20	*Grainger et al.* [2013]
Eyjafjallajökull	k only	0.3—2.5	*Rocha-Lima et al.* [2014]
Set of 9 Japanese volcanoes	n only	~ 0.5 *	*Kobayashi et al.* [1976]
Igneous rocks			
Basalt	n and k	0.4—50	*Pollack et al.* [1973]
		0.185—0.4	*Egan et al.* [1975]
Andesite	n and k	0.4—50	*Pollack et al.* [1973]
		0.185—0.4	*Egan et al.* [1975]
Pumice	n and k	0.2—40	*Volz* [1973]
Obsidian	n and k	0.21—40	*Pollack et al.* [1973]
Granite	n and k	5—40	*Toon et al.* [1977]
Volcanic material from Oregon, USA	n only	~ 0.5 *	*Kittleman* [1963]

* Measurements made using the Becke line method with white light.

as knowledge of the size distribution of particles (scattering cross-sections are required, computed from Mie theory). There does not appear to be an account, in the literature, of how experimental uncertainties propagate into errors associated with the retrieved imaginary refractive indices, or any mention of modelling errors associated with the model approximations; values of k are typically reported to a precision of 0.0001, with no estimate of uncertainty.

The imaginary refractive index of Eyjafjallajökull ash, at 0.3 – $2.5\,\mu$m, was retrieved by *Rocha-Lima et al.* [2014] from measurements of the spectral reflectance of a mono-layer of the particles on Nuclepore® filters. The extinction efficiency of the mono-layer was calculated through a simple application of the Lambert-Beer

law, and was measured for a range of known filter mass loading values. Mie theory was then used to match the measured extinctions by varying both the real and imaginary part of the refractive index. They reported an average retrieved value for the real-refractive index of $n = 1.68$, which is significantly higher than other measurements of the real refractive index of Eyjafjallajökull ash. The real value was then kept constant at $n = 1.68$ and a retrieval of k was performed separately. The reported errors in k from this method were approximately 0.0005.

The real refractive index of volcanic ash has been measured by normal reflectance from a compressed pellet of the sample. The paper by *Krotkov et al.* [1999] indicates that Fresnel reflectivity expressions were used to determine the real refractive index of the pellet from measurement of the normal reflectance. However, there is likely to be a significant component of diffuse reflectance, due to surface anomalies, from compressed pellets of ash particles at the wavelengths investigated in the paper (0.34, 0.36 and $0.38\,\mu$m), and there is no indication of how this was accounted for. Similarly, compressed pellets typically have a significant void component, which causes the reflectance to differ from the Fresnel expressions, as outlined in *Felske et al.* [1984].

The real refractive index has been measured using the Becke line method for volcanic ash from a suite of Japanese volcanoes [*Kobayashi et al.*, 1976] and volcanic material from Oregon, USA [*Kittleman*, 1963]. The Becke line is an optical phenomenon observed at the interface between materials of different n when viewed under a microscope [*Becke*, 1896], and can be used to systematically check ash or rock samples against liquids of known refractive index until a match is found. Previous investigations have used white light for the microscope's sub-stage illumination, and so the reported results must be considered an average across visible wavelengths.

The complex refractive index of Aso ash, at 1–$20\,\mu$m, was retrieved by *Grainger et al.* [2013] from spectral extinction measurements of the suspended ash. The retrieval method, outlined in *Thomas et al.* [2005], involves forward modelling the extinction produced by the particles through Mie theory and using a damped harmonic oscillator model to represent the complex refractive index of the particles in terms of a finite set of band parameters. The method requires knowledge of the size distribution of the suspended ash particles, as well as *a priori* knowledge of the short-wave real refractive index of the particles. The result for Aso ash, presented in *Grainger et al.* [2013], is described as "preliminary", and uncertainties in the retrieved result were not given.

The complex refractive index of igneous rocks and glasses were measured by *Pollack et al.* [1973]. The method involved making highly polished slabs of the material. For wavelengths in the range $0.2 - 5\,\mu$m, Beer's law was applied to determine the imaginary refractive index from spectral transmissions measurements through slabs of varying thickness. Once k was known, n could be determined from spectral reflectance measurements of the highly polished glasses, at a single angle, through application of the Fresnel equation. In the wavelength range 5–$50\,\mu$m, the materials were reported to be too highly absorbing to make reliable transmission measurements, and complex refractive index was determined from spectral reflectance measurements alone. This required modelling the complex refractive index using the oscillator band model of *Spitzer and Kleinman* [1961]. Similar measurements of other volcanic materials were made by *Egan et al.* [1975], *Volz* [1973] and *Toon et al.* [1977]. However, measurements of these volcanic materials are only ever an approximation to real ash, and direct measurements of ash are preferable.

1.4.4 Other methods for measuring aerosol complex refractive index

This section details methods for measuring the complex refractive index of solid aerosol micro-particles, that could, in theory, be applied to volcanic ash. One group of methods for determining real refractive index involves measuring the transmission through particles suspended in a mounting liquid. These methods can be subset into three groups: the immersion liquid set method; the temperature method; and the wavelength method. The methods all rely on the principle that when there is match in real refractive index between the liquid and the particles, light scattering by the particles is minimised and the transmission of light through the suspension is maximised. The immersion set method involves preparing the powder in a set of mounting liquids of known refractive index and making measurements of the transmitted intensity through the suspension; the liquid that maximises the transmission has a real refractive index most closely matched to the particles. Typically a Gaussian-like distribution is seen if transmission is plotted against the real refractive index of the mounting liquids. The temperature method involves suspending the particles in a liquid with known thermo-optical properties. The temperature of the liquid-particle suspension is varied, keeping the wavelength of incident light constant, until a maximum in the transmitted light is observed. Similarly the wavelength method involves suspending the sample in a single liquid,

Table 1.2: Summary of techniques for measuring the refractive index of aerosols.

Method	Refractive index component	References: Theory and experimental
Previously applied to volcanic ashes		
Diffuse reflectance	k only	*Theory*: Kubelka-Munk [*Munk*, 1931] *Experimental*: *Patterson* [1981]; *Patterson et al.* [1983]; *Patterson* [1994]; *Krotkov et al.* [1999]
Filter sample reflectance	k only	*Theory*: Mono-layer particle reflectance; De-Lambert's law and Mie theory; *Martins et al.* [2009] *Experimental*: *Rocha-Lima et al.* [2014]
Normal reflectance from a compressed pellet	n only	*Theory*: Fresnel equations [*Hecht*, 1998] *Experimental*: *Krotkov et al.* [1999]
Extinction of suspended ash particles	n and k	*Theory*: Mie extinction and the CDHO model; *Thomas et al.* [2005] *Experimental*: *Grainger et al.* [2013]
Becke line method	n only	*Theory*: *Becke* [1896] *Experimental*: *Kittleman* [1963]; *Kobayashi et al.* [1976]
Applied to other aerosols		
Transmission measurements in immersion liquids	n only	*Niskanen and Erik Peiponen* [2013]
Angular scattering measurements	n and k	Ensemble: *Han et al.* [2009] Single particle: *Dick et al.* [2007]

but varying the wavelength of light to determine the maximum transmission, and relies on knowing the wavelength dependency of the liquid's real refractive index. *Niskanen and Erik Peiponen* [2013] reported that the methods can be used to determine the real refractive index of solid particles, at discrete wavelengths in the range 200 – 500 nm, to an accuracy of ± 0.005. However, a possible disadvantage of this method is that it required 4 g of sample per measurement, as reported in *Niskanen and Erik Peiponen* [2013], and multiple measurements were required to locate the transmission maximum. This poses problems when only a small mass of the sample of interest is available.

Another group of methods for measuring aerosol complex refractive index involve making angular scattering measurements, and rely on modelling the scattering produced by particles using Mie theory (in principle, T-matrix methods could be used for known non-spherical particles, but typically spheres are assumed). These methods can be subset into two groups: methods that measure the volume scattering coefficient, β^{sca}, for an ensemble of particles; and those that measure the angular scattering profile of individual particles. An example of measurements of an ensemble were performed by *Han et al.* [2009]: An integrated nephelometer was used to determine β^{sca} of ambient aerosol at three wavelengths in the visible, and along with aerodynamic particle sizing measurements Mie theory was used to retrieve the complex refractive index. Single particle aerosol scattering measurements of ambient aerosol particles were made by *Dick et al.* [2007] at 488 nm; scattered intensity was measured with PMTs at 7 different scattering angles, and sphericity was assessed from 8 different PMTs at $\Theta = 55°$; Mie theory retrievals could then be performed on sufficiently spherical particles, to determine n with a reported uncertainty of ± 0.02.

1.5 The volcanic ash samples

The Earth Observation Data Group (EODG), University of Oxford, has acquired a significant collection of volcanic ash samples over the years from a wide range of eruptions globally. Measurements performed on these samples will be presented in the remainder of this thesis. The samples are summarised in Table 1.3. The source volcano, collection date, and any information available about the samples are given. Samples will be referred to by their sample code as given in the table. The ash samples detailed in Table 1.3 orginate from sources covering the main volcanic rock types: basalt, andesite, dacite and rhyolite. For example, Grímsvötn

is a basaltic volcano with low silica content [*Hreinsdóttir et al.*, 2014], whereas the Chaitén volcanic caldera is rhyolitic having a high silica content [*Dagaa et al.*, 2014].

Table 1.3: Summary of the volcanic ash samples and their samples codes used to reference the samples. Where available literature references on how the samples were collected and processed are included. The mass percentage SiO_2 content of the sample, measured using XRF analysis, are also presented where available.

Sample code	Volcano, SiO_2, and sample description	Collection date
VA1	*Volcano:* Mount Aso, Japan. *SiO_2:* 52.6 %. *Description:* Collected by Tony Hurst from 1 m deposited layer. Wide particle size range.	1993
VA2	*Volcano:* Eyjafjallajökull, Iceland. *SiO_2:* 55.6 %. *Description:* Collected by Evegenia Ilyinskaya, from a bridge over the Holtsa river west of Ásólfsskáli farm, $\sim$6 km from source. Visibility was $<$ 10 m at time of collection due to ash.	17/4/2010
VA3	*Volcano:* Eyjafjallajökull, Iceland. *SiO_2:* 57.8 %. *Description:* A tourist sample originating from the 14$^{\text{th}}$ April eruption. Collection location unknown. Provided by Evegenia Ilyinskaya.	4/2010
VA4	*Volcano:* Grímsvötn, Iceland. *SiO_2:* 49.1 %. *Description:* Collected 200 m from the vent. Very coarse ash. Provided by Evegenia Ilyinskaya.	1/6/2011
VA5	*Volcano:* Grímsvötn, Iceland. *SiO_2:* 49.4 %. *Description:* Collected in Skaftafell. Provided by Árman Höskuldsson, University of Iceland.	25/5/2011
VA6	*Volcano:* Mount Etna, Italy. *SiO_2:* 47.0 %. *Description:* Collected near to Zafferana by Elisa Carboni, University of Oxford.	27–30/12/2002

Continued on the next page...

Table 1.3: *... Continued from the previous page.*

Sample code	Volcano and sample description	Collection date
VA7	*Volcano:* Eyjafjallajökull, Iceland. SiO_2*:* 58.5 %. *Description:* Collected in Gígjökull; decimal degrees (DD) coordinates: 63.676014, -19.633019. Believed to originate from the 19 – 20$^{\text{th}}$ May eruption. Collected by Daniel Peters, Rutherford Appleton Laboratory (RAL).	13/6/2010
VA8	*Volcano:* Eyjafjallajökull, Iceland. SiO_2*:* 59.2 %. *Description:* Collected in Gígjökull; DD coordinates: 63.66939, -19.630433. Believed to originate from the 19 – 20$^{\text{th}}$ May eruption. Collected by Daniel Peters, RAL.	13/6/2010
VA9	*Volcano:* Eyjafjallajökull, Iceland. SiO_2*:* 58.8 %. *Description:* Very proximal to vent; DD coordinates: 63.677737,-19.609212. Believed to originate from the 19 – 20$^{\text{th}}$ May eruption. Collected by Daniel Peters, RAL.	13/6/2010
VA10	*Volcano:* Mount Etna, Italy. SiO_2*:* 47.6 %. *Description:* Collected by Simona Scollo, National Institute of Geophysics and Volcanology.	1/7/2001
VA11	*Volcano:* Chaitén, Chile. SiO_2*:* 73.2 %. *Description:* Supplied by Tamsin Mather, University of Oxford. *Reference: Watt et al.* [2009]	2008
VA12	*Volcano:* Dabbahu, Afar region, Ethiopia. SiO_2*:* 71.7 %. *Description:* Collected by Clive Oppenheimer very close to the vent within days of the September eruption.	5/9/2005

Continued on the next page...

Table 1.3: *... Continued from the previous page.*

Sample code	Volcano and sample description	Collection date
VA13	*Volcano:* Dabbahu, Afar region, Ethiopia. *SiO_2:* 70.2 %. *Description:* Collected by Clive Oppenheimer very close to the vent within days of the September eruption.	5/9/2005
VA14	*Volcano:* Mount Etna, Italy. *SiO_2:* 47.1 %. *Description:* Overnight deposit collected by Giardini Naxos at DD coordinates: 37.8298095, 15.2698673.	1/11/2002
VA15	*Volcano:* Eyjafjallajökull, Iceland. *SiO_2:* 58.0 %. *Description:* Collected by Susan Louglin.	15–16/5/2010
VA16	*Volcano:* Mount Tongariro, New Zealand. *SiO_2:* 59.4 %. *Description:* Collected by Keith Towers.	2012
VA17	*Volcano:* Askja, Iceland. *SiO_2:* 70.7 %. *Description:* Sample taken from layer C of the 1875 eruption deposit. *Reference: Sparks et al.* [1981]	1981
VA18	*Volcano:* The Fontana lapilli deposit, Maya region, Nicaragua. *Description:* Layer C deposit, $< 65\,\mu$m fraction. Collected by Susan Louglin.	Currently unknown.
VA19	*Volcano:* Nisyros, Greece. *SiO_2:* 69.7 %. *Description:* $< 65\,\mu$m fraction. Collected by Susan Louglin. *Reference: Longchamp et al.* [2011].	2011
VA20	*Volcano:* Mount Okmok, Alaska, USA.	7/2008
VA21	*Volcano:* Augustine, Alaska, USA. *Reference: Larsen et al.* [2010].	13/1/2006
VA22	*Volcano:* Mount Spurr, Alaska, USA. *Reference: Harbin et al.* [1995].	8/1992
VA23	*Volcano:* Mount Redoubt, Alaska, USA.	1990

1.6 Thesis overview and motivation

The motivation for the work presented in this thesis is to improve measurements of the complex refractive index of volcanic ash particles over a broad range of wavelengths (from the UV and visible through to the infrared). These measurements are needed for modelling radiative transfer through suspended volcanic ash in the Earth's atmosphere and can be directly applied to improve remote sensing retrieval algorithms.

A substantial proportion of this thesis covers measurements of the transmission of radiation through a volcanic ash cloud suspended in an aerosol cell, using a Fourier transform spectrometer at infrared wavelengths and diffraction grating spectrometers in the visible and UV. This work builds on earlier work presented in *Grainger et al.* [2013], where the complex refractive index of Mt Aso ash was presented. The complex refractive index of ash particles can be retrieved from the measured extinction spectra using a classical damped harmonic-oscillator (CDHO) model to represent the complex refractive index of the ash in terms of a finite set of band parameters (representing the interaction of radiation with bound electrons within the ash). The CDHO model and the retrieval scheme are presented in *Thomas et al.* [2005]. In the earlier work a log-normal particle size distribution was assumed and the parameters N_0, r_{m}, and S were retrieved. However, difficulties were encountered modelling the measured extinction and this was likely because the size distribution was not well described by a log-normal distribution. The work presented in this thesis differs from previous work because a suite of sampling and sizing instruments were used to measure the mass and size distribution of particles directly after passing through the aerosol cell, allowing the measured size distribution to be used in retrievals. In addition, the wavelength range of the measurements has been extended by using diffraction grating spectrometers to make transmission measurements in the UV and visible.

The retrieval of complex refractive index from aerosol cell transmission measurements has significant advantages over other methods. Principally the method makes a direct measurement of the optical path of a suspended ash cloud in the lab, analogous to remote sensing measurements of ash clouds in the atmosphere. Furthermore, the method does not involve any physical alteration of the ash particles

which may affect their complex refractive index. The only other possibility allowing measurement over such a wide range of wavelengths would be measurements of the reflectance from polished slabs of the ash, previously applied to igneous rocks [*Pollack et al.*, 1973; *Volz*, 1973; *Egan et al.*, 1975; *Toon et al.*, 1977]. However, this would involve melting the ash to form pellets, altering its physical structure and likely affecting the complex refractive index.

Representing the complex refractive index of the particles in terms of the CDHO model requires *a priori* knowledge of the complex refractive index of the particle in the shortwave limit [*Thomas et al.*, 2005]. It is therefore necessary to have independent measurements of the complex refractive index of the volcanic ash at visible wavelengths. In Chapter 2 measurements of the complex refractive index of the ash samples are presented at three discrete wavelengths in the visible (450, 546.7, and $650\,$nm) using optical microscope measurements. The Becke line method was used to measure the real refractive index, n, and a new method involving measurements of the attenuation of light in individual particles is presented to determine the imaginary refractive index, k, of particles. A significant disadvantage of the optical microscope methods is they are limited by the resolving power of the microscope, and could only be applied to particles with radii larger than $10\,\mu$m. A significant proportion of atmospheric volcanic ash particles have smaller radii, and these particles tend to have lower settling velocities and are transported further.

Chapter 3 outlines a method for retrieving the real refractive index of submicron particles from angular reflectance measurements, close to the critical angle, of a colloidal suspension of the particles. The motivation for these measurements was to develop a method capable of measuring the real refractive index (the method is shown to have very low sensitivity to the imaginary refractive index) of the fine fraction of the ash, so that any variation in real refractive index with particle size could be investigated (by comparing with the Becke results). A coherent scattering model (CSM), developed by *Barrera and García-Valenzuela* [2003], is used to model the coherent reflectance from the colloid. A rigorous sensitivity analysis is performed to analyse the theoretical accuracy of the method and retrieval results are presented for experimental reflectance data on three samples: monodisperse polystyrene latex calibration particles, a polydisperse sand sample, and a polydisperse volcanic ash sample.

Chapters 4, 5, and 6 concern the transmission measurements of suspended volcanic ash particles in an aerosol cell. In Chapter 4 the theory needed to interpret the spectroscopic transmission measurements as well as the microphysical sizing

measurements is outlined. Chapter 5 outlines the experimental method and apparatus, and presents the results of calibration measurements performed on pure quartz (SiO_2) samples. In Chapter 6 results for the mass extinction efficiency (MEC) of various volcanic ash samples are presented. The complex refractive index of two quartz samples and two Eyjafjallajökull ash samples are retrieved using the CDHO model. The complex refractive index of the Eyjafjallajökull ash is applied to satellite remote sensing measurements using the ORAC retrieval scheme. Differences in retrieved quantities, compared to assuming the refractive index of pumice measured by *Volz* [1973], are discussed.

Chapter 2

Optical microscope measurements of complex refractive index

2.1 Published work and contributions

A portion of the work presented in this chapter has been published in *Ball et al.* [2015]. Part of the work was performed by James Ball as an MPhys student project, designed and supervised by myself and Don Grainger. Before this work began, I performed initial Becke line measurements refining the method, calibrated the microscope and determined the CCD camera pixel resolution. Measurements of the complex refractive index of 10 samples were performed by James Ball as well as the calibration of the attenuation method, under my supervision. Help interpreting the results from a volcanological perspective was provided by Tamsin Mather and David Pyle (both of the Department of Earth Sciences, University of Oxford). Technical assistance and advice was provided by Dan Peters (RAL). The relations between complex refractive index and compositional parameters, presented in this chapter but not in the published paper, were determined by myself and Gemma Prata (Department of Earth Sciences, University of Oxford).

2.2 Introduction

The chapter details optical microscope measurements made to determine the complex refractive index of volcanic ash samples at wavelengths of $450\,\text{nm}$, $546.7\,\text{nm}$, and $650\,\text{nm}$. The motivation for these measurements was to establish reference complex refractive indices for each of the volcanic ash samples at wavelengths in the visible. The real part of the ashes' refractive index was measured using the long-established Becke line method. A new and novel method for determining the

imaginary part of the refractive index, from measurements of the attenuation of light within individual particles, will be introduced.

2.2.1 A review of the Becke line method; real refractive index

The Becke line test is a technique used in transmitted-light microscopy and was first outined by the mineralogist Friedrich Johann Karl Becke [*Becke*, 1896]. The technique allows the relative real refractive index of two materials to be established. For the application to aerosol particles, the most useful method is to systematically compare the aerosol to immersion liquids of known refractive index.

The Becke line is an optical phenomenon associated with the vertical interface between two substances with differing real refractive indices when observed on the stage of an optical microscope in a sub-stage illumination set-up. The Becke line is a line of concentrated bright light that either appears just inside or just outside the particle's boundary. The Becke line is only visible when the particle is slightly out of focus (i.e. the focal point of the microscope's objective lens lies just above or below the particle) and providing the real refractive index of the particle differs from the medium in which it is immersed. For the Becke line to be seen the sample must be illuminated from below by nearly parallel light. This is best achieved with a long focal length condensing lens and with the sub-stage aperture diaphragm stopped down to render the incident light nearly parallel.

Aerosol particles commonly have a lens-like shape; they are thicker at their centre compared to their edge. Figures 2.1a and 2.1b demonstrate how such particles can refract sub-stage incident light. The two media depicted in the figures have real refractive indices N (shown as the blue medium) and n (shown as white), and $N > n$. Figure 2.1a shows a particle immersed in a material with a lower refractive index. Light incident on the centre of the particle is minimally refracted whilst light incident close to the edge of the particle is greatly refracted. Figure 2.1a demonstrates that if such a particle is viewed with the microscope's objective focal point just above the particle, a concentration of light is seen inside the particle's boundary. Figure 2.1b demonstrates the refraction of light by a particle with a lower refractive index than the immersion material. In this case, the divergent effect of the particle on the incident light means that when viewed with the focal point above the particle, a concentration of light is seen outside the particle's boundary. In summary, with the focal point above the particle, a concentration of light is seen on the side of the boundary that has a higher refractive index.

Figure 2.1: Demonstration of Becke line formation. The curvature of lens-like particles refracts sub-stage incident light, as demonstrated in **(a)** and **(b)**, resulting in the formation of a Becke line when viewed with the microscope's focal point just above (or below) the particle. A vertical interface also results the formation of a Becke line, as demonstrated in **(c)** and **(d)**. For a vertical interface the effect relies on the incident light being slightly converging or diverging. Finally, **(e)** and **(f)** show microscope images of a particle with the Becke line inside and outside of the particle's boundary, respectively. The two media have real refractive indices n and N, such that $N > n$.

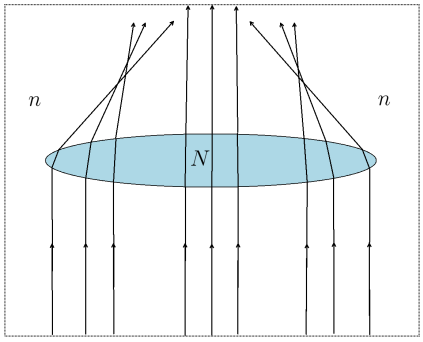

(a) A lens like particle with a higher refractive index than the immersion medium.

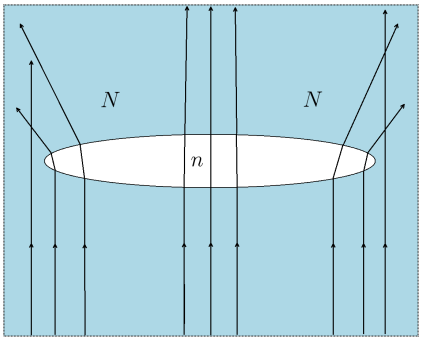

(b) A lens like particle with a lower refractive index than the immersion medium.

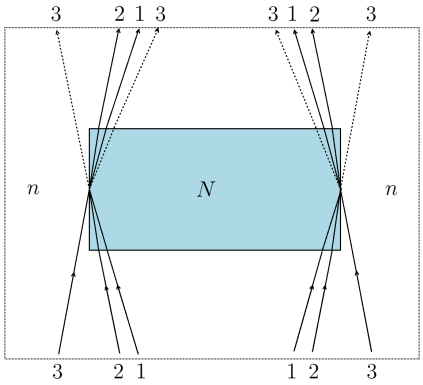

(c) A slab with a higher refractive index than the immersion medium.

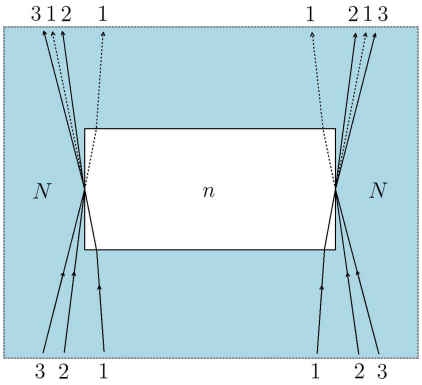

(d) A slab with lower refractive index than immersion medium.

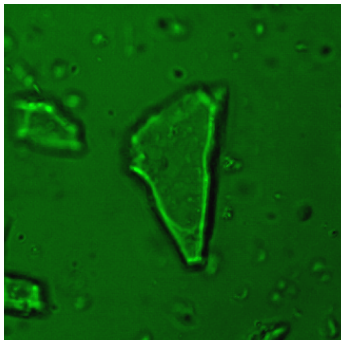

(e) Microscope image of the Becke line inside a particle.

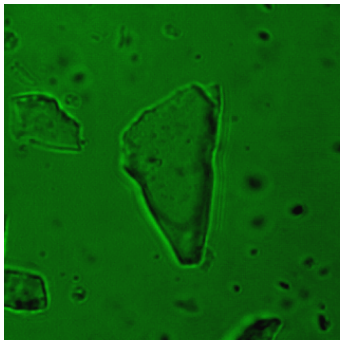

(f) Microscope image of the Becke line outside a particle.

Figures 2.1c and 2.1d demonstrate how a vertical interface also produces a Becke line. When viewed with the microscope's focal point above the slab refraction, ordinary reflection and total internal reflection act together to produce a concentration of light on the side of the vertical boundary in the medium with a higher refractive index.

Conversely, if the particle or slab is viewed with the focal point of the microscope's objective lens below (rather than above) the fragment, the Becke line is seen on the side of the boundary with a lower refractive index. Thus, if the focus of the microscope is moved gradually from below the fragment to above, the Becke line is seen to cross the boundary from the medium with a lower refractive index into the medium with a higher refractive index. Figure 2.5 shows a series of images of Cape Verde Dust with a 546.1 nm (green) optical filter in place: In the successive images the objective focal point is moved from below the particles to above, and the Becke line is seen to move from the immersion liquid into the particles, thereby indicating that the dust sample has a higher refractive index than the immersion liquid.

An aerosol sample can be systematically checked against liquids of known refractive index in order to determine the refractive index of the sample. Typically the sample refractive index is found to sit between two liquids (in the tests performed the refractive index of the liquids was incremented by 0.01), although a perfect match with the sample may also be observed. For samples such as volcanic ash, there is commonly a degree of inhomogeneity with respect to composition and therefore refractive index. In such cases a survey of numerous particles within the sample can be performed to establish the mean value of the real refractive index of the sample. A detailed description of the experimental method adopted is given below.

A disadvantage of the Becke line method is that it cannot return the refractive index of individual particles, because the sytematic checking of the sample against different liquids requires that a new suspension be generated and different particles are observed. Rather, through a statistical approach surveying the direction of Becke line displacement for a number of particles in each liquid, the mean real refractive index of particles in the sample can be estimated. Another disadvantage of the method is that it is limited by the resolving power of the microscope, and therefore can only be used to determine the refractive index of particles above a particular size.

2.2.2 A new attenuation method for the imaginary refractive index

Previous studies have used diffuse reflectance techniques to find the imaginary component of the refractive index of volcanic ash, for example *Patterson* [1994] and *Rocha-Lima et al.* [2014]. This approach identifies the value of k over a broad range of wavelengths but requires complex iterative procedures and forward modelling as well as knowledge of the size distribution of the ash and assumptions about the shape of particles. The attenuation method, presented in this chapter, is a relatively simple technique to determine k at discrete wavelengths in the visible spectrum. It requires no *a priori* knowledge of the size distribution or shape of particles.

Figure 2.2: Diagram of two beams of light passing through the ash/liquid mixture. The beam labelled L_0 passes through unattenuated whereas the beam labelled L_1 is attenuated due to absorption by the particle. The path length of light through the particle is d.

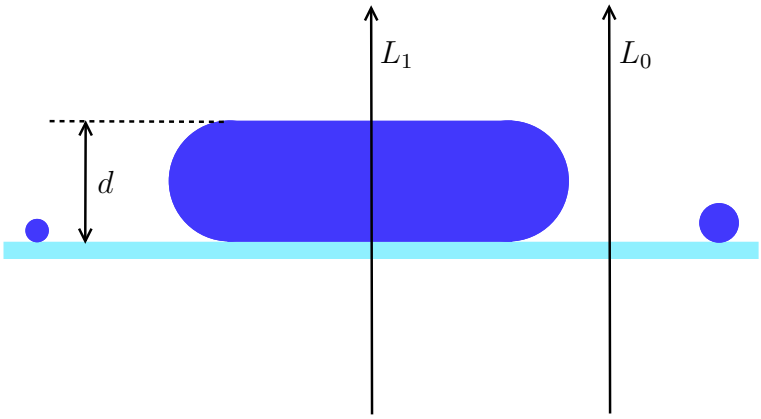

The principle of the new method is to measure the attenuation of light through individual particles observed using the optical microscope, as illustrated in Fig. 2.2. If the particle is suspended in a non-absorbing liquid which closely matches the particle's real refractive index, then light passes directly through the particle without changing direction due to refraction. In addition, the matching real refractive indices mean reflectance at the particle-liquid boundary is negligible, and reflectance at the slide-particle boundary is equal to reflectance at the slide-liquid boundary. Therefore the path of light that travels past a particle is identical to the path of light travelling through the particle, except that the light travelling through the particle is attenuated due to absorption by the particle. With reference to Fig. 2.2, we can therefore take the transmission, T, of the particle to be the ratio of the

radiance of light passing through the particle, L_1, to the radiance of light passing by the particle, L_o, such that:

$$T = \frac{L_1}{L_0} = e^{-\beta^{\mathrm{abs}} d}, \tag{2.1}$$

where β^{abs} is the volume absorption coefficient of the particle and d is the path length of light through the particle. The volume absorption coefficient is related to the imaginary part of the particle refractive index, k, and the wavelength of light, λ, by:

$$\beta^{\mathrm{abs}} = \frac{4\pi k}{\lambda}. \tag{2.2}$$

It will be demonstrated that CCD digital images of particles in matched refractive index liquids observed through the optical microscope can be analysed to measure L_0 and L_1, and a method to measure d will be outlined, such that k can be calculated according to:

$$k = \frac{\lambda}{4\pi d} \ln\left(\frac{L_0}{L_1}\right). \tag{2.3}$$

2.2.3 X-ray fluorescence (XRF) compositional analysis

In addition to the complex refractive index measurements, compositional analysis was performed on the same ash samples by Gemma Prata of the Department of Earth Sciences, University of Oxford. The aim was to investigate the connection between complex refractive index and the elemental and molecular composition of the samples.

XRF is a well-established technique for measuring the bulk composition of materials [*Grieken and Markowicz*, 2002]. It relies on the principle that when a material is exposed to high energy X-rays or gamma radiation with energy greater than the ionisation potential electrons are ejected from constituent atoms, including electrons from inner atomic orbitals. The ionised atoms are unstable and electrons in higher energy orbitals fall to fill the empty inner orbitals, resulting in the secondary emission of photons with energy quanta characteristic of the atom. Statistical analysis of the secondary emission can be used to determine the atomic and molecular composition of the material.

2.3 Experimental method and materials

2.3.1 Preliminary considerations

2.3.1.1 Optimal microscope set-up

The Becke line is best observed when the sample is illuminated from below by near-parallel light; similarly near-parallel light is required for the attenuation method. This was achieved by employing a long focal length condensing lens and by stopping down the sub-stage aperture diaphragm to close to its minimal diameter. The microscope used was the Nikon Eclipse 80i shown in Fig. 2.3, and a 20x objective lens was used in all tests. A halogen lamp provided white light sub-stage illumination. The sample was viewed through the microscope eyepiece and via a CCD digital camera connected to a computer monitor.

Before experiments it was necessary to check that the condensing lens and aperture were aligned with the objective lens along the optical axis of the system. Then, with the aerosol fragments in focus, the vertical height of the condensing lens was adjusted to give a uniform illumination of the field of view. With the halogen light brightness set to its maximum value and with the chosen wavelength filter in place in front of the camera sensor, the sub-stage aperture diaphragm was stopped down to nearly the smallest aperture — the criteria being to maximise the contrast and visibility of the Becke line at the edges of aerosol fragments.

Figure 2.3: The Nikon Eclipse 80i optical microscope used in the Becke and attenuation experiments. The full microscope is shown in (a) and the microscope stage is shown in (b).

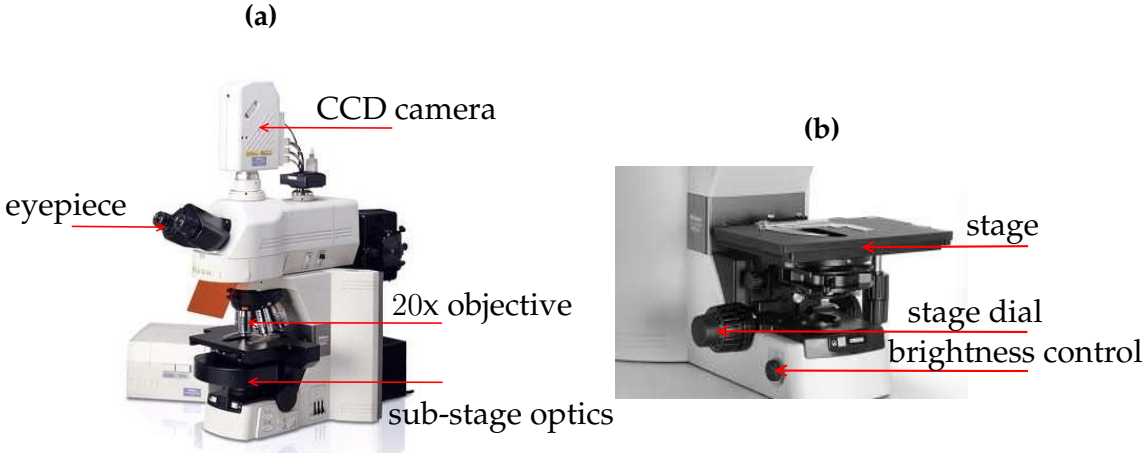

2.3.1.2 The refractive index liquids and discrete wavelength filters

The refractive index matching liquids used in the tests on aerosol samples were manufactured by Cargille Laboratories. The liquids used were incremented by 0.0100 in refractive index, and covered a range of refractive indices from $n = 1.4600$ to $n = 1.8000$ (all having a standard error of $\pm\, 0.0002$). The quoted refractive index values were for light of 589.3 nm and a temperature of $25\,^{\circ}$C.

The tests was performed on each sample at three different wavelengths in the visible: 450 nm, 546.7 nm and 650 nm. This was achieved using optical filters placed in front of the CCD camera sensor. Each filter had a bandwidth (full width at half maximum) of 10 nm about the peak transmission wavelength. The filters were produced by Comar Optics Ltd (and had item codes: 450 *IL* 25, 546 *IL* 25 and 650 *IL* 25). The liquid refractive indices are standardised and quoted at a wavelength of 589.3 nm. However, the Cauchy equations for the liquids were also supplied by their manufacturer, so that their refractive index at a given wavelength could be determined. The coefficient of variation with temperature of the liquids is known, so that the refractive index of the liquid at a given temperature could, in theory, be calculated. However, all tests were performed in a laboratory thermostatically regulated at $25\,^{\circ}$C, to ensure the Cauchy liquids were accurate without the need for temperature corrections.

2.3.1.3 Sample preparation

A clean spatula was used to transfer approximately 3 mg of the ash sample into a clean vial. Approximately 5 ml of the chosen Cargille liquid was then added using a micropipette with a clean tip. The aerosol sample and liquid mixture was shaken vigorously to disperse the particles evenly in the liquid. The ratio of Cargille liquid to particulate sample ensured that the fragments were well separated by the liquid, providing a clear view of the liquid-fragment boundaries. Care was taken to prevent contamination of the refractive index liquids; the liquid's container was quickly re-sealed after use. Two or three drops of the mixture were placed onto a clean glass slide with a glass cover-slip on top. The sample slide could then be mounted on the microscope stage for viewing.

2.3.1.4 Pixel scale and resolving the Becke line

The pixel scale of the CCD was determined by taking images of a graticule using the microscope in a set-up identical to that used in tests on ashes. Fig 2.4a shows a

full field-of-view image of the graticule using the 20x objective lens and Fig 2.4c is a digitally magnified version showing the graticule's $10\,\mu$m increment. From the graticule images it was determined that the width of one pixel was $0.20\,\mu$m.

Figures 2.4b and 2.4d show fragments of an ash sample mounted in a Cargille liquid. Fig. 2.4b is the full field-of-view image, and Fig. 2.4d is a digitally magnified version. Figures 2.4c and 2.4d are identically magnified. The image of the ash fragments was recorded with the focal point of the objective slightly below the particles in order to produce a Becke line (the line is visible just outside the particles indicating the ash has a higher refractive index than the Cargille liquid). Figures 2.4c and 2.4d can be compared to determine the minimum particle size for which the Becke line can be easily distinguished. It can be seen that for particles with a radius less than $1\,\mu$m it becomes very difficult to distinguish the Becke line; the minimum particle radius that the Becke line technique can be applied to using this set-up is $1\,\mu$m. However, all of the Becke tests performed were for particles with $r > 10\,\mu$m. This was so that they could be directly compared to results for the imaginary refractive index from the attenuation method, which could only be applied to particles larger than $10\,\mu$m, as will be discussed in more detail later.

2.3.2 Method: Real refractive index

Initially a slide of the sample was prepared, using the method detailed above, in the 1.50 refractive index liquid, or a different starting liquid was chosen if it was believed likely closer to the refractive index of the sample. The Becke line displacements of fragments in the field-of-view were checked by raising the 20x objective lens so that its focal point passed from below the particles to above. When the refractive index of the particles differed greatly from the liquid the particle contrast was high and the Becke line displacement was larger for a given elevation of the objective lens. Additionally, the Becke line displacement was seen to be in the same direction for the vast majority of particles. When the refractive index of the liquid was close to the mean particle refractive index the particles appeared fainter and blended more into the surrounding liquid. The Becke line displacements for the same particles were checked at each of the three wavelengths — $450\,$nm, $546.7\,$nm and $650\,$nm — by putting the appropriate filter in front of the digital camera sensor. Still images of the Becke line displacement as the objective lens was raised were recorded, so that they could be re-analysed and checked later. This became particularly useful when there was a significant degree of inhomogeneity in the sample and when close to matching the sample's refractive index. The

Figure 2.4: The pixel width was measured as $0.20\ \mu$m using images of the graticule: shown in (a) and (c). The images (a) and (b) are full field-of-view images of the graticule and VA4 fragments, respectively. The images (c) and (d) are identically magnified versions of (a) and (c), respectively. It can be seen that the Becke line can be resolved for particles larger than $1\ \mu$m.

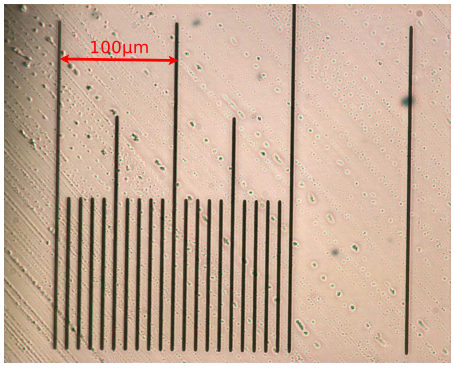

(a) Full field-of-view image of the graticule.

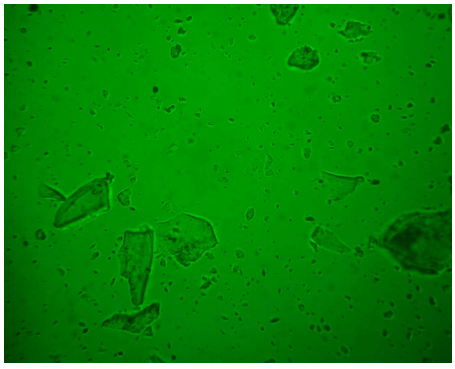

(b) Full field-of-view image of VA4 fragments.

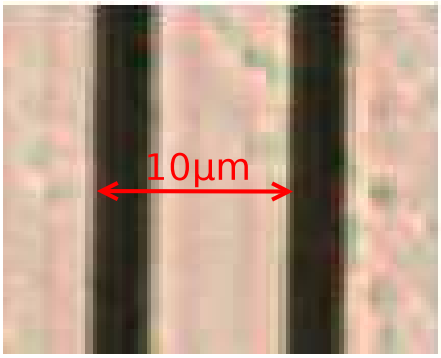

(c)

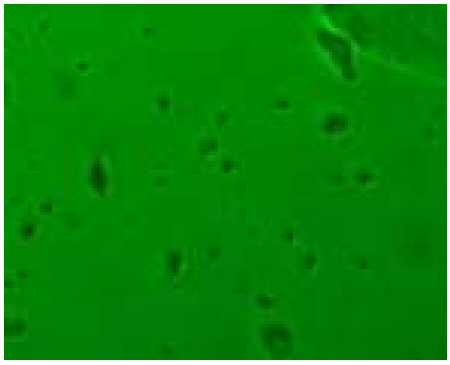

(d)

Becke line displacements of sample particles were systematically checked and recorded in different refractive index liquids to deduce the real refractive index of the sample. Figure 2.5 shows an example of the Becke line displacements when the 20x objective lens focal point is raised from under to above particles. In this example, the Becke line is seen to move from liquid into particles, indicating the fragments have a higher refractive index than the mounting liquid.

The task of determining the mean particle refractive index was simpler when the refractive index of particles in the sample was nearly homogeneous. If this was the case, systematically checking the particles against the liquids typically determined that the particle refractive index fell between two liquids incremented by 0.01, or a near perfect match with a single liquid was found. When the particle refractive index was found to lie between two liquids, it was appropriate to assign

Figure 2.5: In images (a) through to (d) the objective lense's focal point was raised from below the particles to above the particle and the Becke line moves into the particles, indicating they have a higher refractive index than the liquid. The sample was VA4 in the 1.50 Cargille refractive index liquid and the 546.7 nm filter was mounted.

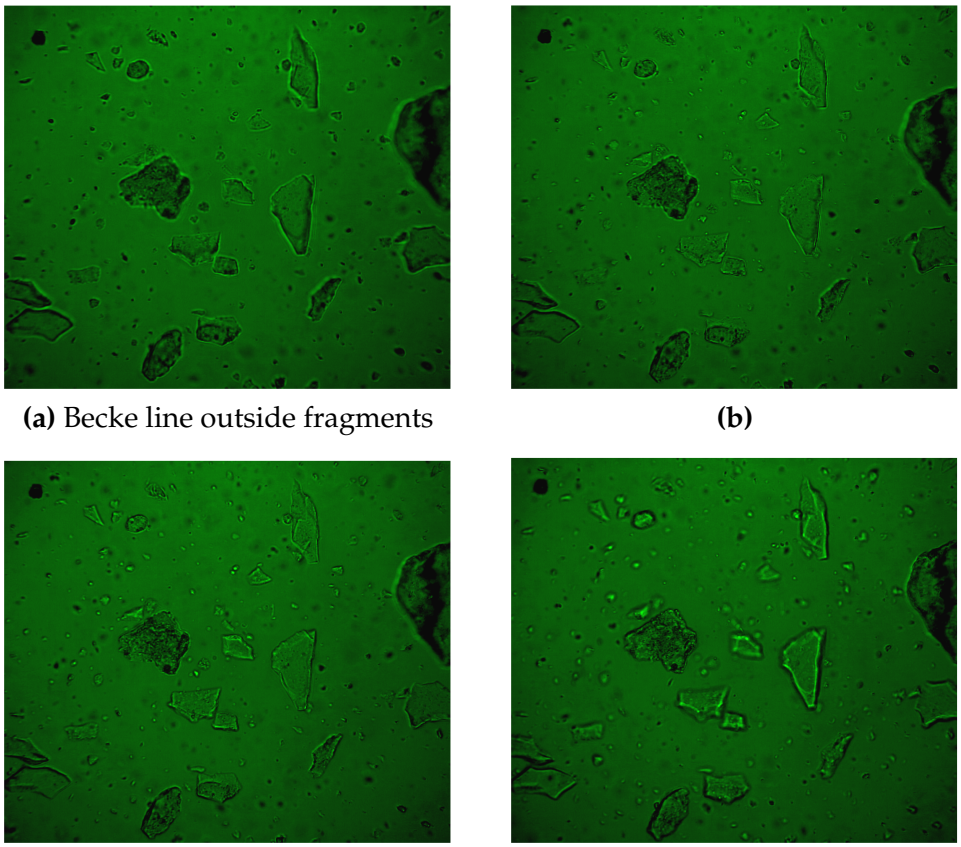

(a) Becke line outside fragments **(b)**

(c) **(d)** Becke line inside fragments

the refractive index of the particle to be the mid-point refractive index of the two liquids.

However, the refractive index of particles in a typical sample of volcanic ash has a noticeable degree of inhomogeneity. Once the refractive index of the liquid was close to the sample, it was common to see Becke lines passing in opposite directions over the boundaries of different particles and with some particles appearing to blend with the liquid. In such cases a survey of 30 particles was taken in a number of mounting liquids. Table 2.1 shows an example of the results of such a survey. A disadvantage of the Becke line method is that it is not possible to analyse the same particles in different refractive index liquids. Therefore the results of the survey, presented in Table 2.1, are for a different set of 30 particles in each liquid.

From Table 2.1 it would be concluded that out of 30 particles, 7 particles have a refractive index of 1.595, 6 have a refractive index of 1.60, and 18 have a refractive index of 1.605. A number-weighted average could then be taken, giving the mean refractive index of the ash as 1.602. Note that for simplification in this example the corrections to the refractive index of the liquids for wavelength, using the liquids' Cauchy equations (see Section 2.3.1.2), have not been applied.

Table 2.1: An example survey of 30 particles in three different liquids observing whether the Becke line displaces into or out of the particles as the objective lens is raised.

	Number of particles		
Cargille liquid, n	Into	Blending	Out
1.59	30	0	0
1.60	18	6	7
1.61	0	0	30

2.3.3 Method: Imaginary refractive index

The principle of the attenuation method was outlined in Section 2.2.2. The mean refractive index of an ash sample was first determined using the Becke line method given above. The ash sample was then mounted in the Cargille liquid that most closely matched its real refractive index. With reference to Fig. 2.2, it was necessary to measure the radiance of light passing through an individual particle, L_1, the radiance of light passing through only the mounting Cargille liquid, L_0, and the particle depth, d, so that Eq. (2.3) could be used to determine the imaginary refractive index of the particle. The intensities L_1 and L_0 were determined from analysing the digital images of ash fragments.

2.3.3.1 CCD camera calibration

The photographs taken from the CCD digital camera were stored as bitmap images, where each pixel had a red (R), green (G) and blue (B) coordinate, ranging from 0 to 255. The gamma correction applied to the images was set to one to avoid non-linearity between input luminescence and output pixel coordinates. To convert pixel measurements to transmission, neutral density filters of quoted absorbance[1], $\mathcal{A}$, with values: 0.1, 0.15, 0.2, 0.3, 0.6, 1, and 2 were used to provide known

[1]Defined as: $\mathcal{A} = -\log_{10} T$,

Figure 2.6: Camera calibration: neutral density filters were used to determine the relationship between transmission and R, G or B pixel value for wavelength 650, 546.7 or 450 nm, respectively. A close linear relationship was found at the three wavelengths with a small zero-point offset.

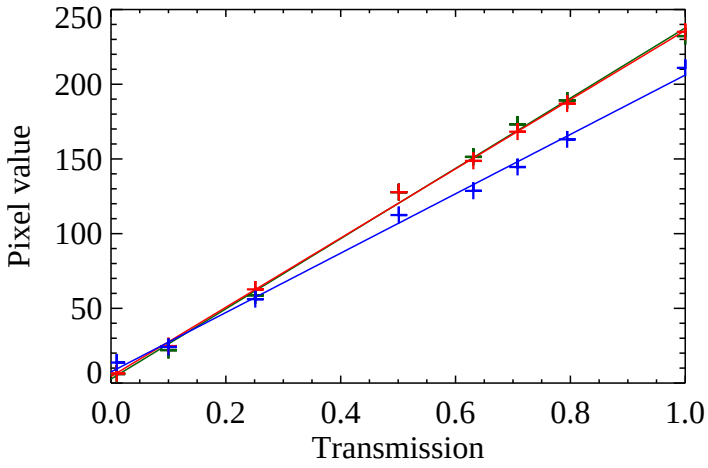

readings of transmission and hence relative radiance. For each of the wavelengths of the filtered, illuminating light, a set of images was taken of the neutral density filters, as well as one of the unobstructed stage (100% transmission) and one of the stage obstructed by a thick, opaque medium (0% transmission). The brightness of the microscope lamp was set at each wavelength so that the maximum pixel value read just below 255 for a photograph of the unobstructed stage, providing the widest possible range of values from which to calibrate the camera. Figure 2.6 shows the camera calibration results. It can be seen that the R (at 450 nm), G (at 546.7 nm) and B (at 650.0 nm) pixel values have a close linear correlation to the radiance of light with a small zero-point offset.

It follows that transmission could be related to the pixel value according to:

$$T = \frac{L_1}{L_0} = \frac{X_1 - C}{X_0 - C}, \tag{2.4}$$

where X_1 and X_0 were the R, G or B pixel values for the attenuated and unobstructed light, respectively, and C is the zero-point offset at the relevant wavelength. Substituting into Eq. (2.3) yields and expression for the imaginary refractive index in terms of pixel values:

$$k = \frac{\lambda}{4\pi d} \ln\left(\frac{X_0 - C}{X_1 - C}\right). \tag{2.5}$$

2.3.3.2 Particle measurements

An ash sample was prepared, using the method detailed in Section 2.3.1, in the matching Cargille liquid. An individual ash particle was selected and the microscope stage was positioned so that the particle was located at the focal point of the 20x objective lens. Photographs of the ash particle were taken with each of three wavelength filters in place. These images were analysed and for each fragment the average colour coordinate of a square of pixels located at the centre of the particle was measured and assigned as the value of X_1. The process was restricted to particles larger than $10\,\mu$m, because of the limit in sensitivity of the camera (the attenuation is proportional to d) and also in order to average over an acceptable number of pixels at the centre of the particle. The average colour coordinate was also recorded for four squares of pixels outside of the particle (where light was unobstructed), then averaged and assigned as the value of X_0. The length, x_1, and breadth, x_2, of the particle in pixels were also measured and converted into microns using the pixel scale ($1\,\text{pixel} = 0.20\,\mu$m). Figure 2.7 shows an example of this analysis applied to a particle image.

Figure 2.7: Photograph of an ash fragment of VA22 (Mount Spurr, 8/1992 eruption) with the 546.7 nm filter in place. The average G coordinate was calculated for a square of pixels at the centre of the particle and for 4 unobstructed locations outside the particle. The width and breadth of the particle are also shown, as well as the image scale.

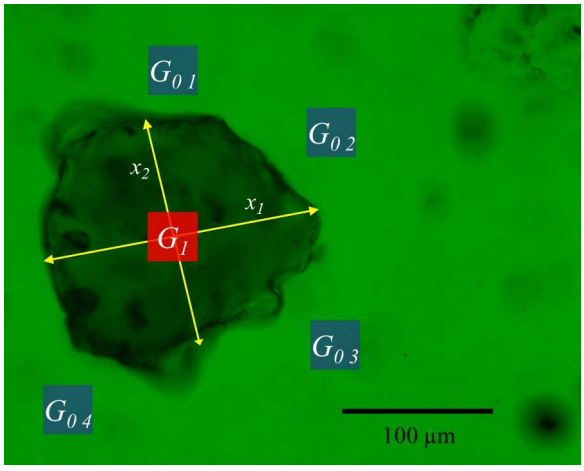

The depth of the particle, d, was calculated as follows. The relative vertical position of the base of the particle was located by positioning the stage so that the microscope image was focused on the upper surface of the glass slide. The position of the stage was then read from the stage dial, which was accurate to the nearest

micron. The stage was then adjusted to focus the upper surface of the particle, visible due to small imperfections on the particle's surface. The new vertical position was read from the dial and the difference between the previous reading was calculated to give the particle depth, d. The value of the imaginary refractive index for the particle was then calculated using Eq. (2.5). Finally the particle was assigned to one of three categories based on its appearance: *clear* (crystal or vitric), *opaque* (dark), or *intermediate*. This process was repeated for a survey of 30 particles in each sample, at each wavelength of light.

2.3.3.3 Generation of k from individual particle measurements

To find a value for the imaginary part of the refractive index which was representative of the ash sample as a whole, an appropriate method of averaging the k values of the particles was required. Due to effects such as fragmentation of the erupted particles, there was no guarantee that chemical composition, and therefore k, was independent of particle size [*Zimanowski et al.*, 2003].

The ash samples were assumed to be an external mixture of individually homogeneous particles. Therefore, an effective imaginary part of the refractive index for the samples was calculated by taking a volume-weighted average of a sample of N particles:

$$k_{ash} = \frac{\sum_{i=1}^{N} V_i k_i}{\sum_{i=1}^{N} V_i} \tag{2.6}$$

where V_i are the volumes of the individual particles. The exact morphology of the individual particles was not recorded. However, it could be considered reasonable to model an ash particle with width, length and depth measurements as either an idealised cuboid or an idealised ellipsoid, and in both cases $V \propto x_1 x_2 d$. The fact that only the *relative* volume of the particles mattered meant that the product of the particle dimensions ($x_1 x_2 d$) could be taken to be a basis for the weights. The uncertainties in k_{ash} were calculated as the volume weighted standard deviation about the volume weighted mean.

2.3.3.4 Validation

To validate the method's ability to find the complex refractive index of volcanic ash, a control substance with a known complex refractive index was measured. A Hoya neutral density glass of class *ND-03* was used because:

- it had levels of attenuation similar to that of volcanic ash,

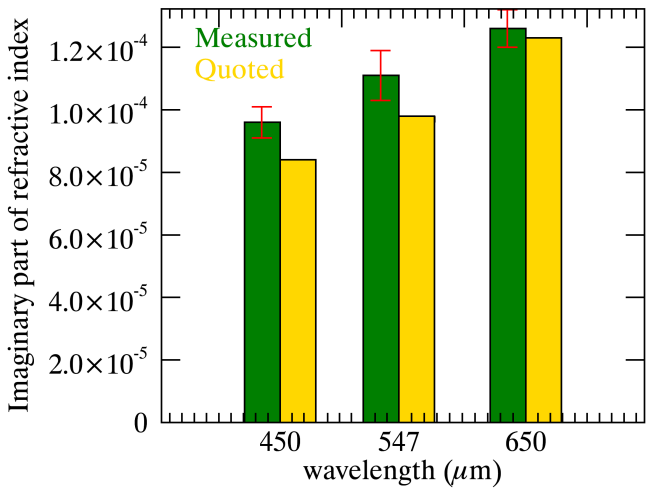

Figure 2.8: A comparison of the imaginary part of the refractive index of the Hoya neutral density glass quoted by the manufacturer (shown is the gold bars) and values retrieved using the attenuation method (shown as green bars). The errors are given by the standard deviation of the weighted sample mean, calculated from the individual particle weights and the spread in the measured k values.

- it was manufactured to be homogeneous throughout its structure,
- the real part of the refractive index and the internal transmission were precisely quoted over a wide range of wavelengths.

To roughly emulate the morphology and size distribution of volcanic ash, the glass was crushed, producing fragments ranging in size and shape. The Becke line test was used to determine the real part of the refractive index for the control sample at 450.0 nm, 546.7 nm and 650.0 nm. At each wavelength, the measured values matched the values quoted by the manufacturer to within the resolution set by the incrementation of the refractive index liquids ($\Delta n = 0.01$). The attenuation method was used to retrieve the imaginary part of the refractive index. A comparison of the measured values to the manufacturer's quoted values is shown in Figure 2.8. At 650.0 nm the measurements show a close match to the value quoted by the manufacturer. However, at 450.0 nm and 546.7 nm the manufacturer's values were slightly below the measured values. The imaginary part of the refractive index of the *ND-03* glass was significantly less than most of the ashes measured, typically by an order of magnitude. Furthermore, as the differences ($< 2 \times 10^{-5}$) between the measured and quoted glass k values were significantly less than the reported errors ($> 4 \times 10^{-5}$) on the ash samples, also usually by an order of magnitude, they were not investigated further.

2.4 Results and Analysis

2.4.1 Real and imaginary refractive index

The real part of all 22 ashes was measured using the Becke line method and the results are presented in Table 2.2. The imaginary part of a subset of 11 of the ashes was measured using the new attenuation method and the results are presented in Table 2.3 — in future the method will be applied to all ashes to complete the set. This subset of samples was also classified according to their average particle volume, average aspect ratio and the categories (*clear*, *intermediate* and *opaque*) of individual particles. Figure 2.9 shows the results for the 11 ashes for which both the real and imaginary refrective indices were measured.

The real part of the refractive index was measured to a precision of ± 0.01, determined by the resolution of the mounting liquids. The ash with the smallest real refractive index at all wavelengths was VA11 Chaitén with values of 1.508 at 450 nm, 1.502 at 546.7 nm and 1.499 at 650 nm. The ash with largest real refractive index at all three wavelengths was VA5 Grímsvötn with values of 1.629 at 450 nm, 1.608 at 546.7 nm and 1.597 at 650 nm. The expected dispersion relation, of real refractive index decreasing with wavelength in the visible, was found to apply for all samples (excluding VA13, which showed near-constant real refractive index), and can be seen in Fig.2.9a.

The imaginary refractive index was measured for ~ 30 particle in each sample, and the volume averaged mean was calculated according to Eq. (2.6); these are the values reported in Table 2.3. The volume averaged value of k gives an effective imaginary refractive index, representative of the ash sample as a whole. The uncertainty associated with the value of k was calculated as the volume weighted standard deviation about the volume weighted mean. Within a sample, the majority of the individual k measurements were clustered around a modal peak, with some samples showing secondary peaks at higher k values, demonstrating the different classes of particles present. Unsurprisingly, the particles with the lower values of k were generally classified as *clear* and the *intermediate* and *opaque* particles were more highly absorbing.

Within the given errors the results for k of VA15 (Eyjafjallajökull 15-16/5/2010) matched those for Eyjafjallajökull ash investigated by *Rocha-Lima et al.* [2014] at 546.7 nm and 650.0 nm. The value of k at 450.0 nm was below that given by *Rocha-Lima et al.* [2014]. Nonetheless, the proximity of these results for differently retrieved samples is encouraging. The values of k for the ashes in *Patterson* [1981]

Table 2.2: The real part of the refractive index of the ash samples at 450, 546.7 and 650 nm measured using the Becke line method. The value of n is the mean from a survey of 30 sampled particles, and the uncertainties are from the resolution of the refractive index liquids used.

	Real part of the refractive index, n		
Ash Sample	450 nm	546.7 nm	650 nm
VA1, Aso, 1993	1.577 ± 0.01	1.562 ± 0.01	1.553 ± 0.01
VA2, Eyjafjallajökull, 17/4/2010	1.572 ± 0.01	1.562 ± 0.01	1.554 ± 0.01
VA3, Eyjafjallajökull, 2010	1.554 ± 0.01	1.546 ± 0.01	1.548 ± 0.01
VA4, Grímsvötn, 1/6/2011	1.623 ± 0.01	1.608 ± 0.01	1.596 ± 0.01
VA5, Grímsvötn, 25/5/2011	1.629 ± 0.01	1.608 ± 0.01	1.597 ± 0.01
VA6, Etna, 27–30/12/2002 [a]		1.600 ± 0.01	
VA7, Eyjafjallajökull, 6/2010	1.554 ± 0.01	1.543 ± 0.01	1.536 ± 0.01
VA8, Eyjafjallajökull, 6/2010	1.554 ± 0.01	1.538 ± 0.01	1.536 ± 0.01
VA9, Eyjafjallajökull, 6/2010	1.560 ± 0.01	1.543 ± 0.01	1.541 ± 0.01
VA10, Etna, 7/2001	1.599 ± 0.01	1.589 ± 0.01	1.581 ± 0.01
VA11, Chaitén, 2008	1.508 ± 0.01	1.502 ± 0.01	1.499 ± 0.01
VA12, Afar, 26/9/2005	1.521 ± 0.01	1.513 ± 0.01	1.507 ± 0.01
VA13, Afar, 26/9/2005	1.516 ± 0.01	1.516 ± 0.01	1.519 ± 0.01
VA14, Etna, 1/11/2002	1.605 ± 0.01	1.593 ± 0.01	1.582 ± 0.01
VA15, Eyjafjallajökull, 15–16/5/2010	1.561 ± 0.01	1.553 ± 0.01	1.554 ± 0.01
VA16, Tongariro, 2012	1.537 ± 0.01	1.529 ± 0.01	1.527 ± 0.01
VA17, Askja	1.516 ± 0.01	1.510 ± 0.01	1.509 ± 0.01
VA19, Nisyros	1.520 ± 0.01	1.516 ± 0.01	1.515 ± 0.01
VA20, Okmok, 7/2008	1.594 ± 0.01	1.582 ± 0.01	1.579 ± 0.01
VA21, Augustine, 13/1/2006	1.535 ± 0.01	1.530 ± 0.01	1.529 ± 0.01
VA22, Spurr, 8/1922	1.570 ± 0.01	1.563 ± 0.01	1.555 ± 0.01

[a] Missing data: Becke line was indistinguishable for 450 and 650 nm.

and *Patterson et al.* [1983], at the wavelengths under investigation here, were in the range $0.0006 - 0.004$. This fits reasonably well with the values of k found by the attenuation method.

Across all three wavelengths VA14 (Etna 01/11/2002) was measured to be the most highly absorbing with values of the imaginary part of the refractive index of 0.00201 at 450.0 nm, 0.00230 at 546.7 nm and 0.00208 at 650.0 nm. The sample was formed predominantly of dark finely-crystalline particles. Furthermore, even the *clear* glass particles appear more absorbing compared to the *clear* glass particles within the other samples. Across all three wavelengths VA17 (Askja) was meas-

Table 2.3: The imaginary part of the index of refraction for the volcanic ash samples at 450.0 nm, 546.7 nm and 650.0 nm measured using the new attenuation method. The values of k are volume weighted averages of ~ 30 sampled particles and the uncertainties are the volume weighted standard deviation.

	Imaginary part of the refractive index, k		
Ash Sample	450.0 nm	546.7 nm	650.0 nm
VA1, Aso	0.00136 ± 0.00012	0.00124 ± 0.00018	0.00124 ± 0.00020
VA5, Grím.	0.00155 ± 0.00027	0.00142 ± 0.00018	0.00129 ± 0.00017
VA11, Chai.	0.000314 ± 0.00012	0.000508 ± 0.00021	0.000471 ± 0.00018
VA14, Etna	0.00170 ± 0.00018	0.00193 ± 0.00021	0.00208 ± 0.00023
VA15, Eyja.	0.000488 ± 0.00047	0.00108 ± 0.00058	0.000850 ± 0.00069
VA16, Tong.	0.000696 ± 0.00024	0.00106 ± 0.00029	0.00107 ± 0.00028
VA17, Askja	0.000221 ± 0.000083	0.000159 ± 0.000044	0.000147 ± 0.000039
VA19, Nis.	0.000230 ± 0.000061	0.000325 ± 0.000094	0.000391 ± 0.00014
VA20, Okmok	0.00126 ± 0.00016	0.00145 ± 0.00023	0.00130 ± 0.00017
VA21, Aug.	0.000425 ± 0.00010	0.000549 ± 0.000097	0.000517 ± 0.00013
VA22, Spurr	0.000939 ± 0.00010	0.00105 ± 0.000083	0.00125 ± 0.00010

Table 2.4: Characterisation of the volcanic ash specimens. The particle categorisation, average volume and average aspect ratio of the subset of 11 ash samples for which imaginary refractive index measurements were also made.

Volcano	Number of particles in category			Av. particle volume	Av. aspect ratio
	Clear	Intermediate	Opaque	($\times 10^6\ \mu$m^3)	
VA1	18	6	6	0.31 ± 0.4	1.54 ± 0.41
VA5	0	27	3	0.13 ± 0.1	1.71 ± 0.63
VA11	19	8	3	0.07 ± 0.1	1.58 ± 0.61
VA14	10	6	14	0.31 ± 0.4	1.42 ± 0.41
VA15	7	14	9	1.2 ± 3.0	1.47 ± 0.30
VA16	2	15	13	0.38 ± 0.7	1.40 ± 0.36
VA17	30	0	0	0.049 ± 0.03	1.74 ± 0.57
VA19	23	4	3	0.018 ± 0.02	1.81 ± 0.73
VA20	5	18	8	0.1 ± 0.1	1.56 ± 0.53
VA21	14	16	0	2.4 ± 2.0	1.38 ± 0.42
VA22	12	11	7	2.0 ± 1.0	1.39 ± 0.33

Figure 2.9: The (a) real and (b) imaginary parts of the refractive index of 11 ash samples at 450, 546.7 and 650 nm. The errors of the real part are from the resolution of the refractive index liquids. The errors in the imaginary part are from the volume weighted standard deviation about the volume weighted mean, from a survey of ~ 30 particles.

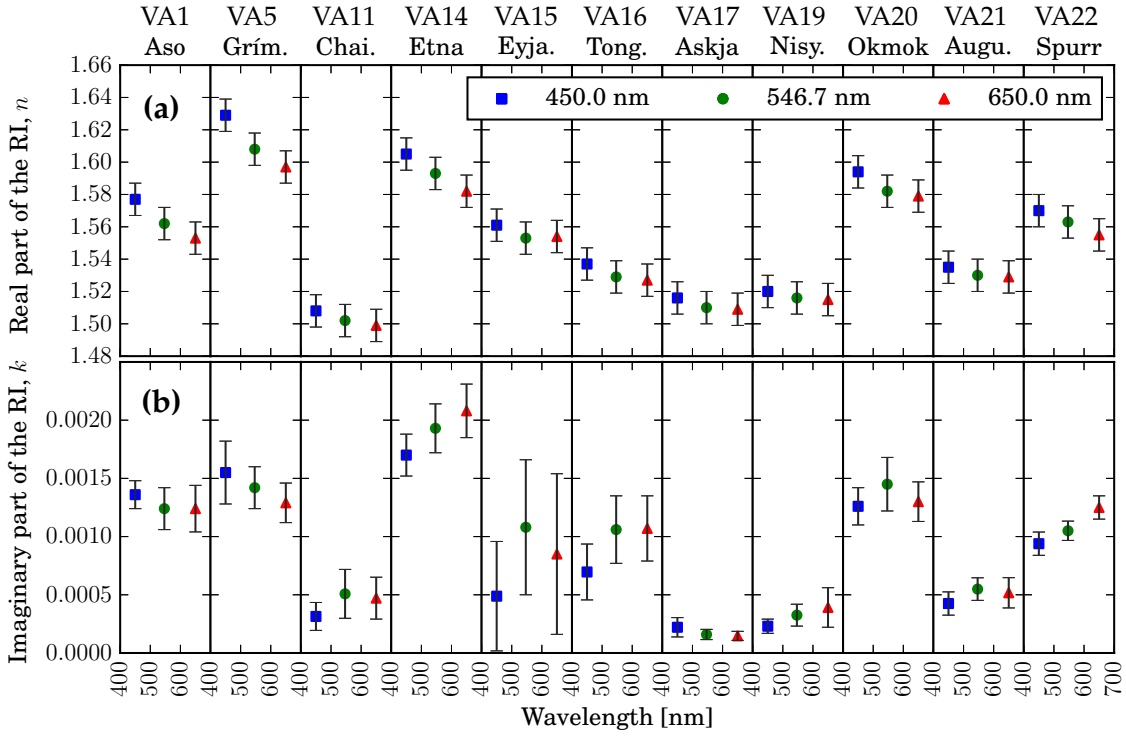

ured to have the smallest values of the imaginary part of the refractive index with values of 0.000221 at 450.0 nm, 0.000159 at 546.7 nm and 0.000147 at 650.0 nm. All particles measured in this sample appeared glassy and were categorised as *clear*.

There was a large variation in the errors associated with each of the different samples. The error in k for VA15 (Eyjafjallajökull 15-16/5/2010) was especially large; indeed it was comparable to the retrieved value. The particles within this sample were particularly difficult to classify. Not only were the *clear*, *intermediate* and *opaque* groups not easily spotted but the particles themselves were not homogeneous. The particles were often dark in parts but clear in others whilst some contained fused fragments or bubbles encased in glass. VA22 (Spurr 8/1992), on the other hand, exhibited the smallest relative error. The particles within this sample could be classified with ease, and the particles were tightly distributed about the modal values of each group.

2.4.2 Composition and complex refractive index

Table 2.5: XRF bulk compositional analysis of the ash samples, performed by Gemma Prata. Values are given as percentages by mass.

Sample Code	SiO_2	TiO_2	Al_2O_3	Fe_2O_3	MnO	MgO	CaO	Na_2O	K_2O	P_2O_3	SO_3	LOI*	Total
VA1	52.55	0.81	17.50	8.44	0.121	3.32	8.18	2.64	1.624	0.228	1.035	2.88	99.34
VA2	55.56	1.68	14.39	10.17	0.224	2.32	4.99	5.00	1.813	0.405	0.207	2.78	99.53
VA3	57.77	1.42	14.70	9.32	0.208	3.34	4.92	5.28	2.047	0.249	0.010	−0.16	99.10
VA4	49.13	2.84	13.25	14.87	0.213	5.20	9.63	2.82	0.468	0.305	0.377	−0.42	98.67
VA5	49.40	2.75	13.27	14.61	0.207	5.44	9.71	2.80	0.477	0.298	0.160	−0.93	98.21
VA6	47.04	1.69	16.32	11.37	0.169	6.27	10.42	3.31	1.921	0.524	< 0.003	−0.02	99.03
VA7	58.48	1.28	14.30	8.90	0.210	2.85	4.36	5.50	2.225	0.234	0.006	−0.08	98.28
VA8	59.19	1.30	14.58	8.92	0.209	2.89	4.33	5.51	2.243	0.234	< 0.003	−0.11	99.28
VA9	58.75	1.30	14.47	9.02	0.208	3.03	4.44	5.44	2.176	0.240	0.003	−0.03	99.05
VA10	47.56	1.66	17.16	10.98	0.168	5.34	9.90	3.67	1.958	0.542	0.015	−0.23	98.71
VA11	73.23	0.15	13.83	1.60	0.062	0.34	1.51	4.18	2.957	0.062	< 0.003	1.33	99.25
VA12	71.68	0.24	11.72	3.25	0.091	0.12	0.58	4.83	4.404	0.023	< 0.003	2.20	99.14
VA13	70.21	0.29	12.07	3.52	0.097	0.26	0.91	4.65	4.303	0.035	0.015	2.77	99.12
VA14	47.14	1.76	17.47	11.38	0.171	5.18	9.89	3.60	2.048	0.574	0.056	−0.09	99.18
VA15	58.03	1.44	14.76	9.32	0.206	3.27	4.95	5.29	2.031	0.256	< 0.003	−0.16	99.40
VA16	59.37	0.65	16.41	6.59	0.065	1.98	4.32	2.22	1.258	0.136	0.246	5.96	99.20
VA17	70.65	0.84	12.28	4.35	0.110	0.84	2.56	3.96	2.317	0.167	< 0.003	1.02	99.10
VA19	69.67	0.31	13.16	2.34	0.090	0.96	1.49	2.49	3.573	0.081	0.015	4.85	99.02

*LOI refers to Loss On Ignition.

Table 2.5 summarises the results of the XRF compositional analysis, performed on the samples by Gemma Prata. The analysis was performed on pellets formed by melting ash particles and re-solidifying; the results give the bulk composition of the ash sample. The values given in Table 2.5 are percentages by mass for the particular oxide. Of the 22 available samples, a subset of 18 were analysed using XRF.

2.4.2.1 SiO_2 and complex refractive index

Figure 2.10 shows mass percentage SiO_2 plotted against: (a) real refractive and (b) imaginary refractive index. The data points have been numbered according to their source volcano. The uncertainty in the SiO_2 mass percentages obtained from the XRF analysis is less than 1 % [*Rousseau*, 2001]. The uncertainties in refractive index are included as error bars.

Figure 2.10 shows a distinct gap in data points for SiO_2 mass percentages between 60 and 69. *Reubi and Blundy* [2009] compared the published SiO_2 content of igneous whole rocks to the SiO_2 content of melt inclusions, and found that although igneous whole rocks show a peak in abundance for intermediate compositions (59 to 66 wt % SiO_2) the melt inclusions have a distinct dearth in abundance in this

Figure 2.10: The relationship between mass percentage SiO_2 content and: **(a)** real refractive index; **(b)** imaginary refractive index. The data points are numbered accordring to their source volcano, as given in the key. The uncertainty associated with the real and imaginary refractive indices are shown using error bars.

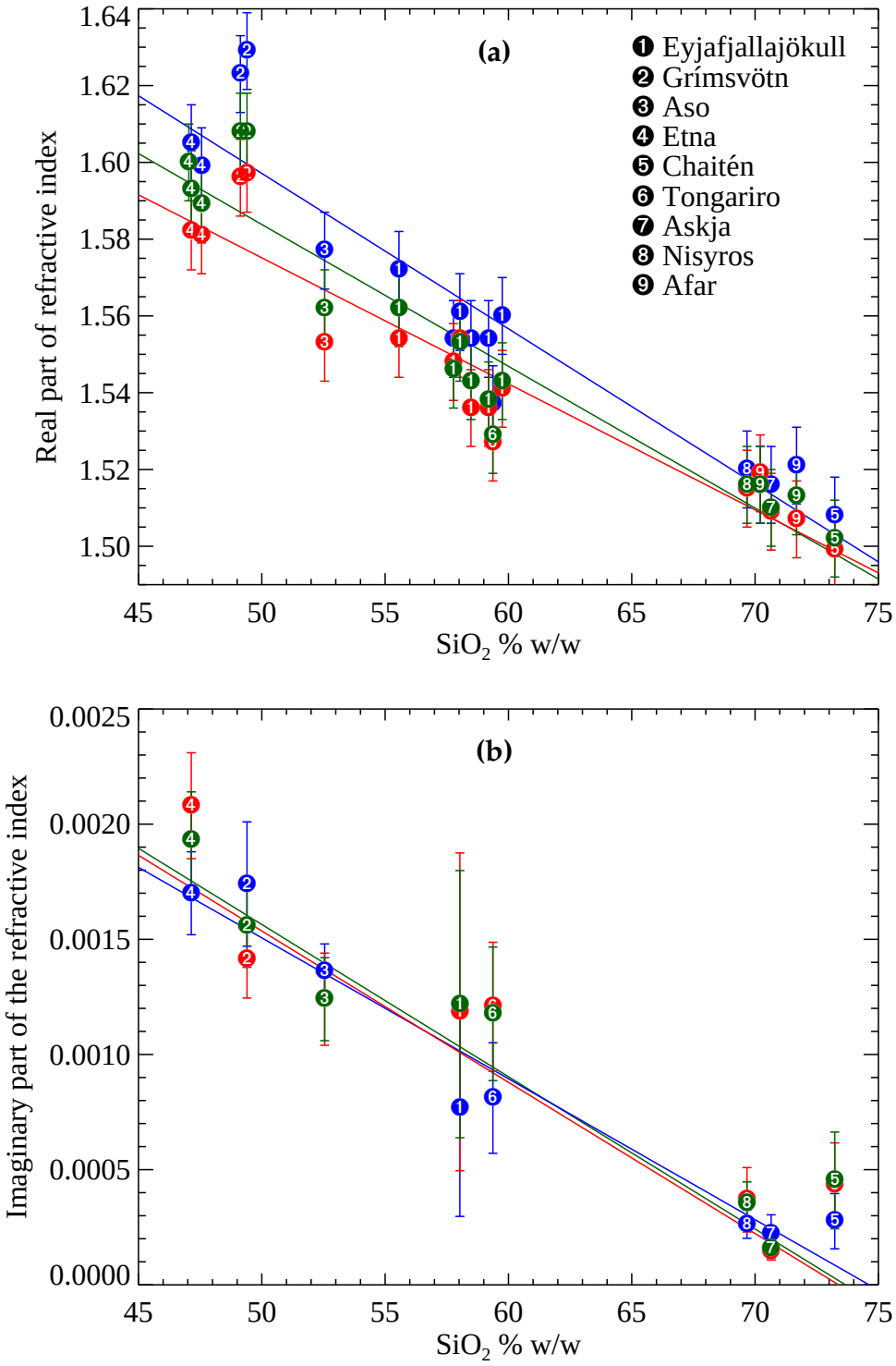

Figure 2.11: The relationship between NBO/T and: **(a)** real refractive index; **(b)** imaginary refractive index. The data points are numbered according to their source volcano, as given in the key. The uncertainty associated with the real and imaginary refractive indices are shown using error bars.

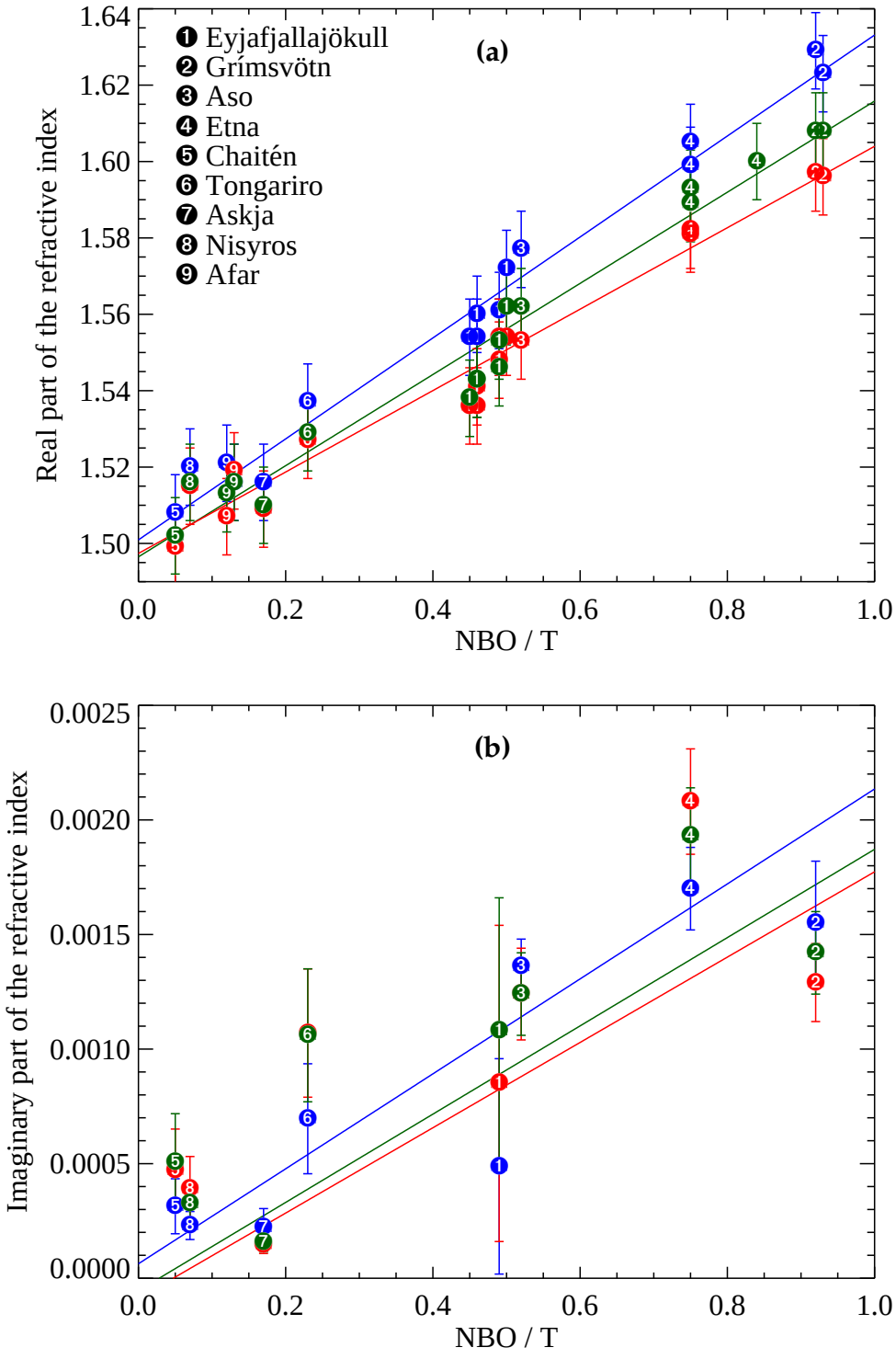

region. Melt inclusions form from the quenching of the liquid melt, which is distinguished from the magma defined as the mixture of the liquid and solid crystals. In the paper it is argued that compositional discrepancy between the whole rock and the melt inclusions can be explained by magma mixing with upper crustal rocks. Since the liquid melt fragments to form volcanic ash, the gap in Figure 2.10 is consistent with the observed dearth in intermediate melt inclusions.

Figure 2.10 also includes linear fits to the data points at the three wavelengths. In Figure 2.10a the line equations are: $Y = -0.004048X + 1.800$ (450 nm); $Y = -0.003694X + 1.769$ (546.7 nm); and $Y = -0.003284X + 1.739$ (650 nm). At each of the three wavelengths the value of the Pearson product moment correlation coefficient (PPMC), defined in Appendix A.1, is approximately -0.95 for the sample of 18 ashes, demonstrating there is a strong linear correlation. The results indicate that knowledge of a volcanic ash sample's SiO_2 content can be used to estimate the real refractive index at a particular wavelength (by application of the relevant line equation), with a standard error of: 0.012 (450 nm), 0.011 (546.7 nm) and 0.010 (650 nm). Conversely, a measurements of real refractive index can be used to estimate SiO_2, with a standard error of approximately 3.0 %.

In Figure 2.10b the error-weighted best-fit line equations are: $Y = -6.118 \times 10^{-5}X + 0.004567$ (450 nm); $Y = -6.611 \times 10^{-5}X + 0.004870$ (547.6 nm); and $Y = -6.611 \times 10^{-5}X + 0.004821$ (650 nm). The values of the PPMC at the three wavelengths are: -0.97, -0.96 and -0.94, respectively, indicating a strong linear relationship. The sample size in this case was 8; the subset of ashes which had both a measurement of imaginary refractive index and XRF analysis performed. The results indicate that a measurement of SiO_2 content can be used to estimate imaginary refractive index with a standard error of: 0.00015 (450 nm), 0.00020 (546.7 nm) and 0.00026 (650 nm). Conversely, the standard error in an estimate of SiO_2 mass percentage based on knowledge of imaginary refractive index is 3.1 %.

2.4.2.2 NBO/T and complex refractive index

An important parameter in characterising the molecular structure of silicate glasses is the ratio of non-bridging oxygen atoms per tetrahedrally coordinated cations (NBO/T) [*Mysen*, 1983]. Pure SiO_2 is most commonly found in the form of quartz having a tetrahedral lattice structure, in which nearly all oxygen atoms act as bridges between two silicon atoms. Such oxygen atoms are named bridging oxygen (BO). Adding metal oxide causes the formation of nonbridging oxygen atoms

(NBO). These oxygen atoms are bonded to network modifying metal cations as well as cations that are tetrahedrally arranged in the silica lattice.

The NBO/T value for a particular sample can be calculated from its bulk composition, according to the following expression:

$$\frac{\mathrm{NBO}}{\mathrm{T}} = \frac{1}{\mathrm{T}} \sum_i n M_i^{n+} \tag{2.7}$$

where T denotes the number of tetrahedrally coordinated cations (calculated from molar proportions), and M^{n+} denotes network-modifying cations (calculated as the difference between total oxygen negative charge $2 \times \mathrm{O}$ minus the positive charge of tetrahedrally coordinates cations $4 \times \mathrm{T}$), and n is the electrical charge of the i^{th} cation.

Values for NBO/T were calculated by Gemma Prata (Department of Earth Sciences, University of Oxford) through application of Eq. (2.7). Figure 2.11 shows (a) real refractive index, and (b) imaginary refractive index, plotted against the results for NBO/T for the ash samples. The data points have been numbered according to their source volcano and the error bars indicate the uncertainty in refractive index values. Uncertainties in NBO/T are likely to be $< 1\,\%$ (G. Prata, personal communication).

In Figure 2.11a the plotted lines of best fit at the three wavelengths have equations: $Y = 0.1321X + 1.501$ (450 nm); $Y = 0.1193X + 1.496$ (546.7 nm); and $Y = 0.1066X + 1.497$ (650 nm). The PPMC value in all three cases is approximately 0.98 demonstrating a very strong linear correlation for this samples of 18 ashes. The results indicate that the standard error in estimating the real refractive index of an ash based on knowledge of its NBO/T value, is 0.006 (less than the uncertainty on the individual Becke line measurements).

In Figure 2.11b the error-weighted line equations are: $Y = 0.002072X + 6.309^{-5}$ (450 nm); $Y = 0.001926X - 5.440 \times 10^{-5}$ (546.7 nm); and $Y = 0.001862X - 8.802 \times 10^{-5}$ (650 nm). The linear correlation for the sample of 8 is less strong with PPMC values of: 0.90 (450 nm) , 0.86 (546.7 nm) and 0.80 (650 nm). The standard deviation in imaginary refractive index about the lines of best fit is approximately 0.0003.

2.5 Chapter conclusions and discussion

A portion of the work presented in this chapter has been published in *Ball et al.* [2015]. The new attenuation method is a relatively simple extension of the Becke

line procedure. The accuracy of the Becke method and the attenuation method were assessed by measuring the complex refractive index of Hoya neutral density glass (which has a precisely known complex refractive index) and found to have an accuracy of < 0.01 ($\approx 0.6\,\%$ for volcanic ash measurements) and $< 2 \times 10^{-5}$ ($\approx 2\,\%$) for the real and imaginary parts of the refractive index, respectively. The values for ash real refractive index were in the range 1.51 – 1.63 at $450\,$nm, 1.50 – 1.61 at $546.7\,$nm, and 1.50 – 1.59 at $650\,$nm. The values for the imaginary refractive index ranged 0.22 – 1.70×10^{-3} at $450\,$nm, 0.16 – 1.93×10^{-3} at $546.7\,$nm and 0.15 – 2.08×10^{-3} at $650\,$nm. The measurements were applied to particles with a radius larger than $10\,\mu$m.

The complex refractive indices of the ashes were compared to their measured mass percentage SiO_2 content (determined from XRF compositional measurements performed by Gemma Prata, Department of Earth Sciences). A strong linear correlation was found between real refractive index and SiO_2 content, and imaginary refractive index and SiO_2 content. The results indicate that a measurement of SiO_2 can be used to estimate real refractive index and imaginary refractive index with a standard error of approximately 0.01 and 0.0002, respectively, at either 450, 546.7 or $650\,$nm. The relationship between the parameter NBO/T (non-bridging oxygen atoms per tetrahedral cations) and complex refractive index was also investigated. An extremely strong linear correlation between NBO/T and the real part of the ashes' refractive index was found; knowledge of NBO/T allowed real refractive index to be estimated with a standard error of 0.006. These relationships have yet to be published.

The Becke line method is a standard procedure and returned good results. The resolution of the mounting liquids used was 0.01, and had finer resolution liquids been used the accuracy of results could have been improved. The averaging procedure was not as rigorous as that used for the attenuation method, but the observed variation in n was generally small and it is unlikely a volume averaged mean would have yielded noticeably different results. The expected dispersion relation of real refractive index decreasing with wavelength was observed in all, bar one, ash samples. This provides reassurance in the accuracy of the method, and suggests the uncertainty in returned values was probably less than the resolution of the mounting liquids given the statistical approach used. The values obtained for the real refractive index of the Hoya *ND-03* glass matched the manufacturer's quoted values to within 0.01 at all three wavelengths.

In this chapter a new attenuation method has been outlined for measuring the imaginary refractive index of particles based on the analysis of digital microscope images. Volume averaged values for k were determined for each ash sample, based on a survey of 30 particles and measurements of the attenuation inside individual particles and their dimensions. Uncertainties in the returned k values for ash samples were taken as the volume weighted standard deviation about the volume weighted mean. The standard deviations varied significantly between different ash samples. It is difficult to assess whether these variations represented real variation in k between individual particles within each ash sample or were associated with the precision of the attenuation method. A new study surveying a much larger number of particles within ash samples would likely shed light on this, and would substantiate the reproducibility of these results.

The overall k values calculated by volume-averaging the values of the constituent particles required the assumption that the ashes were an external mixture of particles, each of a uniform consistency. However, in the Chaitén (VA11), Eyjafjallajökull (VA15) and Nisyros (VA19) ash samples there existed fragments that were either fused from a mixture of different materials or contained bubbles of volcanic gas causing a breakdown in the above assumption. The inhomogeneities within the particles would mean the particles have a broad range of k values rather than falling into the three distinct distributions of *clear*, *opaque* and *intermediate*. In turn, this would have led to a larger standard deviation in the measurements and a larger standard error associated with the overall value of k. There has been some debate as to whether volume-averaging the constituent materials of a particle can be used to find an effective refractive index of atmospheric aerosol particles which are internally mixed [*Bohren and Huffman*, 1983; *Gillespie et al.*, 1978; *Lindberg et al.*, 1993]. It has been suggested that the Bruggeman and Maxwell Garnett mixing rules may map the the constituent parts of an individual particle to its overall effect more accurately [*Chýlek et al.*, 1988]. However, the large errors associated with the samples for which the external mixing assumption was not entirely valid, incorporates the necessary caution with which the results of this chapter for the Chaitén (VA11), Eyjafjallajökull (VA15) and Nisyros (VA19) ash samples should be viewed.

A limitation of the particle attenuation method was that it was unable to test the particles with a size parameter lower than about 120 due to the sensitivity of the camera (at visible wavelengths this corresponds to particles less than about $10\,\mu$m). These particles, although individually small, constitute a large combined

volume within each sample. Additionally, there is evidence that smaller aerosol particles are relatively more absorbing [*Lindberg and Gillespie*, 1977] so that the current method may bias k to a value smaller than that for the distribution as a whole. Furthermore, smaller particles are expected to experience longer atmospheric lifetimes hence contributing more to the optical properties of the older, dispersed plumes that are often of interest especially in terms of aviation hazards. In future work the samples could be filtered so that only the finest particles remain. They could then be suspended in a liquid of a matched refractive index and the extinction could be measured. Providing they are small enough, the Rayleigh approximation would mean that extinction would be entirely due to absorption, and the imaginary part of the refractive index could be retrieved and compared to that of the larger particles measured in this chapter.

The disparity between the quoted and measured values of k for the Hoya *ND-03* glass at 450.0 nm and 546.7 nm was small but concerning. The fact that the measured and quoted values aligned at $650.0\,\text{nm}$ signifies that the disparity was caused by an unaccounted-for refractive effect which is therefore more significant at shorter wavelengths. However, these discrepancies were significantly less than the uncertainty associated with the measured ash k values, typically by an order of magnitude. In future, it would be useful to validate the attenuation method on a more highly absorbing test material, having a known k value closer to the ashes.

The comparison of the complex refractive index of the ash samples with their composition shows that SiO_2 content is highly correlated with both real and imaginary refractive index. SiO_2 content is widely used to classify volcanic ashes; *Kobayashi et al.* [1976] found that SiO_2 content in volcanic ash samples was correlated with each of: Al_2O_3, Fe_2O_3 + FeO, FeO, MgO, CaO, Na_2O, TiO_2, and MnO content. Therefore, given that the primary constituents of ash are closely correlated with SiO_2, and that composition determines complex refractive index, it is hardly surprising that a close relationship between complex refractive index and SiO_2 has been established. The relationship between real refractive index and SiO_2 content of volcanic materials has been investigated already by, for example, *Kittleman* [1963] who found a similar correlation for Becke line results obtained using white light. The results presented in this chapter are an improvement on previous studies because three discrete wavelengths in the visible have been analysed separately, and measurements of the imaginary part of the refractive index have also been made and shown to correlate with SiO_2 content. The results of this chapter indicate that very good estimates of the complex refractive index of volcanic ash,

at discrete wavelengths across the visible, can be made when XRF bulk compositional data are available.

Another interesting result is the strong correlation between the parameter NBO/T and real refractive index; the correlation was stronger than for SiO_2 content. The result, established in collaboration with Gemma Prata (Department of Earth Sciences, University of Oxford), suggests that non-bridging oxygen atoms play an important role in the light-matter interaction of volcanic ashes at visible wavelengths; this correlation for volcanic ashes has not been reported elsewhere.

However, the relationship between optical absorption, SiO_2 content and NBO of CaO-MgO aluminosilicate glasses was investigated by *Novatski et al.* [2008]. They found that absorption decreased with SiO_2 content, consistent with the results for imaginary refractive index presented in this chapter for volcanic ashes. In *Novatski et al.* [2008] it is argued that increasing SiO_2 in CaO-MgO aluminosilicate glasses reduces NBO/T, and at visible wavelengths this is associated with a decrease in the number of colour centres associated with the absorption of photons at characteristic wavelengths in the visible.

Chapter 3

Retrieving the real refractive index of scatterers from colloidal reflectance measurements

3.1 Published work and contributions

A significant portion of the work presented in this chapter has been published in *Reed et al.* [2016]. I performed all of the experiments, the modelling, the data analysis, and the sensitivity analysis. Daniel Peters provided help with aligning and calibrating the apparatus, and programming the refractometer scanning routine. Andy Smith provided help using non-spherical scattering code within the sensitivity analysis. Don Grainger provided significant insight and advice throughout.

3.2 Introduction

This chapter outlines a technique for retrieving the real refractive index of monodisperse and polydisperse submicron particles from angular reflectance measurements, close to the critical angle, of a colloidal suspension of particles. The accuracy to which reflectance measurements of colloidal suspensions of particles can be used to determine scatterer properties, in particular the real refractive index of particles, is investigated. The Fresnel equations describing the reflection at the interface between two homogeneous media and critical angle refractometers have long been used to measure the refractive index of homogeneous materials. However, modelling the reflection from a colloidal suspension is significantly more complex because it must take into account the scattering of incident light by particles in the colloid.

For many years scientists have studied the propagation of light in turbid media containing randomly positioned particles. *Rayleigh's* paper: "On the transmission of light through an atmosphere containing small particles in suspension, and on the origin of the blue of the sky", can be considered an early example. The theories must take into account, in some way, the multiple scattering of light by particles. The approaches to the problem can broadly be split into two groups: incoherent and coherent theories. The incoherent approaches to radiative transfer in turbid media are typically derived heuristically by considering the scattering and attenuation of radiance in an elemental volume; cross-sections derived for single-scattering treatments (Mie theory or T-matrix methods) are used to determine the elemental volume extinction. The DISORT algorithm [*Stamnes et al.*, 1988] is an extremely versatile manifestation of the incoherent approach, useful in many remote sensing applications. However, more fundamentally, the fields satisfy the wave equation of electrodynamics and it is more rigorous to start with analytic wave theories to derive RT from there; this is the coherent approach. There has been considerable work in this area, and the mathematical techniques employed mostly invoke the T-matrix formalism and use N-particle Green's functions within the integral formalism of Maxwell's equations [*Tsang and Kong*, 1980, 1982; *Kuga et al.*, 1996; *Loiko et al.*, 2000; *Barrera and García-Valenzuela*, 2003]. The coupled multiple scattering equations can be approximated to varying levels of accuracy depending on the level of statistical information available for the system (and computational power available to evaluate their solution numerically): for example knowledge of the number density of scatterers, or the two-particle correlation function. Therefore when applying such theories, for example in the application presented in this chapter, it is important to evaluate the regime to which they safely apply.

The coherent scattering model (CSM) developed by *Barrera and García-Valenzuela* [2003] and summarised further in *Gutiérrez-Reyes et al.* [2012] is used in this chapter to model the coherent reflectance from colloids; the model is used to retrieve the real refractive index of the scattering particles from experimental angular reflectance measurements close to the critical angle. The model has been shown to be consistent with experimental reflectance data [*García-Valenzuela et al.*, 2005a], in an experimental set-up very similar to the one presented here, and experiments have been performed, using similar theories, with a focus on determining the size of particles [*García-Valenzuela et al.*, 2008, 2010; *Sánchez-Pérez et al.*, 2011]. The derivation, presented in *Barrera and García-Valenzuela* [2003], for the coherent reflectance from a half-space of random scatterers uses wave scattering theory to determine

the coherent reflectance and transmittance from a single thin slab of scatterers, and then integrates over a semi-infinite pile to determine the half-space amplitude reflection coefficient. The scattering produced by a thin slab is calculated assuming that the positions of particles are uncorrelated (i.e. the exclusion volume of particles is ignored) and that the exciting field at each particle is the incident field only and does not have any component from the field scattered by other particles within the slab (i.e. there is a single scattering approximation within each thin slab). Multiple scattering is taken into account when integrating over multiple slabs. The approach is similar to the "cascade of layers" method for multiple scattering, presented in *Tsang and Kong* [2001]. The CSM is valid for dilute concentrations of particles, but can handle particles of any size [*García-Valenzuela et al.*, 2005a].

An important concept in studies of turbid media is that of an effective medium; this is the idea that the propagation of light in the medium can be understood in terms of a set of continuous optical constants typically associated with a homogeneous medium. For example, is there an effective complex refractive index for the turbid medium that can be used within the equations of continuum electrodynamics (e.g. the Fresnel equations) to describe the propagation of light? In *Barrera and García-Valenzuela* [2003] it is shown that the CSM amplitude reflection coefficient, derived from wave scattering theory, is consistent with continuum electrodynamics and the concept of an effective medium, providing the effective medium possesses both an effective dielectric response, ϵ^{eff}, and an effective magnetic susceptibility, μ^{eff}. The electrodynamic response of colloids has been shown to be nonlocal in nature *Barrera et al.* [2007]; the derived effective responses presented in *Barrera and García-Valenzuela* [2003] depend on the angle of the incident wavevector. In this chapter the effective medium notation is adopted because it allows the problem of scattering from a multi-layered system to be conceptualised in terms of successive applications of Fresnel's equations. However, the derivation of the theory does not rely on the concept of an effective medium and comes from a purely wave-scattering approach.

3.3 Theory

A forward model, **F**, is required that relates measured reflectance as a function of incidence angle to the optical properties of the particles, principally their real

refractive index, n_{p}. The model chosen for this purpose was the coherent scattering model (CSM) outlined in *Barrera and García-Valenzuela* [2003].

3.3.1 The scattering amplitude matrix

Following *Bohren and Huffman* [1983], for a plane wave with an electric field of the form $\mathbf{E}_{\mathrm{i}} = \mathbf{E}_{0\mathrm{i}} \exp\left(i\mathbf{k}_{\mathrm{i}} \cdot \mathbf{r} - i\omega t\right)$ incident on an arbitary particle at the origin the relationship between the scattered far field and incident field is:

$$\begin{pmatrix} E_{\parallel}^{\mathrm{S}} \\ E_{\perp}^{\mathrm{S}} \end{pmatrix} = \frac{\exp\left(ikr\right)}{-ikr} \begin{bmatrix} S_2\left(\theta\right) & S_4\left(\theta\right) \\ S_3\left(\theta\right) & S_1\left(\theta\right) \end{bmatrix} \begin{pmatrix} E_{\parallel}^{\mathrm{i}} \\ E_{\perp}^{\mathrm{i}} \end{pmatrix} \tag{3.1}$$

where the subscripts $\parallel$ and $\perp$ denote parallel and perpendicular, respectively, with respect to the scattering plane, which is the plane containing the incident and scattered wave vectors, and where θ is the scattering angle between the two wave vectors. For a spherical particle, $S_3\left(\theta\right) = S_4\left(\theta\right) = 0$; this condition also holds for the configurationally averaged scattering amplitude functions of non-spherical particles randomly orientated in an isotropic medium [*Mishchenko et al.*, 2000].

3.3.2 The Fresnel equations

The Fresnel equations describe the reflection at an interface between two homogeneous media: an incident medium and a transmission medium. They are derived by considering a plane wave incident on an interface between two media and from the boundary requirement that the tangential component of the electric and magnetic fields be continuous across the interface — see, for example, *Lvovsky* [2013]. In the derivation it is assumed that the transmission medium extends infintely beyond the interface, such that there is no additional component to the reflection amplitude arising from reflection at a second interface: the Fresnel amplitude reflection coefficients are therefore half-space amplitude reflection coefficients for homogeneous media. The expressions for the reflection amplitude for the E-field polarised perpendicular ($\perp$) to the plane of incidence and for the E-field parallel ($\parallel$) to the plane of incidence may be written in terms of the complex permittivity ϵ and complex permeability μ of the two media:

$$r_{\perp}^{\mathrm{Fres}} = \left(\frac{E_{\mathrm{r}}}{E_{\mathrm{i}}}\right)_{\perp} = \frac{\mu_{\mathrm{t}} n_{\mathrm{i}} \cos\left(\theta_{\mathrm{i}}\right) - \mu_{\mathrm{i}} n_{\mathrm{t}} \cos\left(\theta_{\mathrm{t}}\right)}{\mu_{\mathrm{t}} n_{\mathrm{i}} \cos\left(\theta_{\mathrm{i}}\right) + \mu_{\mathrm{i}} n_{\mathrm{t}} \cos\left(\theta_{\mathrm{t}}\right)}, \tag{3.2}$$

$$r_{\parallel}^{\mathrm{Fres}} = \left(\frac{E_{\mathrm{r}}}{E_{\mathrm{i}}}\right)_{\parallel} = \frac{\epsilon_{\mathrm{t}} n_{\mathrm{i}} \cos\left(\theta_{\mathrm{i}}\right) - \epsilon_{\mathrm{i}} n_{\mathrm{t}} \cos\left(\theta_{\mathrm{t}}\right)}{\epsilon_{\mathrm{i}} n_{\mathrm{t}} \cos\left(\theta_{\mathrm{i}}\right) + \epsilon_{\mathrm{t}} n_{\mathrm{i}} \cos\left(\theta_{\mathrm{t}}\right)}, \tag{3.3}$$

where the subscripts i, r, and t refer to the incident, reflected, and transmitted rays respectively. The angles θ_{i}, θ_{r}, and θ_{t} are measured between the interface normal and the incident, reflected, or transmitted wavevector respectively. Knowledge of the complex refractive index:

$$n = \sqrt{\epsilon\mu/\mu_0\epsilon_0}, \tag{3.4}$$

is insufficient to determine the interface reflection amplitude: μ and ϵ must be known individually. The exception being materials with no magnetic response, such that $\mu = \mu_0$ and $n = \sqrt{\epsilon/\epsilon_0}$, where knowledge of n is sufficient. The amplitude reflection coefficient, r, is related to the reflectance, R (the ratio of the reflected radiance to the incident radiance; the quantity measured by a detector), according to $R = |r|^2$.

The reflected wave is in the specular direction, i.e. $\theta_{\mathrm{r}} = \theta_{\mathrm{i}}$, and the direction of the transmitted wave is determined by the ratio of the phase velocities of light in the two media (Snell's Law). Both of these results follow from the requirement that the angular frequency ω and overall phase of the incident, reflected, and transmitted waves be equal in the plane of the interface. Snell's law can be expressed in terms of the refractive index of the two media as:

$$\sin\left(\theta_{\mathrm{t}}\right) n_{\mathrm{t}} = \sin\left(\theta_{\mathrm{i}}\right) n_{\mathrm{i}} \tag{3.5}$$

3.3.3 N-layered slab system

Consider the case of a general N-layered system depicted in Fig. 3.1. The z-direction is defined to be perpendicular to the slab interfaces, with positive z going rightwards in Fig. 3.1. Using the composition law of amplitude [*Vigoureux*, 1992; *Grossel et al.*, 1994], the amplitude reflection coefficient at the first interface $\Gamma_{0,1}$ can be expressed as:

$$\Gamma_{0,1}\left(\theta_0\right) = \frac{r_{0,1}^{\mathrm{hs}}\left(\theta_0\right) + \Gamma_{1,2}\left(\theta_1\right) \exp\left(2ik_1^z \Delta z_1\right)}{1 + r_{0,1}^{\mathrm{hs}}\left(\theta_0\right) \Gamma_{1,2}\left(\theta_1\right) \exp\left(2ik_1^z \Delta z_1\right)}, \tag{3.6}$$

where $\Gamma_{1,2}\left(\theta_1\right)$ is the amplitude reflection coefficient for light in medium 1 incident at angle θ_1 on the interface with medium 2. The term $r_{0,1}^{\mathrm{hs}}\left(\theta_0\right)$ is a half-space amplitude reflection coefficient: it is the amplitude reflection coefficient at the interface

$0 \rightarrow 1$ if medium 1 were to extend infinitely beyond the interface; removing all other interfaces the equation simplifies to: $\Gamma_{0,1}(\theta_0) = r^{\mathrm{hs}}_{0,1}(\theta_0)$. Equation (3.6) can be readily generalised to give the amplitude reflection coefficient of light in slab m incident on the interface with slab $(m+1)$:

$$\Gamma_{m,\,m+1}(\theta_m) = \frac{r^{\mathrm{hs}}_{m,\,m+1}(\theta_m) + \Gamma_{m+1,\,m+2}(\theta_{m+1}) \exp\left(2ik^z_{m+1}\Delta z_{m+1}\right)}{1 + r^{\mathrm{hs}}_{m,\,m+1}(\theta_m)\,\Gamma_{m+1,\,m+2}(\theta_{m+1}) \exp\left(2ik^z_{m+1}\Delta z_{m+1}\right)}, \tag{3.7}$$

where k^z_m is the z-component of the wavevector of light in medium m, such that $k^z_m = k_m \cos\theta_m$ and where $k_m = 2\pi/\lambda_m$ is the wave number in medium m. The width of slab m is Δz_m. The angle θ_m of light with respect to the z-axis in medium m can be calculated for a given system incidence angle θ_0 by m successive applications of Snell's law:

$$\theta_m = \sin^{-1}\left(\frac{n_{m-1}}{n_m}\sin\theta_{m-1}\right). \tag{3.8}$$

Figure 3.1: Reflection from an N-layered system of slabs. Only the penetrating beam is shown after the initial interface. The compound amplitude reflection coefficient at the initial interface, $\Gamma_{0,1}$, has a component from reflection at each subsequent interface according to Eq. (3.7).

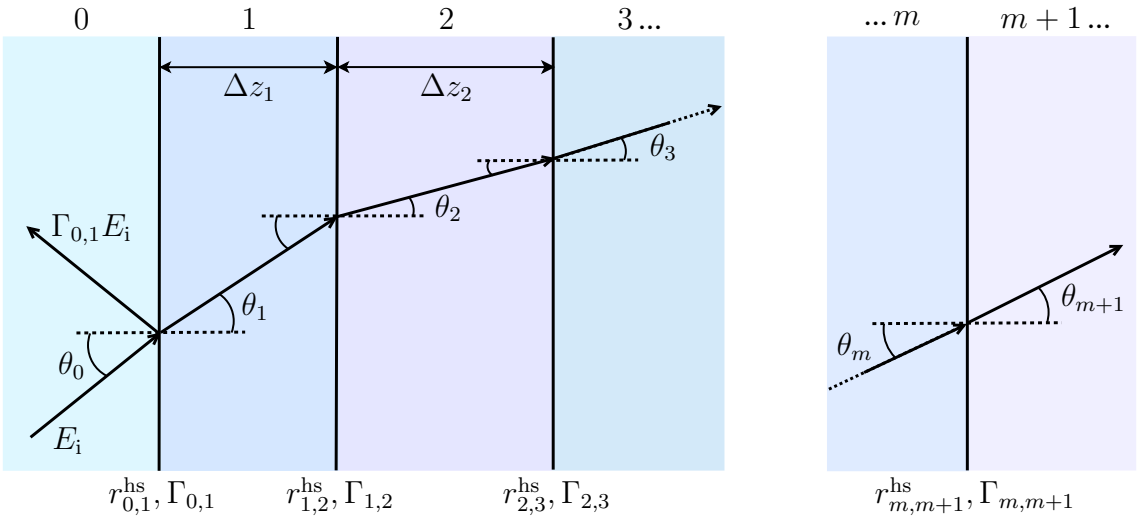

3.3.4 The coherent scattering model (CSM) and the effective optical properties of a colloidal system

As outlined in *Barrera and García-Valenzuela* [2003], taking into account the Mie scattering of particles, it is possible to determine an effective electric permittivity ϵ^{eff}

and magnetic permeability μ^{eff} for a dilute system of random spheres that describe the propagation of the coherent beam. These derived optical coefficients are not continuous functions of space, but depend on the angle of light with respect to the z-axis and the light's polarisation. When ϵ^{eff} and μ^{eff} are substituted into Eq. (3.2) or (3.3), employing Eq. (3.4), an expression for the amplitude reflection coefficient of a half-space of dilute random spheres is established. It is important to note the half-space amplitude reflection coefficient is derived from wave scattering theory and does not rely on the interpretation of the system as an effective medium. The effective optical coefficients depend on the Mie scattering amplitude functions $S_j\left(\theta, x, m_{\text{p}}/m_{\text{m}}\right)$ as defined in *Bohren and Huffman* [1983], where $j = 1$ is employed for $\perp$ polarised light and $j = 2$ for $\parallel$ polarised light. The Mie scattering amplitude functions depend on the ratio of the complex refractive index of the particles to the complex refractive index of the surrounding medium, $m_{\text{p}}/m_{\text{m}}$. In the retrievals presented in this chapter, it is assumed that the particles are non-absorbing (the uncertainty associated with retrievals of n_{p} arising from assuming $k_{\text{p}} = 0$ is shown to be negligible in section 3.5) and the suspension medium is non-absorbing, so that $m_{\text{p}}/m_{\text{m}} = n_{\text{p}}/n_{\text{m}}$. The Mie scattering amplitude functions also depend on the size paramter of particles: $x = 2\pi a/\lambda_{\text{m}}$, where $\lambda_{\text{m}} = n_{\text{m}}/\lambda_0$ is the wavelength of light in the suspension medium and λ_0 is the vacuum wavelength. The effective optical properties for $\perp$ polarised incident light are:

$$\frac{\mu_{\perp}^{\text{eff}}}{\mu_0} = 1 + i\gamma \frac{S_{-}^{(1)}\left(\theta_{\text{i}}\right)}{\cos^2\theta_{\text{i}}}, \tag{3.9}$$

$$\frac{\epsilon_{\perp}^{\text{eff}}}{\epsilon_0} = 1 + i\gamma \left[2S_{+}^{(1)}\left(\theta_{\text{i}}\right) - S_{-}^{(1)}\left(\theta_{\text{i}}\right)\tan^2\theta_{\text{i}}\right], \tag{3.10}$$

where

$$S_{+}^{(j)}\left(\theta_i\right) = \frac{1}{2}\left[S\left(0\right) + S_j\left(\pi - 2\theta_{\text{i}}\right)\right], \tag{3.11}$$

$$S_{-}^{(j)}\left(\theta_{\text{i}}\right) = S\left(\theta_{\text{i}}\right) - S_j\left(\pi - 2\theta_{\text{i}}\right). \tag{3.12}$$

Here $\gamma = 3f/2x^3$, and f is the volume filling fraction occupied by the particles.

For $\parallel$ polarised incident light, the corresponding expressions are:

$$\frac{\epsilon_{\parallel}^{\text{eff}}}{\epsilon_0} = 1 + i\gamma \frac{S_{-}^{(2)}\left(\theta_{\text{i}}\right)}{\cos^2\theta_{\text{i}}}, \tag{3.13}$$

$$\frac{\mu_{\parallel}^{\text{eff}}}{\mu_0} = 1 + i\gamma \left[2S_{+}^{(2)}\left(\theta_{\text{i}}\right) - S_{-}^{(2)}\left(\theta_{\text{i}}\right) \tan^2\theta_{\text{i}} \right]. \tag{3.14}$$

Substitution of Eqs. (3.9) and (3.10) for $\perp$ polarised light or Eqs. (3.13) and (3.14) for $\parallel$ polarised light into Eq. (3.2) or (3.3) yields Eq. (3.15) an expression for the amplitude reflection coefficient for a half-space of random particles r_{hs}, as depicted in Fig. 3.2a. The centres of the particles lie in the region $z > 0$ but due to the finite size of the particles some protrude into the region $z < 0$. The expression for the half-space amplitude reflection coefficient is:

$$r_{\text{hs}}^{\text{eff}}\left(\theta_{\text{i}}\right) = \frac{\gamma S_j\left(\pi - 2\theta_{\text{i}}\right)/\cos\theta_{\text{i}}}{i\left(\cos\theta_{\text{i}} + \left\{\cos^2\theta_{\text{i}} + 2i\gamma S\left(0\right) - \frac{\gamma^2}{\cos^2\theta_{\text{i}}}\left[S\left(0\right)^2 - S_j\left(\pi - 2\theta_{\text{i}}\right)^2\right]\right\}^{1/2}\right) - \frac{\gamma S(0)}{\cos\theta_{\text{i}}}} \tag{3.15}$$

where $j = 1$ for $\perp$ polarised incident light and $j = 2$ for $\parallel$ polarised light.

The z-component of the wavevector of the coherent beam in the scatterting medium k_z^{eff} is given by:

$$k_z^{\text{eff}} = \sqrt{\left(k_{\text{m}}^z\right)^2 - 2i\chi S\left(0\right) k_{\text{m}}^z/\cos\theta_{\text{i}} + \left(\chi^2/\cos^2\theta_{\text{i}}\right)\left[S_j\left(\pi - 2\theta_{\text{i}}\right)^2 - S\left(0\right)^2\right]} \tag{3.16}$$

where $\chi = -3f/2a^3k_{\text{m}}^2$ and a is the particle radius. Note that Eqs. (3.15) and (3.16) are derived from a wave-scattering approach, and do not rely on the interpretation of the system as an effective medium [*Barrera and García-Valenzuela*, 2003; *Gutiérrez-Reyes et al.*, 2012].

Now consider the case of an interface (located at $z = 0$) between an incident medium ($z < 0$) and a turbid medium ($z > 0$) containing randomly located spheres with a dilute concentration, as depicted in Fig. 3.2b. Given the condition that no particles in the turbid medium may protrude into the incident medium, the centres of all particles must lie in the region $z > a$. Thus there exists an excluded slab of width $\Delta z = a$ in which the centres of particles may not lie and application of Eq. (3.6) yields the interface amplitude reflection coefficient:

$$r = \frac{r_{\text{i,m}}^{\text{Fres}} + r_{\text{hs}}^{\text{eff}}\left(\theta_{\text{m}}\right)\exp\left(2ik_{\text{m}}^z a\right)}{1 + r_{\text{i,m}}^{\text{Fres}} r_{\text{hs}}^{\text{eff}}\left(\theta_{\text{m}}\right)\exp\left(2ik_{\text{m}}^z a\right)}, \tag{3.17}$$

where $r_{\text{i,m}}^{\text{Fres}}$ is the Fresnel amplitude reflection coefficient for an interface between a homogeneous medium with refractive index n_{i} and a homogeneous medium with refractive index n_{m}.

Figure 3.2: Reflection from two systems containing random spheres.

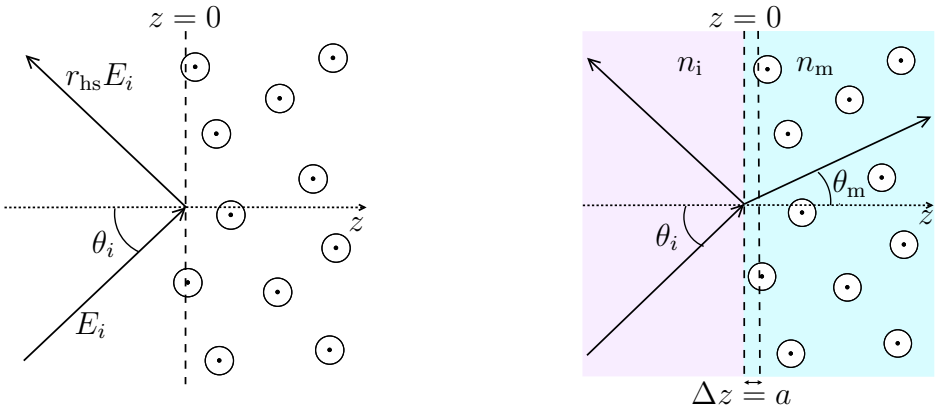

(a) Reflection from a half-space of spheres.

(b) Reflection at an interface between an incident medium and a turbid medium containing randomly located spheres.

3.3.5 Polydisperse systems

The expressions for the optical coefficients are easily modified to account for polydisperse particle size distributions. The amplitude scattering function $S_j(\theta, a)$, in Eqs. (3.9), (3.10), (3.13) and (3.14), is replaced by an average value integrated over the size distribution: $\int_0^\infty S_j(\theta, a)\, n(a)\, da$, where $n(a)$ is the normalised size distribution function (such that $\int_0^\infty n(a)\, da = 1$).

As outlined in *García-Valenzuela et al.* [2005a], an additional complication arises when modelling the reflection at an interface between an incident medium and a turbid medium containing a random dilute system of polydisperse particles: a particle of radius a cannot approach closer than a to the interface, resulting in the relative density of smaller particles increasing as the interface is approached. Thus the size distribution close to the interface is modified according to:

$$n(a, z) = U(z - a)\, N(a), \tag{3.18}$$

where $U(x)$ is a step function defined by: $U(x) = 0$ for $x < 0$, and $U(x) = 1$ for $x \geq 0$. Sufficiently far from the interface, the distribution is described by the unmodified distribution $n(a)$.

In order to model the coherent reflection from a polydisperse colloid, the system can be split into three parts: the incident medium at $z < 0$; a transition region inside the colloid consisting of N slabs of equal width Δz extending from $z = 0$

to $z = N\Delta z$; and finally a region with the unmodified bulk distribution $n(a)$ occupying $z > N\Delta z$. In the model approximation, within the transition region, the size distribution of particles is assumed to be constant within each slab but varies between slabs. Figure 3.3 demonstrates how the particle size distribution in slab m of the transition region is restricted to particles with radius $a < m\Delta z$. Such a system provides an approximation that tends to the modified distribution described by Eq. (3.18) as Δz becomes small and N large.

Figure 3.3: Illustration of modelling the reflection from a polydisperse colloid, using an N-slab transition region extending from $z = 0$ to $z = N\Delta z$. The diagram illustrates how in slab m the distribution of particles is restricted to those with radius $a < m\Delta z$.

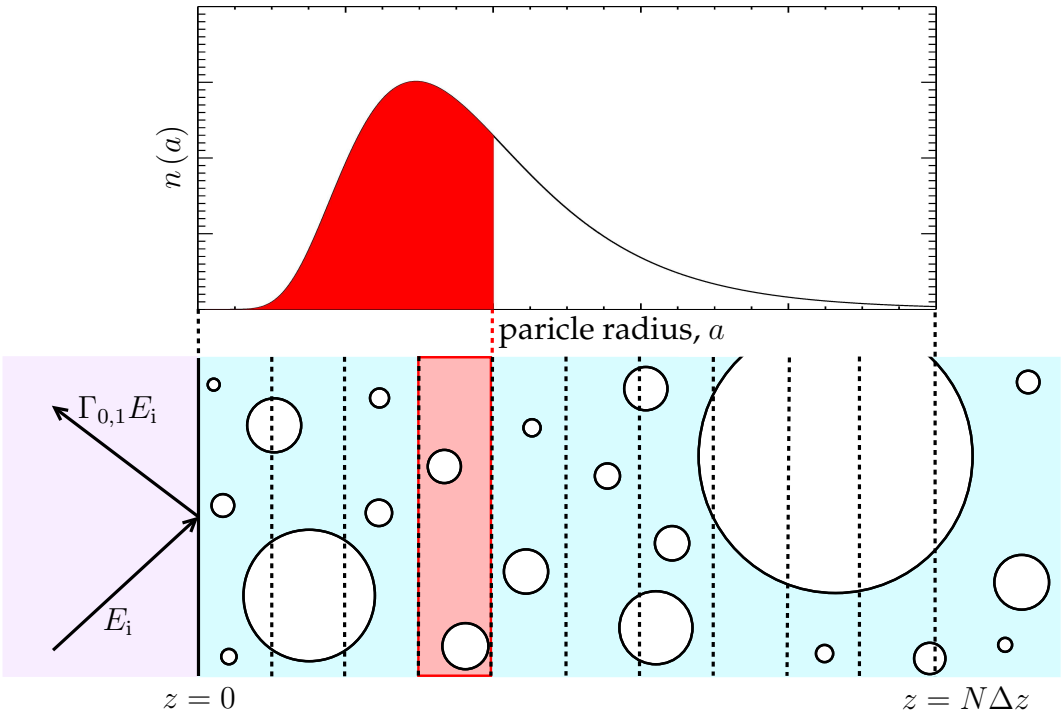

In order to determine the amplitude reflection coefficient for the approximate model system depicted in Fig. 3.3, Eqs. (3.9) and (3.10) or (3.13) and (3.14) (depending on the polarisation) must be used to establish the effective optical properties of each slab, integrating the amplitude scattering function $S_j(\theta, a)$ over the appropriately truncated particle size distribution. For slab m the appropriate replacement being: $\int_0^{m\Delta z} S_j(\theta, a)\, n(a)\, da$. In the region $z > N\Delta z$ the appropriate replacement is the integral over the entire distribution: $\int_0^{\infty} S_j(\theta, a)\, n(a)\, da$.

Once the effective optical properties of each region of the approximate model system have been established, the system amplitude reflection coefficient, Γ_{01}, can be readily calculated using successive applications of Eq. (3.7). The treatment of the system as a series of slabs is similar to the approach outlined in *García-Valenzuela et al.* [2005b], however the approach presented here is simpler because it requires only successive applications of Eq. (3.7) rather than calculation of the individual reflection and transmission amplitude coefficients of thin slabs. In the retrievals performed on the polydisperse volcanic ash and the polydisperse sand sample, a log-normal distribution was assumed with a median radius, a_0, and a geometric standard deviation, S:

$$N(a) = \frac{1}{\sqrt{2\pi}\ln(S)\,a}\exp\left\{\frac{[\ln(a)-\ln(a_0)]^2}{2\ln^2(S)}\right\}. \tag{3.19}$$

3.4 The experimental apparatus and methods

3.4.1 Overview of the apparatus

The apparatus is designed to measure the reflectance, R, as a function of incidence angle, θ_{i}, about an interface between an incident medium and a colloid. The experimental setup is illustrated in Fig. 3.4. An AlGaInP laser diode produces a collimated beam of light ($\lambda_0 = 635\,\mathrm{nm}$) which enters a semicircular BK7 glass optic at normal incidence to the curved surface. The refractive index of the glass optic is $n = 1.51454$ at the laser wavelength [*Sumitra Optical glass Inc.*, 2012]. The beam is then incident on the back surface of the optic at the interface with the sample medium. The volume of the sample region was approximately $1\,\mathrm{cm}^3$, with a depth of $1\,\mathrm{cm}$. A matte black cover slip was used to minimise reflection at the sample to cover slip interface. The coherent component of the reflected beam exits the optic in the specular direction at normal incidence to the curved surface, and travels to a silicon photodetector.

The laser diode and detector are mounted on the arms of a goniometer driven by a stepper motor, and can rotate fully about the optic. The centre of rotation of the arms is aligned with the centre of curvature of the optic, ensuring the beam enters and exits the optic at normal incidence to the curved surface. The setup allows capture of reflectance for a full range of incidence angles ($0^\circ \leq \theta_i \leq 90^\circ$) with a minimum angular interval, determined by the stepper motor, of $\Delta\theta_{\mathrm{i}} = 0.3^\circ$.

Figure 3.4: Schematic of the experimental setup. The $635\,\text{nm}$ incident beam from the AlGaInP laser diode enters the optic at normal incidence. It is then reflected at the back surface of the optic at the interface with the sample medium, before exiting the optic and travelling to the detector.

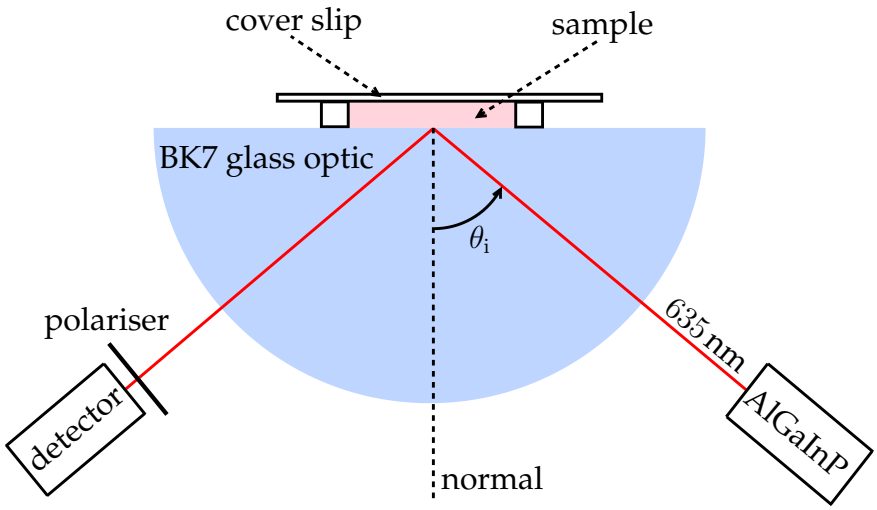

The angular positions of the laser and detector arms of the goniometer were controlled by a microcontroller, allowing an automated scanning routine to be pre-programmed. For a typical reflectance scan, the laser and detector were rotated in synchronisation, such that the detector remained aligned along the specular direction as θ_i varied.

In all of the reflectance scans performed, a polarising filter was placed in front of the detector and aligned such that the only light reaching the detector was the component with the E-field perpendicularly polarised ($\perp$) with respect to the plane of incidence (the plane of incidence is the plane containing the incident wavevector and the vector normal to the reflecting surface). The incident laser beam was unpolarised. The apparatus was completely enclosed in a sealed dark-box, preventing stray radiation from reaching the detector.

Before tests were performed on colloidal samples, the accuracy of the apparatus was tested by performing reflectance scans on distilled water (the refractive index of which is known to high accuracy). The goniometer allows the incidence angle, θ_i, to be measured with an uncertainty of $0.05°$; a digital angle gauge was used to measure the angular positions of the goniometer arms at the stepper motor locations and repeatability was tested. The uncertainty in the laser power over the duration of a typical reflectance scan was found to be approximately 1%; this was determined by making repeat detector readings over a prolonged period, with the laser directly incident on the detector. The reflectance data recorded for distilled

water was used (employing Fresnel reflectance theory) to accurately obtain its refractive index to within 0.1%, in agreement with error propagation estimates; these validation experiments are detailed in the next section.

Tests were performed on three aerosol types: spherical polystyrene test particles, a commercial sand sample and a volcanic ash sample. The correct preparation of samples was crucial to obtain reliable reflectance data. Proper dispersal of the aerosol particles in the suspension liquid was required. In all cases ultrasonic vibration was used immediately before reflectance scans were performed in order to evenly disperse the sample in the suspension liquid. In addition, an ultrasonic vibrator was attached to the optic and used throughout scans to maintain uniform dispersal.

3.4.2 Validating apparatus accuracy: Fresnel reflectance measurements

In order to verify the accuracy and repeatability of the apparatus, two-media Fresnel reflectance measurements were made for two interfaces: the BK7 glass optic to air; and BK7 glass to distilled water. A single angular reflectance scan was performed for the Bk7 glass optic to air interface, whereas nine scans were performed for the BK7 glass to distilled water interface to test repeatability. The experimental data were fitted using Eq. (3.2), the Fresnel reflectance equation for $\perp$ polarised light, using a least squares fit weighted by experimental errors. For the case of the BK7 glass optic to air interface, the refractive index of air was assumed to be $m_{\text{air}} = 1.0000 + i0.0000$ and the complex refractive index of the incident medium (BK7 glass) was retrieved. For the case of the BK7 glass to distilled water experiment, the refractive index of the BK7 glass optic was taken as $m_{\text{BK7}} = 1.51454 + i0.00000$, at the laser wavelength of $635\,\text{nm}$, as quoted by *Sumitra Optical glass Inc.* [2012], and the complex refractive index of the transmitted medium (distilled water) was retrieved.

Error propagation analysis was performed to analyse how experimental uncertainties propagated into the retrieved values for the real and imaginary parts of refractive index. The error propagation formalism of *Rodgers* [2000] was used; the approach is outlined in detail later in this chapter, in Section 3.5. Table 3.1 summarises the error propagation results for the BK7 glass optic to distilled water interface. The combined uncertainty in the retrieval of the real and imaginary part of the distilled water's refractive index are 0.00103 and 0.000433, respectively.

Table 3.1: Error propagation for the validation experiments on the BK7 glass optic to distilled water interface, using the Fresnel equations. The results here are for a single angular reflectance scan.

		Propagated uncertainties	
Error term, e	σ_e	$\lvert\partial n_{\text{water}}/\partial e\rvert\,\sigma_e$	$\lvert\partial k_{\text{water}}/\partial e\rvert\,\sigma_e$
Incidence angle, θ_i	0.05°	0.00102	0.000042
Laser power, LP	1%	0.00013	0.000431
Combined		0.00103	0.000433

Figure 3.5: Fresnel reflectance validation scans: (a) shows one of the nine scans of the BK7 optic to distilled water interface; (b) shows the measurement of the BK7 glass to air interface.

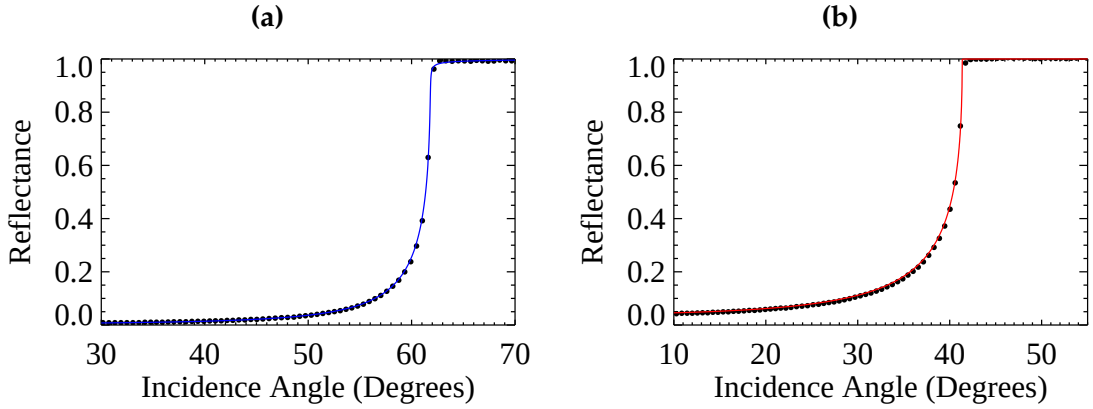

Figure 3.5a shows the angular reflectance measured from one of the nine repeat scans for the BK7 glass optic to distilled water interface, and the fitted Fresnel reflectance curve is shown in blue. Table 3.2 summarises the retrieval results for each of the nine scans. The repeatability of the results is highly encouraging. The mean retrieved complex refractive index from the scans was $< m_{\text{water}} >= 1.33235 + i0.00032$, which compares to the value of $1.3321 + i0.00000$ measured by *Daimon and Masumura* [2007] with a difference of $\Delta n_{\text{water}} = 0.00025$ in the real part and of $\Delta k_{\text{water}} = 0.00032$ in the imaginary part. The difference in the real part is within the propagated uncertainty in the mean from nine scans whereas the difference in the imaginary part is slightly larger; the propagated uncertainties for a mean taken from nine scans are: 0.00034 and 0.00014 for the real and imaginary part, respectively (the uncertainty in the mean taken from N individual measurements is $\sigma/\sqrt{N}$ if σ is the uncertainty associated with individual measurements). It is possible the purity of the distilled water was not 100 %. The distilled water

was taken from the Clarendon laboratory's general supply and its purity was not verified, which may explain the small discrepancy in the imaginary part.

Table 3.2: Retrieval results for the validation experiments on the BK7 glass optic to distilled water interface, using the Fresnel equations. The mean and standard deviation, σ, in the retrieved values for the nine angular reflectance scans are also shown.

Exp. number	n_{water}	k_{water}
1	1.33198	0.00026
2	1.33210	0.00025
3	1.33239	0.00023
4	1.33243	0.00035
5	1.33242	0.00032
6	1.33246	0.00028
7	1.33251	0.00038
8	1.33242	0.00041
9	1.33237	0.00037
mean	1.33235	0.00032
σ	0.00017	0.00008

The reflectance scan for the BK7 glass to air interface is shown in Fig. 3.5b, with the fitted Fresnel reflectance curve shown in red. The retrieved complex refractive index of the glass was: $m_{\text{BK7}} = 1.51332\,(\pm 0.00125) + i0.00002\,(\pm i0.00047)$, where propagated uncertainties are shown in brackets. The value of $1.51454 + 0.00000i$ is quoted by [*Sumitra Optical glass Inc.*, 2012]. The difference in the real part is approximately one sigma, whereas the difference in the imaginary part is within propagated uncertainties.

3.4.3 Method: Monodisperse polystyrene latex test particles

Reflectance measurements were performed on colloids containing polystyrene latex spherical beads produced by Sigma-Aldrich UK. The sample supplied by the manufacturer was quoted to contain a fraction of $10.0 \pm 0.5\,\%$ w/w latex to water and between 0.3 to $1.5\,\%$ of a soluble polymer dispersant (used to stabilise the particles against flocculation and agglomeration). The sample was manufactured to be monodisperse, with a quoted particle radius of $a = 260\,\text{nm}$ and a quoted coefficient of variation in size of $\leq 3\,\%$.

Diluted samples were produced by adding a measured mass of distilled water to a measured quantity of the $10.0 \pm 0.5\,\%$ w/w sample. Scales accurate to $0.0001g$ were used for sample preparation, with a typical diluted sample having a mass of $\sim 1\,$g. It was therefore possible to determine the volume filling fraction of the diluted samples (the volume filling fraction of a particular constituent in a mixture is defined as the ratio of the volume of the constituent to the total volume of the mixture) to within $\pm 5\,\%$ resulting from the uncertainty associated with the undiluted sample's mass fraction.

The undiluted sample was placed in an ultrasonic bath for $15\,$seconds before dilutions were made, to ensure proper dispersal of the polystyrene beads. It was found that the diluted samples required a longer period of $3\,$minutes in the ultrasonic bath to ensure proper dispersal (determined by eye) possibly due to a reduction in the concentration of the soluble polymer dispersant. Reflectance scans were performed on polystyrene latex sphere suspensions in distilled water at five different volume filling fractions up to a maximum value of $f = 10.3\,\%$.

3.4.4 Method: polydisperse sand sample

A commercial sand sample was used to test the application to a polydisperse sample with an expected uniform composition with particle size. The results of a sensitivity analysis, shown in section 3.5, performed on the polydisperse CSM assuming a log-normal distribution indicate that uncertainty in the retrieval of refractive index has a minimum for a size parameter of approximately 1.9, and the uncertainty increases with increasing size parameter. For a laser wavelength of $635\,$nm, a size parameter of 1.9 corresponds to a modal radius of approximately $190\,$nm. It is therefore necessary, for a typical sand or volcanic ash sample, to separate the fine fraction from the bulk. A sedimentation process was applied for this purpose.

In preparation of the sample used for reflectance scans, approximately $100\,$grams of the original sand sample was dispersed in the $900\,$ml of distilled water, and left to settle for $24\,$hours. After this period, with only a fine fraction of sand particles remaining in suspension, the suspension was drawn off from the sedimented fallout. This suspension of fine sand was then condensed down by gentle heating such that water was lost by evaporation.

It was then necessary to condense down the sample so the volume filling fraction of the sand was high enough to produce a significant reflectance signal (i.e. a

reflectance curve differing sufficiently from that of distilled water, due to the scattering effect of sand particles). An iterative process was adopted: a reflectance scan was performed using approximately 3 ml of the sample and the reflectance curve was plotted and compared to the reflectance curve of distilled water; then depending on the strength of the signal, the sample was further condensed. This process was repeated until the reflectance signal was judged to be sufficiently high so as to give an accurate retrieval.

Once the reflectance signal was sufficiently high (and the retrieval performed on the data indicated a volume filling fraction $> 3\,\%$) repeated scans were performed whilst incrementally increasing the concentration of particles to give a range of volume filling fractions.

3.4.5 Method: polydisperse ash sample

A commercially purchased sample of fine Icelandic volcanic ash, of unverified origin, was used to verify the technique. The method adopted for the ash sample was similar to that used for the sand sample. The exception being that the bulk mass of the ash sample available for experiments was considerably less. The same ratio of distilled water to bulk sample was used for the sedimentation process, using a mass of 20 grams of ash. Two samples were produced in this way; one was allowed to settle for 12 hours (sample A) whilst the period for the second was 24 hours (sample B).

A similar process, as outlined in section 3.4.4, was applied to condense down the sample to a high enough ash volume filling fraction to achieve suitable reflectance data.

3.5 Sensitivity analysis

In order to determine how measurement errors and other errors propagate through the forward model into uncertainty associated with the retrieved real refractive index n_{p}, a sensitivity analysis was performed for the monodisperse model and the polydisperse model.

3.5.1 Error propagation formalism

The error analysis formalism outlined in *Rodgers* [2000] is followed here. For the general problem, the measurement vector, $\mathbf{y}$, is related to the state vector, $\mathbf{x}$, and

the measurement error, $\boldsymbol{\epsilon}$, via:

$$\mathbf{y} = \mathbf{F}\left(\mathbf{x}, \mathbf{b}\right) + \boldsymbol{\epsilon}, \tag{3.20}$$

where $\mathbf{F}(\mathbf{x}, \mathbf{b})$ is the forward model, and $\mathbf{b}$ is the set of assumed forward model parameters. In this application, the measurement vector $\mathbf{y}$ contains the set of m detector readings recorded for the specularly reflected beam at m values of the incidence angle θ_{i}. The state vector $\mathbf{x}$ contains all retrieved parameters, including the real refractive index of the particles n_{p}. The vector $\mathbf{b}$ consists of quantities that influence the measurement and are known to some level of accuracy, but are not retrieved quantities.

After linearising about a reference state, $\mathbf{x}_0$, Eq. (3.20) becomes:

$$\mathbf{y} - \mathbf{F}(\mathbf{x}_0, \mathbf{b}) = \mathbf{K}(\mathbf{x} - \mathbf{x}_0) + \boldsymbol{\epsilon}, \tag{3.21}$$

where $\mathbf{K}$ is the Jacobian defined by $\mathbf{K}_{ij} = \partial \mathrm{F_i}(\mathbf{x})/\partial \mathrm{x_j}$, corresponding to the partial derivative of a forward model element with respect to a state vector element. The dimensions of $\mathbf{K}$ are $m \times n$.

When a retrieval is performed on the experimental data, a best estimate of the state, $\hat{\mathbf{x}}$, is produced:

$$\hat{\mathbf{x}} = \mathbf{R}\left(\mathbf{y}, \mathbf{b}\right), \tag{3.22}$$

and after linearising this becomes:

$$\hat{\mathbf{x}} = \mathbf{G}\mathbf{y}, \tag{3.23}$$

where $\mathbf{G}$ is the gain matrix and represents the sensitivity of the retrieved state to changes in the measurement vector, $\mathbf{G} = \partial \mathbf{R}/\partial \mathbf{y}$.

A least squares retrieval weighted by measurement error was performed on experimental data to determine the best estimate of the state, $\hat{\mathbf{x}}$. The minimised function was therefore:

$$\left(\mathbf{y} - \mathbf{K}\mathbf{x}\right)^{\mathrm{T}} \mathbf{S}_{\epsilon}^{-1} \left(\mathbf{y} - \mathbf{K}\mathbf{x}\right), \tag{3.24}$$

where $\mathbf{S}_{\epsilon}$ is the measurement error covariance matrix, defined by $S_{ij} = \langle \epsilon_i \epsilon_j \rangle$, with ϵ_i being the error associated with the i^{th} measurement. The gain matrix for this type of retrieval takes the form:

$$\mathbf{G} = \left(\mathbf{K}^{\mathrm{T}} \mathbf{S}_{\epsilon}^{-1} \mathbf{K}\right) \mathbf{K}^{\mathrm{T}} \mathbf{S}_{\epsilon}^{-1}. \tag{3.25}$$

The propagated uncertainty in the retrieved state, $\mathbf{S}_x$, has two contributions. The first contribution, $\mathbf{G}\mathbf{S}_\epsilon\mathbf{G}^{\mathrm{T}}$, results from the application of the retrieval to the measurement error. The second contribution, $\mathbf{G}\mathbf{K}_b\mathbf{S}_b\mathbf{K}_b^{\mathrm{T}}\mathbf{G}^{\mathrm{T}}$, results from errors associated with forward model parameters, with $\mathbf{K}_b = \partial\mathbf{F}/\partial\mathbf{b}$ being the sensitivity of the forward model to forward model parameters. The combined uncertainty associated with the retrieved state is:

$$\mathbf{S}_x = \mathbf{G}\mathbf{S}_\epsilon\mathbf{G}^{\mathrm{T}} + \mathbf{G}\mathbf{K}_b\mathbf{S}_b\mathbf{K}_b^{\mathrm{T}}\mathbf{G}^{\mathrm{T}}. \tag{3.26}$$

3.5.2 Modelling error

Often, simplifying assumptions are made because the real physics is either not known or cannot be modelled accurately. The modelling error is given by:

$$\mathbf{G}\Delta\mathbf{f} = \mathbf{G}\left[\mathbf{f}\left(\mathbf{x}, \mathbf{b}, \mathbf{b}'\right) - \mathbf{F}\left(\mathbf{x}, \mathbf{b}\right)\right], \tag{3.27}$$

where $\mathbf{f}$ contains the correct physics and $\mathbf{b}'$ contains additional model parameters.

3.5.3 Computing sensitivities

In order to evaluate the uncertainty in retrieved quantities the forward model sensitivities, $\mathbf{K}$ and $\mathbf{K}_b$, must be computed. These are simply linearisations of the forward model — Eq. (3.21) — and therefore vary as a function of the state vector $\mathbf{x}$.

In order to compute these sensitivities, one element of the state vector was perturbed by a fraction of 10^{-5} about a reference state, $\mathbf{x}_0$. The forward model was then applied to compute the resulting perturbed measurement vector. The sensitivity derivative could then be calculated. By repeating for each element of the state vector, consecutive columns of the Jacobian, $K_{ij}(\mathbf{x}_0) = \partial F_i(\mathbf{x}_0)/\partial x_j$, were computed.

In addition to computing the propagated uncertainties at this reference state, it is also useful to investigate how the propagated uncertainties vary with position in state space (or assumed model parameter space). Of particular interest is how these uncertainties vary with particle refractive index, and also with particle radius. For example, in order to investigate how the propagated uncertainties vary with particle refractive index, n_{p}, requires recalculation of the Jacobian over the desired range of n_{p}, whilst keeping the remaining parameters of the reference state fixed.

3.5.4 Sensitivity analysis of the monodisperse model and the polystyrene latex test particle retrieval

The analysis presented here is tailored to the type of retrieval performed on the polystyrene latex test particles. The reference state $\mathbf{x}_0$ was taken as the retrieved state from the retrieval on reflectance data from a polystyrene latex sample with a measured volume filling fraction of $f = 6.70\,\%$. In the polystyrene particle retrievals the monodisperse model was used (the particles were manufactured to be monodisperse, with a coefficient of variation in size of $\leq 3\,\%$ quoted by the manufacturer). The state vector took the form $\mathbf{x} = (n_\mathrm{p}, n_\mathrm{m})$. The parameter n_m was retrieved rather than fixed at the value of the refractive index of distilled water, because the presence of the polymer dispersant in the distilled water likely affects its refractive index. The volume filling fraction, f, which had been measured with an uncertainty of $5\,\%$ was fixed at its measured value in the retrieval and thus formed an element in the vector of assumed model parameters; additional assumed model parameters were such that $\mathbf{b} = (f, a, \lambda)$.

Figure 3.6 summarises the contributions to the combined uncertainty in the retrieval of real refractive index resulting from measurement uncertainties and uncertainties associated with assumed model parameters. The plots show how these error contributions vary (about the reference state) with particle refractive index and with size parameter — Figs. 3.6a and 3.6b, respectively.

Table 3.3 sets out the contributions to propagated uncertainty at the reference state: the $f = 6.70\,\%$ retrieval result. It can be seen that the $5\,\%$ uncertainty associated with the measured volume filling fraction contributes to the largest uncertainty in the retrieved real refractive index.

The uncertainty from assuming non-absorbing particles was calculated as follows. We can then take the imaginary particle refractive index to be zero, $k_\mathrm{p} = 0$, providing we assign a parameter error comparable to the true magnitude of k_p. *Xiaoyan et al.* [2003] found k_p for polystyrene to be less than 0.001 for $\lambda < 800\,\mathrm{nm}$. The contribution to the propagated uncertainty is then given by $\mathbf{G}\mathbf{K}_b\mathbf{S}_b\mathbf{K}_b^\mathrm{T}\mathbf{G}^\mathrm{T}$, as detailed in Eq. (3.26), assuming a parameter error in k_p of 0.001. The resulting propagated uncertainty in the retrieval of n_p was found to be less than 0.001 for all values of x and n_p investigated.

In theory there is no restriction on including the imaginary refractive index of the particles in the forward model. However, the value of the imaginary refractive index of polystyrene in the visible is very low and has very little effect on the

Figure 3.6: The contributions to uncertainty in the retrieval of real refractive index for a monodisperse system plotted against (a) real refractive index and (b) size parameter. The contributions to the uncertainty and the combined uncertainty are shown: — volume filling fraction, — incidence angle, — laser power, — particle radius, — laser wavelength and — combined uncertainty. Uncertainty resulting from assuming non-absorbing particles was less than 0.001. The reference state was taken to be the retrieved state for a polystyrene latex sample with a measured volume filling fraction $f = 6.70\,\%$.

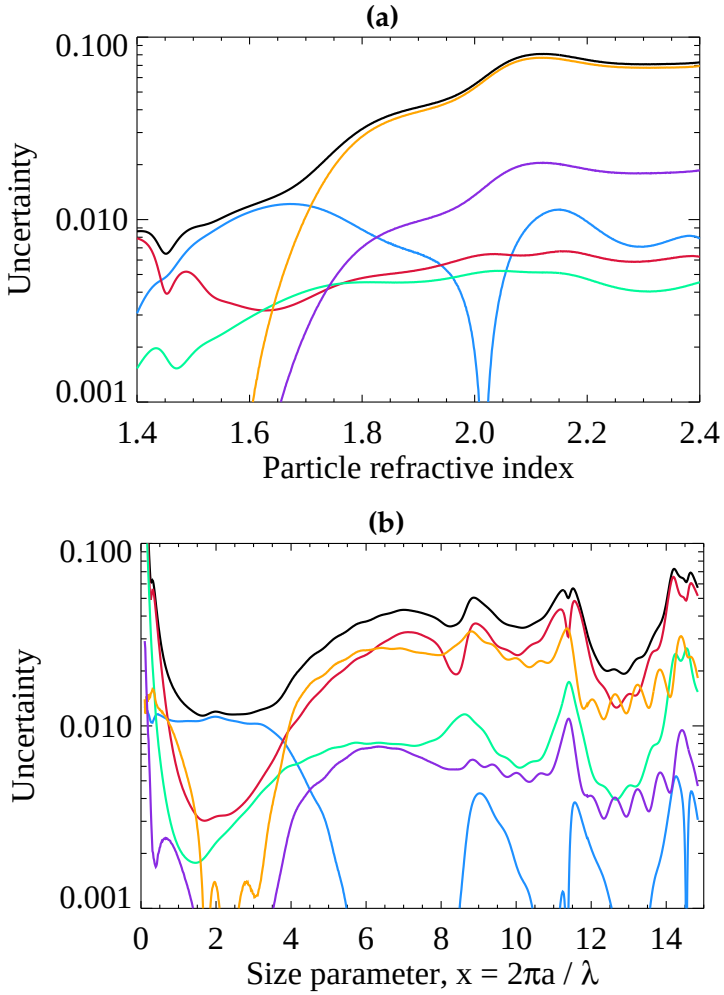

reflectance of the system or the retrieval of n_{p}, as demonstrated by the results of this sensitivity analysis.

3.5.5 Sensitivity analysis for the polydisperse model and the sand and ash retrievals

This analysis is tailored to the type of retrieval performed on the sand and the volcanic ash samples. The polydisperse model, taking into account the interface

Table 3.3: Summary of contributions to the propagated uncertainty in the retrieval of n_p for the retrieval using the monodisperse CSM performed on the polystyrene latex particle reflectance data. The values shown were calculated at the retrieved state of the $f = 6.70\,\%$ scan.

Error Term, e	σ_e	Propagated uncertainty, $\left\lvert\frac{\partial n_\mathrm{p}}{\partial e}\right\rvert \sigma_e$.
Volume filling fraction, f	$5\,\%$	0.01070
Incidence angle, θ_i	$0.05°$	0.00331
Laser power, LP	$1\,\%$	0.00279
Particle radius, a	$3\,\%$	0.00039
Non-absorbing assumption		0.00004
Laser wavelength, λ	$5\,\mathrm{nm}$	0.00001
Combined uncertainty		0.01154

region using a 50 slab system, was applied to experimental reflectance data from these samples. The choice of 50 slabs for the transition region is discussed later in Section 3.6.2; the choice is motivated by the convergence of reflectance curves predicted by the polydisperse CSM as the number of slabs is increased. A log-normal particle size distribution was assumed, controlled by the median radius, a_0, and geometric standard deviation, S. For these retrievals the state vector took the form $\mathbf{x} = (n_\mathrm{p}, n_\mathrm{m}, f, a_0, S)$, whilst the assumed model parameter vector had the form $\mathbf{b} = (\lambda)$. The reference state $\mathbf{x}_0$ was taken to be the retrieved state for a retrieval performed on sand reflectance data in which the retrieved volume filling fraction was $f = 5.01\,\%$.

Figure 3.7 summarises the error contributions in the retrieval of real refractive index as a function of particle refractive index and size parameter — Fig. 3.7a and Fig. 3.7b, respectively. The size parameter is defined in terms of the median radius of the log-normal distribution: $x = 2\pi a_0/\lambda$. It can be seen from Fig. 3.7b that the minimum for combined uncertainty occurs for a size parameter of approximately 1.9, which for a laser wavelength of $635\,\mathrm{nm}$ corresponds to a median radius of $190\,\mathrm{nm}$. The variations in propagated uncertainty with size parameter may reflect changes in the scattering efficiency of particles. The sharp increase in propagated uncertainty as the size parameter approaches unity can likely be explained by the rapidly decreasing scattering efficiency in the Rayleigh limit.

Table 3.4 shows the values of propagated uncertainty in the retrieval of real refractive index from each of the error terms. The particular values shown in the table apply for the polydisperse retrieval, employing a 50 slab interface region,

Figure 3.7: The contributions to uncertainty in the retrieval of real refractive index for a polydisperse distribution taking into account the interface region using a 50 slab system: — incidence angle, — laser power, — non-spherical effects, — non-absorbing assumption and — combined uncertainty. The reference state was taken to be the retrieved state for the sand retrieval with a retrieved volume filling fraction of $f = 5.01\,\%$.

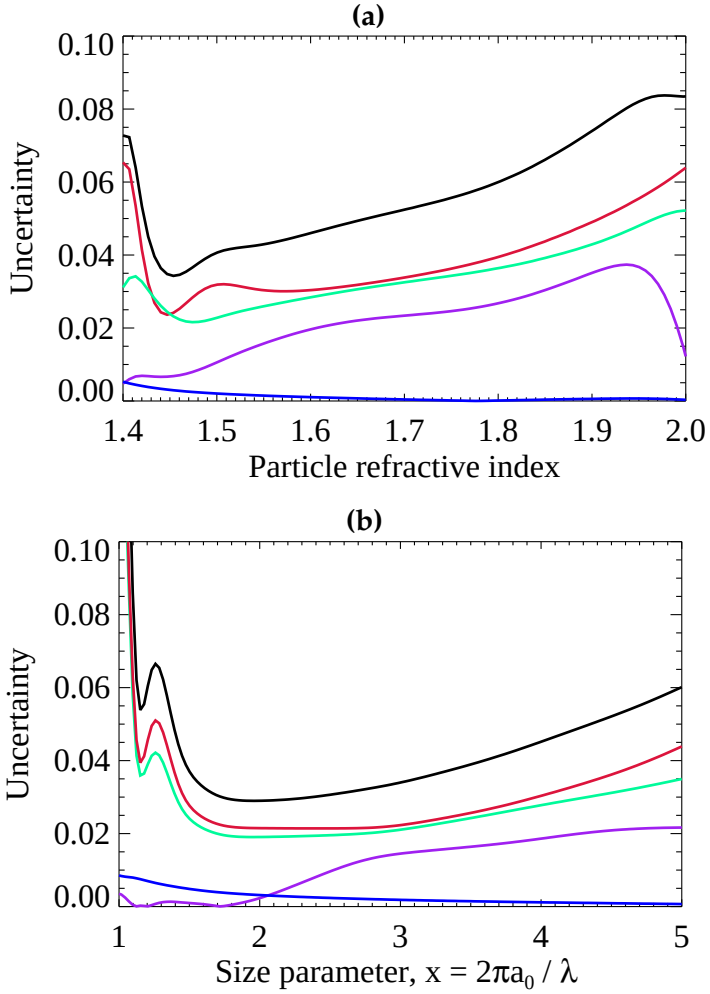

performed on a sand sample with a retrieved volume filling fraction of $f = 5.01\,\%$ (see Table 3.6 for the full state vector). The largest error terms come from uncertainty in the measured incidence angles at which the reflectance detector readings are made, and uncertainty in the laser power.

The uncertainty from assuming non-absorbing particles was calculated using a method identical to that outlined above for the monodiperse case. The imaginary particle refractive index was fixed at $k_\mathrm{p} = 0$ and assigned a parameter uncertainty of 0.001 — *Ball et al.* [2015] measured the imaginary refractive index of Eyjafjallajökull ash to be 0.000850 ± 0.00069 at $650\,\mathrm{nm}$. The propagated uncertainty was then

Table 3.4: Summary of the contributions to the propagated uncertainty in the retrieval of n_p for the polydisperse model taking into account the interface region using a 50 slab system. The reference state was taken to be the retrieved state for the sand retrieval with a retrieved volume filling fraction of $f = 5.01\,\%$.

Error Term, e	σ_e	Propagated uncertainty, $\left\lvert\frac{\partial n_\mathrm{p}}{\partial e}\right\rvert \sigma_e$.
Incidence angle, θ_i	$0.05°$	0.0301
Laser power, LP	$1\,\%$	0.0276
Non-spherical effects		0.0185
Non-absorbing assumption		0.0012
Laser wavelength, λ	$5\,\mathrm{nm}$	0.0001
Combined uncertainty		0.0449

calculated according to Eq. (3.26). As can be seen in Fig. 3.7 and Table 3.4 the forward model sensitivity to k_p is small.

The modelling error associated with assuming spherical particles (and therefore Mie scattering) was estimated. T-matrix scattering code, described in *Mishchenko and Travis* [1998], was used to calculate the configurationally averaged scattering amplitude functions, S_1 and S_2, for randomly orientated spheroids with an aspect ratio of 1.5 — an average aspect ratio of 1.47 ± 0.30 for Eyjafjallajökull ash was found in *Ball et al.* [2015]. The forward model result using these non-spherical scattering amplitude functions was subtracted from the forward model result using Mie scattering amplitude functions to give $\Delta\mathbf{f}$. The gain matrix was then applied to compute the propagated uncertainty, according to Eq. (3.27).

3.6 Results

3.6.1 Monodisperse polystyrene latex spheres

The monodisperse CSM was used within a least squares retrieval weighted by measurement errors — see Eq. (3.24) — to retrieve the state vector $\mathbf{x} = (n_\mathrm{p}, n_\mathrm{m})$ from the experimental reflectance scans on the suspensions of polystyrene latex particles with varying volume filling fractions in distilled water. The refractive index of the suspension medium n_m was retrieved because of the additional polymer dispersant present, which is likely to alter slightly the refractive index of the distilled water used to suspend the polystryrene particles. The volume filling fraction for each scan was fixed at its measured value in the retrieval. The vector of as-

sumed model parameters had the form $\mathbf{b} = (f, a, \lambda)$, with the particle radius fixed at $a = 260\,\text{nm}$ and the incidence wavelength fixed at $\lambda = 635\,\text{nm}$.

Figure 3.8: Reflectance scans for polystyrene latex spheres in distilled water at differing volume filling fractions. Shown are the fitted reflectance curve — using the monodisperse CSM and the Fresnel reflectance curve - - - for a suspension medium containing no scatterers with a refractive index equal to the retrieved value of n_m.

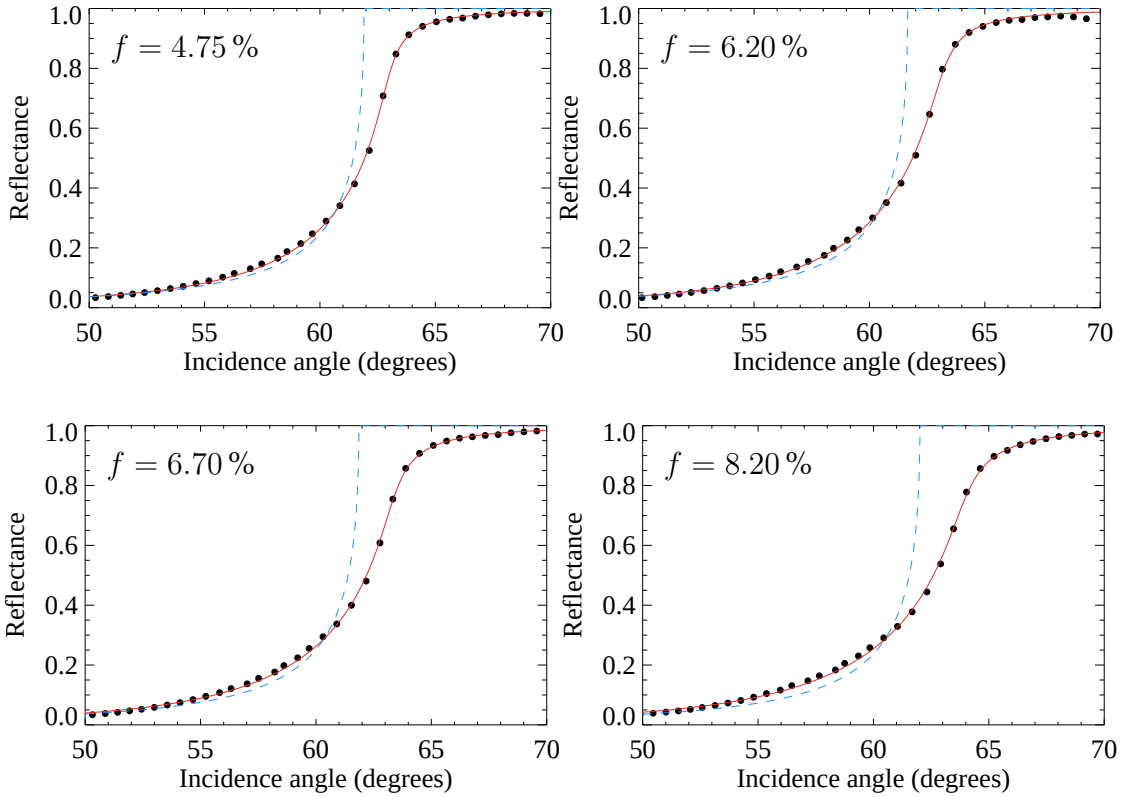

Figure 3.8 shows the experimental data points at different volume filling fractions. The fitted reflectance curves are shown in red. The Fresnel reflectance for a homogeneous medium (containing no scatterers) with a refractive index equal to the retrieved value of n_m is shown as a dashed blue line.

Table 3.5 summarises the retrieval results for the polystryrene latex sphere suspensions of varying volume filling fraction. The weighted mean refractive index from the polystryrene scans is $< n_\text{p} >= 1.5931 \pm 0.0052$ at $635\,\text{nm}$. This compares to the value for the refractive index of polystyrene of 1.5870 ± 0.001 at $635\,\text{nm}$ according to *Kasarova et al.* [2007].

Table 3.5: Summary of polystyrene latex sphere retrieval results using the monodisperse CSM.

Measured f (%)	Retrieved n_{p}	Retrieved n_{m}
4.75	1.6045 ± 0.0127	1.3364
6.20	1.5932 ± 0.0120	1.3337
6.70	1.5933 ± 0.0117	1.3359
8.27	1.5868 ± 0.0111	1.3379
10.36	1.5906 ± 0.0109	1.3398

3.6.2 Polydisperse sand sample

The number of slabs, N, used to model the transition region was determined by analysing reflectance curves, produced by the forward model, increasing N in increments of 5 (with all other parameters fixed). The analysis was performed with parameters fixed at: $n_{\mathrm{p}} = 1.58$, $n_{\mathrm{m}} = 1.33$, $f = 5.0\,\%$, $a_0 = 400\,\mathrm{nm}$, and $S = 1.2$. The results of this analysis are shown in Fig. 3.9. It was found that the reflectance curves rapidly converged. The improvement in increasing the number of slabs beyond 50 was small; the maximum difference in reflectance for $N = 50$ compared to $N = 100$ was less than $0.1\,\%$ (i.e. less than $10\,\%$ of the laser power uncertainty).

Figure 3.9: Differences in reflectance calculated using the polydisperse CSM when increasing numbers of slabs are use to model the interface region. The notation used in the key is: $R\,(N)$, where N is the number of slabs used in the model. The red curve shows that the maximum difference in reflectance when modelling the transition region with $N = 100$ compared to $N = 50$ is less than $0.1\,\%$. Remaining parameters were fixed at: $n_{\mathrm{p}} = 1.58$, $n_{\mathrm{m}} = 1.33$, $f = 5.0\,\%$, $a_0 = 400\,\mathrm{nm}$, and $S = 1.2$.

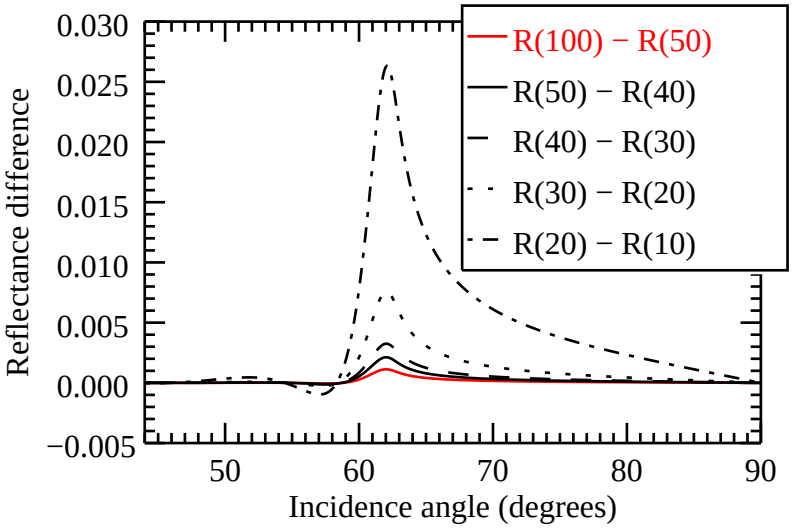

The polydisperse CSM using a 50 slab system to model the interface region was employed in the retrievals. The particle size distribution was assumed to be log-normal. The median radius a_0 and width parameter S were retrieved. The state vector for the retrieval took the form $\mathbf{x} = (n_\mathrm{p}, n_\mathrm{m}, f, a_0, S)$ and the parameter vector was $\mathbf{b} = (\lambda)$. A least squares retrieval weighted by measurements errors was employed. The suspension medium refractive index was included as a retrieved parameter, as it is possible that the sand sample has a small component of soluble material which may alter slightly the refractive index of the distilled water used to suspend the sand.

Table 3.6: Summary of the retrieval results on the sand sample.

n_p	n_m	f (%)	a_0 (nm)	S
1.6099 ± 0.0586	1.3338	3.66	424.6	1.145
1.6211 ± 0.0553	1.3317	4.41	417.0	1.146
1.5837 ± 0.0449	1.3323	5.01	402.1	1.127
1.5603 ± 0.0446	1.3339	5.56	450.2	1.108
1.5530 ± 0.0551	1.3353	6.06	432.8	1.183
1.5370 ± 0.0548	1.3310	6.08	435.7	1.184

Table 3.6 summarises the retrieval results for the sand sample. The mean refractive index for the sand from the 6 scans is $< n_\mathrm{p} >= 1.576 \pm 0.021$ at 635 nm. This compares to values measured using the Becke line technique of 1.566 ± 0.01 at 546.1 nm and 1.560 ± 0.01 at 650 nm.

3.6.3 Polydisperse volcanic ash sample

The same type of retrieval, outlined in section 3.6.2, was used for the volcanic ash reflectance data. As with the sand retrievals, the suspension medium refractive index was included as a retrieved parameter because the volcanic ash is likely to have a small soluble component that may alter slightly the refractive index of the distilled water used to suspend the ash.

Table 3.7 summarises the retrieval results for the volcanic ash samples. Sample A and sample B were produced from the same bulk ash sample, but were left to settle for 12 hours and 24 hours respectively for the sedimentation process. Table 3.7 shows a clear variation in the retrieved log-normal size distribution parameters between the two samples.

Table 3.7: Summary of the retrieval results on samples made from an Icelandic volcanic ash. Sample A underwent a 12 hour sedimentation process whilst for Sample B the period was 24 hours.

Sample	n_{p}	n_{m}	f (%)	a_0 (nm)	S
A	1.5684 ± 0.0710	1.3346	3.18	314.5	1.278
A	1.5597 ± 0.0523	1.3345	8.23	314.1	1.285
A	1.5269 ± 0.0549	1.3358	9.19	323.8	1.313
B	1.5561 ± 0.0573	1.3334	5.97	208.2	1.503
B	1.5535 ± 0.0596	1.3369	9.48	241.6	1.426
B	1.5308 ± 0.0587	1.3366	10.66	255.1	1.411

The mean refractive index from the 6 scans on volcanic ash was $< n_{\mathrm{p}} >= 1.553 \pm 0.024$ at 635 nm. The same volcanic ash sample's refractive index was measured using the Becke line method and was found to be 1.546 ± 0.01 at 546.1 nm and 1.548 ± 0.01 at 650 nm. The Becke line method is only applicable to particles with a radius larger than approximately 500 nm, as determined by the resolvable limit of the optical microscope used for the technique. Comparison with the result obtained using the reflectance measurements indicates no evidence of a variation in refractive index between the Becke line size regime and the size regime of the reflectance measurements (indicated by the retrieved modal radii in Table 3.7).

3.7 Chapter conclusions and discussion

The work presented in this chapter has been published in *Reed et al.* [2016]. The chapter details a method for determining the real refractive index of submicron aerosol particles from angular reflectance measurements, close to the critical angle, of a dilute colloidal suspension of the particles. The coherent scattering model of *Barrera and García-Valenzuela* [2003] has been applied to model the reflectance from the colloidal suspension, and an extension of the model has been developed which properly accounts for the modified particle size distribution close to the medium to colloid interface. The theoretical accuracy of the method has been analysed; A rigorous sensitivity analysis has been performed to determine how experimental uncertainties and uncertainty in assumed model parameters propagate into uncertainty associated with the retrieved real refractive index of colloidal particles, for both the monodisperse and polydisperse models. Experimental reflectance data, at a wavelength of 635 nm, were obtained for monodisperse spherical latex particles, a polydisperse sand sample and a polydisperse volcanic ash sample. The retrieved

real refractive index of the polystyrene particles matched, to within propagated uncertainties, the known refractive index of polystryrene. The retrieved real refractive indices of the sand and volcanic ash samples matched, to within propagated uncertainties, the values measured using the Becke line method on the same samples.

The extension of the coherent scattering model, presented in Section 3.3.5, to properly account for the modified size distribution close to the incident medium to colloid interface is required because the relative density of smaller particles increases as the interface is approached. The amplitude reflection coefficient for the system can be calculated straightforwardly through successive applications of Eq. (3.7), the composition law of amplitude. The approach is simpler and more intuitive than the treatment presented in *García-Valenzuela et al.* [2005b], which requires calculation of both the transmission and reflection amplitude coefficients of individual thin slabs. Based on the convergence of polydisperse reflectance curves with increasing number of slabs, it was found that modelling the transition region with 50 slabs was sufficient to accurately represent the system.

The results of the sensitivity analysis for monodisperse particles of known size, presented in Section 3.5.4, indicates that their real refractive index can be retrieved with an uncertainty of approximately 0.01 from a single angular reflectance scan, providing that their real refractive is less than 1.6 and the size parameters of particles is in the approximate range $\sim 1.0 - 3.5$ (corresponding to radii of approximately $100 - 300$ nm, at the laser wavelength of 635 nm). Even for larger particles, for example those with a size parameter in the range of $4.0 - 12$, the uncertainty in the retrieval of real refractive index remains fairly constant at around 0.04, providing that the real refractive index of particles is not too high. For monodisperse samples (where particle size is known), the accuracy of the retrieval from a single angular reflectance scan is comparable to the liquid immersion transmission method for solid particles of *Niskanen and Erik Peiponen* [2013]. However a disadvantage of the immersion liquid transmission method outlined in *Niskanen and Erik Peiponen* [2013] is it requires repeat measurements (typically 10 or more), using ~ 4 g of powder per measurement, in order to locate the minimum in the transmission of light. By comparison a single reflectance scan of the polystyrene or volcanic ash sample required only ~ 0.1 or 0.25 g respectively (assuming $f \sim 10\,\%$), and repeat scans could be performed on the same sample.

An advantage of the liquid immersion transmission method is that it is completely independent of the size distribution of particles. However, the results of

the sensitivity analysis of the polydisperse CSM, indicate that the real refractive index of particles can be retrieved without sizing information, with an uncertainty of 0.04, from a single angular reflectance scan, providing a log-normal particle size distribution can be safely assumed (the median radius and geometric standard deviation being retrieved parameters), for particles with a real refractive index in the range ~ 1.43 – 1.6 and median size parameters ~ 1.5 – 3.5. Reflectance measurements have already been studied and the sensitivity for determining particle size has been investigated, for example *García-Valenzuela et al.* [2008], however the sensitivity to real refractive index has not yet been investigated. Also the application of a rigorous error propagation formalism, as presented in this chapter, has not been applied in the literature to the problem of determining scatterer properties from colloidal reflectance measurements.

In the forward model used to predict the reflectivity from the colloidal suspensions, spherical particles were assumed and therefore the Mie scattering amplitude functions used. However, volcanic ash particles are known to have irregular non-spherical shapes. In principle, there is no reason why non-spherical scattering amplitude functions could not be used in the forward model, replacing the assumed Mie scattering amplitude functions. By employing T-matrix code, included in the sensitivity analysis is an estimate of the systematic uncertainty introduced into the retrieval of real refractive index resulting from non-spherical scattering effects.

An area for possible improvement for retrieving the real refractive index of ash samples from this method would be to incorporate independent sizing measurements of the aerosol. In the retrievals performed on the reflectance data from the polydisperse sand and ash samples, a log-normal distribution was assumed with a_0 and S being retrieved parameters. If accurate independent sizing data could be obtained for the submicron aerosol (for example from a scanning mobility particle sizer or an aerodynamic particle sizer), their incorporation could significantly reduce uncertainties associated with the retrieval of real refractive index for polydisperse samples, and any modelling inaccuracy in assuming a log-normal size distribution.

The experimental data and retrieval results, presented in this chapter, go some way to supporting the method as a viable and accurate technique for measuring the real refractive index of submicron volcanic ash particles, however the results are by no means an exhaustive evaluation of the method. One problem is the comparison of the results derived from the reflectance measurements for submicron

particles and those obtained using the Becke line method which can only be applied to particles larger than approximately $1\,\mu$m. Furthermore, without independent sizing data, it was not possible to verify the assumption of a log-normal distribution. Additionally, in future it would be useful to apply the method to a range of volcanic ashes having a known range of real refractive index values, to determine whether the method has the ability to accurately distinguish between them with good repeatability.

The coherent scattering model (CSM) is valid for particles of any size but in the limit of a dilute system having $f < 10\,\%$ [*Barrera and García-Valenzuela*, 2003]. Recently, an evaluation of the model and other similar models compared to experimental data has been undertaken by *Morales-Luna et al.* [2016] in order to establish the range of validity of the models without performing retrievals. It was found that the CSM was in good agreement with experimental data at all of the particle parameters evaluated in the paper (including parameters very similar to those in this chapter), however it was argued that the so called "heuristic approximation" model, outlined in the paper was slightly better at higher particle volume filling fractions. As future work, it would be useful to compare these models with more complex multiple scattering models capable of handling high density systems: a prime candidate would be the multiple scattering theory for discrete scatterers under the so called "quasi-crystalline with coherent potential" approximation, outlined comprehensively in *Tsang and Kong* [2001]. The approach of *Tsang and Kong* [2001] has the disadvantage of being highly mathematically involved requiring computationally heavy numerical evaluation for particles of comparable size to the incident wavelength, in contrast to the relatively succinct expressions of the CSM.

Chapter 4

Theory of aerosol transmission spectroscopy and sizing measurements

4.1 Introduction

This chapter summarises the theory needed to interpret spectroscopic extinction measurements of dispersed volcanic ash, as well as microphysical sizing measurements of volcanic ash. The chapter will also detail the principles of operation of the instruments used for these measurements. The theory outlined in this chapter will be applied in the following chapter to analyse data from experiments performed on volcanic ash dispersed in an aerosol cell.

4.2 Optical theory

4.2.1 Transmission of radiation through an aerosol

For a homogeneous random collection of particles, depicted in Fig.4.1, the transmission of radiation through the aerosol particles, $T_{\mathrm{a}}(\lambda) = L_{\mathrm{t}}(\lambda)/L_{\mathrm{i}}(\lambda)$ where L_{i} is the incident radiance (W m^{-2} steradian^{-1}) and L_{t} is the transmitted radiance, can be expressed via Bouguer's law as:

$$T_{\mathrm{a}}(\lambda) = \exp\left(-\beta^{\mathrm{ext}}(\lambda)\, x\right), \tag{4.1}$$

where $\beta^{\mathrm{ext}}(\lambda)$ is the aerosol volume extinction coefficient at wavelength λ, and x is the path-length through the aerosol. For a particle size distribution, $N(r)$, where

$N(r)\,dr$ is the number of particles per unit volume with radii between r and $r+dr$, the extinction coefficient can be calculated according to:

$$\beta^{\text{ext}}(\lambda) = \int_0^\infty \pi r^2 Q^{\text{ext}}(r, m(\lambda), \lambda)\, N(r)\, dr, \tag{4.2}$$

where Q^{ext} is the extinction efficiency for a particle of radius r, having a complex refractive index $m(\lambda)$. The extinction efficiency can be computed with Mie theory (valid for spherical particles) or using T-matrix methods (to deal with non-spherical particles). The extinction coefficient, β^{ext}, is related to the optical path, τ, according to:

$$\tau = \beta^{\text{ext}} x. \tag{4.3}$$

Figure 4.1: Transmission through a random collection of aerosol particles with a size distribution, $N(r)$, and complex refractive index, $m(\lambda)$.

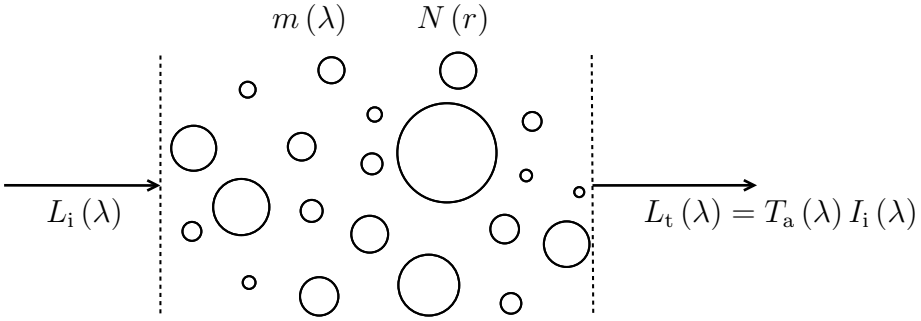

4.2.2 Practical measurements of aerosol transmission

In practice, measuring the aerosol transmission involved first making a measurements of the background radiance, L_{b}. This was the radiance of the source attenuated by losses in the optical system, which directs the beam into the aerosol cell (e.g. losses in the KBr cell window), and further attenuated by gas absorption due to any gases present in the cell (or along the optical path) whilst the background measurement was made. Therefore, the measured background radiance, L_{b}, is given by:

$$L_{\text{b}}(\lambda) = L_{\text{s1}}(\lambda) \times T_{\text{o1}}(\lambda) \times T_{\text{g1}}(\lambda), \tag{4.4}$$

where $T_{\text{o1}}(\lambda)$ is the transmission of the optical system at the time of the background measurement, T_{g1} is the transmission due to gases present in the cell at the

time of the background measurement, and $L_{\mathrm{s1}}(\lambda)$ is the source radiance at the time of the background measurement.

The aerosol was then pumped into the cell and a second measurement of radiance was made. This measurement radiance, L_{m}, therefore had an additional attenuation due to the aerosol particles:

$$L_{\mathrm{m}}(\lambda) = L_{\mathrm{s2}}(\lambda) \times T_{\mathrm{o2}}(\lambda) \times T_{\mathrm{g2}}(\lambda) \times T_{\mathrm{a}}(\lambda), \tag{4.5}$$

where $T_{\mathrm{a}}(\lambda)$ is the aerosol transmission. $T_{\mathrm{o2}}(\lambda)$, $T_{\mathrm{g2}}(\lambda)$, and $L_{\mathrm{s2}}(\lambda)$ are the optical transmission, gas transmission, and source radiance, respectively, at the time of the second measurement.

The measurement transmission, T_{m}, was the ratio of the measurement to the background radiance and was given by:

$$T_{\mathrm{m}} = \frac{L_{\mathrm{m}}}{L_{\mathrm{b}}} = \frac{L_{\mathrm{s2}} T_{\mathrm{o2}} T_{\mathrm{g2}} T_{\mathrm{a}}}{L_{\mathrm{s1}} T_{\mathrm{o1}} T_{\mathrm{g1}}}. \tag{4.6}$$

Providing it could be assumed that the source radiance and the transmission of the optical system remained constant between the two measurements, i.e. $L_{\mathrm{s1}} = L_{\mathrm{s2}}$ and $T_{\mathrm{o1}} = T_{\mathrm{o2}}$, then the expression for the measured transmission simplified to:

$$T_{\mathrm{m}} = \frac{T_{\mathrm{g2}} T_{\mathrm{a}}}{T_{\mathrm{g1}}}, \tag{4.7}$$

Provding gas lines are not close to saturation, writing $T_{\mathrm{g2}} = T_{\mathrm{g}} T_{\mathrm{g1}}$ where T_{g} is the transmission due to any additional gas molecules present in the cell when the second measurement is made compared to the first, allows Eq.(4.7) to be written as:

$$T_{\mathrm{m}} = T_{\mathrm{g}} T_{\mathrm{a}}. \tag{4.8}$$

If Eq. (4.8) is assumed, any change in the source radiance or the optical system transmission between the two measurements will introduce systematic error.

Figure 4.2 shows an example of measurements of L_{m} and L_{b} for one of the aerosol experiments. Water vapour and CO_2 gas absorption features are present in both the background and measurement radiance, but appear more strongly in the measurement radiance. Water vapour absorption is present over a wide band of wavelengths around $6.5\,\mu$m (associated with the symmetric v_2 vibration mode) and over a narrow band near $2.7\,\mu$m (v_1 and v_3 modes). CO_2 absorption is present at $4.5\,\mu$m. A strong aerosol absorption feature appears at $9\,\mu$m, resulting from asymmetric Si—O—Si vibrational stretching occurring within the aerosol particles.

Figure 4.2: An example of the background radiance, L_{b}, and the measurement radiance, L_{m}.

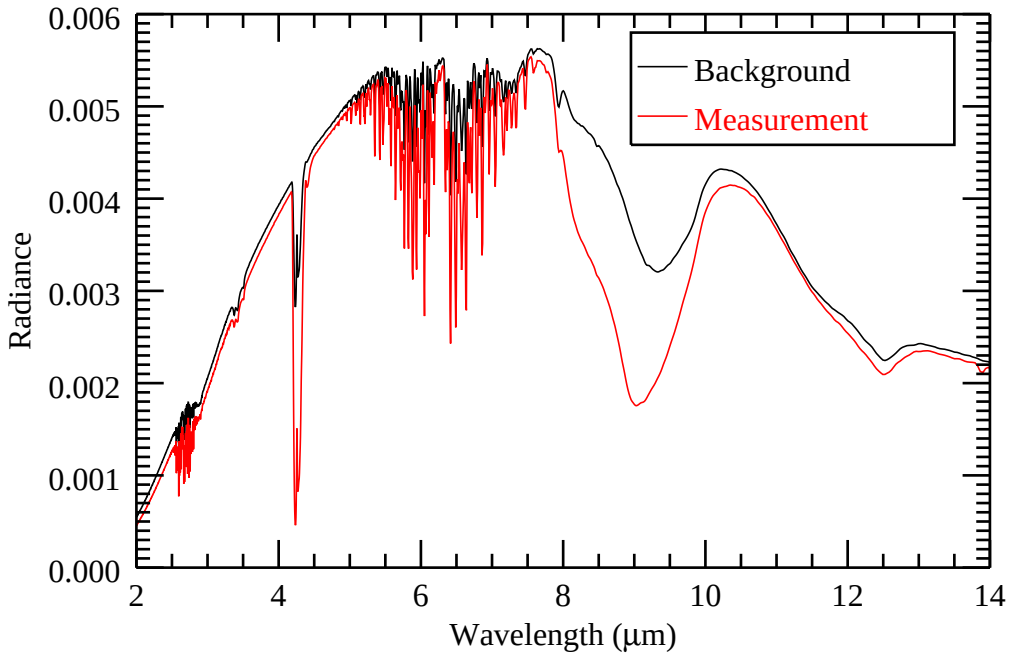

4.2.3 Fourier transform spectroscopy

4.2.3.1 Fourier series and Fourier's inversion theorem

Any continuous, periodic function, $f(x)$, obeying the Direchlet conditions can be represented as the sum of sine and cosine components [*Riley et al.*, 2008]. Noting that $\exp(irx) = \cos(rx) + i\sin(rx)$, the Fourier series expansion can be represented in complex form as:

$$f(x) = \sum_{r=-\infty}^{\infty} c_r \exp\left(\frac{2\pi irx}{L}\right) = \sum_{r=-\infty}^{\infty} c_r \exp(ik_r x), \tag{4.9}$$

where L is the period of the function and where $k_r = 2\pi r/L$ with r an integer. Due to the orthogonality of the exponential functions with differing values of r, by multiplying both sides of Eq. (4.9) by $\exp(-2\pi px/L)$ and integrating over the period L, the coefficients are obtained:

$$c_r = \frac{1}{L}\int_{x_0}^{x_0+L} f(x)\, e^{-ik_r x}\, dx. \tag{4.10}$$

The Fourier transform can be considered as the generalisation of Fourier series. It provides a representation of functions defined over an infinite interval and having no particular periodicity. As the period L tends to infinity, the wavenumber

quantum, $\Delta k_r = 2\pi/L$, becomes vanishingly small, so that Eq. (4.10) may be written as:

$$c_r = \frac{\Delta k_r}{2\pi} \int_{-L/2}^{L/2} f(x)\, e^{-ik_r x} dx, \tag{4.11}$$

and substitution into Eq. (4.9) yields:

$$f(x) = \sum_{r=-\infty}^{\infty} \frac{\Delta k_r}{2\pi} \int_{-L/2}^{L/2} f(u)\, e^{-ik_r u}\, du\, e^{ik_r x}. \tag{4.12}$$

In the limit that Δk_r is vanishingly small, the summation may be replaced by an integral and Eq. (4.12) becomes:

$$f(x) = \frac{1}{2\pi} \int_{-\infty}^{\infty} dk\, e^{ikx} \int_{-\infty}^{\infty} du\, f(u)\, e^{-iku}. \tag{4.13}$$

This result is known as Fourier's inversion theorem, from which we may define the Fourier transform of $f(x)$ by:

$$\tilde{f}(k) = \frac{1}{\sqrt{2\pi}} \int_{-\infty}^{\infty} f(x)\, e^{-ikx}\, dx, \tag{4.14}$$

and its inverse by:

$$f(x) = \frac{1}{\sqrt{2\pi}} \int_{-\infty}^{\infty} \tilde{f}(k)\, e^{ikx}\, dk. \tag{4.15}$$

4.2.3.2 The Michelson interferomater

The Michelson interferometer is the best know amplitude splitting interferometer, and is at the core of most modern Fourier transform spectrometers. The interferometer, shown in Fig. 4.3, consists of two mirrors set at right angles and a beam splitter which divides the incident beam into two beams of roughly equal irradiance. The two beams traverse separate paths, one going to the fixed mirror and one to the movable mirror. The beams are then recombined and travel to the sample chamber and then to the detector.

Consider monochromatic light from the source, in a setup where the path length difference between light travelling to the two mirrors is x and so the phase difference is $\delta = \frac{2\pi}{\lambda} x = 2\pi\nu x$, where $\nu = 1/\lambda = k/2\pi$ is the spectroscopic wavenumber. The combined amplitude of light at the detector is given by $E = E_0 e^{i\omega t} + E_0 e^{i\omega t + \delta}$, and therefore the irradiance of light at the detector is $I(x) = \frac{I(0)}{2}[1 + \cos(2\pi\nu x)]$.

Figure 4.3: Schematic of the Michelson interferometer.

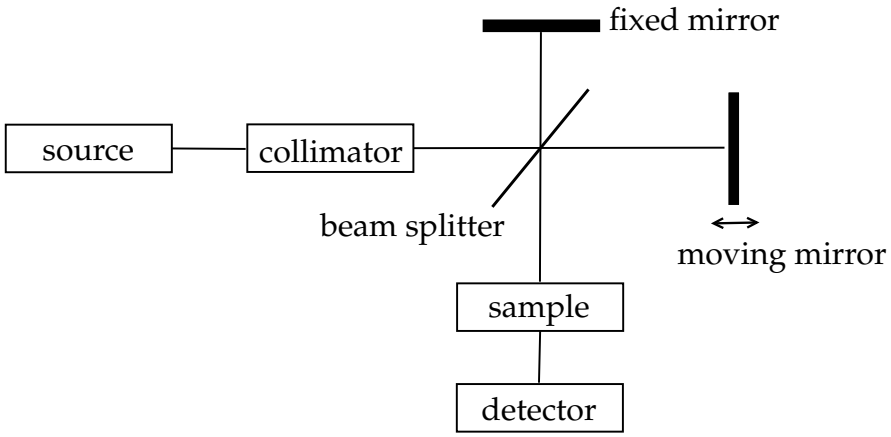

If the light source is not monochromatic, and has a spectral irradiance given by: $S(\nu) = \frac{dI(\nu)}{d\nu}$, then the irradiance is found by integrating over wavenumber:

$$I(x) = \frac{1}{2}\int_0^\infty S(\nu)\left[1 + \cos(2\pi\nu x)\right] d\nu. \tag{4.16}$$

Equation (4.16) gives the expression for the interferogram measured by Fourier transform spectrometer. The right hand side is recognisable as the cosine part of a Fourier transform of $S(\nu)$ (with an added constant). If $I(x)$ is measured by an interferometer by varying the path length difference x, it can be readily inverted, by taking the Fourier transform, to determine the spectral irradiance $S(\nu)$; this is the fundamental operating principle of Fourier transform spectrometers.

Figure 4.4 shows a Gaussian distribution and its interferogram. The width of the interferogram envelope is approximately equal to the reciprocal of the Gaussian width. If the width of the Gaussian is reduced to the extent that the envelope of its Fourier transform becomes comparable to the maximum path length difference that can be achieved by the instrument, information loss will be significant and the feature may not be resolvable.

The introduction of the sample does not alter the physics encapsulated by Eq. (4.16) other than, in the case of an absorbing sample, to diminish the source irradiance function at certain wavenumbers; the Fourier transform of the interferogram is then the transmitted irradiance.

Figure 4.4: A Gaussian distribution and its interferogram. The envelope (shown as the red dashed curve) of the interferogram has a width approximately equal to the reciprocal of the Gaussian width.

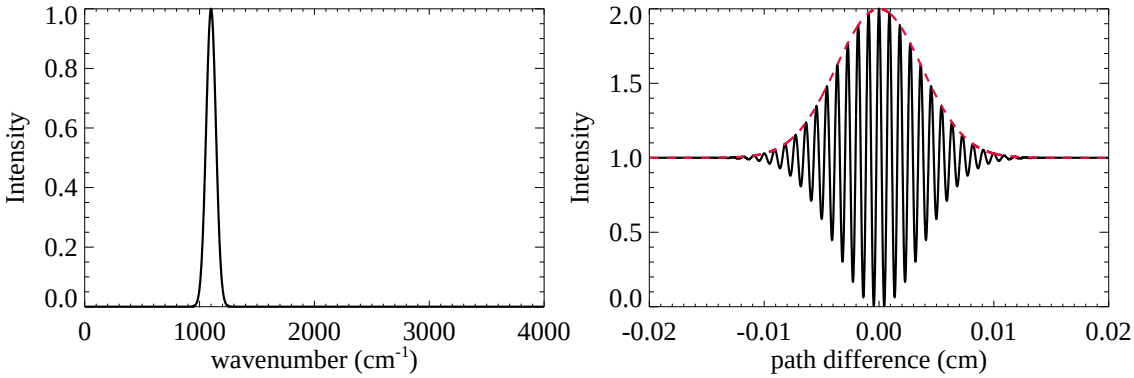

4.2.3.3 Resolution

The resolution, $\Delta\nu_{\min}$, of a Fourier transform spectrometer depends on the maximum optical path length difference, $x_{\max}$, that it can reliably achieve:

$$\Delta\nu_{\min} \approx \frac{1}{x_{\max}}. \tag{4.17}$$

Taking the Fourier transform of the interferogram to determine the spectral distribution assumes that $I(x)$ has been measured over an infinte path length difference. In practice what has been measured is the true interferogram multiplied by the step function $U(x)$, where $U(x) = 1$ for $-x_{\max}/2 < x < x_{\max}/2$ and $U(x) = 0$ elsewhere. The Fourier transform of this 'top-hat' function is a sinc function, namely $\mathrm{sinc}(\pi\nu x_{\max})$. When the Fourier transform of the measured finite interferogram is taken, the result is the true spectral distribution convolved by the sinc function. This has the result of broadening any spectral detail narrower than the sinc width, resulting in the loss of this fine detail. If, for example, the Gaussian shown in Fig. 4.4 were located within a spectral distance $\Delta\nu$ of a second identical Gaussian, then the resultant broadening of the two features would make them indistinguishable. Apodizing functions can be applied to the interferogram to smooth the subsequent Fourier transform, but they can do nothing to undo the loss of information due to the finite maximum path length of the instrument [*Norton and Beer*, 1975]. Modern commercially available IR FTS instruments can achieve maximum path length differences of $15\,\mathrm{cm}$ or larger, allowing a spectral resolution of up to $0.07\,\mathrm{cm}^{-1}$. As an example, the typical spacing of v_1 vibrational mode lines for CO_2 is 2.8–$3.0\,\mathrm{cm}^{-2}$, and for CO it is $4.0\,\mathrm{cm}^{-1}$ [*Banwell*, 1983]. For the

aerosol cell experiments presented in this thesis, the FTS was operated at a resolution of $1.929\,\mathrm{cm}^{-1}$, more than sufficient to resolve slowly varying aerosol extinction features.

4.2.4 Diffraction grating spectroscopy

Diffraction grating spectrometers use a diffraction grating to disperse incident light into an angular distribution of component wavelengths; they are classed as wavefront splitting interferometers. For a diffraction grating illuminated by plane parallel monochromatic light the phase difference, δ, between light emerging from adjacent slits, separated by a distance d, is given by:

$$\delta = \frac{2\pi}{\lambda} d \sin\theta \tag{4.18}$$

where θ is the diffraction angle. The resulting diffraction pattern, for a grating containing N infinitesimal slits, is given by:

$$I(\theta) = \frac{\sin^2(N\delta/2)}{\sin^2(\delta/2)}, \tag{4.19}$$

and taking into account the finite width, w, of slits simply requires multiplying Eq. (4.19) by $\mathrm{sinc}(kw\sin\theta)$. Principal maxima occur at $\delta = \pm n2\pi$, where n is the order of diffraction and has an integer value. There are N peaks for each 2π interval. Using Eq. (4.18), principal maxima occur for:

$$n\lambda = d\sin\theta. \tag{4.20}$$

4.2.4.1 Resolution

Figure 4.5 shows the angular irradiance distribution produced by a grating containing 5 slits. In order for two wavelengths, λ and $\lambda + \Delta\lambda$, to be just-resolvable requires that the principal peak of the second wavelength aligns with the first minima of the first wavelength, as depicted in Fig. 4.5; any closer and the two will be unresolvable. The first minima occurs at $\delta = 2\pi/N$ and therefore the minimum resolvable phase difference, $\Delta\delta_{\mathrm{min}}$, is given by:

$$\Delta\delta_{\mathrm{min}} = \frac{2\pi}{N}. \tag{4.21}$$

Figure 4.5: The spectrograph for a 5-slit grating, for two just-resolvable wavelengths.

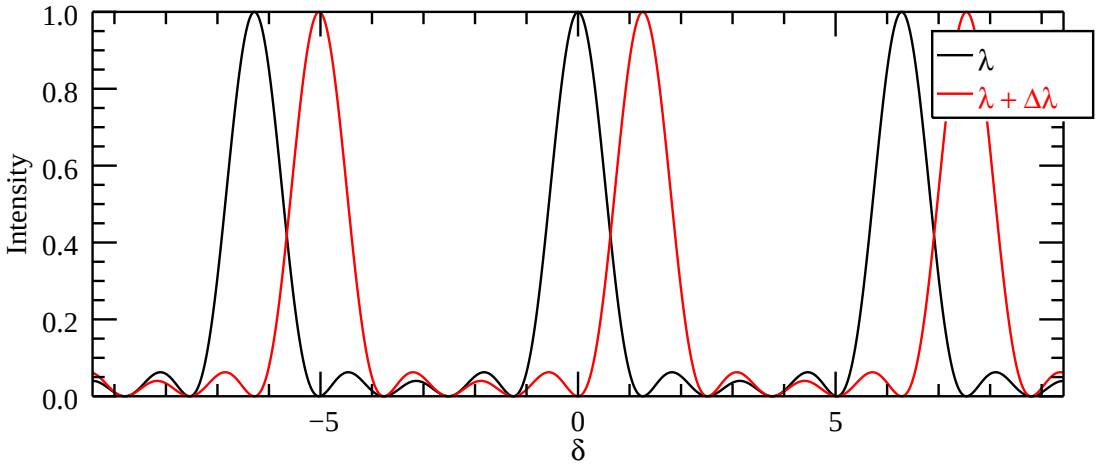

Differentiating Eq. (4.18) with respect to θ yields:

$$\frac{d\delta}{d\theta} = \frac{2\pi}{\lambda} d\cos\theta, \tag{4.22}$$

and therefore the angular separation, $\Delta\theta_{\text{min}}$, of the two just-resolvable wavelengths is:

$$\Delta\theta_{\text{min}} = \frac{\lambda}{Nd\cos\theta}. \tag{4.23}$$

Differentiating Eq. (4.20) gives the angular dispersion of spectral components:

$$\frac{d\lambda}{d\theta} = \frac{d\cos\theta}{n}, \tag{4.24}$$

and so the minimum resolvable wavelength difference, $\Delta\lambda_{\text{min}}$, is found by combining Eq. (4.22) and Eq. (4.24):

$$\Delta\lambda_{\text{min}} = \frac{\lambda}{Nn}. \tag{4.25}$$

Eq. (4.25) gives the theoretical resolution limit of a diffraction grating. In a real diffraction grating spectrometer, the resolution is further limited due to a number of effects. For example, the finite width of the spectrometer's entrance slit or the pixel density on its CCD detector may further limit the resolution. Generally, the entrance slit width will become resolution limiting if the image of the slit in the detector's plane is larger than the separation, Δx_{min}, of the principal peaks of two just-resolvable spectral components. However, a compromise is required because

a smaller entrance slit results in a lower measured irradiance reducing the signal to noise ratio.

In the aerosol cell experiments two Ocean Optics S2000 diffraction grating spectrometers were used covering the UV – NIR. The instruments use a reflection gratings with angled facets (so that the zero order reflection is not in the same direction as the incident light). The two S2000 spetrometers were configured to cover different spectral ranges: one covered $200 < \lambda < 850\,\text{nm}$ with a resolution $\Delta\lambda_{\min} = 1.33\,\text{nm}$, whilst the second covered $530 < \lambda < 1100\,\text{nm}$ with a resolution $\Delta\lambda_{\min} = 1.17\,\text{nm}$.

4.3 Theory of microphysical sizing measurements

There are numerous definitions of particle radii and various notations are used in the literature. Different sizing instruments return different radii based on their principles of operation, so it is important to clearly define the appropriate radius and establish relationships betweem the different definitions.

Some sizing instruments apply known equations for the drag force experienced by aerosol particles passing through a gas. The equations for the drag force vary depending on the flow regime of the system, and as a result the equations that relate the different definitions of particle radii will also vary. The purpose of this section is to summarise the definitions of particle radius, outline the principles of operation of the sizing instruments with which measurements have been made, and clearly detail the equations that relate the radii returned by the instruments.

4.3.1 The physical radius (r_{p}) and equivalent radii

The simplest description of a particle is its geometric or physical radius, r_{p}. For a spherical particle the physical radius is clear, however for non-spherical or porous particles the appropriate length is less obvious. Non-spherical or in some cases non-standard density particles can be characterised by *equivalent radii*. An equivalent radius is typically defined as the radius of a sphere that would give the same result for a given instrument as the particle under consideration.

4.3.2 The volume equivalent radius (r_{ve})

The volume equivalent radius is defined as the radius of a spherical particle with the same volume as the particle under consideration. For porous particles contain-

ing internal voids, the volume equivalent radius is the radius if the particle were re-shaped into a sphere whilst maintaining the internal void volume [*DeCarlo et al.*, 2004; *Hinds*, 1999].

4.3.3 Mass equivalent radius (r_{me})

The concept is almost identical to that of r_{ve} except that the mass equivalent radius r_{me} does not include internal voids. For a particle with no internal voids, $r_{\mathrm{me}} = r_{\mathrm{ve}}$. For particles with internal voids, $r_{\mathrm{me}} < r_{\mathrm{ve}}$ [*DeCarlo et al.*, 2004].

4.3.4 The Navier-Stokes equation and the Reynolds number

The Navier-Stokes equation describes the motion of a viscous fluid substance, and can be used to describe the motion of a gas around a particle. It is derived by considering the pressure-gradient, viscous and external forces acting on a moving volume of fluid [*Andrews*, 2000]. The form for an incompressible fluid can be expressed as:

$$\frac{\partial \mathbf{u}}{\partial t} + \mathbf{u} \cdot \nabla \mathbf{u} = -\frac{1}{\rho}\nabla p + \mathbf{f} + \frac{\mu}{\rho}\nabla^2 \mathbf{u}, \tag{4.26}$$

where $\frac{1}{\rho}\nabla p$ is the pressure gradient force, $\mathbf{f}$ is the external force (for the case of gravity $\mathbf{f} = -g\mathbf{k}$), $\frac{\mu}{\rho}\nabla^2\mathbf{u}$ is the viscous force, and $\mathbf{u}\cdot\nabla\mathbf{u}$ represents the inertia of the fluid.

The Reynolds number, Re, is an important dimensionless quantity used to characterise the flow regime of a system. The Reynolds number is defined as the ratio of inertial forces to viscous forces:

$$\begin{aligned} \mathrm{Re} = \frac{|\text{inertial forces}|}{|\text{viscous forces}|} = \frac{|\mathbf{u}\cdot\nabla\mathbf{u}|}{\left|\frac{\mu}{\rho}\nabla^2\mathbf{u}\right|} &\sim \frac{u^2/L}{\mu u/\rho L^2} \\ &\sim \frac{uL\rho}{\mu}, \end{aligned} \tag{4.27}$$

where u and L are a characteristic velocity and a characteristic length, respectively, for the flow.

When viscous forces dominate over inertial forces, $\mathrm{Re} \ll 1$ and the flow regime is described as *Stokesian* or having *Stokes flow*. For the common case of an incompressible Newtonian fluid the equations of motion reduce to:

$$\mu\nabla^2\mathbf{u} - \nabla p + \mathbf{f} = 0, \tag{4.28}$$

$$\nabla \cdot \mathbf{u} = 0, \tag{4.29}$$

where Eq. (4.28) comes from the reduced form of the Navier-Stokes equation and Eq. (4.29) is true for an incompressible fluid.

4.3.5 Flow regimes and the Knudson number

Sizing instruments often use the relationship between the drag force on a particle and some other force. As well as depending on the size and shape of particles, the drag force will vary according to the flow regime. An important quantity in characterising the flow regime of a gas around a particle is the Knudson number, Kn, defined as:

$$\mathrm{Kn} = \frac{\ell}{r}, \tag{4.30}$$

where ℓ is the mean free path of gas molecules. The limit of $\mathrm{Kn} \ll 1$ is called the *continuum* regime, the limit of $\mathrm{Kn} \gg 1$ is called the *free-molecular* regime, and intermediate values $0.1 < \mathrm{Kn} < 10$ are referred to as the *transition* regime.

Drag in the continuum regime is given by Stokes law. Stokes law, first outlined by George Stokes in 1851, is derived by solving the Stokes flow equations of motion, Eq. (4.28) and Eq. (4.29), for flow around a rigid sphere, with $\mathbf{f} = 0$, and using the boundary conditions of non-slip (zero velocity vector) at the surface of the sphere and a uniform velocity field at large distances from the sphere — see, for example, *Wen* [1996]. Integrating the pressure field solution over the surface of the sphere gives:

$$F_{\mathrm{drag}} = 6\pi\mu V r_{\mathrm{p}}, \tag{4.31}$$

where V is the velocity of the particle with respect to the fluid and μ is the dynamic viscosity ($\mathrm{kg\,m^{-1}\,s^{-1}}$) of the fluid. Note that the Stoke's drag is expressed here in terms of the physical radius, r_{p}. The derivation assumed a spherical particle and is therefore only strictly valid for spheres. For non-spherical particles, an equivalent radius must be used, along with a correction factor to account for increased (or decreased) drag. The correction comes through the dynamic shape factor, χ. The particle's Reynolds number, $\mathrm{Re_p}$, is given by:

$$\mathrm{Re_p} = V r_{\mathrm{p}} \rho_{\mathrm{g}} / \mu, \tag{4.32}$$

where ρ_{g} is the gas density. When $\mathrm{Re} > 0.1$, Stokes law must be corrected for non-Stokesian effects [*DeCarlo et al.*, 2004].

In the transition and free-molecular regimes, the relative velocity at the surface cannot be safely assumed zero. The resulting reduced drag is no longer negligible for $\mathrm{Kn} > 0.1$. The reduced drag is determined by the Cunningham slip correction factor [*Cunningham*, 1910], altering Eq. (4.31) to:

$$F_{\mathrm{drag}} = \frac{6\pi\mu V r_{\mathrm{p}}}{C_{\mathrm{c}}\left(r_{\mathrm{p}}\right)}. \tag{4.33}$$

The Cunningham slip correction was parameterised by *Allen and Raabe* [1985] as:

$$\begin{aligned} C_{\mathrm{c}}\left(\mathrm{Kn}\right) &= 1 + \mathrm{Kn}\left[\alpha + \beta\exp\left(-\frac{\gamma}{\mathrm{Kn}}\right)\right], \\ C_{\mathrm{c}}\left(r\right) &= 1 + \frac{\lambda}{r}\left[\alpha + \beta\exp\left(-\frac{\gamma r}{\lambda}\right)\right], \end{aligned} \tag{4.34}$$

where α, β and γ are empirically determined constants for the particular particle-fluid system under consideration. For solid particles they found: $\alpha = 1.142$, $\beta = 0.558$ and $\gamma = 0.999$, valid to within $2.1\,\%$ for all particle sizes. Equation (4.33) using Eq. (4.34), is valid for solid particles for all Kn providing $\mathrm{Re} < 0.1$.

The non-Stokesian ($\mathrm{Re} > 0.1$) effect on the drag force was parameterised, for example by *Cheng et al.* [1993]. A Reynolds number dependant factor $\left(1 + a\mathrm{Re}^{b}\right)$ was used, where a and b were empirically determined, giving a drag force of the form:

$$F_{\mathrm{drag}} = \frac{6\pi\mu V r_{\mathrm{p}}}{C_{\mathrm{c}}\left(r_{\mathrm{p}}\right)}\left(1 + a\mathrm{Re}^{b}\right). \tag{4.35}$$

4.3.6 The dynamic shape factor χ

Non-spherical particles have a larger surface area in contact with the fluid. As a result there tends to be an increased drag force exerted on the particle by the fluid. The exception being streamlined particles, where the drag force is reduced. A further correction to Eq. (4.31) is therefore required for non-spherical particles referred to as the dynamic shape factor, χ, first introduced by *Fuchs* [1965]. The dynamic shape factor is defined as the ratio of the drag force on the non-spherical particle to the drag force that would be experienced by its volume equivalent particle moving at the same velocity with respect to the fluid:

$$\chi = \frac{F^{\mathrm{p}}_{\mathrm{drag}}}{F^{\mathrm{ve}}_{\mathrm{drag}}}. \tag{4.36}$$

The general equation for the drag on any particle for all values of Kn, and $\mathrm{Re} < 0.1$, can be expressed as:

$$F_{\mathrm{drag}} = \frac{6\pi\mu V\chi r_{\mathrm{ve}}}{C_{\mathrm{c}}\left(r_{\mathrm{ve}}\right)}. \tag{4.37}$$

4.3.7 Electrical mobility radius r_{m}

The electrical mobility radius, r_{m}, is defined as the radius of a sphere having the same terminal velocity in a constant electric field as the particle under consideration. The electrical mobility radius is relevant to instruments such as a scanning mobility particle sizer (SMPS). The principle of such instruments is to give a particle a known charge and then rapidly establish a balance between the electric force on the particle in a constant electric field and the drag force on the particle; the unique terminal velocity at which this balance occurs can then be related to the particle's size. The electric force experienced by the particle is given by:

$$F_{\mathrm{elec}} = neE, \tag{4.38}$$

where e is the elemental unit of charge, n is the number of charges on the particle, and E is the electric field strength. The electrical mobility, Z_{p}, is defined as the terminal velocity, V_{t}, of the particle per unit electric field strength:

$$Z_{\mathrm{p}} = \frac{V_{\mathrm{t}}}{E}. \tag{4.39}$$

At terminal velocity the electric and drag forces are equal; combining Eq. (4.33), Eq. (4.38) and Eq. (4.39) yields:

$$Z_{\mathrm{p}} = \frac{neC_{\mathrm{c}}\left(r_{ve}\right)}{6\pi\mu\chi r_{\mathrm{ve}}} = \frac{neC_{\mathrm{c}}\left(r_{m}\right)}{6\pi\mu r_{m}}. \tag{4.40}$$

Often the charging probability for a non-spherical sphere is different to that of its volume equivalent particle [*Rogak et al.*, 1993]. However, assuming that the particle under consideration and its volume equivalent counterpart have the same charge, the relationship between the electrical mobility radius and the volume equivalent radius is given by:

$$\frac{r_{\mathrm{m}}}{C_{\mathrm{c}}\left(r_{\mathrm{m}}\right)} = \frac{r_{\mathrm{ve}}\chi}{C_{\mathrm{c}}\left(r_{\mathrm{ve}}\right)}. \tag{4.41}$$

For spherical particles, $r_{\mathrm{m}} = r_{\mathrm{ve}}$. For non-spherical particles with $\chi > 1$, the electrical mobility radius is larger than the volume equivalent radius, $r_{\mathrm{m}} > r_{\mathrm{ve}}$.

Eq. (4.41) is important when considering the measurements returned by an SMPS or a DMA.

4.3.8 The aerodynamic radius r_{a}

The aerodynamic radius, r_{a}, is defined as the radius of a spherical particle with standard density ($\rho_0 = 1.0\,\mathrm{g/cm^3}$) that has the same terminal settling velocity as the particle of interest. The terminal settling velocity, V_{t}, is reached when the gravitational force, F_{g}, equals the drag force, F_{drag}. In the discussion below the Stokesian and non-Stokesian regimes are considered, motivated by the fact that aerodynamic particle sizing instruments may span both regimes and commonly have particle Reynolds numbers in the range 0.1 – 100 (sometimes referred to as the near-Stokesian regime).

4.3.8.1 Stokesian regime: $\mathrm{Re} < 0.1$

In the Stokesian regime the balance of forces is given by:

$$F_{\mathrm{g}} = \rho_{\mathrm{p}} \frac{4}{3} \pi r_{\mathrm{ve}}^3 = \frac{6\pi\mu V_{\mathrm{t}} r_{\mathrm{ve}} \chi}{C_{\mathrm{c}}\left(r_{\mathrm{ve}}\right)} = F_{\mathrm{drag}}. \tag{4.42}$$

For a standard density (ρ_0) particle with a spherical shape ($\chi = 1$) and radius r_{a}, this becomes:

$$F_{\mathrm{g}} = \rho_0 \frac{4}{3} \pi r_{\mathrm{a}}^3 = \frac{6\pi\mu V_{\mathrm{t}} r_{\mathrm{a}}}{C_{\mathrm{c}}\left(r_{\mathrm{a}}\right)} = F_{\mathrm{drag}}. \tag{4.43}$$

Since the definition of aerodynamic radius requires a sphere of standard density with the same terminal settling velocity, V_{t} can be eliminated between Eq. (4.42) and Eq. (4.43) to determine the relationship between volume equivalent radius and aerodynamic radius:

$$r_{\mathrm{a}} = r_{\mathrm{ve}} \sqrt{\frac{1}{\chi} \frac{\rho_{\mathrm{p}}}{\rho_0} \frac{C_{\mathrm{c}}\left(r_{\mathrm{ve}}\right)}{C_{\mathrm{c}}\left(r_{\mathrm{a}}\right)}}, \tag{4.44}$$

Then using the empirical expression of Eq. (4.34) for the Cunningham slip correction, this becomes:

$$r_{\mathrm{a}} = r_{\mathrm{ve}} \sqrt{\frac{1}{\chi} \frac{\rho_{\mathrm{p}}}{\rho_0}} \left\{ \frac{1 + \frac{\lambda}{r_{\mathrm{ve}}} \left[\alpha + \beta \exp\left(\frac{-\gamma r_{\mathrm{ve}}}{\lambda}\right)\right]}{1 + \frac{\lambda}{r_{\mathrm{a}}} \left[\alpha + \beta \exp\left(\frac{-\gamma r_{\mathrm{a}}}{\lambda}\right)\right]} \right\}^{1/2}, \tag{4.45}$$

which, if r_{a} is known, must be solved numerically for r_{ve}.

4.3.8.2 Non-Stokesian regime: $\mathrm{Re} > 0.1$

The drag force must be modified to include non-Stokesian effects — Eq. (4.35). For any particle the balance of forces is given by:

$$F_{\mathrm{g}} = \rho_{\mathrm{p}} \frac{4}{3} \pi r_{\mathrm{ve}}^3 = \frac{6\pi\mu V_{\mathrm{t}} r_{\mathrm{ve}} \chi}{C_{\mathrm{c}}\left(r_{\mathrm{ve}}\right)} \left(1 + a\mathrm{Re}_{\mathrm{n}}^b\right) = F_{\mathrm{drag}}, \tag{4.46}$$

where Re_{n} is the Reynolds number of the, in general, non-spherical particle with volume equivalent radius r_{ve}. For a spherical particle ($\chi = 1$) with unit density ρ_0, the balance is given by:

$$F_{\mathrm{g}} = \rho_0 \frac{4}{3} \pi r_{\mathrm{a}}^3 = \frac{6\pi\mu V_{\mathrm{t}} r_{\mathrm{a}}}{C_{\mathrm{c}}\left(r_{\mathrm{a}}\right)} \left(1 + a\mathrm{Re}_{\mathrm{s}}^b\right) = F_{\mathrm{drag}}, \tag{4.47}$$

where Re_{s} is the Reynolds number of a spherical particle of radius r_{a}.

Eliminating V_{t} between Eq. (4.46) and Eq. (4.47) yields:

$$r_{\mathrm{a}} = r_{\mathrm{ve}} \sqrt{\frac{\rho_{\mathrm{p}}}{\rho_0} \frac{C_{\mathrm{c}}\left(r_{\mathrm{ve}}\right)}{C_{\mathrm{c}}\left(r_{\mathrm{a}}\right)} \frac{1}{\chi} \frac{\left(1 + a\mathrm{Re}_{\mathrm{s}}^b\right)}{\left(1 + a\mathrm{Re}_{\mathrm{n}}^b\right)}}, \tag{4.48}$$

which motivates defining a non-Stokesian shape factor, χ_{ns}, determined through application of Eq. (4.36):

$$\chi_{\mathrm{ns}} = \frac{\chi\left(1 + a\mathrm{Re}_{\mathrm{n}}^b\right)}{\left(1 + a\mathrm{Re}_{\mathrm{s}}^b\right)}. \tag{4.49}$$

Equation (4.49) demonstrates the need for care when retrospectively correcting for shape: the dynamic shape factor varies according to the flow regime of the system. Fortunately, under the near-Stokesian conditions found in a typical aerodynamic particle sizing instrument, and for aerodynamic radii close to $1\,\mu$m, the following approximation holds reasonably well [*Cheng et al.*, 1993]:

$$\frac{\left(1 + a\mathrm{Re}_{\mathrm{n}}^b\right)}{\left(1 + a\mathrm{Re}_{\mathrm{s}}^b\right)} \simeq 1. \tag{4.50}$$

4.3.9 Aerodynamic Particle Sizers

Figure 4.6 shows the basic setup in the measurement chamber of an aerodynamic particle sizer (APS). The principle is to measure the time-of-flight of particles between two points in an accelerating flow field. To acheive this, a particle flow and sheath flow are constricted through a nozzle, accelerating the flow. Laser beams are directed perpendicular to the page in Fig. 4.6. Light is scattered as a particle passes

through the beam, and the scattered light is collected by an elliptical mirror and measured by the detector (a photomultiplier tube). The design may vary between different instruments; for example, some instruments have separate PMTs for each beam.

Figure 4.6: Diagram of the measurement region in a typical APS. The laser beams are directed perpendicular to the page. Light is scattered when a particle passes through each beam. The time between detector peaks gives the time of flight for the particle.

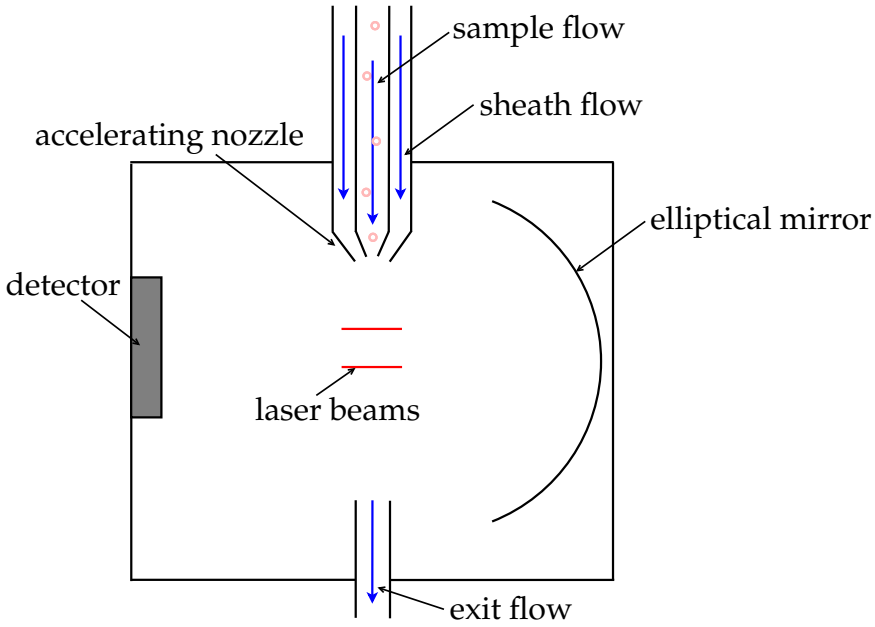

Particles are accelerated due to the drag forces generated in the accelerating air stream. The inertia of particles causes their velocity to lag behind the gas velocity. The accelerating drag force experienced by a particle is proportional to its radius and its relative velocity with respect to the gas flow, whilst its inertia to the applied force is proportional to its mass. Using Eq. (4.37), the general force equation can be expressed as:

$$\frac{6\pi r_{\mathrm{ve}}\mu\chi}{C_{\mathrm{c}}\left(r_{\mathrm{ve}}\right)}\left(U_{\mathrm{g}}-v\right)=\frac{4}{3}\pi r_{\mathrm{ve}}^{2}\rho_{\mathrm{p}}\frac{dv}{dt}, \tag{4.51}$$

where U_{g} is the gas velocity and v is the particle velocity. Since Eq. (4.37) was assumed, Eq. (4.51) is valid for any particle size and shape, providing $\mathrm{Re} < 0.1$. If the particle has an initial velocity v_0 after time t its velocity $v\left(t\right)$ is accelerated

towards the fluid velocity U_{g}, according to:

$$\begin{aligned} U_{\mathrm{g}} - v\left(t\right) &= \left(U_{\mathrm{g}} - v_0\right) \exp\left(-t/\,\tau\right), \\ \tau &= \frac{4 r_{\mathrm{ve}}^2 \rho_{\mathrm{p}} C_{\mathrm{c}}\left(r_{\mathrm{ve}}\right)}{18 \mu \chi}, \end{aligned} \tag{4.52}$$

where the constant τ is the particle relaxation time and depends on the particle radius. Solving for position, $s\left(t\right)$, given that the initial position of the particle was s_0 yields:

$$s\left(t\right) = s_0 + U_{\mathrm{g}} t - \tau\left(U_{\mathrm{g}} - v_0\right)\left[1 - \exp\left(-t/\,\tau\right)\right]. \tag{4.53}$$

Equation (4.53) demonstrates how the time of flight measurement of the particle between two positions can be related to the particle radius. In a real APS instrument the problem is complicated somewhat because the gas velocity, U_{g}, is a function of position inside the instrument (the gas accelerates as it passes through the nozzle and into the measurement region). However, the position dependence of the gas velocity field will be known for the instrument, allowing the time of flight measurement to be uniquely related to the particle's radius.

A typical APS instrument allows the density of particles to be input, and assumes that the particles are spherical, $\chi = 1$. However, it is common to operate the APS with the particle density set at $\rho = 1.0\,\mathrm{g/cm^3}$, so that the instrument returns the aerodynamic radius, r_{a}, of particles.

Table 4.1 summarises the technical details of the Model LD APS manufactured by Amherst Process Instruments. This instrument was used to size particles in the aerosol cell experiments. The time-of-flight of particles are measured between two laser beams positioned 1 mm apart. Two separate PMTs measure the light scattered by particles from each beam and convert this into a pulse sent to the data acquisition system. The PMT voltage can be set between 600 to 1200; higher voltages increase sensitivity to smaller particles, but have greater noise and need longer run times. Starting and ending signals for the same particle are distinguished from other signals by considering all signals over $100\,\mu$s and by correlating signals of the same irradiance.

The nozzle in the Model LD APS accelerates particles to near-supersonic velocity. The flow inside the measurement chamber is non-Stokesian (high Reynolds number) [*Thornburg et al.*, 1999] — the drag force is therefore given by Eq. (4.35). Equations (4.51), (4.52) and (4.53) are then modified for non-Stokesian affects by including the Reynolds dependent factor $\left(1 + a\mathrm{Re}^b\right)$. The internal software of the

instrument uses calibration curves, derived from a combination of theory and experimental data, to relate the measured time-of-flight for a particle to its aerodynamic radius r_{a}. Once aerodynamic sizing data are acquired with the APS, they can be retrospectively corrected for shape and non-standard density using Eq. (4.48).

Table 4.1: Technical summary of the Model LD, Amherst Process Instruments, APS. Information according to the user manual, unless otherwise stated.

Specification	Details
Size channels:	167 channels with aerodynamic radius mid-points from 0.051 to $107\,\mu$m, logarithmically spaced. Instrument returns number of counts per bin over measurement interval.
Number density:	Up to a maximum value of 1000 particles/cc [*Thornburg et al.*, 1999].
Flow regime:	Non-Stokesian, high Reynolds number; near-supersonic flow generated by the nozzle [*Thornburg et al.*, 1999].
Sample flow rate:	Variable 0.1 to 2.5 litres/min. Set at 0.6 litres/min for aerosol cell experiments.
PMT voltage:	Variable 600 to 1200 V. Set at 1150 V for aerosol cell runs to maximise sensitivity to small particles.
Measuring interval:	Set at 120 seconds for aerosol cell experiments. Measurement time logged for each run.
Data output:	Via PC to individual text file for each measurement. Measurements set to run consecutively during aerosol cell experiments. Each measurement contains number of counts for each bin and string with time stamp, sample flow rate, measurement interval, and other instrument settings.

4.3.10 Scanning Mobility Particle Sizer

4.3.10.1 Principle of operation

The principle of a scanning mobility particle sizer (SMPS) is to apply a well defined charge distribution to the input aerosol, and to then classify the aerosol based on the electrical mobility — defined in Eq. (4.39) — of the particles in an applied electric field. An SMPS usually consists of a differential mobility analyser (DMA), to separate particles by Z_{p}, connected to some form of particle counter. For the aerosol cell experiments an SMPS was used consisting of the Grimm 5.5-900 DMA

connected to the Grimm 5.403 condensation particle counter (CPC). The two components of the SMPS will be covered in the following sections.

4.3.10.2 Differential mobility analyser

Figure 4.7 shows the Grimm DMA, part of the Grimm SMPS. Before entering the DMA the sample-air flow passes through an impactor (Grimm Kit No. 5.525) followed by a nuetralizer (Grimm Model 5.521). The impactor prevents particles that are too large from entering the DMA. It consists of an impaction nozzle directing flow to an impaction plate; smaller particles are able to follow the gas streamlines around the 90° bend whereas larger particles collect on the plate (see *Hinds* [1999] for a detailed description). The neutralizer contains a radioactive alpha source, ^{241}Am, with an intensity of 3.7 Bq. The alpha emitter is used to ionize air molecules, creating a bipolar ionic atmosphere. The positive and negative air ions are attracted to oppositely charged aerosol particles passing through. Given sufficient time inside the neutralizer the aerosol charge distribution will reduce to the Fuchs equilibrium distribution [*Fuchs*, 1963].

The DMA consists of a central anode rod with a variable voltage that can be set between 20 and $10,000$ V and a grounded coaxial outer tube. The set-up creates a radial E-field directed towards the central anode. The gas flow inside the DMA is precisely controlled; a laminar sheath flow of clean air is established (in the y direction in Fig. 4.7) and merges with a thin annular layer of the sample flow containing the aerosol. The equation of motion of the particle, in the direction of the applied E-field (the x-direction), can be expressed as:

$$neE - \frac{6\pi\mu v_x \chi r_{\mathrm{ve}}}{C_{\mathrm{c}}\left(r_{\mathrm{ve}}\right)} = \frac{4}{3}\pi r_{\mathrm{ve}}^3 \rho_{\mathrm{p}} \frac{dv_x}{dt}. \tag{4.54}$$

After time t, if the initial velocity of the particle is v_0, the velocity of the particle is given by:

$$\begin{aligned} v_x\left(t\right) &= V_{\mathrm{t}} - \left(V_{\mathrm{t}} - v_0\right)\exp\left(-t/\tau\right), \\ V_{\mathrm{t}} &= \frac{neEC_{\mathrm{c}}\left(r_{\mathrm{ve}}\right)}{6\pi\mu r_{\mathrm{ve}}\chi}, \\ \tau &= \frac{2r_{\mathrm{ve}}^2 \rho_{\mathrm{p}} C_{\mathrm{c}}\left(r_{\mathrm{ve}}\right)}{9\mu\chi}, \end{aligned} \tag{4.55}$$

Figure 4.7: Diagram of a differential mobility analyser (DMA). The central anode and grounded outer electrode produce a radial E-field. Only particles with a particular range of radii have a trajectory that allows them to pass to the counter.

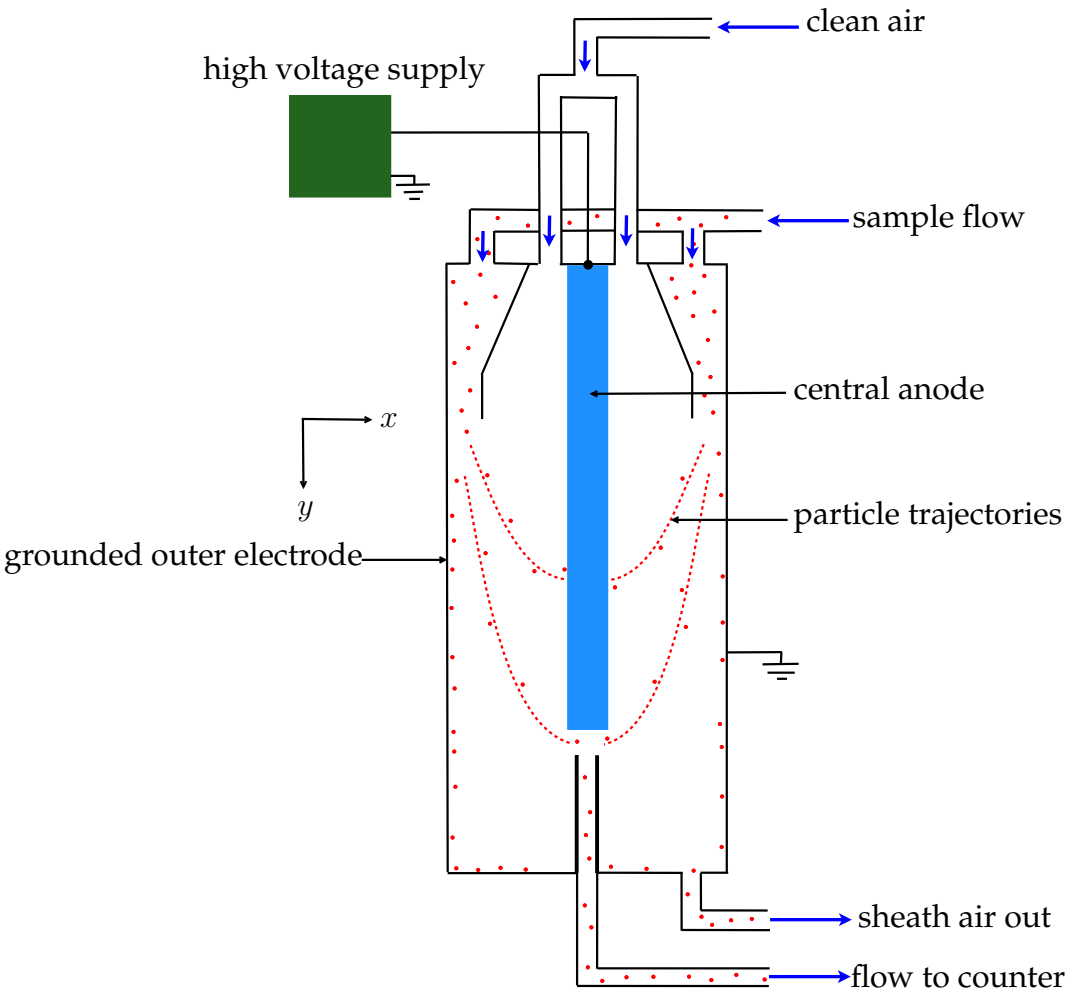

where V_t is the terminal velocity of the particle and τ is the relaxation time. If the particle starts at x_0 then its position after time t is given by:

$$x\left(t\right) = x_0 + v_\mathrm{t}t + \tau\left(v_\mathrm{t} - v_0\right)\exp\left(-t/\tau\right). \tag{4.56}$$

The motion of the particles in the y-direction is set by the sheath flow velocity v_y. Only particles with a particular trajectory will reach the gap between the lower end of the anode and the flow to the particle counter. Suppose the length of the anode from the point of introduction of the aerosol to the gap centre is Y, and the radial distance from the aerosol annulus to the central anode is X. If the gap has a half width ΔY, the time of flight range for particles passing through the gap from the aerosol introduction point must be given by $t = \left(Y \pm \Delta Y\right)/v_y$. Equation (4.56)

Table 4.2: Technical summary of the SMPS consisting of the Grimm Model 5.5-900 DMA connected to the Grimm 5.403 CPC.

Specification	Description
DMA	
Size channels:	Mid-point electrical mobility radii from 5 nm to 437.5 nm. The number of channels can be set up to 255. The channels are logarithmically spaced. During the aerosol cell experiments 44 channels were used. The instrument returns number density of particles in particles/cc for each bin.
Measurement interval:	~ 7 mins. Controlled by Grimm PC software which controls the DMA voltage, to scan over the channels.
Sample flow rate:	0.3 litres/min.
Sheath air flow:	3.0 litres/min.
Length:	63 cm.
Tube diameter:	8 cm.
CPC	
Number density:	1×10^{-3} to 10^5 particles/cc.
Coincidence:	< 2 % at 10^4 particles/cc.
Measurement interval:	~ 7 mins. Determined by the DMA scan time.
Sample flow rate:	0.3 or 1.5 litres/min. Set at 0.3 litres/min for compatibility with the DMA.
Radioactive source:	^{241}Am, alpha emitter, with radioactivity of 3.7 Bq. The radioactive source is housed in the neutralizer.
Humidity:	Accepts sample flow with 0 – 95 % relative humidity.
Dimensions:	$26 \times 29 \times 11$ cm.
Weight:	11.5 kg.
Data output:	The DMA and CPC work together, controlled by Grimm PC software, and produce a single text file containing consecutive measurements. Each measurement has a time stamp and number density data for the 44 channels.

can be simplified by assuming the particle instantly reaches terminal velocity, so that $x\left(t\right) = v_{\mathrm{t}}t$. Thus the radii of particles passing through the gap is given by:

$$r_{\mathrm{ve}} \pm \Delta r_{\mathrm{ve}} = \frac{neEC_{\mathrm{c}}\left(r_{\mathrm{ve}}\right)}{6\pi\mu}\frac{\left(Y \pm \Delta Y\right)}{Xv_y}. \tag{4.57}$$

Equation (4.57) demonstrates how by varying the central anode voltage (which determines the radial electric field strength E), the differential mobility analyser

can scan over different particle size bins. The selected sample flow then passes to a condensation particle counter (CPC), which determines the number density of particles in the particular radius bin.

4.3.10.3 Condensation particle counter

Standard optical particle counters have difficulty sizing ultra-fine particles with a rapid drop-off in counting efficiency for radii below $100\,\mathrm{nm}$. This is because these particles have small scattering cross sections, σ^{sca}, making detection by laser scattering unfeasible. The principle of a CPC is to first enlarge particles by using them as condensation nuclei to create liquid droplets in a supersaturated gas. These larger liquid droplets are then easily detected using conventional laser scattering.

In the saturator of the GRIMM CPC, n-Butanol is evaporated at $35\,^{\circ}\mathrm{C}$ and the vapour is mixed with the sample flow. The vapour and sample then pass into a condenser chilled at $10\,^{\circ}\mathrm{C}$. The temperature drop in the condenser results in nucleus condensation and growth of liquid droplets with a radius of approximately $5\,\mu\mathrm{m}$. The precisely controlled saturation level ensures that every particle forms a liquid drop and no droplets form without the presence of a particle. The droplets are then detected by perpendicular light scattering, which with precise flow control inside the instrument allows the number density of particles to be determined.

4.3.11 Optical particle counter (OPC)

Figure 4.8: Diagram of the laser measuring chamber in the GRIMM, model 1.801, OPC. Image taken from the GRIMM model 1.801 user manual.

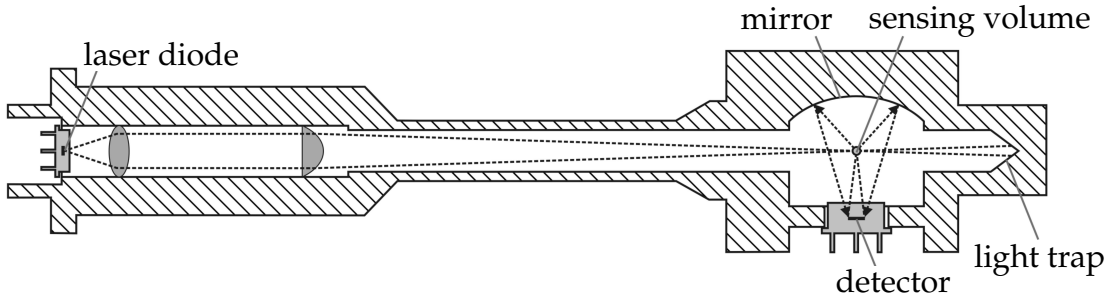

Optical particle counters measure the irradiance of light scattered by individual particles to determine their size. Figure 4.8 shows the laser measuring chamber of the Grimm Model 1.801 OPC. The flow of particles is perpendicular to the page, passing through the sensing volume. As individual particles pass through the

Table 4.3: Technical summary of the Grimm Aerosol Technik Model 1.801 OPC according to the user manual.

Specification	Description
Laser wavelength:	$\lambda = 780\,\text{nm}$.
Size channels:	Set to 15 channel configuration. Reverse cumulative distribution returned, giving the counts for particles with radii (μm) greater than: 0.15, 0.2, 0.25, 0.375, 0.4, 0.5, 0.8, 1.0, 1.5, 2.0, 2.5, 3.75, 5.0, 7.5, and 10.0, in each bin.
Number density:	1×10^{-3} to $2,000$ particles/cc.
Reproducibility:	$\pm 3\,\%$ over the 15 channels.
Sample flow rate:	Maintained at 1.2 litres/min $\pm 5\,\%$.
Measuring interval:	6 seconds: Determined by the channel configuration.
Data storage interval:	60 seconds.
Sample air:	Input air must be 4 to $40\,^{\circ}\text{C}$ and $< 95\,\%$ relative humidity.
Data output:	Via PC and Windows software, saved to text file. Data consists of 9 sizing distributions per minute. After the first six seconds a string containing the time stamp, error code, the internal sample pump voltage, and 5 optional accessory units is reported.
Dust collection:	47 mm PTFE filter. Exit air is particle free.
Weight:	1.7 kg
Dimensions:	$24 \times 13 \times 7$ cm.

sensing region they scatter the laser beam. The scattered light reflected by the solid angle of the mirror is measured by the detector.

The OPC must then relate the measured scattered irradiance to the size of the particle. The scattering produced by an arbitrary particle is determined by its shape, size and complex refractive index. The OPC assumes Mie scattering, i.e. that the particles are spheres. It must also assume a refractive index for the particles. The irradiance of scattered light, I_s, is given by integrating Mie phase function, $P\left(\theta, x, \tilde{m}\right)$, over the solid angle of the mirror:

$$I_\text{s} = I_\text{i} \sigma^\text{sca} R \int_\text{mirror} P\left(\theta\right) d\Omega, \tag{4.58}$$

where I_i is the incident laser irradiance, R is the reflectivity of the mirror, and σ^sca is the Mie scattering cross-section. Both σ^sca and P are functions of the size parameter, $x = 2\pi r/\lambda$, and complex refractive index, m, of the particles. The measurement of I_s can be numerically inverted to uniquely determine the particle radius,

r, providing a complex refractive index is assumed. Clearly the measurement of highly non-spherical particles, or particles whose complex refractive index is not known, poses problems for optical particles counters, and may introduce significant systematic error into the measurements.

Table 4.3 gives the technical summary of the Grimm Aerosol Technik Model 1.801 OPC used to size particles in the aerosol cell experiments. Sample flow through the instrument is maintained at 1.2 litres/min $\pm 5\,\%$ controlled by the instrument's internal pump and pressure sensor. The instrument is designed for ambient aerosol measurement, and can be used to detect aerosol number densities in the range $1 - 2,000$ particles/cc. At number densities greater than $2,000$ particles/cc coincidence of particles inside the measuring chamber becomes significant. In the aerosol cell experiments, the sample flow was diluted by a factor of ~ 80 to ensure that the particle number density was within the operating limits of the instrument.

4.4 Chapter summary

This chapter summarises the optical theory needed to interpret spectroscopic extinction measurements of dispersed volcanic ash, as well as the microphysical theory needed to analyse sizing measurements. The principles of operation of the instruments used to make these measurements were also outlined. Particular care is needed when interpreting sizing data returned from different instruments because they may return different radii. For example, an SMPS measures the electrical mobility radius, r_{m}, and an APS returns the aerodynamic radius, r_{a}, of particles. The natural choice for interpreting extinction measurements is to convert these radii to the volume equivalent radius, r_{ve}. Both the SMPS and APS apply known equations for the drag force experienced by particles in a gas. The drag force equation varies depending on the flow regime of the particle-gas system, and therefore so do the radii conversion equations. The equations also depend on the shape of particles, through the dynamic shape factor, χ, as well as the density of particles, ρ_{p}. Accordingly, any error in assumed values for these parameters will contribute to systematic error in the resulting size distribution of particles.

Chapter 5

The aerosol cell experiments

5.1 Experimental method and apparatus

Experiments were performed at the Rutherford Appleton Laboratory's Molecular Spectroscopy facilty between 9 March and 25 June 2015 on a set of 11 potential geo-engineering powders and 18 volcanic ash samples. Before entering the cell the samples were dispersed in nitrogen gas using either the Wright dust feeder (WDF) or a mechanical blade disperser (an adapted coffee grinder). Once inside the cell, optical measurements were made of the dispersed aerosol with a Bruker Vertex-80 Fourier transform spectrometer (FTS) in the IR and two Ocean Optics S2000 CCD spectrometers covering UV, visible, and NIR wavelengths. After leaving the cell, the microphysical properties of the aerosol were measured using a suite of sizing and sampling instruments.

5.1.1 Aerosol preparation and dispersal

A constant, reproducible supply of well-dispersed aerosol was desired in order to establish a constant number density of suspended aerosol inside the cell. All samples were prepared by sieving with a $45\,\mu$m meshed sieve to remove coarse particles and were dried overnight at $100\,^{\circ}$C. Figure 5.1 shows the experimental setup for loading the cell with aerosol. There are two possible dispersal methods for supplying aerosol to the cell: the EMMS Wright dust feeder or the mechanical blade disperser (an adapted coffee grinder). The system can be switched between the two mechanisms by closing or opening valves V1a and V1b, as appropriate. The dispersed aerosol enters the top of the cell, and is mixed within the cell by the action of the turbulent injector controlled by mass flow controller 1 (MFC1).

Figure 5.1: Experimental set-up for loading of the aerosol cell with dispersed aerosol sample.

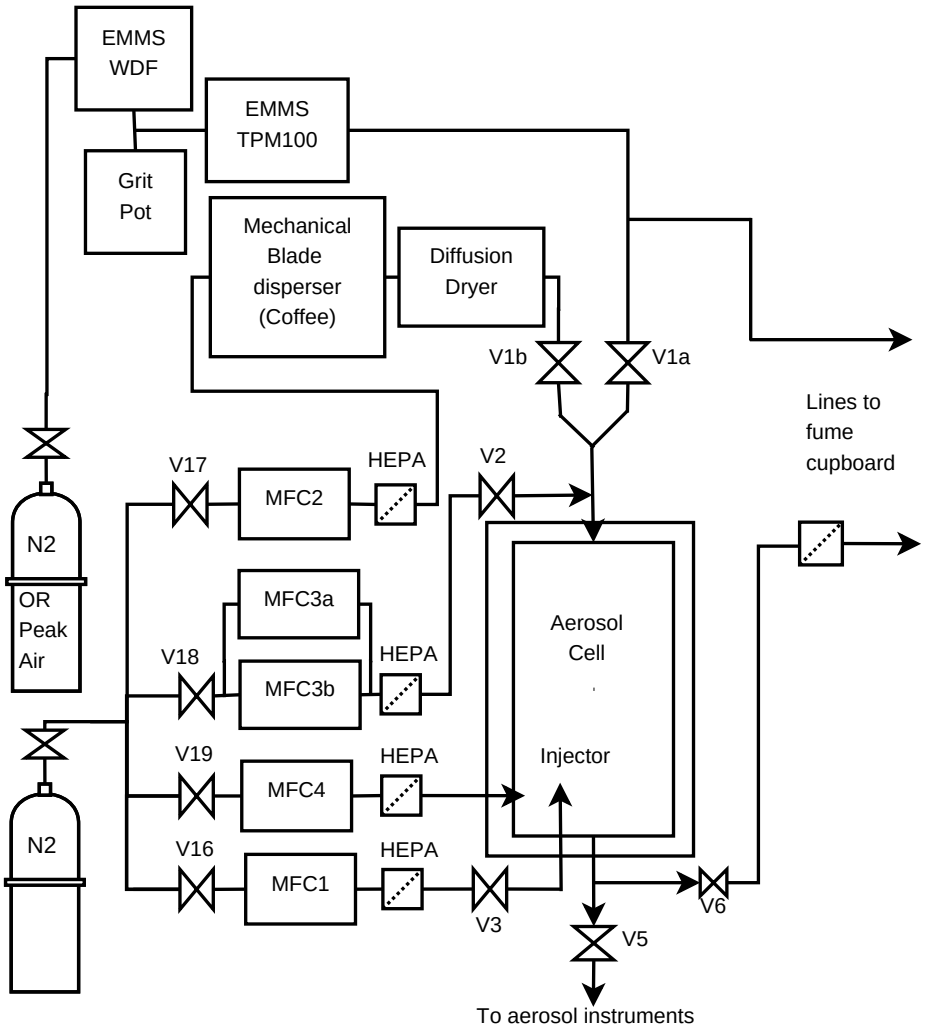

5.1.1.1 The Wright dust feeder

Where possible the samples were dispersed using the Wright dust feeder manufactured by EMMS Ltd, shown in Fig. 5.2 with the constituent parts labelled. The WDF is designed to supply a constant rate of aerosol, and to ensure the sample is properly dispersed. The dried and sieved sample was compressed into one of the WDF cups using a hydraulic press to ensure a consistent compaction pressure.

Figure 5.2: The Wright dust feeder (WDF). The key components are labelled to the right.

1 Cutter base unit
2 WDF controller
4 Rate sensor
7 Cup 2 cover
8 Cup 1 (small)
9 Cup 2 (medium)
10 Cup 3 (large)
11 Cup sensor sleeve
12 Compression rod, cup 1
13 Compression rod, cup 2
14 Compression rod, cup 3
15 Cup 1 blade extender
16 Cup 1 blade
17 Cup 2 blade
18 Outlet port

Figure 5.3 shows the internal mechanism of the WDF. The cylindrical cup containing the compacted sample rotates downwards towards the fixed blade. The WDF was supplied with a flow of nitrogen gas, 2.0 litres/min at 2.0 bar, from a Peak Scientific nitrogen generator. The gas flow passes through an annular gap between the blade platform and the cup wall, and along a radial groove from the outer edge of the blade. As the cup is rotated downwards the blade comes into contact with the surface of the compacted sample, removing a thin layer. The gas flows along the blade groove entraining cut material. Gas and sample exit through an axial hole at the centre of the blade and travel to the venturi. The rapid change in fluid pressure through the venturi acts to separate the material into individual particles (or at least reduces the number of agglomerated particles). After passing vertically down through the venturi the flow passes a $90°$ bend to the horizontal, with a grit pot positioned to capture particles unable to pass the bend. The curvilinear trajectory of larger particles is such that due to their higher momentum they

Figure 5.3: Diagram of the Wright dust feeder's internal mechanism.

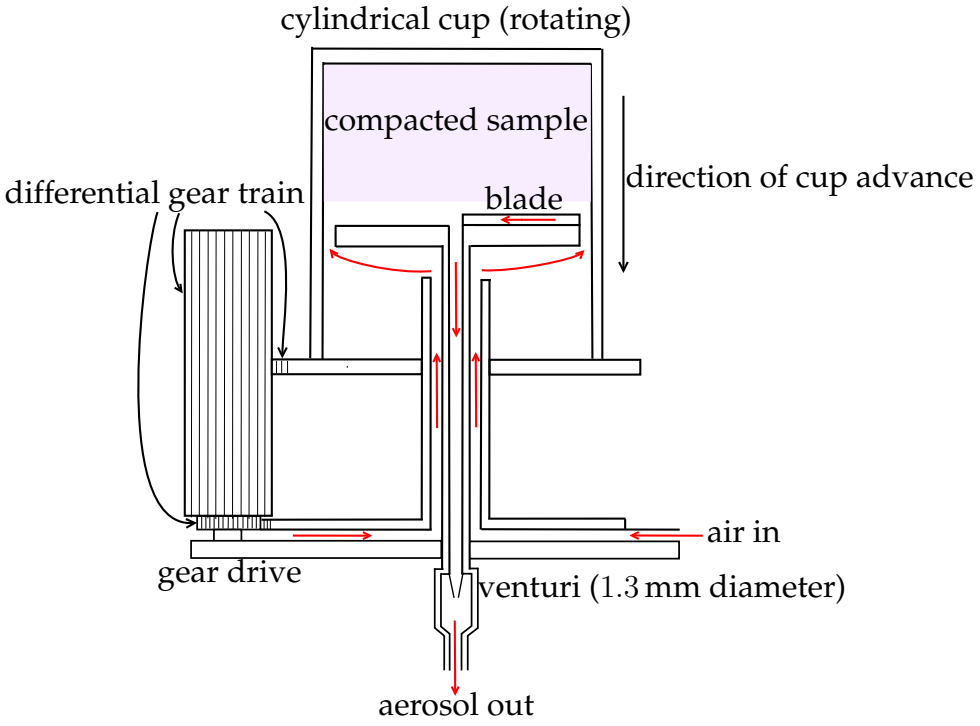

are unable to follow the gas flow streamlines and are collected in the grit pot; this particular bend removes $\sim 80\,\%$ of particles with a radius larger than $10\,\mu$m [1].

Dispersal tests were performed, with the WDF disconnected from the aerosol cell, to determine the optimal operational parameters. The EMMS total particulate monitoring transducer (TPM) was used to monitor the quantity and uniformity of aerosol dispersed by the WDF. It was found that preparation of the sample cake inside the WDF cup was critical in preventing the cake from regularly collapsing or cracking during WDF dispersal. The sample cake was made by adding a small layer of sample (approximately 1–2 mm thick) and then compressing into the cup using the compression rod and a hydraulic press. It was found that most samples gave good dispersal with 3.0 ton compression in the large WDF cup, although a number of the volcanic ash samples required 4–5 tons to remain stable. Some samples were incapable of forming a stable compacted cake — in these cases the mechanical blade dispersal method was used.

[1] According to a calculation performed using the Particle Loss Calculator [*von der Weiden et al.*, 2009]. A full discussion of particle losses will be given in Section 5.1.3.2.

5.1.1.2 Mechanical blade dispersal (the coffee grinder)

In cases where the Wright dust feeder could not be used, dispersal was achieved using an adapted coffee grinder. Approximately $2\,\mathrm{g}$ of the sample were placed in the chamber of the coffee grinder. The coffee grinder was adapted so that the nitrogen gas flow could be passed across its internal chamber and its blade rotation rate was reduced to optimise dispersal. With the flow passing through the chamber, the coffee grinder blades were activated dispersing the sample into the flow. The coffee grinder could not be completely sealed and so was operated with a positive nitrogen gas over-pressure to ensure the sample remained as dry as possible. As an additional precaution, the gas and sample flow entered a diffusion dryer after the coffee grinder, before going on to the cell.

5.1.2 Optical measurements

In order to measure the aerosol extinction over a large range of wavelengths, two optical systems were used inside the cell. Figure 5.4 is a horizontal cross section of the aerosol cell, and shows the optical paths of the two systems.

Measurements in the IR were made using a Bruker Vertex-80 Fourier transform spectrometer (FTS), operating at a resolution of $1.929\,\mathrm{cm}^{-1}$. The FTS was able to alternate between two sources: a globar (GB) or a halogen lamp (HL). Using the globar the working range was approximately 670–$5000\,\mathrm{cm}^{-1}$ (15–$2\,\mu$m) and with the halogen lamp the working range was extended slightly to 670–$10000\,\mathrm{cm}^{-1}$ (15–$1\,\mu$m). A White cell [*White*, 1942] with eight passes was used to increase the optical path inside the cell to $3.52\,\mathrm{m}$; a White cell makes use of three spherical concave mirrors of the same radius of curvature to reflect a beam multiple times across a volume to increase the optical path and sensitivity to low concentrations of sample.

In the shortwave, a deuterium tungsten halogen source was used. The source was coupled to a collimator and the light was sent on a single pass through the cell, with an optical path perpendicular to that of the IR measurements. The optical path of this shortwave system was $0.427\,\mathrm{m}$. At the opposite end the light was focused into a bifurcated optical fibre which split the beam along two separate optical fibres passing to two Ocean Optics S2000 CCD diffraction grating spectrometers. One S2000 spectrometer was configured to cover the range 200 – $850\,\mathrm{nm}$ with a resolution of $1.33\,\mathrm{nm}$, whilst the other covered the range 530 – $1100\,\mathrm{nm}$ with a resolution of $1.17\,\mathrm{nm}$.

Figure 5.4: A horizontal cross section of the aerosol cell is show in **(a)** and an image of the aerosol cell taken during experiments is shown in **(b)**. The left – right arrow in **(b)** indicates the IR multipass path; the visible path is shown perpendicular to this.

(a)

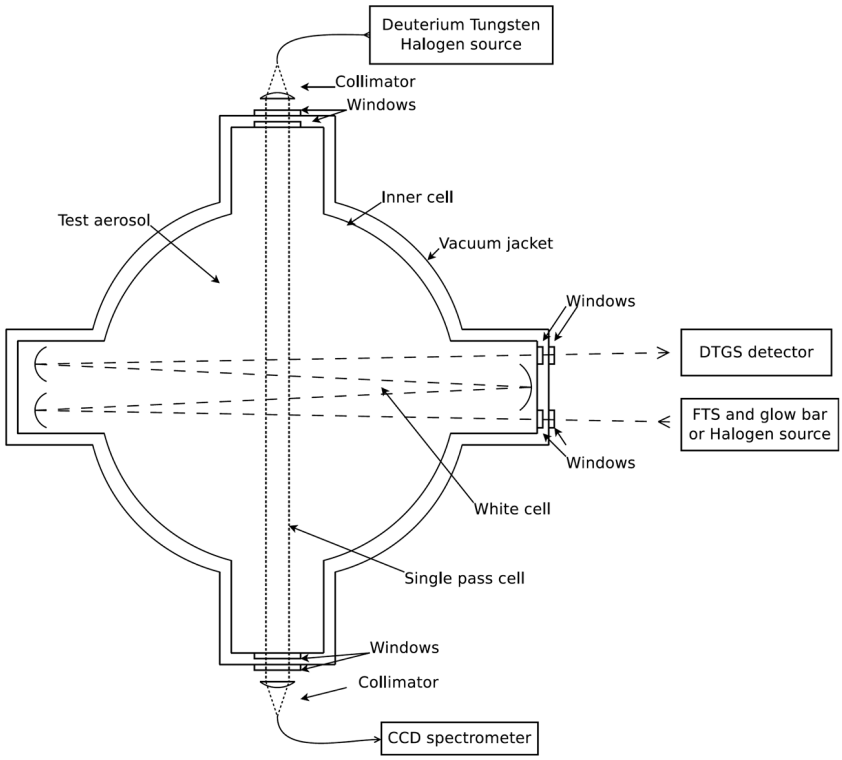

(b)

5.1.3 Microphysical measurements

Figure 5.5 shows the experimental set-up of the aerosol microphysical measurements made downstream of the aerosol cell. After exiting the cell the aerosol is sampled by three sizing instruments: an APS, the Aerosizer LD manufactured by Amherst Process Instruments; an OPC, the Model 1.801 manufactured by Grimm Aerosol Technik; and an SMPS (consisting of the Model 5.5-900 DMA classifier connected to the Model 5.403 CPC, both also manufactured by Grimm Aerosol Technik). The operating principles of these instruments are outlined above, and summaries of the instruments are presented in Table 4.1, 4.2, and 4.3

Figure 5.5: Experimental set-up of the aerosol microphysical measurements made downstream of the aerosol cell.

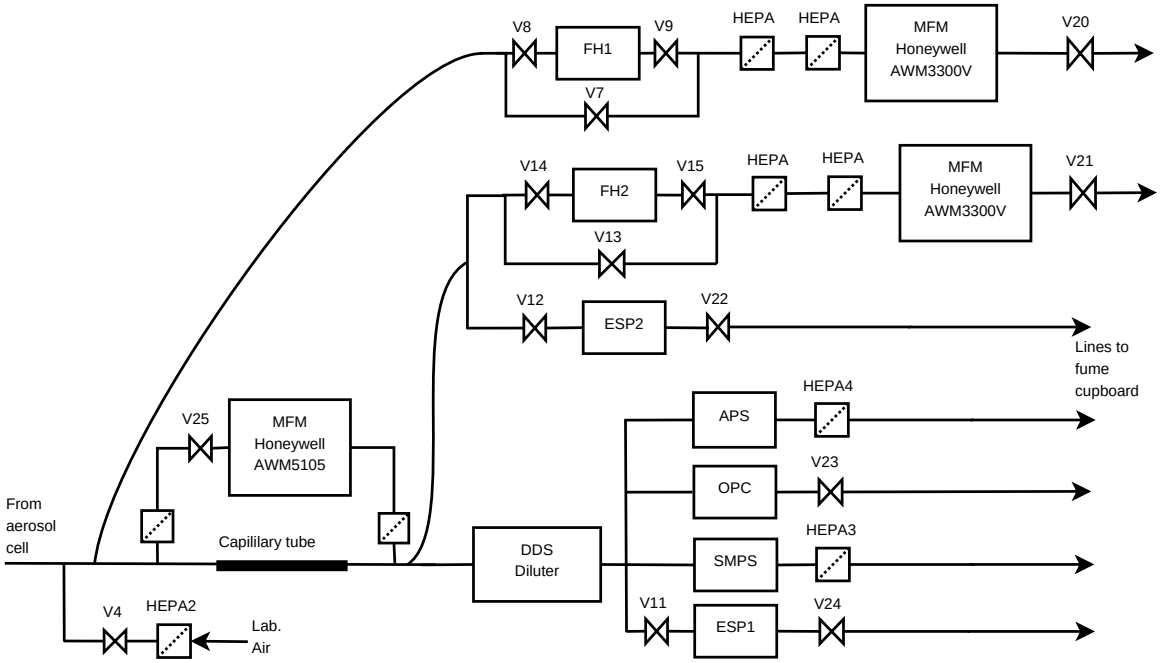

The set-up depicted in Figure 5.5 allows two filter samples to be taken. Filter holder 1 (FH1) can be used to sample aerosol exiting the cell without dilution in order to make direct mass loading measurements. The gas flow rate (in litres/min) passing through FH1 is measured by mass flow meter 1 (MFM1). Filter holder 2 (FH2) can be used to sample aerosol exiting the cell at diluted number densities, and was used to collect filter samples suitable for imaging with a scanning electron microscope (SEM).

5.1.3.1 Aerosol dilution

The three aerosol instruments are designed to be sensitive to ambient aerosol number densities. The aerosol flow from the cell must be diluted before entering the sizing instruments. With reference to Fig. 5.5, this is achieved as follows. After exiting the aerosol cell via V5 the aerosol flow splits between a flow going to FH1 (filter holder 1) and a flow going to a capillary connected in parallel with a mass flow meter and HEPA (High-efficiency particulate arrestance) filters. FH1 can therefore be opened to sample the direct cell aerosol concentration (without dilution). On the other hand the capillary connected in parallel with the MFM and HEPA filter acts to dilute the flow: flow through the capillary is restricted as it has a reduced diameter (3.7 mm compared to an initial tube diameter of 4.6 mm) whilst the flow passing to the MFM has particulates removed by the two HEPA filters before rejoining the capillary sample flow. The arrangement of the capillary connected in parallel with the MFM and two HEPA filter will be referred to as the *RAL diluter*.

After passing through the RAL diluter, the flow splits again. One path goes to filter holder 2 (FH2). FH2 was used to take filter samples suitable for scanning electron microscope (SEM) imaging. Suitable filter samples must sample a relatively low concentration of particles in order to ensure the surface of the filter is not saturated — without particle overlap — so that individual particles can be viewed by the SEM against the filter background. The second path at the split goes to the Dynamic Dilution System (DDS), model 560, manufactured by Topas GmbH. The DDS allows a dilution value to be set for the aerosol flow through it (at 1.0 litre/min the dilution range is $1:10$ through to $1:370$). The DDS was set to produce a dilution of $1:20$ for all of the aerosol cell experiments.

The experimental arrangement, depicted in Fig. 5.5, allows the dilution at any of the sizing instruments or filter holders to be calculated. This is because the flow through each of the sizing instruments (APS, OPC and SMPS) is fixed; additionally, continuous mass flow measurements are made by the three mass flow meters and a fixed dilution is produced by the DDS. The dilution from the cell to the sizing instruments is calculated as follows.

Define Q_{A}, Q_{O} and Q_{S} as the fixed flow (in litres/min) through the APS, OPC and SMPS respectively. Define the mass flow measured through FH1 by the connected mass flow meter as Q_1, the measured flow through FH2 as Q_2, and the flow measured by the mass flow meter in the RAL diluter as Q_{RAL}. The fractional dilution produced by the DDS is $D_{\mathrm{DDS}} = 1/20$, and the fractional dilution produced by

the RAL diluter is defined as: D_{RAL}. The total flow of the system, i.e. the total flow passing V5 is given by:

$$Q_{\mathrm{total}} = Q_{\mathrm{A}} + Q_{\mathrm{O}} + Q_{\mathrm{S}} + Q_1 + Q_2. \tag{5.1}$$

The dilution produced by the RAL diluter (and therefore the dilution from the cell to FH2) is given by:

$$D_{\mathrm{RAL}} = \frac{Q_{\mathrm{total}} - Q_{\mathrm{RAL}} - Q_1}{Q_{\mathrm{total}} - Q_1}, \tag{5.2}$$

and so the total dilution, D_{sizing}, of the sample flow from the aerosol cell to the sizing instruments is given by:

$$D_{\mathrm{sizing}} = D_{\mathrm{RAL}} D_{\mathrm{DDS}} = \left(\frac{Q_{\mathrm{total}} - Q_{\mathrm{RAL}} - Q_1}{Q_{\mathrm{total}} - Q_1} \right) D_{\mathrm{DDS}}. \tag{5.3}$$

5.1.3.2 Particle losses

Whenever aerosols are transported in tubing systems there will be particle losses due to a number of effects. These include diffusion losses, sedimentation, inertial deposition around bends, and inertial deposition with contraction of the tubing radius [*von der Weiden et al.*, 2009]. It therefore follows that the 'in cell' aerosol size distribution will differ from the 'at instrument' distribution even after dilution has been taken into account. The efficiency, η, for a particular section of tubing is defined as:

$$\eta = \frac{\mathrm{Number\ of\ particles\ exiting\ the\ section}}{\mathrm{Number\ of\ particles\ entering\ the\ section}}. \tag{5.4}$$

The Particle Loss Calculator (PLC), detailed in *von der Weiden et al.* [2009], is software that can be used to calculate efficiency curves for aerosol tubing. Detailed drawings and measurements were made of all of the tubing used in transporting aerosol from the point of dispersal (the WDF or mechanical blade disperser) through to the cell and then on to each of the sizing instruments and filters. The tubing could be split into a series of sections, and for each section the following measurements were made: inclination angle to the horizontal, bend angle, initial tubing diameter, and final tubing diameter. These parameters, as well as the gas flow rate, Q, through each section and an assumed value for the particles' dynamic shape factor, χ, were input into the PLC software to determine the efficiency curves, calculated using the equations outlined in *von der Weiden et al.* [2009], for

Figure 5.6: Efficiency curves for aerosol tubing, calculated using the Particle Loss Calculator, and based on detailed measurements of tubing dimensions and orientation.

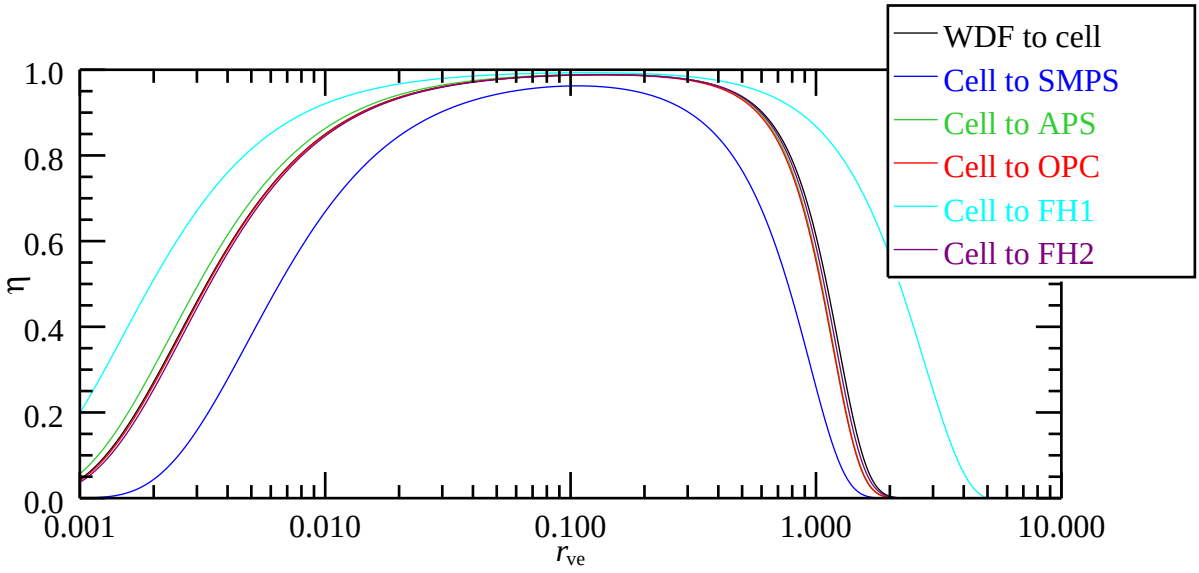

the following sections: WDF → cell, cell → FH1, cell → FH2, cell → APS, cell → SMPS, and cell → OPC.

Figure 5.6 shows the efficiency, η, plotted against volume equivalent radius, r_{ve}, calculated using the PLC, for each of the sections assuming a dynamic shape factor of $\chi = 1.36$ (this is the value measured by *Cartwright* [1962] for quartz particles). It can be seen that apart from the sections cell → SMPS and cell → FH1, the remaining curves are very similar and difficult to distinguish in the plot. The section cell → FH1 has the widest curve indicating that mass measurements made by FH1 efficiently sample the in-cell distribution.

5.1.4 Experimental run procedure

A consistent experimental run procedure was applied to all samples. The time taken to collect sufficient measurement data, and to completely purge the cell of aerosol after measurements, allowed one sample to be measured per day. The aerosol sizing instruments (OPC, APC and SMPS) were started 60 minutes in advance of loading the cell with aerosol, in order to allow sufficient warm-up time, as recommended by the instruments' user manuals. The deuterium tungsten halogen source for the Ocean Optics spectrometer was turned on 90 minutes in advance

of experiments with the source shutter kept closed. This was necessary to ensure the source reached a steady state temperature, and therefore a steady state output radiance. The FTS was kept running continuously making measurements through the cell and alternating between the GB and HL source. Each FTS measurement took approximately 1.0 minute and comprised 68 complete scans of the Michelson interferometer's moving mirror. There were 4 minutes between successive GB or HL measurements due to the time taken to switch between sources and complete the interferometer's mirror scans. The Ocean Optics detector was set to make continuous measurements once the source was turned on, with each measurement taking approximately 20 seconds.

It was necessary to measure the background radiance, L_{b}, whilst the cell is empty and the source is on, and the measurement radiance, L_{m}, when the cell contains aerosol, so that the measurement transmission could be calculated according to:

$$T_{\mathrm{m}}(\nu) = L_m(\nu) / L_{\mathrm{b}}(\nu) . \tag{5.5}$$

At least 20 minutes of repeated background source measurements were recorded before the cell was loaded with aerosol. Additionally, in order to correct for any drift of the source radiance, 20 minutes of background measurements were taken once the cell had been completely purged of aerosol. The 'before' and 'after' mean background radiance measurements could then be linearly interpolated to the 'aerosol in cell' measurement time to give a best guess of the true background radiance at the time of the aerosol measurement.

The Ocean Optics measurement and background intensities required an additional correction due to dark current radiance. The Ocean Optics source needed 90 minutes warm-up time, and during this time the source shutter was kept closed so that the detector made continuous dark current radiance measurements. After the 90 minutes had elapsed, the source shutter was opened, and 20 minutes of background measurements were taken. The dark current radiance, L_{d}, could then be subtracted, to give the measurement transmission as:

$$T_{\mathrm{m}}(\nu) = (L_{\mathrm{m}} - L_{\mathrm{d}}) / (L_{\mathrm{b}} - L_{\mathrm{d}}) \tag{5.6}$$

Once background source measurements were complete, loading the cell with aerosol could begin. The WDF cup containing the compressed sample was mounted onto the WDF. With V1a closed initially, the nitrogen gas supply to the WDF

from the Peak Scientific generator was turned on supplying 2.0 litres/minute at 2.0 bar and the WDF cutter rate was set to 0.5 rpm. Refering to Fig. 5.1, with V1a closed all of the output flow from the WDF passes to the fume cupboard. Once it was verified, using the TPM, that the WDF output was reasonably constant with time and that the sample cake was stable under the cutting action of the WDF blade, it was possible to begin drawing aerosol into the cell.

Before loading the cell with aerosol, the cell was kept in a 'mirror purging' state. A flow, controlled by MFC4, splits between the two sets of mirrors at either end of the cell, which together form the White cell, and the cell windows. The purging flow was directed across the mirror surfaces and windows to prevent the aerosol from settling and sticking on these surfaces. In the mirror purging state, the total mirror purging flow was set at 500 scm controlled by MFC2, and this was the only flow into the cell. Flow out of the cell was via V6 to the fume cupboard, with V5 closed so that the sizing instruments were disconnected. The mirror-purging state was the default state for the cell, and was returned to once experiments were complete and after the cell had been completely purged of aerosol.

The system was switched from the mirror-purging state to the aerosol-in-cell state by: opening V1a with the WDF running so that aerosol is drawn into the cell; setting the turbulent jet flow, controlled by MFC1, to 700 scm; opening V5 and closing V6, so that flow exiting the cell passes to the sizing and sampling instruments. The turbulent jet was used to increase mixing inside the cell, helping the aerosol to fill the cell homogeneously. The jet enters at the bottom of the cell and is directed vertically upwards.

Once the system was in the aerosol-in-cell phase, continuous repeated optical and sizing measurements were made automatically. The radiance measured by the FTS could be monitored and compared to a background source radiance measured earlier in the day — this gave a good indication of the extinction signal, and could be used to determine whether there was sufficient aerosol number density inside the cell (typically a drop in radiance of $> 20\,\%$ at around $6000\,\mathrm{cm}^{-1}$ was targeted). The number densities measured by the sizing instruments were also monitored. If the extinction signal was not high enough, the WDF cutter rate was increased (the maximum value was 1.0 rpm). The time over which repeat measurements could be made was determined by the amount of sample available. Where possible the experiment was kept in the aerosol-in-cell phase for 2 hours.

Figure 5.5 shows a schematic of the aerosol microphysical measurements made downstream of the aerosol cell. Once V6 is opened at the beginning of the aerosol-

in-cell phase, the OPC, APS, and SMPS make continuous repeated sizing measurements. The set-up allows two filter samples to be taken. Before runs filter holder 1 (FH1) and filter holder 2 (FH2) were loaded with filters. The masses of the filters were measured beforehand using a micro-balance accurate to 0.0001 g. FH1 was used to make direct (undiluted) mass loading measurements, and was loaded with 47 mm diameter polycarbonate filters (Product code: JVWP04700) manufactured by Merck Millipore Corporation. FH2 was used to take samples that could be imaged using a scanning electron microscope, and was loaded with 47 mm diameter polytetrafluoroethylene (PTFE) filters (Product code: VCTP04700) also manufactured by Merck Millipore. By default flow was allowed to bypass the filters. Approximately 20 minutes after the start of the aerosol-in-cell phase (to ensure the cell had reached a steady state), filter exposure was started: by opening V8 and V9, and closing V7, for FH1; and by opening V14 and V15, and closing V13, for FH2. The filters were exposed for 1 hour, if possible, and the start and end times of the exposures were recorded. The masses of the loaded filters were measured, and they were labelled and stored in sealed filter cases.

Once all of the available sample had been dispersed in the WDF or measurements had been made for more than 2 hours, it was necessary to completely purge the cell of aerosol. The system was switched from the aerosol-in-cell state to the 'aerosol purging' state as follows: the WDF was turned off; the turbulent jet was increased to 1400 scm; the top purge was started and set to 2200 scm; V1a was closed and V6 was opened. In the aerosol-purging state the aerosol sizing instruments are still connected and can be used to monitor the drop-off in aerosol number densities exiting the cell. Excess flow travels via V6 to the fume cupboard. Once the number densities are almost negligible, the system can be switched back to the default mirror-purging state. Completely emptying the cell of aerosol took approximately 2 hours.

5.2 Data analysis

5.2.1 Analysis of spectral data: radiance and transmission

As outlined in Section 4.2.2, the measurement transmission, T_{m}, can be expressed as:

$$T_{\mathrm{m}}(\nu) = \frac{L_{\mathrm{m}}}{L_{\mathrm{b}}} = \frac{L_{\mathrm{S2}} T_{\mathrm{o2}} T_{\mathrm{g2}} T_{\mathrm{a}}}{L_{\mathrm{S1}} T_{\mathrm{o1}} T_{\mathrm{g1}}}, \tag{5.7}$$

and providing the source radiance and optical system transmission remain constant between the time of the background radiance measurement, L_{b}, and the aerosol radiance measurement, L_{m}, (i.e. $L_{\mathrm{S2}} = L_{\mathrm{S1}}$ and $T_{\mathrm{o2}} = T_{\mathrm{o1}}$) then Eq.5.7 simplifies to:

$$T_{\mathrm{m}}(\nu) = T_{\mathrm{g}}(\nu) \times T_{\mathrm{a}}(\nu) \tag{5.8}$$

where T_{g} is the transmission due to additional gas molecules at the time L_{m} is measured compared to at the time L_{b} is measured.

The measurement transmission, $T_{\mathrm{m}}(\nu)$, was calculated according to Eq. (5.5) for FTS measurements, and the modified expression subtracting dark current radiance, Eq.(5.6), was used for Ocean Optics measurements. The measurement radiance, L_{m}, was calculated as the mean across the time period over which the filters were exposed. The background radiance, L_{b}, was calculated as follows: the mean radiance over a 20 minute period immediately before the cell was loaded and the mean radiance over a 20 minute period once the cell had been completely purged of aerosol were calculated (with the source on in both cases); a linear interpolation to the median filter exposure time was calculated to capture any possible drift in the source radiance. For the Ocean Optics measurements, the dark current radiance, L_{d}, was calculated as the mean radiance over the 20 minute period where the device was on but the detector shutter was closed.

The standard error in the measured radiance was taken to be the standard deviation in radiance for the time period over which the mean was calculated. Errors were propagated through to transmission, and other derived quantities, using standard error propagation formulae.

5.2.1.1 Removal of gas absorption lines and in-cell relative humidity

The Peak Scientific nitrogen generator, which supplied the WDF, did not provide $100\,\%$ pure nitrogen gas. All other gas supplied to the mass flow controllers was pure nitrogen. Contaminating H_2O and CO_2 absorption features were present in both L_{b} and L_{m}. These can be seen in Fig. 4.2. The most likely source of the water lines in the background radiance was water vapour present in the optical system which directed the FTS source to the cell. This system was periodically evacuated after several days of experiments and the background gas lines were seen to diminish. The gas absorption features were typically stronger in L_{m} compared to

Figure 5.7: Gas line removal from T_{m} of VA22 measured using the FTS and HL source. The black curve is the original measured transmission. The blue curve shows the transmission after H_2O lines have been removed, and the red curve is the final transmission after both H_2O and CO_2 lines have been removed.

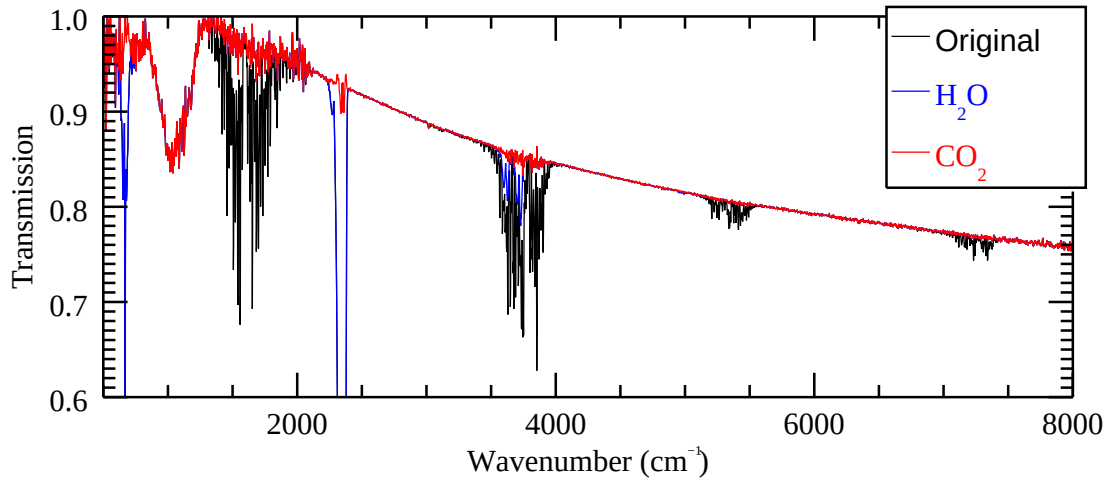

L_{b}. This was likely because of H_2O and CO_2 contamination in the Peak Scientific nitrogen generator supply.

It was necessary to determine T_{g}, so it could be removed from Eq.(5.8), leaving T_{a}. To achieve this, it was assumed that T_{a} would be smoothly varying over tens of wavenumbers, and that rapid spikes in the measurement transmission spectra, T_{m}, were attributable to gas absorption. Therefore the ratio of the measured transmission to the measured transmission with a boxcar smoother applied to it was calculated. The same quantity was calculated with the Reference Forward Model, `http://www.atm.ox.ac.uk/RFM` [*Dudhia*], modelling H_2O and CO_2 gases, and a retrieval was performed to determine the concentration of gases that best fit the data. The concentrations of gases formed the state vector, the ratio of the measurement transmission to the smoothed measurement transmission was the measurement vector, and the RFM was the forward model. The Levenberg-Marquardt method, detailed in *Rodgers* [2000], was used to search for the best estimate of the state.

Figure 5.7 shows an example of gas line removal for the FTS measurement with the HL source and sample VA22. The gas retrieval was first performed for H_2O in the spectral region $1400 < \nu < 2000\,\mathrm{cm}^{-1}$, where there are strong H_2O lines and no CO_2 lines. The blue curve shows the spectra after the transmission due to the retrieved concentration of H_2O has been removed. Secondly, the concentration of

CO_2 was retrieved using the spectral region $2250 < \nu < 2450\,\mathrm{cm}^{-1}$, where there is strong CO_2 absorption but no H_2O absorption. The red curve shows the final transmission after both H_2O and CO_2 lines have been removed. In this particular example the retrieved concentrations of H_2O and CO_2 were 498 and 238 ppm (parts per million), respectively. It can be seen that whilst the gas absorption features have been mostly removed there is still a small amount of residual present in the red curve of Fig. 5.7. Spectral regions where residual gas absorption remained after the removal process had been applied were not included in the aerosol extinction results.

The retrieved in-cell concentration of H_2O could be used to estimate the relative humidity, RH, inside the cell as follows. For a system of ideal gases the partial pressure, p_i, of a constituent gas and the total pressure, P, of all gases are related to the partial volume, v_i, that would be occupied by the constituent gas on its own and the total volume, V, of all the gases according to:

$$\frac{p_i}{P} = \frac{v_i}{V}. \tag{5.9}$$

The concentration of the gas in units of parts per million by volume (PPMV) is related to the partial volume according to:

$$\frac{\mathrm{PPMV}}{10^6} = \frac{v_i}{V}. \tag{5.10}$$

Therefore using the definition of RH, Eq. (A.3), the relative humidity inside the cell can be related to the retrieved concentration of water vapour, $\mathrm{PPMV}_{\mathrm{H_2O}}$, according to:

$$\mathrm{RH} = \frac{\mathrm{PPMV}_{\mathrm{H_2O}}}{10^6} \times \frac{P}{e_\mathrm{s}}. \tag{5.11}$$

Where RH values are reported in this chapter, the saturation pressure of water vapour, e_s, was calculated according to the equation of *Buck* [1981]. The total pressure, P, was measured for each experiment using an in-cell pressure meter.

5.2.1.2 Volume extinction

Once the aerosol transmission, T_a, had been calculated the volume extinction coefficient, β^ext, could be calculated according to:

$$\beta^\mathrm{ext} = -\frac{\ln T_\mathrm{a}(\nu)}{x}, \tag{5.12}$$

where x is the optical path in the cell. For the FTS White Cell the value of the optical path was $x_{\mathrm{FTS}} = 3.52\,\mathrm{m}$, and for the Ocean Optics single pass system the value was $x_{\mathrm{OO}} = 0.427\,\mathrm{m}$.

5.2.2 Sizing data analysis: At-instrument corrections

This section details the at-instrument corrections applied to sizing data for each instrument. The corrections are necessary to ensure that the distributions from each instrument are represented in terms of the same particle radius; the definitions for the various radii and their relationships have been detailed in previous sections. The appropriate radius for interpreting aerosol exinction measurements is the volume equivalent radius, r_{ve}.

Figure 5.8 shows a summary of the sizing measurements for the three sizing instruments during the aerosol cell experiment performed on a quartz sample (sample number SP16) on the 11^{th} March 2015. In each of these image plots, time is shown on the horizontal axis, $\ln(r_{\mathrm{ve}})$ is shown on the vertical axis (where r_{ve} is the corrected radius and has units of μm), and the color bar indicates $dN/d\ln r_{ve}$ (where N has units of particles/cm^3).

The quartz was dispersed using the Wright dust feeder. Drawing aerosol into the cell began at 15:06, corresponding to a rapid increase in the number density of particles seen by the sizing instruments in Fig. 5.8. A mass filter sample was taken by opening FH1 between 15:42 and 16:42; the filter sampling time is indicated in Fig. 5.8 by the red vertical lines. This was the period over which both extinction and sizing data were analysed.

5.2.2.1 Analysis of SMPS data

The SMPS measures the electrical mobility radius, r_{m}, of particles. The transformation to volume equivalent radius is given by Eq. (4.41). In order to apply Eq. (4.41) knowledge of the dynamic shape factor χ of the sample is required. There are various values quoted in the literature. The most commonly referrenced is *Cartwright* [1962] who found a dynamics shape factor of $\chi = 1.36$ for quartz particles with radii in the range $0.1 - 5\,\mu$m; *Kotrappa* [1971] found a value of $\chi = 1.82$ for particles with radii in the range 0.1–$1\,\mu$m; and more recently *Alexander et al.* [2016] investigated the flow regime dependence and size dependence of the dynamic shape factor of quartz, and found values ranging $\chi = 1.25 - 1.60$ in the free molecular regime and $\chi = 1.1 - 1.34$ in the transition regime. The slip correction parameters

Figure 5.8: Summary of sizing data from the aerosol cell experiment on sample SP16 (quartz). The colour bar shows $dN/d\ln r_{\mathrm{ve}}$, where N has units of particles/cm^3 and r_{ve} has units of μm.

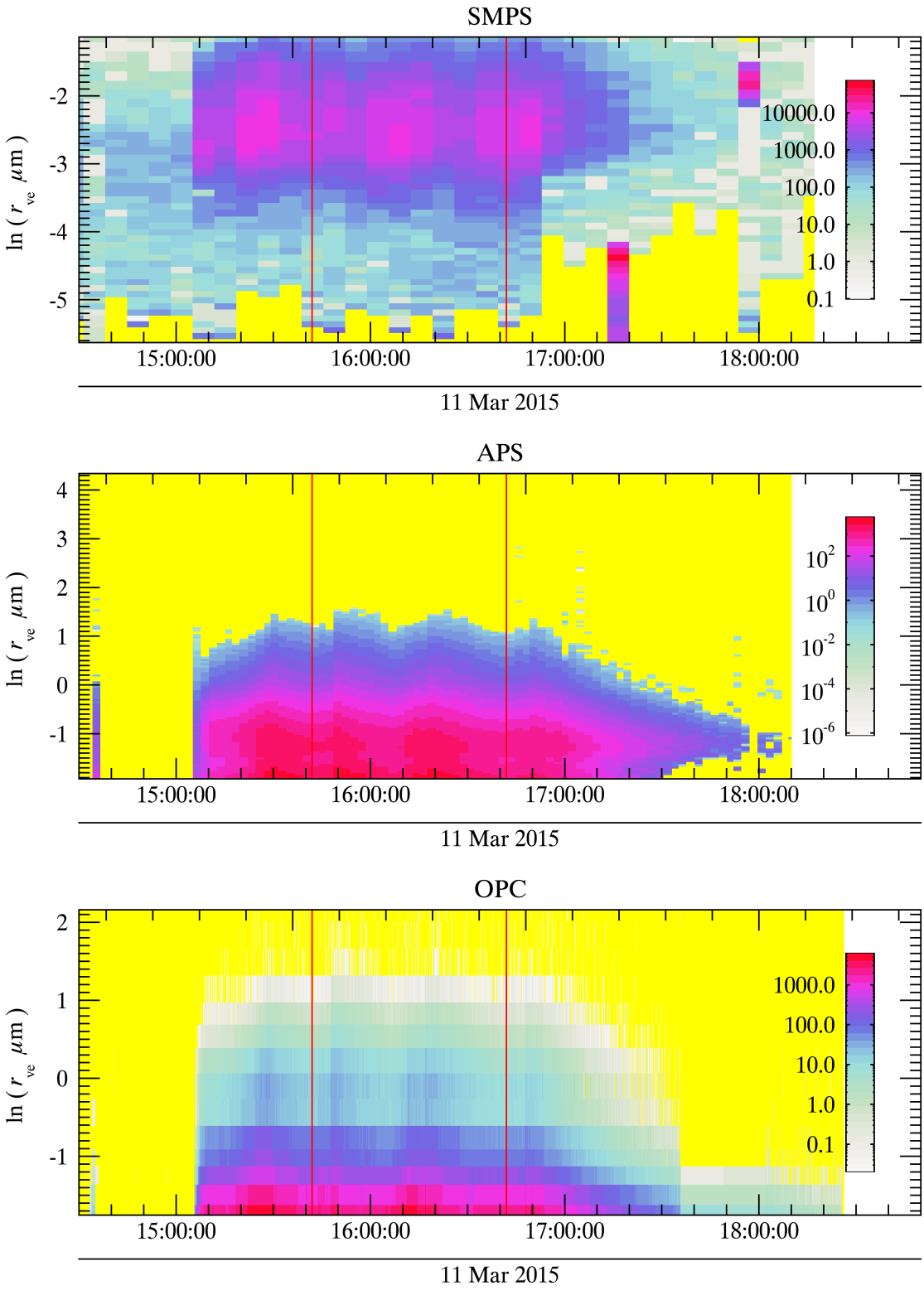

found by *Allen and Raabe* [1985] were assumed. Figure 5.9 shows the transformation assuming a dynamic shape factor of $\chi = 1.36$. The plot shows the mean SMPS distribution over the filter holder exposure period for the experiment on SP16 quartz. The dashed curve shows the original distribution against r_{m} and the solid curve shows the transformed distribution against r_{ve}.

5.2.2.2 Analysis of OPC data

The OPC converts scattered irradiance for individual particles to size, assuming Mie scattering and a particle refractive index of $\tilde{m} = 1.6 + i0.0$. Systematic errors are introduced when measurements are made of highly non-spherical particles, or particles whose refractive index deviates significantly from the assumed value. There is no straightforward way to correct for these effects, and therefore OPC data presented in this chapter have not been altered from values returned by the instrument.

5.2.2.3 Analysis of APS data

The APS measures the aerodynamic radius, r_{a}, of particles. In order to determine the transformation to r_{ve} it is necessary to characterise the flow regime of the instrument. The relevant quantities are the Knudson number, Kn, and the particle Reynolds Number, Re.

The mean free path of nitrogen gas at ambient temperature and pressure is $\ell \sim 0.1\,\mu$m. Therefore for particle radii in the range 0.01 – $10\,\mu$m, the Knudson number ($\mathrm{Kn} = \ell/r$) ranges from 1.0 – 0.01. The particle Reynolds number for a particle in a gas is given by $\mathrm{Re} = V 2 r_{\mathrm{ve}} \rho / \mu$.. For nitrogen gas at standard temperature and pressure, $\rho = 1.25\,\mathrm{kg\,m^{-3}}$ and $\mu = 1.77 \times 10^{-5}\,\mathrm{N\,s\,m^{-2}}$. The Model LD Amherst Process Instruments APS accelerates particles to near supersonic velocity, so we can take $V = 349\,\mathrm{m\,s^{-1}}$ (the speed of sound in nitrogen gas under standard conditions). Therefore for particle radii in the range 0.01 – $10\,\mu$m, the particle Reynolds number ranges from 0.25 – 250.

Given that $\mathrm{Kn} > 0.1$ and $\mathrm{Re} > 0.1$, the appropriate formulation for the correction from aerodynamic radius to volume equivalent radius is given by Eq. (4.48). The same assumptions were made about the dynamic shape factor and the Cunningham slip correction parameter as used for the SMPS analysis (above). Applying Eq. (4.48) also requires the particle density, which for quartz is $\rho_{\mathrm{p}} = 2.65\,\mathrm{g/cm^3}$ [*Haynes*, 2009]. It was assumed that variation in the non-Stoksian correction

Figure 5.9: Correction to SMPS data. Plotted is the mean distribution over the aerosol-in-cell phase measured for quartz (SP16). The dashed curve shows the raw distribution returned by the SMPS. The solid curve shows the distribution after transforming from electrical mobility radius to the volume equivalent radius.

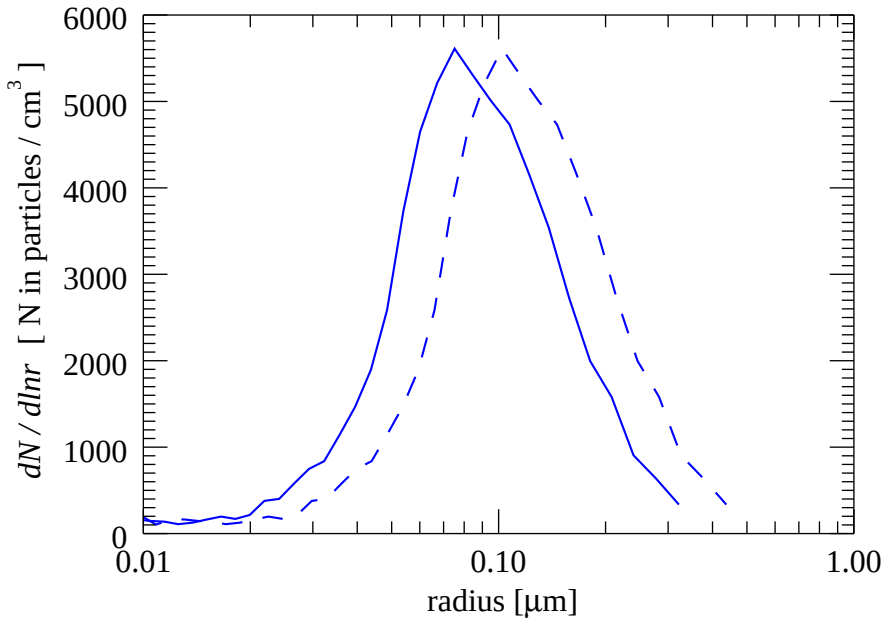

Figure 5.10: Correction to the APS data. Plotted is the mean distribution over the aerosol-in-cell phase for the aerosol cell experiment on quartz (SP16). The dotted curve shows the raw mean distribution measured by the APS. The dashed curve shows the distribution corrected for the counting efficiency η found by *Thornburg et al.* [1999]. The solid curve is transformed from aerodynamic radius r_{a} to volume equivalent radius r_{ve}.

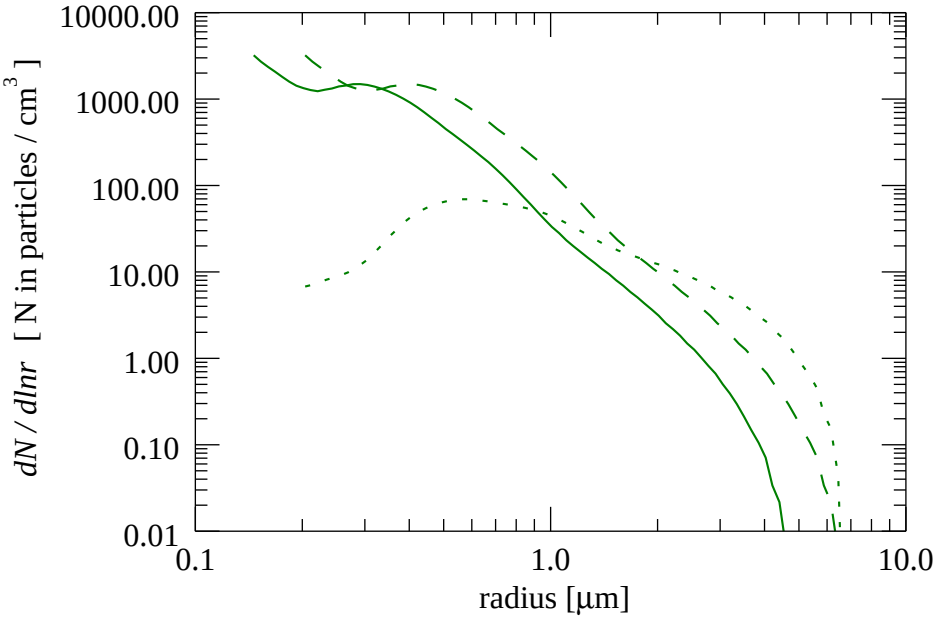

between non-spherical particles and their volume equivalent spheres was small, so that Eq. (4.50) is true; this has been found to hold reasonably well for a typical APS under near-Stoksian conditions [*Cheng et al.*, 1993].

In addition to the radius correction, the Model LD Amherst Process Instruments APS is known to have a significant reduction in fractional counting efficiency, η, for aerodynamic radii smaller than $5\,\mu$m: *Thornburg et al.* [1999] determined the instrument's radius-dependant counting efficiency for aerodynamic radii below $5\,\mu$m by comparing the concentration measured by the APS to a cascade impactor device for monodisperse polystyrene particles with radii in the range 0.150–$5\,\mu$m. The counting efficiency was found by *Thornburg et al.* [1999] to obey the regression curve:

$$\eta = 0.055\left[\log\left(20r_{\mathrm{a}}\right)\right]^{6.60}, \tag{5.13}$$

for similar APS operating parameters as those used during the aerosol cell experiments. They found the regression curve provided a good fit to the data for $r_{\mathrm{a}} > 300\,\mathrm{nm}$; below this the counting efficiency was less than $0.01\,\%$ and the regression curve fit was poor. For this work, it was decided that APS sizing data for $r_{\mathrm{a}} < 300\,\mathrm{nm}$ should be disregarded.

Figure 5.10 shows the effect of correcting for counting efficiency η and transforming from aerodynamic radius r_{a} to volume equivalent radius r_{ve} on the APS size distribution. Plotted is the mean distribution over the filter holder exposure period for SP16 quartz. The dotted curve shows the raw distribution returned by the APS; the dashed curve shows the distribution correcting for counting efficiency η; and the solid curve shows the final distribution after both correcting for counting efficiency and transforming from aerodynamic radius r_{a} to volume equivalent radius r_{ve}.

5.2.2.4 At-instrument corrected distributions

Figure 5.11 shows the at-instrument mean corrected distributions from the SMPS, APS and OPC on the same plot. The distributions from each instrument are distinguished by colour, as given by the plot key. The mean distributions were calculated as the mean in each sizing bin over filter exposure period, and are shown in dark colour. The standard deviation throughout this period are represented by the light coloured curves. The distributions presented in the figure have not been corrected for dilution or particle losses in aerosol tubing (which vary for each instrument)

Figure 5.11: The at-instrument corrected sizing data of the SMPS, APS, and OPC, all plotted against r_{ve}. The standard deviation in the measurements is represented by the the lighter shaded curves.

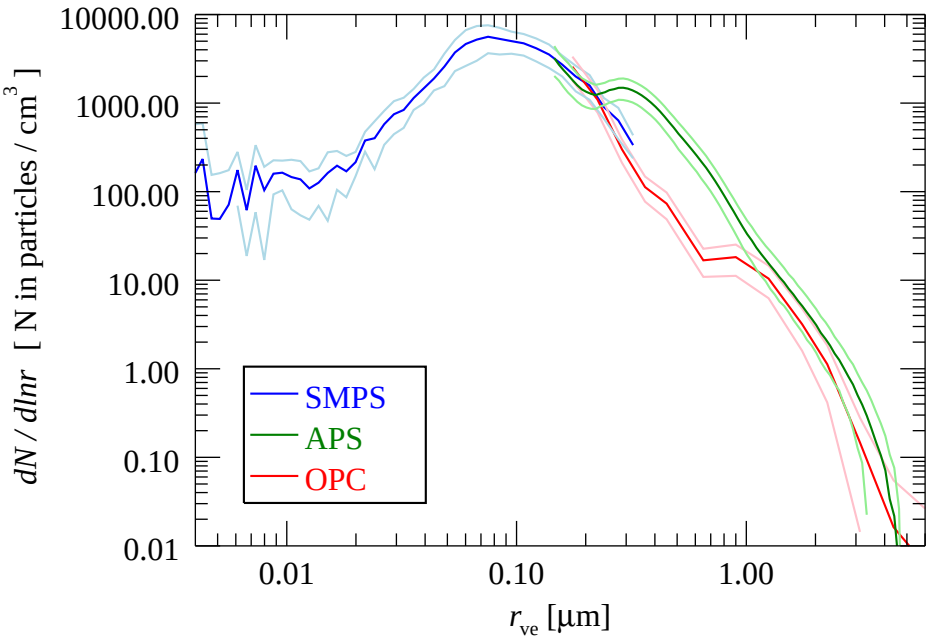

and therefore do not represent the in-cell particle size distribution. In following section, particle loss and dilution corrections will be applied and various methods will be investigated for combining data from the different instruments to produce a best-estimate of the in-cell size distribution.

It can be seen that there are significant discrepancies between the APS and OPC for $r_{ve} < 1.0\,\mu$m, which cannot be explained alone by tubing efficiencies to each of the instruments from the cell. The APS data in this region was judged to be less reliable, due to the very low counting efficiency of the APS found by *Thornburg et al.* [1999]. Furthermore, the OPC instrument had been sent to its manufacturer and re-calibrated in the month prior to the start of experiments.

5.3 Quartz calibration and the in-cell size distribution

The spectral complex refractive index, $m(\nu)$, of pure quartz is well documented in the literature. In order to calibrate the set-up, experiments were performed on two quartz samples, detailed in Table 5.1. Using literature values for the complex refractive index of quartz, the in-cell distribution (determined from the aerosol sizing instrument measurements) could be used to model the spectral extinction

in the cell according to Eq. (4.2). The modelled extinction could then be compared to the measured extinction.

Table 5.1: Summary of the two quartz samples.

Sample ID	Manufacturer	Product Code	Material	Size (MMR†)	Purity
SP15	Tatsumuri Ltd.	CRYSTALITE 5X	Crystaline silica	0.55 μm	$> 99.8\,\%$ SiO_2
SP16	Tatsumuri Ltd.	FUSELEX WX	Amorphous fused silica	0.55 μm	$> 99.98\,\%$ SiO_2

†Mass mean radius: the mass-weighted mean particle radius of the sample according to the manufacturer.

Figure 5.12: The extinction coefficient measured for SP15 quartz. The left plot shows the exinction measured by each instrument, whilst the right plot shows the final combined extinction with error.

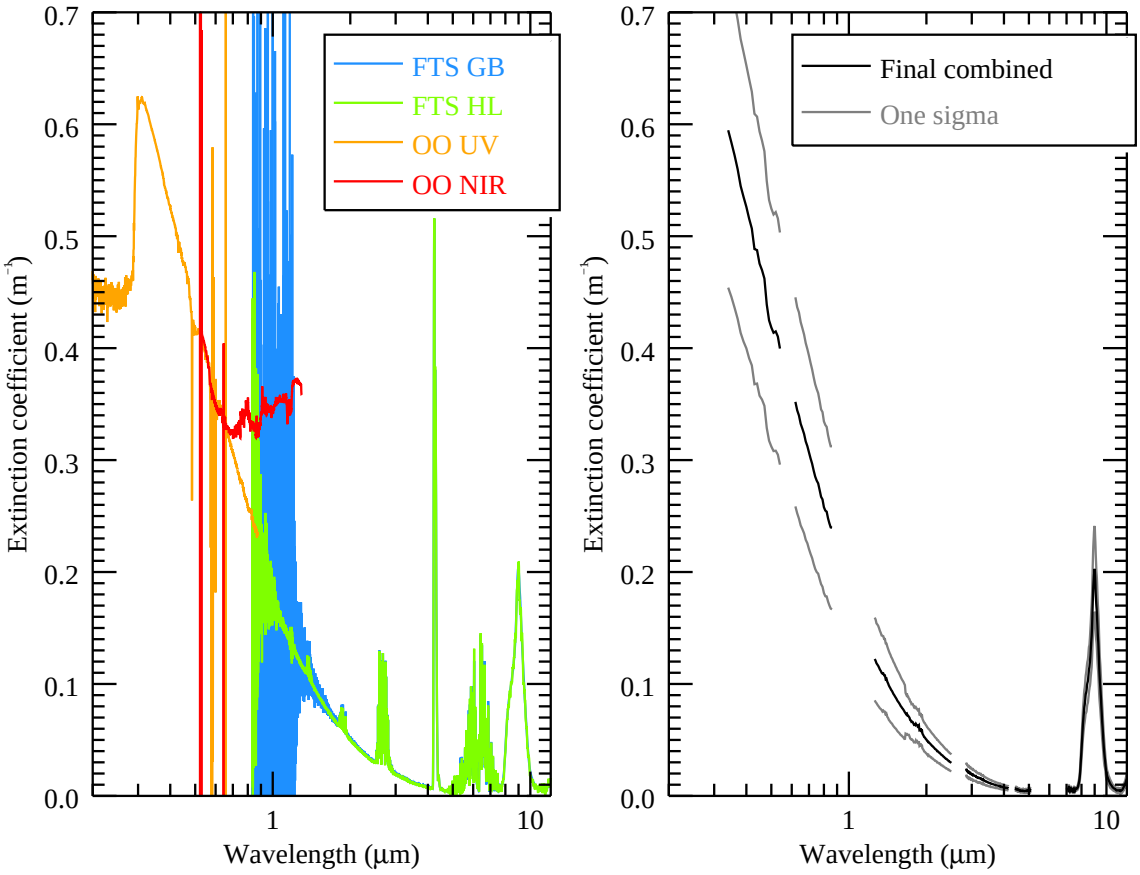

Figure 5.12 shows the measured spectral exinction for SP15 quartz, calculated

according to Eq. (5.12). The plot on the left of Fig. 5.12 shows the mean extinction measured by each instrument over the filter mass measurement time period (without gas removal). The plot on the right is the final combined extinction, and includes the one-sigma uncertainty. The data from different instruments were combined by calculating the error-weighted mean. Regions where the noise was judged to be too high, for example FTS GB data for $\lambda < 1.65\,\mu$m and FTS HL data for $\lambda < 1.25\,\mu$m, were not included, as well as any points where $\beta^{\text{ext}}/\sigma < 1$. Any regions with gas absorption residual, after the gas removal process had been applied, were also removed. In the case of SP15, water vapour residual was present at $2.5 < \lambda < 2.8$ and $5.1 < \lambda < 7.0$, and CO_2 was present at $4.2 < \lambda < 4.4$; these data were not included in the final combined extinction.

In order to determine the in-cell size distributions from the at-instrument size distributions the dilution and the particle loss efficiency curves must be taken into account; these were detailed in sections 5.1.3.1 and 5.1.3.2, respectively. The dilution from the cell to the sizing instruments, D_{sizing}, is given by Eq. (5.3), and the tubing efficiencies, η, are shown in Fig. 5.6 (the curves plotted in the figure assume $\chi = 1.36$). For example, if $N_{\text{i}}(r)$ is the at-instrument size distribution measured by one of the sizing instruments, then the in-cell size distribution, $N_{\text{c}}(r)$, predicted by the instrument is given by:

$$N_{\text{c}}(r) = \frac{N_{\text{i}}(r)}{D_{\text{sizing}}\eta_{\text{i}}(\chi, r)}, \tag{5.14}$$

where $\eta_{\text{i}}(\chi, r)$ is specific to each instrument.

After the in-cell distribution predicted by each instrument was calcalated according to Eq. (5.14) a method was required for combining the distributions to produce the final in-cell distribution. Three methods were investigated:

1. Only the SMPS data were used, and the particle tail (for r_{ve} greater than the largest SMPS bin) was extrapolated from a log-normal fit to the data. This method is referred to herein as 'SMPS only'.

2. The SMPS in-cell distribution was used up to its maximum size bin, and thereafter for larger radii, the OPC data were used having been scaled by a constant factor to match the final size bin of the SMPS (referred to as 'SMPS and OPC').

3. The SMPS data were used up to its maximum size bin, and thereafter for larger radii the APS data were used having been scaled (referred to as 'SMPS and APS').

Methods 2 and 3 both involve scaling other instruments to the SMPS. The SMPS had been sent to its manufacturer (Grimm Aerosol Technik) for calibration a month before experiments began, and was judged most likely to be accurately calibrated.

As discussed in section 5.2.2.1 there is significant variation in the literature of measured values of the dynamic shape factor of quartz. Three values of the dynamic shape factor were investigated, $\chi = 1.00$, 1.36 and 1.82, ranging from assuming spherical particles to the highest value of the dynamic shape factor reported for quartz. For each value of χ the efficiency curves, $\eta(\chi, r)$, for each instrument were re-calculated and so were the at-instrument radius corrections.

The particle loss efficiency curves shown in Fig. 5.6 show a sharp cut-off in efficiency at around 0.7 – $1.0\,\mu$m. When the efficiency curves were computed using the PLC, the software reported a warning that some of the equations were outside of their range of validity, indicating that the resulting curve was only an approximation. When applied directly to correct the sizing instrument data, by dividing the size distribution through by $\eta(r)$, the resulting distributions showed a sharp unphysical spike in number density around the cut-off radius. It was therefore decided that the efficiency correction could only be safely applied for radii smaller than the sharp cut-off, where the efficiency was greater than approximately 0.80 corresponding to $r_{\mathrm{ve}} = 0.7\,\mu$m. A log-normal distribution was fitted to the distribution in the range $0.1 < r < 0.7\,\mu$m and extrapolated to create the distribution tail at $r > 0.7\,\mu$m. To summarise: firstly, the in-cell distributions for each instrument were calculated according to Eq. (5.14); secondly, one of the two methods, detailed above, was adopted to combine instruments into a final in-cell distribution; and finally the distribution tail for $r_{\mathrm{ve}} > 0.7\,\mu$m was extrapolated from a log-normal fit.

The results of the quartz calibration analysis are presented in Fig. 5.13 and Fig. 5.14 for SP15 and SP16, respectively. In the figures there are three columns of plots, calculated for three values of the dynamic shape factor: $\chi = 1.00$, 1.36 and 1.82. The first row of plots shows the in-cell size distributions, $dN/d\ln r_{\mathrm{ve}}$, for each of the three instrument-combination methods: blue indicating SMPS-only, red indicating SMPS-and-OPC, and green indicating SMPS-and-APS. The second row shows $r^3 dN/d\ln r_{\mathrm{ve}}$, which is proportional to the in-cell volume distribution. The third row shows the modelled optical path ($\tau = \beta^{\mathrm{ext}} x$), calculated using Eq. (4.2)

Table 5.2: Summary of SP15 quartz calibration results.

Dynamic shape factor, χ	Scaling factor to match SMPS	Measured/Modelled mass FH1 (⋆)	Measured/Modelled β^{ext} (†)
SMPS only			
1.00	–	1.72 ± 0.02	2.01 ± 0.05
1.36	–	4.70 ± 0.06	5.70 ± 0.17
1.82	–	11.64 ± 0.15	14.17 ± 0.42
SMPS and OPC			
1.00	8.69	1.68 ± 0.02	1.65 ± 0.05
1.36	2.31	4.22 ± 0.06	4.45 ± 0.13
1.82	0.48	11.49 ± 0.15	12.52 ± 0.37
SMPS and APS			
1.00	1.46	1.48 ± 0.02	1.54 ± 0.04
1.36	0.29	3.44 ± 0.05	3.83 ± 0.11
1.82	0.57	1.48 ± 0.02	1.16 ± 0.04

⋆ Uncertainty derives from the propagated uncertainty in the measured value of m_{FH1}.

† Uncertainty derives from the propagated uncertainty in the measured β^{ext}.

Table 5.3: Summary of SP16 quartz calibration results.

Dynamic shape factor, χ	Scaling factor to match SMPS	Measured/Modelled mass FH1 (⋆)	Measured/Modelled β^{ext} (†)
SMPS only			
1.00	–	2.98 ± 0.03	3.83 ± 0.10
1.36	–	8.16 ± 0.07	10.45 ± 0.28
1.82	–	20.05 ± 0.18	25.89 ± 0.72
SMPS and OPC			
1.00	5.25	2.67 ± 0.02	3.27 ± 0.09
1.36	1.71	6.64 ± 0.06	8.14 ± 0.22
1.82	0.39	17.94 ± 0.16	22.87 ± 0.61
SMPS and APS			
1.00	0.97	2.45 ± 0.02	3.11 ± 0.08
1.36	0.27	5.22 ± 0.05	6.85 ± 0.18
1.82	0.28	4.47 ± 0.04	5.60 ± 0.15

⋆ Uncertainty derives from the propagated uncertainty in the measured value of m_{FH1}.

† Uncertainty derives from the propagated uncertainty in the measured β^{ext}.

Figure 5.13: SP15 quartz calibration results. The methods for combining sizing data are represented as follows: — SMPS-only, — SMPS-and-OPC, — SMPS-and-APS.

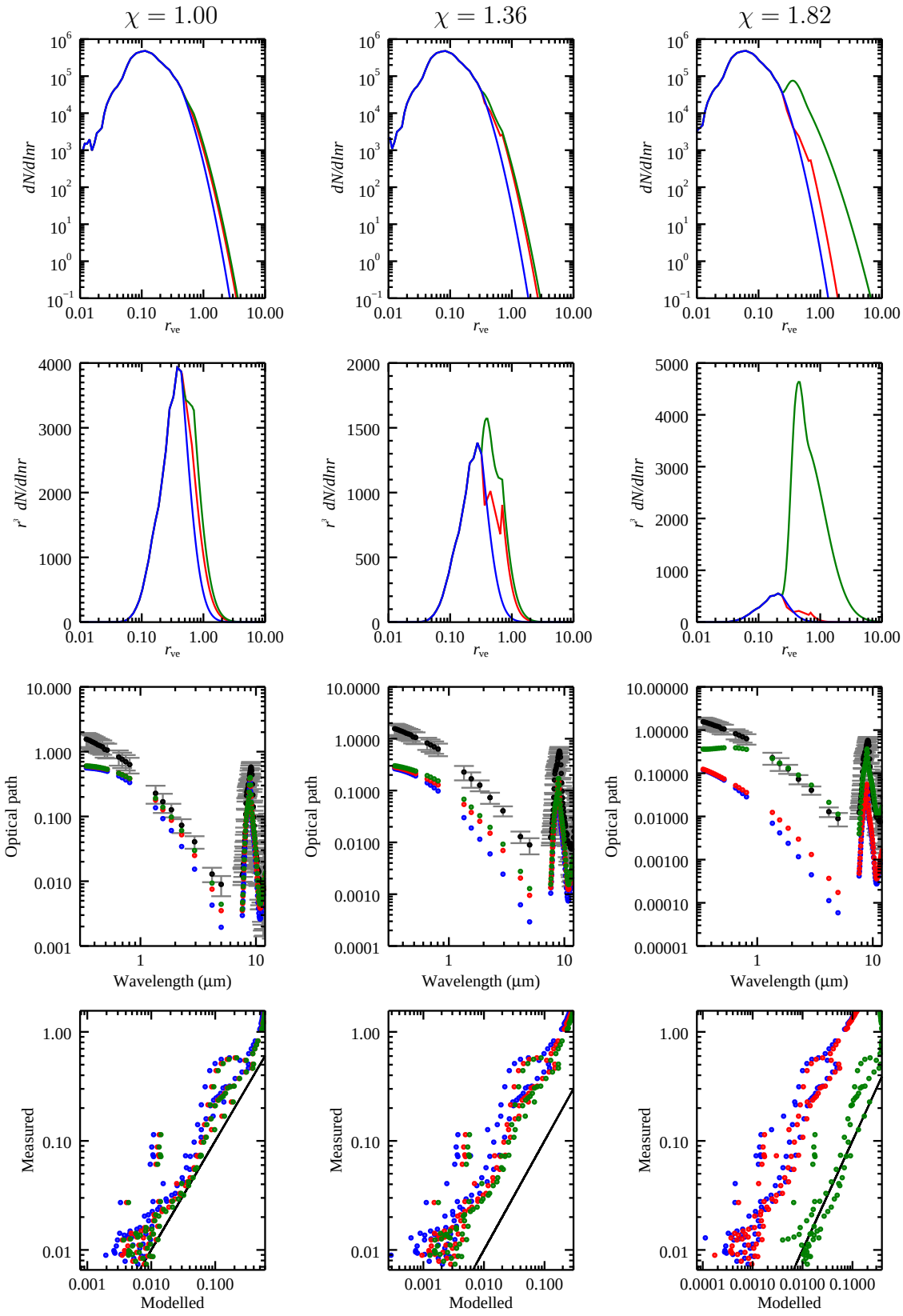

Figure 5.14: SP16 quartz calibration results. The methods for combining sizing data are represented as follows: — SMPS-only, — SMPS-and-OPC, — SMPS-and-APS.

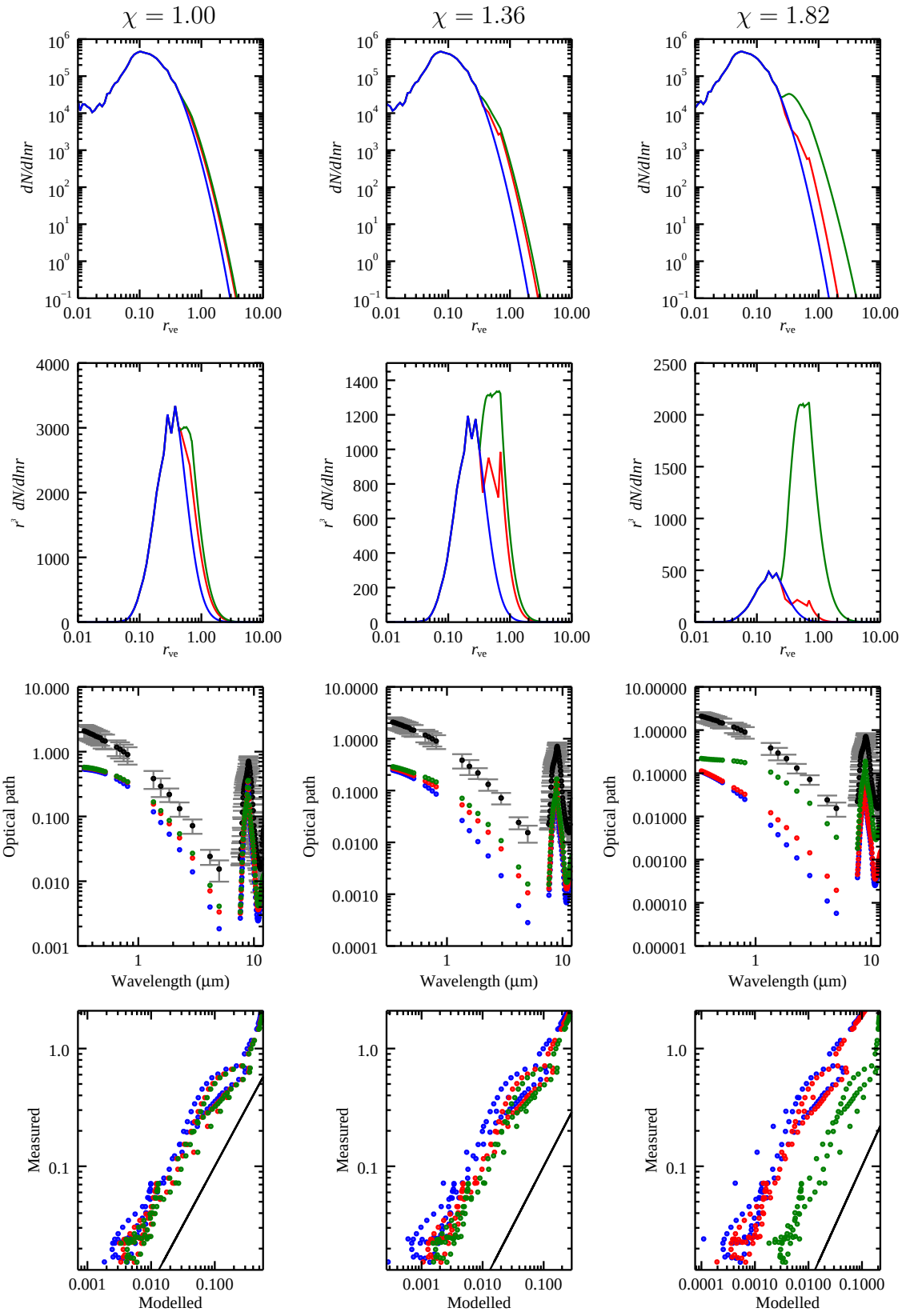

and Mie theory and assuming each of the size distributions (indicated with the appropriate colour). The complex refractive index, $m\left(\lambda\right)$, found for quartz by *Kischkat et al.* [2012], in the range $1.54 < \lambda < 14.3\,\mu$m, and by *Gao et al.* [2013], in the range $0.25 < \lambda < 1.25\,\mu$m, were assumed. The third row also shows the measured optical path (black) with error bars (grey). The fourth row is measured optical path plotted against modelled optical path, with the black line indicating a one-to-one relation.

Table 5.2 and 5.3 summarise the key results of the quartz analysis for SP15 and SP16, respectively. The 'scaling factor to match SMPS' is the scale factor by which either the APS or OPC data (depending on the size distribution combination method) were scaled to form the combined in-cell size distribution. Based on the combined in-cell size distribution, the mass expected on FH1, m_{FH1}, over the filter holder sampling period was calculated according to:

$$m_{\mathrm{FH1}} = \rho_{\mathrm{p}} \frac{4}{3}\pi \int Q_1\left(t\right) \left(\int \frac{dN_{\mathrm{c}}\left(t, r_{\mathrm{ve}}\right)}{d\ln r_{\mathrm{ve}}} r_{\mathrm{ve}}^3 \eta_1\left(r_{\mathrm{ve}}\right) d\ln r_{\mathrm{ve}} \right) dt, \tag{5.15}$$

where t is time, $Q_1\left(t\right)$ is the time-dependent flow measured to FH1 by MFM1, $\frac{dN_{\mathrm{c}}(t,r_{\mathrm{ve}})}{d\ln r_{\mathrm{ve}}}$ is the time-dependent in-cell size distribution, and $\eta_1\left(r_{\mathrm{ve}}\right)$ is the particle loss efficiency curve for tubing from the cell to FH1. The third column of Table 5.2 and 5.3 shows the ratio of the measured value for m_{FH1} to the modelled value calculated using Eq.(5.15). The uncertainty in this value is also shown, propagated from the uncertainty in the measurement of the filter holder's mass deposit. The fourth column shows the ratio of measured to modelled β^{ext}: the value is the error-weighted-mean ratio across the spectrum (at regular intervals in wavenumber). The uncertainty in this value derives from the uncertainty in the measured extinction.

The first two rows of Fig. 5.13 and Fig. 5.14 show how the size distributions vary as a function of the dynamic shape factor, χ. The figures show that by number the peak of the distributions move to smaller r_{ve} as χ is increased, with relatively small increases to the large-radii distribution tail and to the distribution width. However, by volume, these changes to the distribution tail are much more significant, as demonstrated by plots in the second row. The final two rows of plots indicate how well the modelled optical path compares to the measured optical path. For both SP15 and SP16, the general trend is that the closeness of the match decreases as χ is increased; the exception being the SMPS-and-APS distribution where the match decreases from $\chi = 1.00$ to $\chi = 1.36$, but then improves for $\chi = 1.82$. This trend

is borne out in the ratio of measured to modelled β^{ext} in Tables 5.2 and 5.3. For all distributions and values of χ, the quality of the match is better for SP15 (the crystaline quartz sample) compared to SP16 (the amorphous sample). For SP15 the best match for both the modelled m_{FH1} and β^{ext} to their measured values is the SMPS-and-APS distribution with $\chi = 1.82$. For SP16 the best match is also the SMPS-and-APS distribution, but with $\chi = 1.00$.

All three of the size distribution combination methods rely on the SMPS being accurately calibrated; the SMPS-and-OPC and the SMPS-and-APS combination methods involve scaling of the other instrument to match the SMPS. This was motivated by the fact that the SMPS had recently been sent to its manufacturer for calibration. However, despite this it is quite feasible that the SMPS had a counting efficiency less than one. Therefore, the in-cell size distributions, predicted by Eq.(5.14) and using one of the combination methods, were scaled by the ratio of the measured to modelled mass on FH1 (detailed in Tables 5.2 and 5.3). In this way the shape of the size distribution was determined by the sizing instruments, but its magnitude was determined by the mass measurement made by FH1, thereby correcting for the possibility that the SMPS counting efficiency is non-unity. The results of this analysis are presented in Figure 5.15 and 5.16 for SP15 and SP16, respectively.

The first row of Figure 5.15 and 5.16 shows the measured optical path with error bars and the modelled optical path, for each of the mass-scaled size distributions, across the full spectral range (note the logarithmic scale on the wavelength axis). The second row of plots also shows measured and modelled optical path, but in these plots the spectral range is narrowed to cover $7 < \lambda < 14\,\mu$m and has a linear scale. The two absorption peaks in this spectral region are associated with the resonances of Si—O—Si vibrations [*Kitamura et al.*, 2007]: the peak at $9.5\,\mu$m is attributed to asymmetric stretching vibration whereas the peak at $12.5\,\mu$m is attributed to symmetric stretching vibration. The third row shows measured against modelled optical path with the black line indicating a one-to-one relation. It can be seen that when the in-cell size distributions are scaled to match the measured value of m_{FH1} much better agreement is achieved between the measured and modelled optical path, for all values of χ and size distributions.

Tables 5.4 and 5.5 show the results for the ratio of measured to modelled β^{ext} using the mass-scaled size distributions. For both SP15 and SP16, the closest to a ratio of unity is achieved by the SMPS-and-OPC distribution with $\chi = 1.00$. However, it is important to note that the spectral points used to model β^{ext} were evenly

Table 5.4: Summary of SP15 quartz calibration results for size distributions scaled by the measured to modelled m_{FH1} ratio.

Dynamic shape factor, χ	Scale factor	Measured/Modelled β^{ext}
SMPS only		
1.00	1.72	1.17 ± 0.03
1.36	4.70	1.21 ± 0.04
1.82	11.64	1.22 ± 0.04
SMPS and OPC		
1.00	1.68	0.98 ± 0.03
1.36	4.22	1.06 ± 0.03
1.82	11.49	1.09 ± 0.03
SMPS and APS		
1.00	1.48	1.04 ± 0.03
1.36	3.44	1.11 ± 0.03
1.82	1.48	0.77 ± 0.02

† Uncertainty derives from the propagated uncertainty in the measured β^{ext}.

Table 5.5: Summary of SP16 quartz calibration results for size distributions scaled by the measured to modelled m_{FH1} ratio.

Dynamic shape factor, χ	Scale factor	Measured/Modelled β^{ext}
SMPS only		
1.00	2.98	1.29 ± 0.03
1.36	8.16	1.28 ± 0.03
1.82	20.05	1.29 ± 0.04
SMPS and OPC		
1.00	2.67	1.23 ± 0.03
1.36	6.64	1.23 ± 0.03
1.82	17.95	1.28 ± 0.03
SMPS and APS		
1.00	2.45	1.27 ± 0.03
1.36	5.22	1.31 ± 0.03
1.82	4.47	1.25 ± 0.03

† Uncertainty derives from the propagated uncertainty in the measured β^{ext}.

Figure 5.15: Modelled optical path with the in-cell size distribution scaled to match the measured value of m_{FH1}, for SP15 quartz. Black indicates the measured points with error bars (grey). For the modelled points: blue indicates SMPS-only; red indicates SMPS-and-OPC; green inidicates SMPS-and-APS.

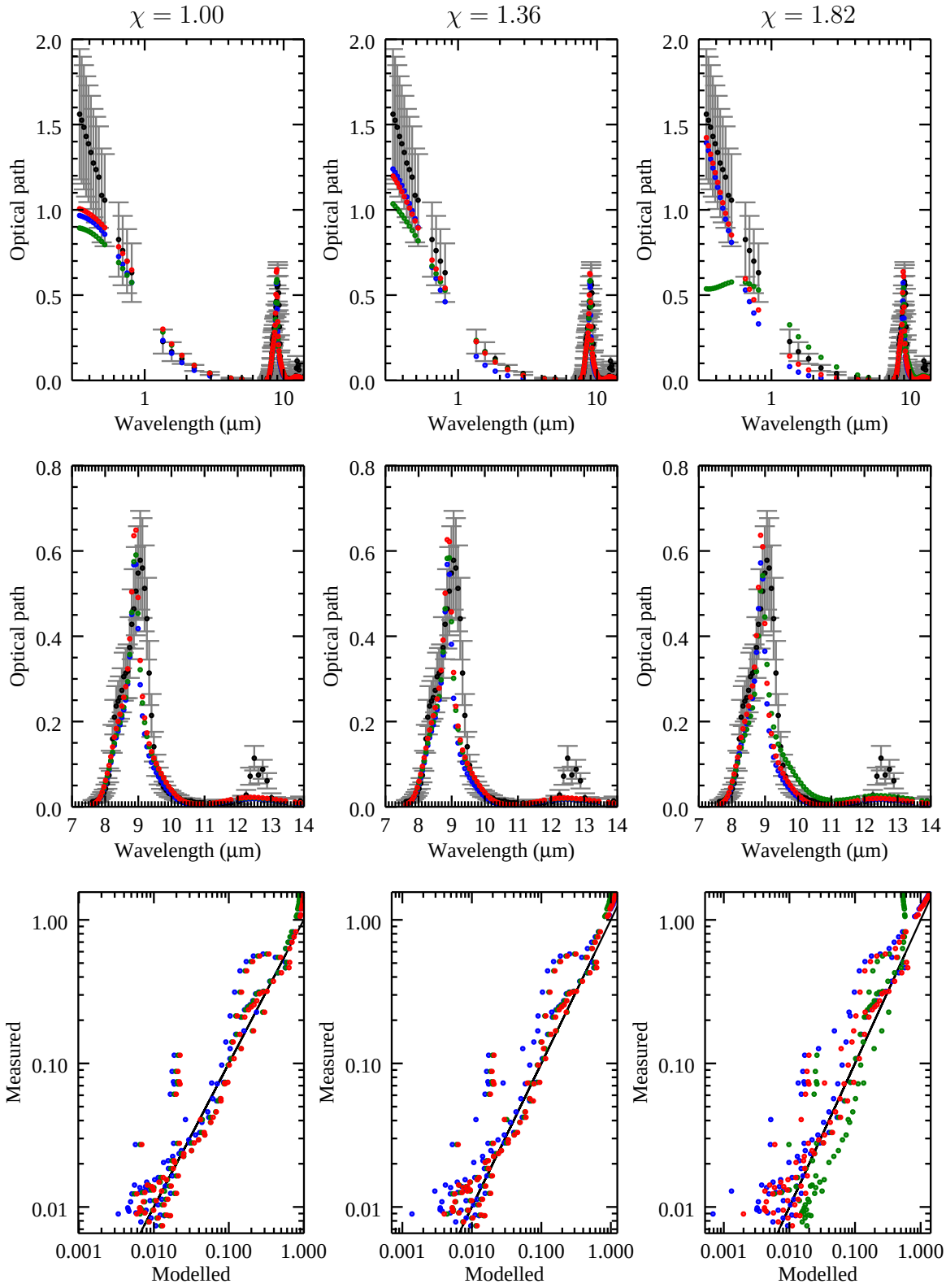

Figure 5.16: Modelled optical path with the in-cell size distribution scaled to match the measured value of m_{FH1}, for SP16 quartz. Black indicates the measured points with error bars (grey). For the modelled points: blue indicates SMPS-only; red indicates SMPS-and-OPC; green inidicates SMPS-and-APS.

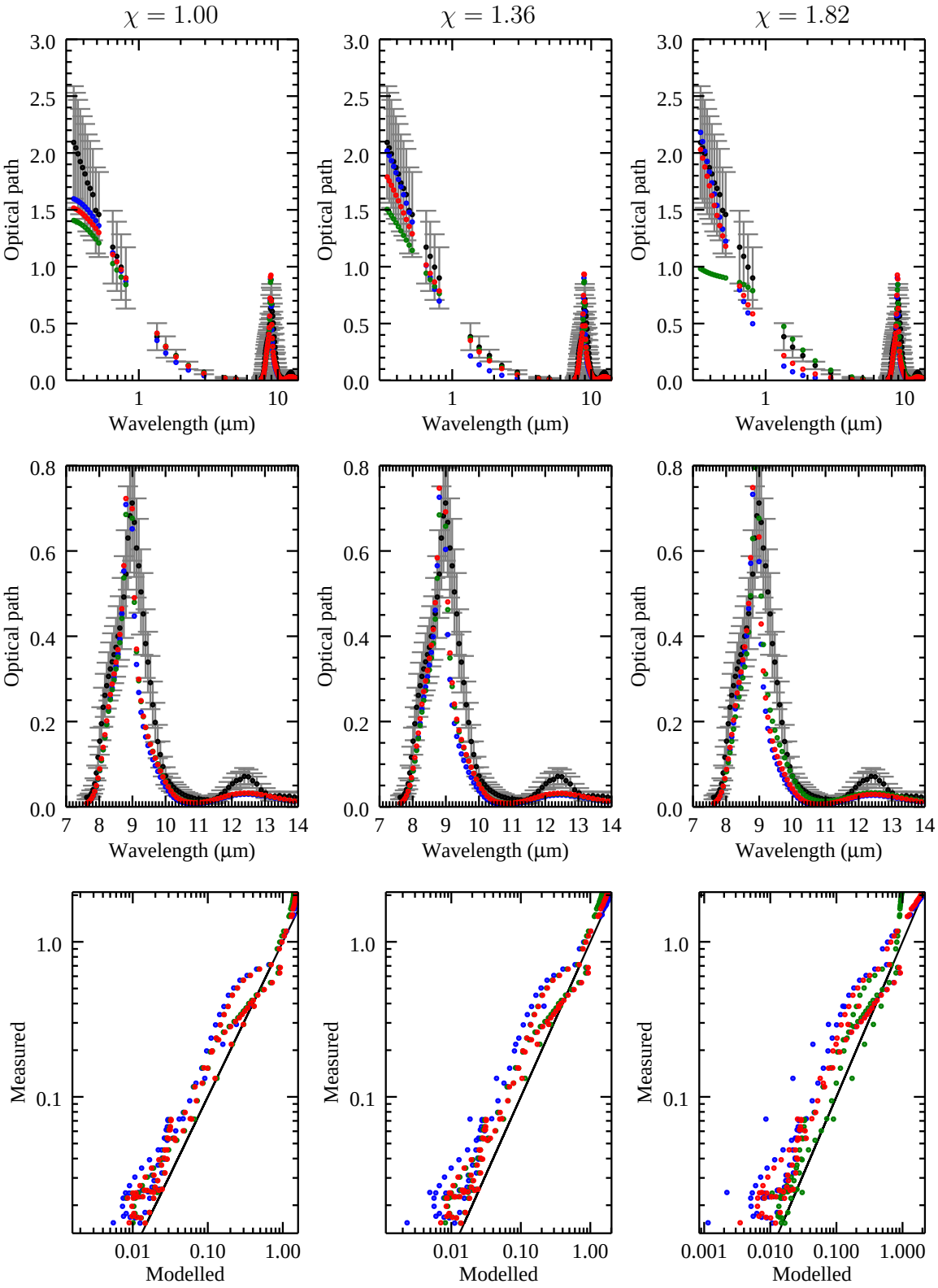

spaced by wavenumber, and there were more points in the infrared compared to the UV and visible where extinction is more sensitive to the particle size distribution. The plots in the first row of Figure 5.15 and 5.16 show that the agreement between the measured and modelled optical path at $\lambda < 7\,\mu$m appears better for $\chi = 1.36$, lying within one sigma through this spectral range, whilst the fit through the infrared is very similar for $\chi = 1.00$ and $\chi = 1.36$. This indicates the SMPS-and-OPC distribution with $\chi = 1.36$ does the best job at fitting the measured extinction through the full measured spectral region. This implies the counting efficiency of the SMPS varied 24–$15\,\%$ between the SP15 and SP16 experiments.

The plots in the second row of Figure 5.15 and 5.16 demonstrate good agreement between measured and modelled extinction for the Si—O—Si vibrational absorption feature close to $9\,\mu$m particularly with respect to the height of the peak. However, the measured peak appears slightly broader than the modelled peaks. For both SP15 and SP16 the height of the measured extinction peak close to $12.5\,\mu$m is somewhat greater than the modelled heights, although the discrepancy is less significant for SP16. It is possible these differences result from variation between the assumed complex refractive index and the true complex refractive index of the measured samples; in the infrared for $\lambda > 7\,\mu$m the extinction is primarily controlled by particle absorption determined by the imaginary part of the particles' complex refractive index. Furthermore, the peak value in the assumed imaginary refractive index for the $12.5\,\mu$m Si—O—Si feature found by *Kischkat et al.* [2012] was $k = 0.22$, whereas values reported in the literature review by *Kitamura et al.* [2007] ranged approximately $0.2 < k < 0.6$. It was argued by *Kitamura et al.* [2007] that discrepancies in literature values of the complex refractive index of quartz, significant particularly for k at wavelengths larger than $9\,\mu$m, were likely due to impurities in samples, the presence of bubbles or point defects, variations in sample preparation techniques and retrieval uncertainties.

5.4 Chapter summary and conclusions

This chapter details the experimental method applied to measure the extinction of suspended volcanic ash particles and quartz calibration particles. The samples were dispersed using the Wright dust feeder which provided a near-constant rate of dispersed aerosol into the aerosol cell. Inside the cell extinction measurements were made in the IR using an FTS with an eight-pass White cell, and in the UV, visible, and NIR using two single-pass CCD diffraction grating spectrometers. The

sources and detection instruments allowed extinction measurements to be made over the range 0.3 – $14\,\mu$m. Upon exiting the cell the aerosol flow passed to a suite of sampling and sizing instruments.

Calibration measurements were made using two quartz samples, and the measured extinction was compared to the modelled extinction predicted by assuming a literature value for the spectral complex refractive index of quartz. For the calibration various methods were investigated for combining the data from the three sizing instruments, taking into account particle loss efficiency curves for the tubing from the aerosol cell to the sizing instruments as well as dilution, to produce a best estimate of the in-cell particle size distribution. It was found that combining data from the SMPS and OPC, assuming a dynamic shape factor $\chi = 1.36$, and scaling the in-cell distribution by the measured filter deposit mass, m_{FH1}, produced a size distribution that was able to most accurately predict the measured extinction through both the visible and IR. For SP15 (crystaline quartz) the error weighted mean ratio between the measured and modelled extinction was 1.06 ± 0.03 and for SP16 (amorphous quartz) the value was 1.23 ± 0.03. Given that there is some fairly significant variation in literature measurements of the spectral complex refractive of quartz [*Kitamura et al.*, 2007], these ratios are very encouraging and demonstrate the accuracy of the measurements.

Chapter 6

MEC results, the complex refractive index, and satellite retrievals

6.1 Volcanic ash mass extinction coefficients

6.1.1 Calculating MEC

The mass extinction coefficient, MEC, is defined as the ratio of the volume extinction coefficient to the mass of aerosol per unit volume, MPV:

$$\mathrm{MEC}\,(\nu) = \frac{\beta^{\mathrm{ext}}\,(\nu)}{\mathrm{MPV}}, \tag{6.1}$$

where the value of MPV inside the cell can be calculated from the in-cell size distribution according to:

$$\mathrm{MPV} = \rho_{\mathrm{p}} \frac{4}{3}\pi \int r_{\mathrm{ve}}^{3} \frac{dN_{\mathrm{c}}}{d\ln r_{\mathrm{ve}}} d\ln r_{\mathrm{ve}}. \tag{6.2}$$

The mass-scaled SMPS-and-OPC size distribution was taken as the in-cell size distribution, according to the results of the quartz calibration analysis. In the absence of independent measurements of shape, a dynamic shape factor of $\chi = 1.36$ was assumed for all of the volcanic ash samples. Given that the size distributions are scaled by the measured value of m_{FH1}, uncertainty in the assumed value of χ will only make very small differences to the value of MPV inside the cell. This is because η_1 was found to vary only very slightly with the three values of χ investigated.

6.1.2 Volcanic ash MEC results and discussion

The results for volcanic ash mass extinction coefficients are presented in Fig. 6.2, which shows all of the volcanic ash samples on the same plot. Individual plots of

the volcanic ash MEC, including the uncertainty, are shown in Fig. 6.3 and Fig. 6.4. Uncertainty in values of the MEC derive from uncertainty associated with the measured β^{ext} and uncertainty associated with the measured filter mass deposit, m_{FH1}, which was used to scale the in-cell size distribution. The mass-scaled in-cell size distributions of the volcanic ashes are shown in Fig.6.1.

Table 6.1 summarises various in-cell parameters: the in-cell aerosol mass per unit volume, MPV; the sample's effective radius, r_{e}; the in-cell concetration of CO_2; the in-cell concetration of H_2O; and the relative humidity, RH, inside the cell. The in-cell MPV and r_{e} were calculated from the mass-scaled in-cell size distribution, with uncertainty in MPV deriving from uncertainty in the measurement of m_{FH1}. The concentrations of CO_2 and H_2O inside the cell were determined from the gas line retrieval (Section 5.2.1.1). Since aerosol extinction may be affected by the relative humidity (see Appendix A.2) it is important that measurements of extinction are accompanied by a value of the RH at which the measurement was made. The in-cell RH was calculated from the retrieved H_2O concentration according to Eq. (5.11).

The figures show considerable variation in the MEC of the measured volcanic ash samples. The extinction curves can be spilt into two approximate spectral regions: the region $\lambda < 7$ where the extinction is dominated by scattering; and the region $\lambda > 7$ where absorption dominates. Looking at the region $\lambda > 7$ (shown in the lower plot of Fig. 6.2 and in the second column of Fig. 6.3 and Fig. 6.4), it can be seen that there is variation in both the width and height of the MEC peak at around $9.5\,\mu$m. As discussed in Section 5.3, for SiO_2 this peak is associated with the asymmetric stretching vibrations of Si—O—Si. Of the nine measurements of MEC shown in Fig.6.2, the largest peak for the $9.5\,\mu$m feature was for VA17 with a value of $\mathrm{MEC} = 1.21 \pm 0.13$. The same sample also had the highest mass percentage of SiO_2 out of the nine, at $70.65\,\%$. The mass compositions of the volcanic ashes were documented in Table 2.5. By comparison, VA16 had a peak value of $\mathrm{MEC} = 0.73 \pm 0.14$ and an SiO_2 content of $59.37\,\%$. For the nine measured samples, the value of the PPMC for the peak MEC values of the $9.5\,\mu$m feature compared to the mass percentage of SiO_2 was 0.77, indicating a fairly strong positive linear correlation between peak height and SiO_2 content.

There also appears to be a weak absorption feature at around $12.5\,\mu$m visible for some samples. It is most prominent in VA17 (which has the highest SiO_2 content of $70.65\,\%$), but also appears to be present for VA19 ($69.67\,\%$ SiO_2) and less clearly for VA7, VA15, and VA16. In contrast, VA1 (SiO_2 content of $52.55\,\%$) is

Figure 6.1: The in-cell mass-scaled volcanic ash size distributions.

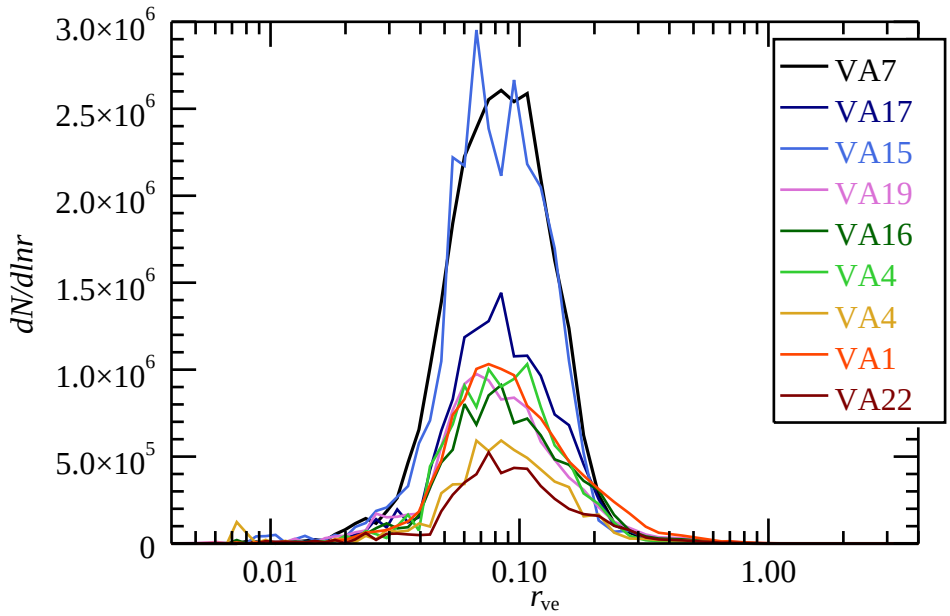

Table 6.1: Summary of in-cell parameters.

Sample	MPV ($\times 10^{-2}$ g/m^3)	r_e (μm)	CO_2 (PPMV)	H_2O (PPMV)	RH (%) †
VA7	5.85 ± 0.13	0.153	261.9 ± 4.2	684.3 ± 1.1	0.276
VA17	4.43 ± 0.14	0.194	257.0 ± 1.4	637.2 ± 0.3	0.257
VA15	5.58 ± 0.14	0.158	241.6 ± 3.8	501.9 ± 0.6	0.202
VA19	5.83 ± 0.14	0.279	230.2 ± 3.5	463.7 ± 0.4	0.187
VA16	4.93 ± 0.09	0.247	255.0 ± 4.7	543.0 ± 0.8	0.219
VA4 [a]	3.21 ± 0.12	0.184	254.9 ± 2.7	497.8 ± 0.4	0.201
VA4 [b]	3.17 ± 0.11	0.254	255.6 ± 3.4	466.9 ± 0.5	0.188
VA1	8.41 ± 0.09	0.296	243.0 ± 5.8	484.3 ± 0.9	0.195
VA22	3.49 ± 0.35	0.283	157.4 ± 4.3	417.0 ± 0.6	0.168

† Propagated uncertainty in RH values were less than three significant figures.

[a] Experiment performed on 12th June 2015.

[b] Experiment performed on 13th June 2015.

Figure 6.2: Volcanic ash MEC results.

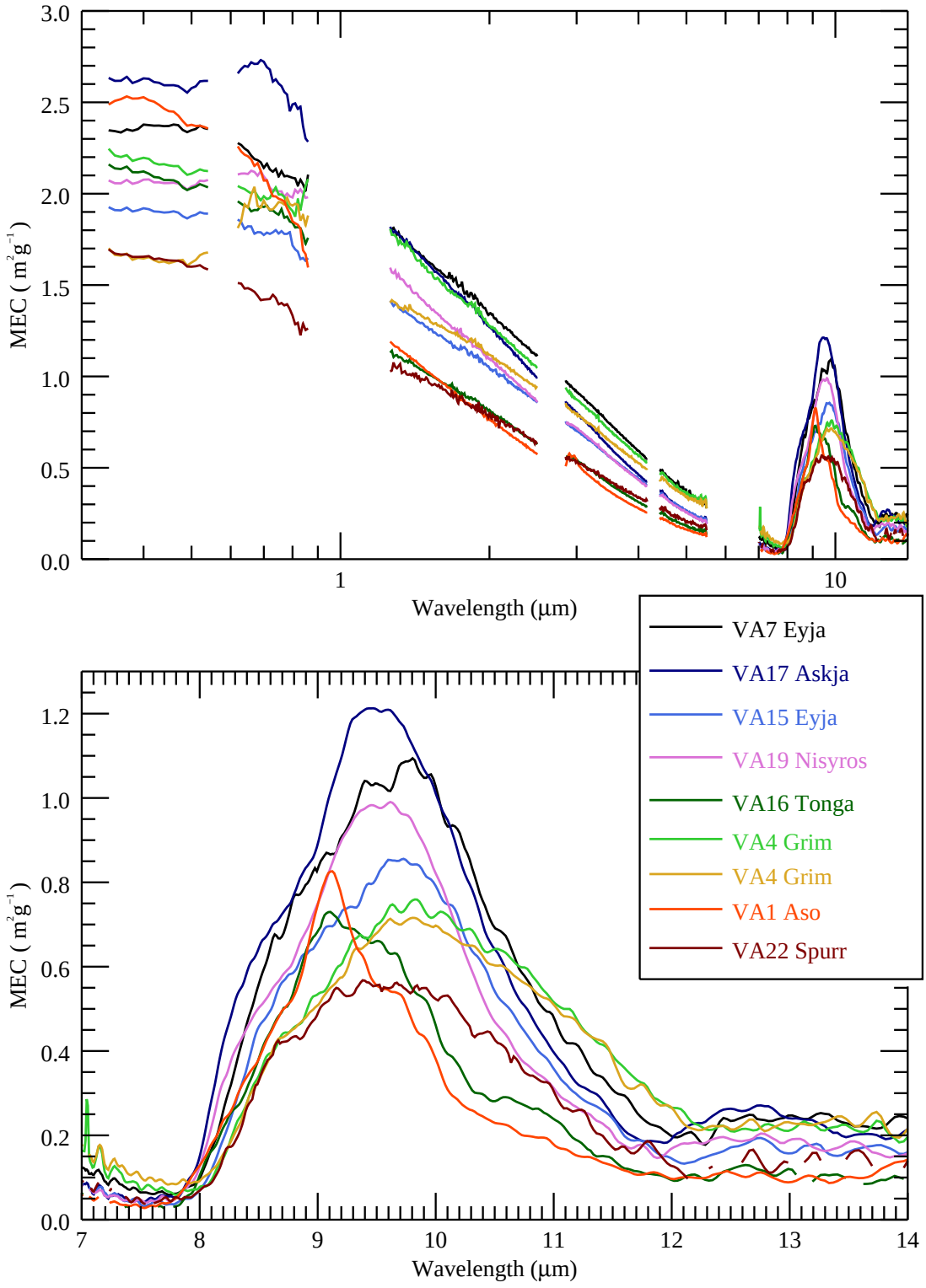

Figure 6.3: Individual plots of the volcanic ash MEC, with uncertainty (grey).

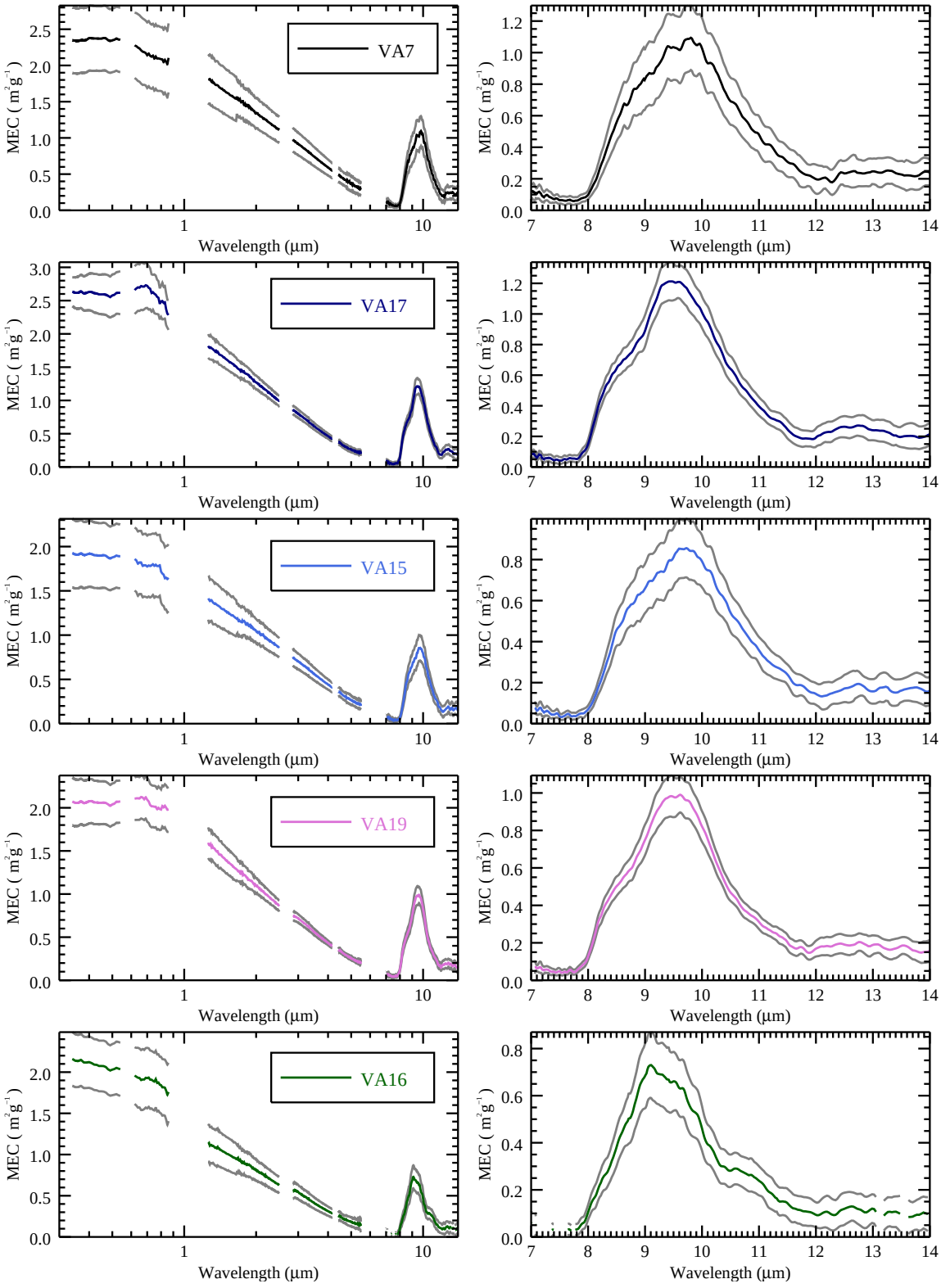

Figure 6.4: Individual plots of the volcanic ash MEC, with uncertainty (grey).

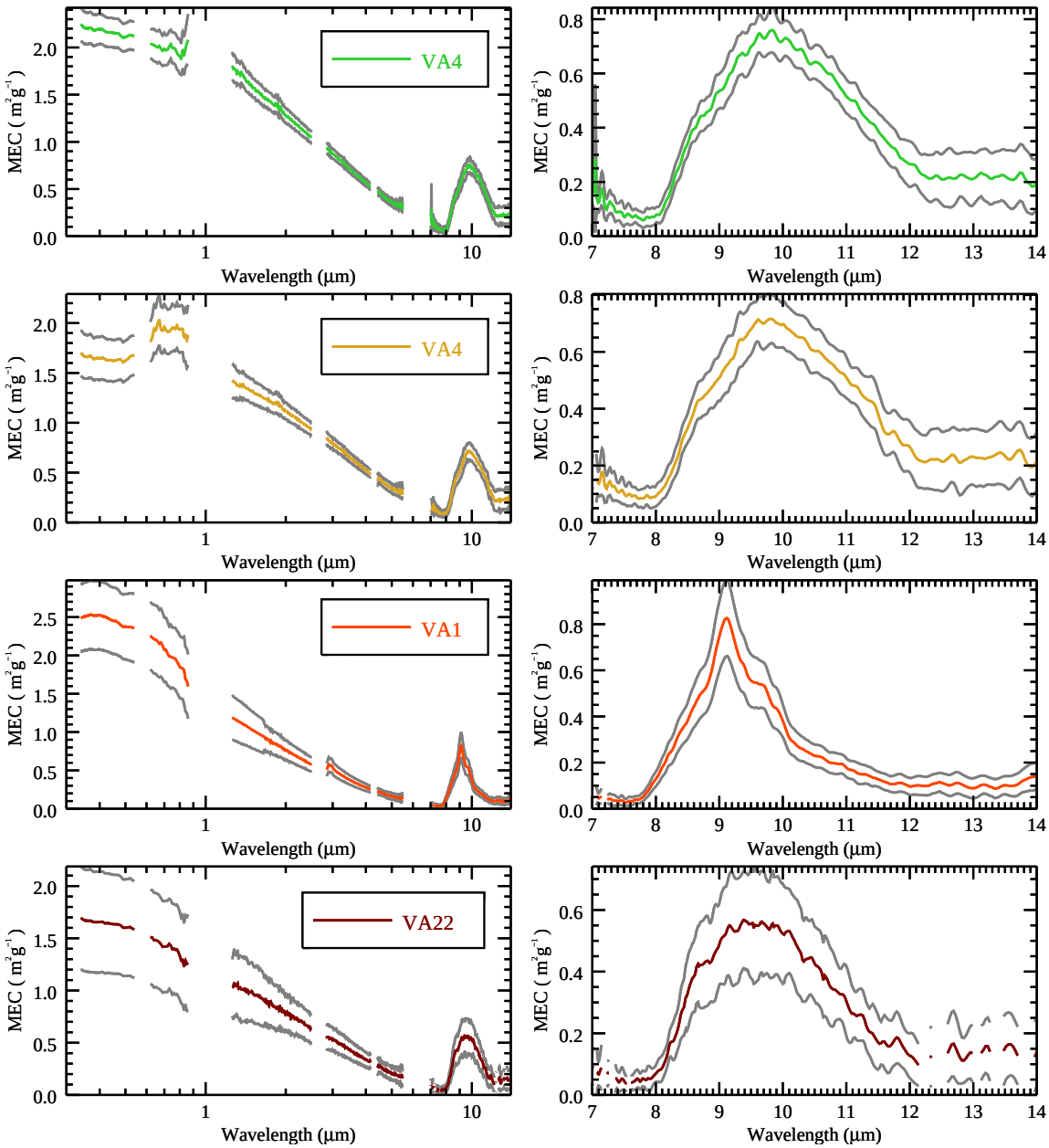

flatter through this region. *Ishimoto et al.* [2016] retrieved the imaginary refractive index of volcanic ash, in the spectral range 750 – $980\,\mathrm{cm}^{-1}$ (13.3 – $11.8\,\mu$m), from satellite infrared sounder data; they found that volcanic ashes with basaltic/andesite features (lower SiO_2 content) tended to have weak absorption through this spectral range whereas rhylotic ashes (higher SiO_2 content) tended to have a distinct absorption feature at $\sim 12.8\,\mu$m. The absorption feature can be attributed to symmetric vibrational stretching of Si—O—Si and/or tetrahedral Al—O stretching vibrations [*Ishimoto et al.*, 2016; *King et al.*, 2004].

In order to investigate the repeatability of the MEC measurements, repeat experiments were performed consecutively on the VA4 volcanic ash sample. The experiments were performed on the 12^{th} and 13^{th} of June 2015. In Fig 6.5 the MEC with uncertainty (first two rows) and size distribution results (bottom row) are overplotted for comparison: black indicates the result for the 12^{th} June experiment, and red inidicates 13^{th} June; uncertainties are indicated by grey and light red for the two experiments, respectively. It can be seen that there is excellent agreement in MEC for $\lambda > 7\,\mu$m between the two days. However, for $\lambda < 4\,\mu$m the MEC curves begin to deviate, with the experiment performed on 12^{th} June showing higher MEC. The difference in the shortwave extinction can likely be explained by differences in the effective radius measured for the two experiments. The effective radius, calculated from the in-cell size distributions, were $r_{\mathrm{e}} = 0.184$ and $0.254\,\mu$m for the 12^{th} and 13^{th} June experiments, respectively. With the composition of the samples being the same on the two days, a smaller effective radius would be expected to produce greater extinction per unit mass of aerosol, in the shortwave, through the Twomey effect (*Twomey* [1977]; see Appendix A.3 for a more detailed discussion of the Twomey effect).

The complex refractive index (with uncertainty) of the volcanic ash samples at three visible wavelengths, measured using the Becke and attenuation method, were presented in Table 2.2 and Table 2.3 for the real and imaginary parts, respectively. The complex refractive index at 450 and $650\,$nm, along with the in-cell size distribution were used to model the predicted MEC at these two wavelengths (the $546.7\,$nm Becke results were not used because MEC data were missing at this wavelength). The MEC was modelled using Eq. (4.2) and Eq. (6.1), and using Mie theory to compute the particle extinction efficiencies. Table 6.2 shows the measured and modelled MEC as well as the ratio of measured to modelled MEC. The uncertainty in the predicted MEC was propagated from uncertainty in the complex refractive index of the sample, as well as uncertainty in MPV; the forward

Figure 6.5: Repeat measurements of VA4 performed on the 12th and 13th of June 2015.

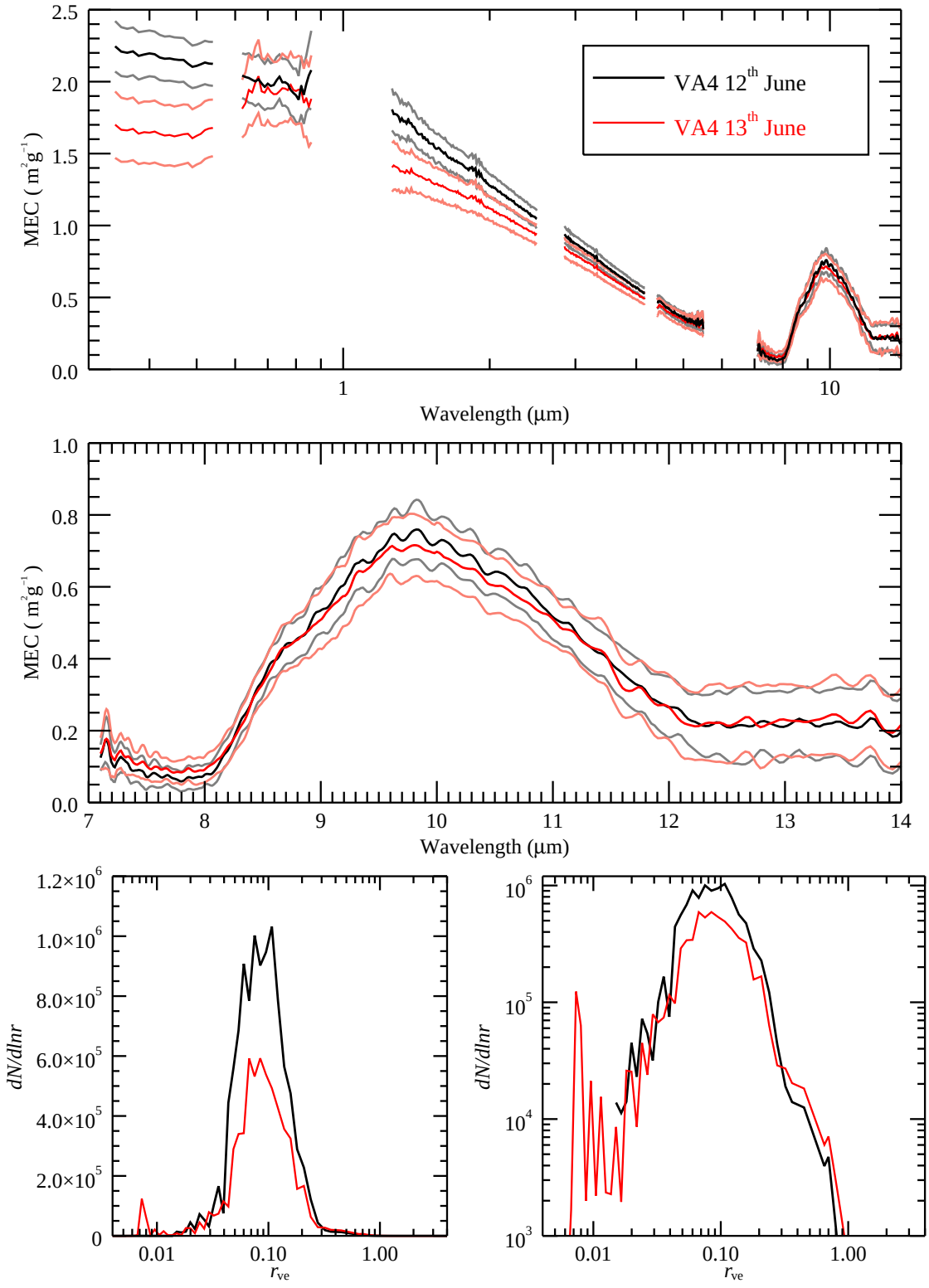

Table 6.2: Modelled and measured MEC at 450 and 546.7 nm. The modelled MEC uses the real and imaginary refractive indices measured using the Becke and attenuation methods.

Sample	Measured MEC (m^2g^{-1})	Predicted MEC (m^2g^{-1})	Measured/Predicted
450 nm			
VA17	2.59 ± 0.30	2.79 ± 0.10	0.93 ± 0.11
VA15	1.90 ± 0.37	3.04 ± 0.11	0.63 ± 0.12
VA19	2.06 ± 0.25	2.20 ± 0.05	0.94 ± 0.11
VA16	2.07 ± 0.31	2.62 ± 0.06	0.79 ± 0.12
VA1	2.45 ± 0.43	2.42 ± 0.04	1.01 ± 0.18
VA22	1.64 ± 0.47	2.48 ± 0.25	0.66 ± 0.20
650 nm			
VA17	2.69 ± 0.35	1.76 ± 0.07	1.53 ± 0.20
VA15	1.82 ± 0.36	1.68 ± 0.06	1.08 ± 0.21
VA19	2.11 ± 0.25	1.72 ± 0.04	1.22 ± 0.15
VA16	1.93 ± 0.36	1.88 ± 0.05	1.02 ± 0.19
VA1	2.20 ± 0.45	1.96 ± 0.04	1.12 ± 0.23
VA22	1.48 ± 0.45	1.97 ± 0.20	0.75 ± 0.24

model relating $m = n + ik$, $dN/d\ln r_{\mathrm{ve}}$, and MPV to MEC was linearised, and the propagated uncertainty in MEC was calculated according to:

$$\sigma^2_{\mathrm{MEC}} = \left(\frac{\partial \mathrm{MEC}}{\partial n}\right)^2 \sigma_n^2 + \left(\frac{\partial \mathrm{MEC}}{\partial k}\right)^2 \sigma_k^2 + \left(\frac{\partial \mathrm{MEC}}{\partial MPV}\right)^2 \sigma^2_{\mathrm{MPV}}, \tag{6.3}$$

where σ_{MEC} is the propagated uncertainty in MEC. And where σ_n, σ_k, and σ_{MPV} are the uncertainties in the measured values of n, k and MPV. The partial derivatives were calculated by making small fractional perturbations of 10^{-5} in n, k and MPV.

Table 6.2 shows that the ratio of measured to predicted MEC is fairly close to unity for most of the ashes. The uncertainty in the ratio is propagated from both the uncertainty in the measured and the predicted MEC. The sample VA1 appears to show the best agreement between measured and modelled MEC, with both the ratios at 450 and 650 nm being within one sigma of unity. However, for some of the other samples, whilst there might be agreement at one of the wavelengths, the agreement at the second wavelength is less good. The Becke and attenuation methods could only be applied to particles with radii larger than approximately $10\,\mu$m, whereas the measured in-cell effective radii for the samples ranged 0.15 to $0.29\,\mu$m. Therefore any variation in composition and complex refractive index

between the larger and smaller sized particles would introduce systematic errors into the predicted extinction. Furthermore, the discrepancies may result from errors in the assumed values for the dynamic shape factor ($\chi = 1.36$) and the density of particles ($\rho_\mathrm{p} = 2.65\,\mathrm{g/cm^3}$). The dynamic shape factor affects the shape of the in-cell size distribution through Eq. (4.41) — the correction to the SMPS sizing data. For example, considering VA19 and assuming either $\chi = 1.00$, 1.36 or 1.82 results in size distributions with effective radii $r_\mathrm{e} = 0.31$, 0.28 and 0.21, respectively. Shortwave extinction resulting from scattering is strongly influenced by the effective radius. Furthermore, the particle density assumption will influence the in-cell particle number density since the in-cell distribution is scaled to match the measured FH1 mass deposit, m_FH1; if the assumed density is too high then the in-cell number density will be low. This will affect the shortwave where the number density of scatterers in crucial; in contrast in the IR, where absorption dominates, it is the total mass of aerosol that is critical. There is significant variation in reported literature values for the density of volcanic ash. *Beckett et al.* [2015] compared the particle density distributions of various volcanic ashes; in all cases the particle density increased for smaller particles but remained constant for radii below $0.5\,\mu$m. For $r < 0.5\,\mu$m they reported $\rho_\mathrm{p} = 2.30\,\mathrm{g/cm^3}$ for Askja 1975 (rhyolitic), $\rho_\mathrm{p} = 2.40\,\mathrm{g/cm^3}$ for Quizapú 1932 (dacitic), $\rho_\mathrm{p} = 2.60\,\mathrm{g/cm^3}$ for Hudson 1991 (andesitic). *Bonadonna et al.* [2011] measured a density of $\rho_\mathrm{p} = 2.738\,\mathrm{g/cm^3}$ for glass particles from the 2010 Eyjafjallajökull eruption. The assumed particle refractive index of $\rho_\mathrm{p} = 2.65\,\mathrm{g/cm^3}$ is therefore towards the higher end of reported values. In future, the density of each ash will be measured using a gas pycnometer in order to remove any systematic error resulting from assuming a value for the particle density.

6.2 Retrieval of complex refractive index

6.2.1 Theory

6.2.1.1 The forward model

The forward model, $\mathbf{F}(\mathbf{x}, \mathbf{b})$, relates the measurement vector, $\mathbf{y}$, to the state vector, $\mathbf{x}$, according to:

$$\mathbf{y} = \mathbf{F}(\mathbf{x}, \mathbf{b}) + \boldsymbol{\epsilon}, \tag{6.4}$$

where $\boldsymbol{\epsilon}$ is the measurement error and $\mathbf{b}$ contains additional fixed parameters assumed by the forward model. In a retreival $\mathbf{x}$ is varied to produce simulated measurements vectors until an optimal fit with the measurement vector is obtained. The problem here is to estimate the real and imaginary parts of the complex refractive index, $m(\lambda)$, of an aerosol from measurements of the transmission, $T_{\mathrm{a}}(\lambda)$, through that aerosol over a range of wavelengths, λ. The forward model, outlined in more detail in Sections 4.2.1 and 4.2.2, can be summarised as:

$$T_{\mathrm{a}}(\lambda) = \exp\left(-\beta^{\mathrm{ext}}(\lambda)\, x\right), \tag{6.5}$$

and,

$$\beta^{\mathrm{ext}}(\lambda) = \int_0^{\infty} \pi r^2 Q^{\mathrm{ext}}(r, m, \lambda)\, N(r)\, dr, \tag{6.6}$$

where x is the path length inside the cell, and $N(r)$ is the measured size distribution. The extinction efficiency, $Q^{\mathrm{ext}}(r, m, \lambda)$, is calculated from Mie theory which assumes the size distribution is formed from homogeneous spheres composed of a material with refractive index $m(\lambda)$. The vector of assumed parameters takes the form:

$$\mathbf{b} = [x, N(r), n_{\mathrm{ref}}], \tag{6.7}$$

where n_{ref} is a reference value of the real refractive index of the particles at a short-wavelength; its significance will be explained in the following section. The problem is under-constrained because at each wavelength there is one measurement of the aerosol transmission for two unknowns — the real and the imaginary parts of the refractive index. To overcome this, the size of the state vector is reduced by parameterising the complex refractive index using a damped simple harmonic oscillator model, following the approach detailed in *Thomas et al.* [2005].

6.2.1.2 The classical damped harmonic oscillator model

The classical damped harmonic oscillator (CDHO) model represents the complex refractive index, $m(\lambda)$, of a material over a range of wavelengths using a finite set of oscillator band parameters and the real refractive index in the small wavelength (high frequency) limit. In the CDHO model the motion of bound electrons within the material is modelled using a forced damped harmonic oscillator (analogous

to direct interband transitions in the quantum mechanical treatment). Considering the motion of an electron in one dimension, the equation of motion can be expressed as:

$$\begin{aligned} m\frac{d^2x}{dt^2} + m\gamma\frac{dx}{dt} + m\omega_0 x &= -eE, \\ E &= E_0 \exp\left(-i\omega t\right), \end{aligned} \tag{6.8}$$

where m is the electron mass, γ is the damping constant, ω_0 is resonant angular frequency, and $-eE_0 \exp\left(-i\omega t\right)$ is the driving force provided by the electromagnetic wave inside the material. The particular integral solution to Eq. (6.8) represents the steady state solution, and can be obtained by substitution of the trial solution $x\left(t\right) = C\exp\left(-i\omega t\right)$ and solving for C which yields:

$$x\left(t\right) = \frac{-eE}{m\left(\omega_0^2 - \omega^2 - i\gamma\omega\right)}. \tag{6.9}$$

The electric dipole moment, $\mathbf{p}$, of the displaced electron and ion system is given by $\mathbf{p} = e\mathbf{d}$ where $\mathbf{d}$ is the displacement vector pointing from the negatively charged particle towards the positive particle. Therefore for N such ion-electron systems per unit volume, the polarisation density, $\mathbf{P}_\mathrm{d}$, resulting from the displacement of electrons is given by:

$$\mathbf{P}_\mathrm{d} = -Ne\mathbf{x} = \frac{Ne^2\mathbf{E}}{m\left(\omega_0^2 - \omega^2 - i\gamma\omega\right)}. \tag{6.10}$$

Inside a material the electric displacement field, $\mathbf{D}$, is defined as:

$$\mathbf{D} = \epsilon_0\mathbf{E} + \mathbf{P}, \tag{6.11}$$

where $\mathbf{P}$ is the total polarisation density and can be expressed as the sum of the polarisation density arising from electromagnetic field induced displacements and a background polarisation density, $\mathbf{P}_\mathrm{b}$, such that: $\mathbf{P} = \mathbf{P}_\mathrm{d} + \mathbf{P}_\mathrm{b}$. For a linear material the displacement current is proportional to the electric field:

$$\mathbf{D} = \epsilon_0\epsilon_\mathrm{r}\mathbf{E}, \tag{6.12}$$

where $\epsilon_\mathrm{r} = \epsilon/\epsilon_0$ is the relative permittivity of the material. Combining Eq. (6.11) and (6.12) gives:

$$\epsilon_\mathrm{r} = 1 + \frac{\mathbf{P}_\mathrm{d} + \mathbf{P}_\mathrm{b}}{\epsilon_0\mathbf{E}} \tag{6.13}$$

Substituting the expression for the polaristion density arising from charge displacements, Eq. (6.10), into Eq. (6.13) yields:

$$\epsilon_{\mathrm{r}}(\omega) = 1 + \chi_{\mathrm{b}} + \frac{Ne^2}{\epsilon_0 m\left(\omega_0^2 - \omega^2 - i\gamma\omega\right)}. \tag{6.14}$$

where $\chi_{\mathrm{b}} = \mathbf{P}_{\mathrm{b}}/\epsilon_0\mathbf{E}$ is the background electric susceptibility. The background polarisation density and susceptibility are a convenient way to represent the high frequency response of the system, when the frequency of the driving electric field is too fast to induce an oscillatory response from the bound electron. In the limit of $\omega \to \infty$, Eq. (6.15) reduces to: $\epsilon_{\mathrm{r}}(\infty) = 1 + \chi_{\mathrm{b}}$, where $\epsilon_{\mathrm{r}}(\infty)$ is a real number.

In a typical material there are multiple resonant frequencies, corresponding to multiple ion-electron configurations, and therefore the general expression for the relative permittivity can be expressed as:

$$\epsilon_{\mathrm{r}}(\omega) = \epsilon_{\mathrm{r}}(\infty) + \sum_{j=1}^{J} \frac{N_j e^2}{\epsilon_0 m\left(\omega_j^2 - \omega^2 - i\gamma_j\omega\right)}. \tag{6.15}$$

for a system of J ion-electron configurations (bands), where N_j is the number of electron-ion systems per unit volume in the j^{th} configuration, ω_j is the j^{th} resonant frequency, and γ_j is the j^{th} damping constant. The classical model encapsulated by Eq. (6.15) bears close resemblance to the quantum mechanical treatment of direct interband transitions using time-dependent perturbation theory [*Wemple and DiDomenico*, 1971]. The classical approach is limited in representing interband transitions because it does not take into account selection rules and the density of states. One possibility is to introduce an 'oscillator strength' parameter f_j obtained from quantum mechanics which pre-multiplies each term in the summation of Eq. (6.15). In any case, for the purposes of the model representation of complex refractive index a single strength parameter, S_j, can be used such that Eq. (6.15) simplifies to:

$$\epsilon_{\mathrm{r}}(\omega) = \epsilon_{\mathrm{r}}(\infty) + \sum_{j=0}^{J} \frac{S_j}{\omega_j^2 - \omega^2 - i\gamma_j\omega}. \tag{6.16}$$

From Eq. (6.16), the real and imaginary parts of the electric susceptibility, $\epsilon_{\mathrm{r}} = \epsilon'_{\mathrm{r}} + i\epsilon''_{\mathrm{r}}$, can be determined:

$$\epsilon'_{\mathrm{r}}(\omega) = \epsilon_{\mathrm{r}}(\infty) + \sum_{j=1}^{J} \frac{S_j\left(\omega_j^2 - \omega^2\right)}{\left(\omega_j^2 - \omega^2\right)^2 + \gamma_j^2\omega_j^2}, \tag{6.17}$$

$$\epsilon''_{\mathrm{r}}(\omega) = \sum_{j=1}^{J} \frac{S_j \gamma_j \omega}{\left(\omega_j^2 - \omega^2\right)^2 + \gamma_j^2 \omega_j^2}. \tag{6.18}$$

For non-magnetic materials the relative permeability is unity ($\mu_{\mathrm{r}} = 1$) and the complex refractive index is given by: $m(\omega) = \sqrt{\epsilon_{\mathrm{r}}(\omega)}$. It follows that the real and imaginary parts of the refractive index can be expressed as:

$$n(\omega) = \left\{ \frac{\left[\epsilon'_{\mathrm{r}}(\omega)^2 + \epsilon''_{\mathrm{r}}(\omega)^2\right]^{1/2} + \epsilon'_{\mathrm{r}}(\omega)}{2} \right\}^{1/2}, \tag{6.19}$$

$$k(\omega) = \left\{ \frac{\left[\epsilon'_{\mathrm{r}}(\omega)^2 - \epsilon''_{\mathrm{r}}(\omega)^2\right]^{1/2} + \epsilon'_{\mathrm{r}}(\omega)}{2} \right\}^{1/2}. \tag{6.20}$$

In the high frequency limit, $n(\infty) = \sqrt{\epsilon_{\mathrm{r}}(\infty)}$ and $k(\infty) = 0$.

Despite the simplicity of the CDHO model it has been shown to accurately represent the complex refractive index of many liquids and solids [*Wemple and DiDomenico*, 1971; *Bertie et al.*, 1994; *Thomas et al.*, 2005]. The primary sources of modelling error using the model derive from: uncertainty in the number of bands; and the inability of the model to represent aysmmetric absorption features [*Thomas et al.*, 2005].

Earlier work (R.G. Grainger, personal communication) showed a difficulty in using this approach, encapsulated by Eq. (6.16), because there is redundancy between $\epsilon_{\mathrm{r}}(\infty)$ and the S_j. Attempts at simultaneously fitting these parameters resulted in sensible fits to the measurements but poor values of refractive indices. This problem was resolved by using a reference value, n_{ref}, of the real part of the refractive index at a visible wavelength to constrain $\epsilon_{\mathrm{r}}(\infty)$. This is achieved by recognising:

$$\epsilon'_{\mathrm{r}}(\omega_{\mathrm{ref}}) = \frac{4n_{\mathrm{ref}}^4 - \epsilon''_{\mathrm{r}}(\omega_{\mathrm{ref}})}{4n_{\mathrm{ref}}^4} \tag{6.21}$$

so that,

$$\epsilon_{\mathrm{r}}(\infty) = \frac{4n_{\mathrm{ref}}^4 - \epsilon''_{\mathrm{r}}(\omega_{\mathrm{ref}})}{4n_{\mathrm{ref}}^4} - \sum_{j=1}^{J} \frac{S_j\left(\omega_j^2 - \omega_{\mathrm{ref}}^2\right)}{\left(\omega_j^2 - \omega_{\mathrm{ref}}^2\right)^2 + \gamma_j^2 \omega_j^2}. \tag{6.22}$$

In summary, the CDHO model represents the complex refractive index from a known value of the real part of the refractive index, n_{ref}, and a set of J band parameters: S_j, ω_j, and γ_j.

6.2.1.3 The forward model Jacobian

In this section analytic expressions for the forward model Jacobian are presented. Analytic expressions are preferable to numerically calculated values because they are more accurate and significantly reduce the retrieval computation time. The forward model Jacobian, $\mathbf{K}$, is the derivative of the forward model with respect to the state vector, i.e. $\mathbf{K} = \partial\mathbf{F}/\partial\mathbf{x}$, and forms a matrix with dimensions $a \times b$ where a is the number of elements in the measurement vector, $\mathbf{y}$, and b is the number of elements in the state vector, $\mathbf{x}$. The elements of the matrix $\mathbf{K}$ are therefore given by:

$$K_{ij} = \frac{\partial F_i(\mathbf{x})}{\partial x_j}. \tag{6.23}$$

The forward modelled aerosol transmission, T_a, varies as a function of the state, $\mathbf{x} = [S_1, S_2, ..., S_J, \omega_1, \omega_2, ..., \omega_J, \gamma_1, \gamma_2, ..., \gamma_J]$, i.e. $T_\mathrm{a} = \mathbf{F}(\mathbf{x})$. The band parameters determine the complex refractive index, and so we can express T_a as a function of n and k. Therefore we can express the total derivative of T_a as:

$$dT_\mathrm{a} = \frac{\partial T_\mathrm{a}}{\partial n} dn + \frac{\partial T_\mathrm{a}}{\partial k} dk. \tag{6.24}$$

The aerosol transmission, T_a, also depends on the size distribution, $N(r)$, and the path length through the cell, x, but these are measured quantities that are fixed in the retrieval — they form the vector $\mathbf{b}$. Differentiating Eq. (6.24) with respect to the strength parameter of the j^{th} band in the CDHO model and holding all other variables constant, yields:

$$\frac{\partial T_\mathrm{a}}{\partial S_j} = \frac{\partial T_\mathrm{a}}{\partial n}\frac{\partial n}{\partial S_j} + \frac{\partial T_\mathrm{a}}{\partial k}\frac{\partial k}{\partial S_j}. \tag{6.25}$$

and because n and k vary as a function of the real and imaginary parts of the electric permittivity, Eq.(6.19) and Eq.(6.20), this can expressed as:

$$\frac{\partial T_\mathrm{a}}{\partial S_j} = \frac{\partial T_\mathrm{a}}{\partial n}\left(\frac{\partial n}{\partial \epsilon'}\frac{\partial \epsilon'}{\partial S_j} + \frac{\partial n}{\partial \epsilon''}\frac{\partial \epsilon''}{\partial S_j}\right) + \frac{\partial T_\mathrm{a}}{\partial k}\left(\frac{\partial k}{\partial \epsilon'}\frac{\partial \epsilon'}{\partial S_j} + \frac{\partial k}{\partial \epsilon''}\frac{\partial \epsilon''}{\partial S_j}\right) \tag{6.26}$$

where,

$$\begin{aligned}\frac{\partial T_\mathrm{a}}{\partial n} &= -x\exp\left(-\beta^{\mathrm{ext}}x\right) \times \frac{\partial \beta^{\mathrm{ext}}}{\partial n} \\ &= -x\exp\left(-\beta^{\mathrm{ext}}x\right) \times \int_o^\infty \pi r^2 \frac{\partial Q^{\mathrm{ext}}}{\partial n} N(r)\, dr,\end{aligned} \tag{6.27}$$

and,

$$\frac{\partial T_{\mathrm{a}}}{\partial k} = -x \exp\left(-\beta^{\mathrm{ext}} x\right) \times \int_o^\infty \pi r^2 \frac{\partial Q^{\mathrm{ext}}}{\partial k} N\left(r\right) dr. \tag{6.28}$$

Analytic expressions for the derivatives of the Mie extinction efficiencies, $\partial Q^{\mathrm{ext}}/\partial n$ and $\partial Q^{\mathrm{ext}}/\partial k$, are presented in *Grainger et al.* [2004]; computational efficiency can be improved by calculating the derivatives and Q^{ext} simultaneously. The additional derivatives in Eq. (6.26) can be expressed:

$$\begin{aligned}
\frac{\partial n}{\partial \epsilon'} &= \frac{1}{2}\left(\frac{\sqrt{\epsilon'^2+\epsilon''^2}+\epsilon'}{2}\right)^{-1/2} \times \frac{1}{2}\left(\frac{\epsilon'}{\sqrt{\epsilon'^2+\epsilon''^2}}+1\right) \\
&= \frac{1}{\sqrt{8(A+\epsilon')}}\left(\frac{\epsilon'}{A}+1\right) = \frac{\epsilon'}{AB}+\frac{1}{B}, \qquad (6.29) \\
\frac{\partial k}{\partial \epsilon'} &= \frac{1}{2}\left(\frac{\sqrt{\epsilon'^2+\epsilon''^2}-\epsilon'}{2}\right)^{-1/2} \times \frac{1}{2}\left(\frac{\epsilon'}{\sqrt{\epsilon'^2+\epsilon''^2}}-1\right) \\
&= \frac{1}{\sqrt{8(A-\epsilon')}}\left(\frac{\epsilon'}{A}-1\right) = \frac{\epsilon'}{AC}-\frac{1}{C}, \qquad (6.30) \\
\frac{\partial n}{\partial \epsilon''} &= \frac{1}{2}\left(\frac{\sqrt{\epsilon'^2+\epsilon''^2}+\epsilon'}{2}\right)^{-1/2} \times \frac{1}{2}\left(\frac{\epsilon''}{\sqrt{\epsilon'^2+\epsilon''^2}}\right) \\
&= \frac{1}{\sqrt{8(A+\epsilon')}}\left(\frac{\epsilon''}{A}\right) = \frac{\epsilon''}{AB}, \qquad (6.31) \\
\frac{\partial k}{\partial \epsilon''} &= \frac{1}{2}\left(\frac{\sqrt{\epsilon'^2+\epsilon''^2}-\epsilon'}{2}\right)^{-1/2} \times \frac{1}{2}\left(\frac{\epsilon''}{\sqrt{\epsilon'^2+\epsilon''^2}}\right) \\
&= \frac{1}{\sqrt{8(A-\epsilon')}}\left(\frac{\epsilon''}{A}\right) = \frac{\epsilon''}{AC}, \qquad (6.32)
\end{aligned}$$

where,

$$A = \sqrt{\epsilon'^2+\epsilon''^2}, \quad B = \sqrt{8(A+\epsilon')}, \quad C = \sqrt{8(A-\epsilon')}. \tag{6.33}$$

The remaining derivatives in Eq. (6.26) are found by differentiating Eq. (6.17) and Eq. (6.18) with respect to S_j, and are:

$$\frac{\partial \epsilon'}{\partial S_j} = \frac{\omega_j^2-\omega^2}{\left(\omega_j^2-\omega^2\right)^2+\gamma_j^2\omega^2}, \tag{6.34}$$

$$\frac{\partial \epsilon''}{\partial S_j} = \frac{\gamma_j \nu}{\left(\omega_j^2-\omega^2\right)^2+\gamma_j^2\omega^2}. \tag{6.35}$$

The derivatives of the forward modelled aerosol transmission, T_{a}, with respect to γ_j or ω_j can be found from similar expressions to Eq. (6.26) by replacing S_j with γ_j or ω_j, respectively. The following derivatives of Eq. (6.17) and Eq. (6.18) can then be used:

$$\frac{\partial \epsilon'}{\partial \gamma_j} = -\frac{2S_j\left(\omega_j^2-\omega^2\right)\gamma_j\omega^2}{\left[\left(\omega_j^2-\omega^2\right)^2+\gamma_j^2\omega^2\right]^2}, \tag{6.36}$$

$$\frac{\partial \epsilon''}{\partial \gamma_j} = \frac{S_j\nu}{\left(\omega_j^2-\omega^2\right)^2+\gamma_j^2\omega^2} - \frac{2S_j\gamma_j^2\omega^3}{\left[\left(\omega_j^2-\omega^2\right)^2+\gamma_j^2\omega^2\right]^2}, \tag{6.37}$$

$$\frac{\partial \epsilon'}{\partial \omega_j} = \frac{2S_j\omega_j}{\left(\omega_j^2-\omega^2\right)^2+\gamma_j^2\omega^2} - \frac{4S_j\omega_j\left(\omega_j^2-\omega^2\right)^2}{\left[\left(\omega_j^2-\omega^2\right)^2+\gamma_j^2\omega^2\right]^2}, \tag{6.38}$$

$$\frac{\partial \epsilon''}{\partial \omega_j} = -\frac{4S_j\gamma_j\omega_j\omega\left(\omega_j^2-\omega^2\right)}{\left[\left(\omega_j^2-\omega^2\right)^2+\gamma_j^2\omega^2\right]^2}. \tag{6.39}$$

6.2.2 Prelimary complex refractive index retrievals

Prelimary retrievals were performed for the complex refractive index from the extinction measurements using the CDHO model. In the prelimary approach the retrievals were initiated using 360 bands evenly spaced by wavenumber across the measurement range. In this approach, a large number of the retrieved band parameters (forming the retrieved state vector) were zero or very close to zero. This resulted in unrealistically large propagated errors in the retrieved complex refractive index. In future work, the bands will be refined by removing redundant bands according to the approach detailed by *Thomas et al.* [2005] allowing a sensible error propagation analysis. However, differences in the refractive index retrieved from the two Eyjafjallajökull samples were small and give an indication of the error associated with the retrieval.

6.2.2.1 Quartz

Figure 6.6 shows the retrieval results for the two quartz samples, SP15 and SP16. The plot on the first row gives a measure of the quality of the fit: Δ/σ, where $\Delta = \mathbf{y} - \mathbf{F}$ and $\mathbf{y}$ is the vector containing the measured extinction at each wavelength and $\mathbf{F}$ is the forward modelled extinction of the retrieved state. The second and

Figure 6.6: Complex refractive index retrieval results for quartz samples SP15 and SP16. The plot on the first row shows the quality of the fit to the measured extinction, Δ/σ, where $\Delta = \mathbf{y} - \mathbf{F}$ and σ is the uncertainty associated with the measurement. The second and third rows show the real and imaginary parts, respectively, of the retrieved refractive index of the two samples and that found by *Kischkat et al.* [2012] and [*Gao et al.*, 2013].

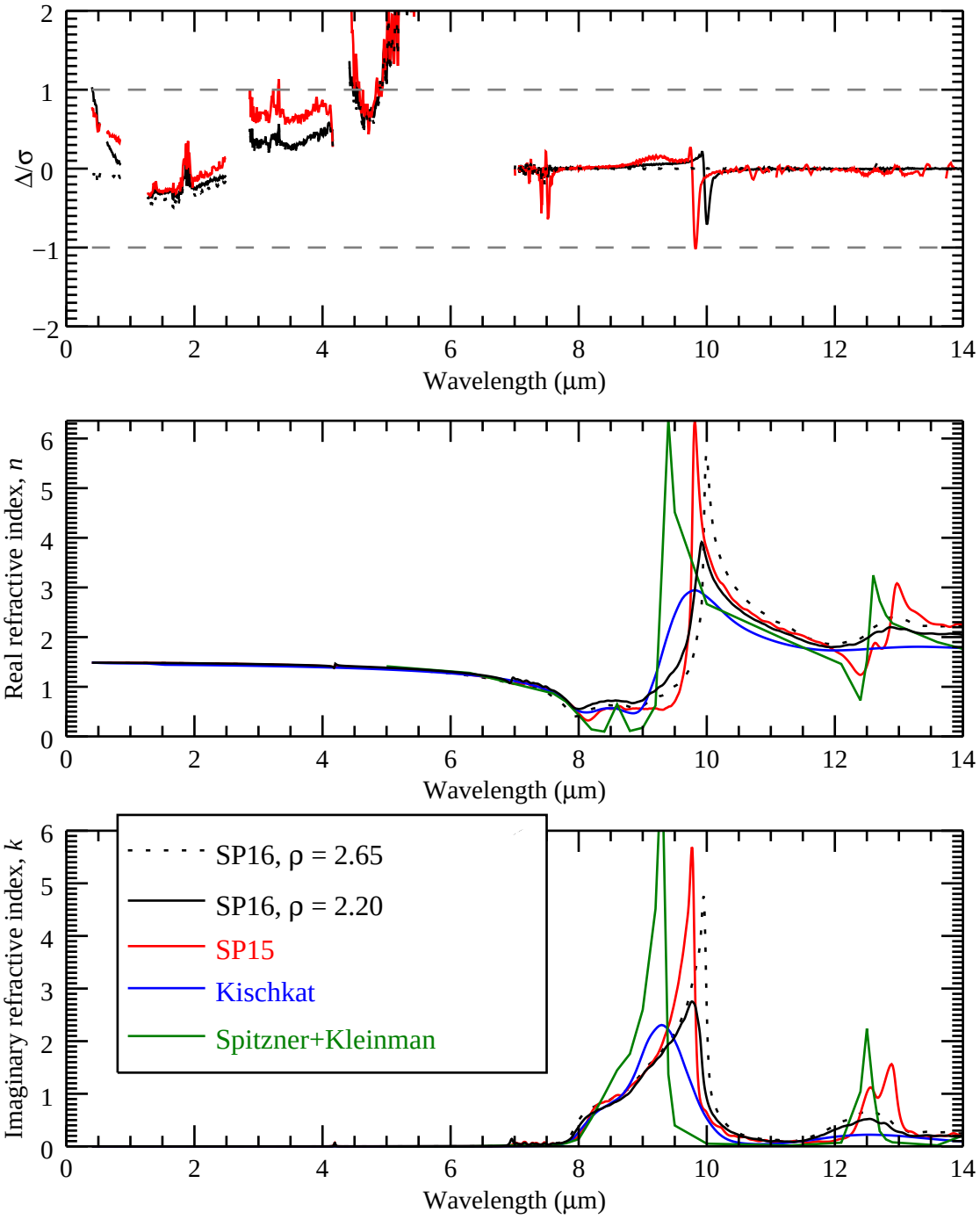

third rows of Fig. 6.6 show the real and imaginary parts, respectively, of the retrieved refractive indices of the two samples. Also included in the plots are literature values for the refractive index of alpha-quartz found by *Spitzer and Kleinman* [1961] and the refractive index of amorphous silica measured by *Kischkat et al.* [2012]. Alpha-quartz is the naturally occuring crystalline form of silicon dioxide (or silica) forming a regular trigonal crystal system. Silicon dioxide can also exist in non-crystalline form as amorphous silica, also referred to as glassy silica or vitreous silica [*Kitamura et al.*, 2007]. The structural arrangement of bonded oxygen and silicon atoms varies between the crystalline and non-crystalline forms, leading to differences in their physical properties [*Agarwal and Tomozawa*, 1997].

The two quartz samples measured in the aerosol cell, SP15 and SP16, were detailed in Table 5.1. SP15 is described as 'crystalline' whereas SP16 is described as being 'amorphous fused silica' by the manufacturer. The density of alpha-quartz is $\rho = 2.65\,\mathrm{g/cm^3}$ whereas the density of amorphous silica is somewhat less at approximately $\rho = 2.2\,\mathrm{g/cm^3}$ [*Mukherjee et al.*, 2001], although the exact density of amorphous silica varies depending on the formation process and temperature [*Vollmayr et al.*, 1996]. The in-cell size distributions were scaled according to the mass measurement on FH1, and therefore if the assumed density was too high the calculated in-cell number density would be lower than its true value. The effect on the retrieved refractive index for SP16, the amorphous silica sample, of changing the assumed density from $\rho = 2.65$ to $2.2\,\mathrm{g/cm^3}$ is shown in Fig. 6.6. The black dashed curve shows the retrieved refractive index assuming a density of $2.65\,\mathrm{g/cm^3}$, whereas the solid black curve shows the retrieved refractive index assuming $2.2\,\mathrm{g/cm^3}$. The change in density results in a fairly significant change to the retrieved refractive index, highlighting the importance of having accurate independent measurements of the density of samples.

With the density correction applied to the amorphous sample (SP16), the peak associated with asymmetric stretching of Si—O—Si at just under $10\,\mu$m aligns well with the crystalline sample (SP15), for both the real and imaginary refractive index. The peak heights of the amorphous sample of the real and imaginary parts are $n = 3.9$ and $k = 2.8$; and for the crystalline sample the values are $n = 6.4$ and $k = 5.7$. The feature at approximately $12.5\,\mu$m, associated with symmetric vibrations of Si—O—Si, shows greater variation between the amorphous and crystalline samples. The amorphous sample shows a low and broad peak whereas the crystalline sample shows a distinct oscillation.

It can be seen that shape of the refractive index curve of crystalline SP15 compares well with that measured by *Spitzer and Kleinman* [1961], whilst the shape of amorphous SP16 is similar to that measured by *Kischkat et al.* [2012]. However, in both cases the peaks of SP15 and SP16 are shifted to larger wavelengths. The location of the peaks associated with the symmetric and antisymmetric vibrations of Si—O—Si can be used to infer information about the ratio of Si atoms to O atoms in silicon oxide [*Tomozeiu*, 2011; *Zacharias et al.*, 1994]. The general molecular formula of silicon oxide can be expressed as SiO_x, and as x decreases below $x = 2$ the peak position of the symmetric Si—O—Si feature shifts to larger wavelengths [*Tomozeiu*, 2011]. The fact that both the peaks for both SP15 and SP16 align, but are shifted to larger wavelengths compared to the refractive index measured by *Spitzer and Kleinman* [1961], may suggest that the two samples have the same composition, but that $x < 2$. The shift could also be a result of other impurities in the sample.

6.2.2.2 Eyjafjallajökull ash

Figure 6.7 shows the refractive index retrieval results for two samples of Eyjafjallajökull volcanic ash, VA7 and VA15. The fit to the measured extinction is excellent for $\lambda > 7\,\mu$m, but for smaller wavelengths there are significant deviations between the forward modelled extinction of the retrieved state and the measured extinction. The extinction at shorter wavelengths is dominated by scattering, and is highly sensitive to the size distribution of particles. The most likely explanation for the deviation at shorter wavelength are errors in the assumed density of particles ($\rho = 2.65\,\mathrm{g/cm^3}$) and/or the assumed dynamic shape factor ($\chi = 1.36$), leading to errors in the calculated in-cell size distribution. The values assumed were taken from literature values for quartz, which might not be representative of the Eyjafjallajökull ash. In future work, measurements of the density of each of the samples will be made using a gas pycnometer. Furthermore, the filter samples taken during each of the aerosol cell runs will be analysed using an SEM. Analysis of the SEM images will provide an independent measurement of the particle size distribution; the method was recently applied by *Smith et al.* [2015] to black carbon particles. SEM image analysis can also provide information about the sphericity[1] of particles [*Riley et al.*, 2003], and formulae have been developed for the drag force on volcanic ash particles as a function of their sphericity [*Ganser*, 1993; *Alfano et al.*, 2011]. Measurements of sphericity from SEM image analysis could therefore be

[1]The sphericity was defined in 2-D by *Riley et al.* [2003] as the ratio of the projected area to the square of the projected perimeter.

Figure 6.7: Complex refractive index retrieval results for Eyjafjallajökull volcanic ash, samples VA7 and VA15, $(\mathbf{y} - \mathbf{F})/\sigma$. The plot on the first row shows the quality of the fit to the measured extinction. The second and third rows show the real and imaginary parts, respectively, of the retrieved refractive index of the two samples, and refractive indices for generic volcanic materials.

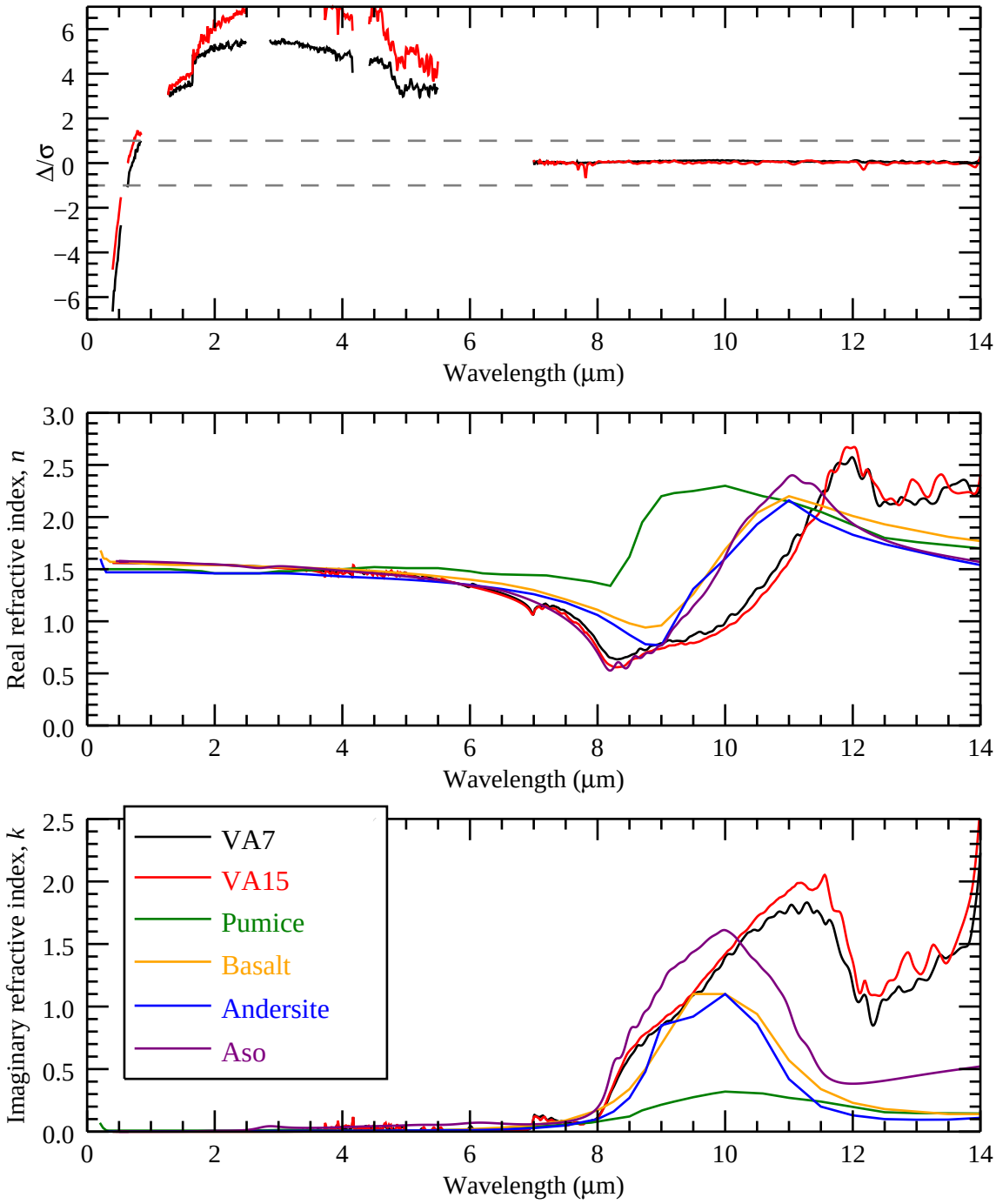

used to correct the SMPS size distribution data, by using the appropriate formula for drag.

At $\lambda > 7\,\mu$m extinction is dominated by absorption and is determined by the total volume of particles in the cell and their complex refractive index. Therefore, providing the calculated total volume of particles is correct, the retrieved complex refractive index for $\lambda > 7\,\mu$m should be accurate even if discrepancies exist between the measured and modelled shortwave extinction due to errors in the particle size distribution. The total volume is constrained by the FH1 mass measurement, so error in the calculated in-cell total particle volume will derive from uncertainty in the mass measurement and any error in the assumed particle density ($\rho = 2.65\,\mathrm{g/cm^3}$). The density of juvenile ash particles has been found to decrease linearly with the logarithm of particle radius, and then remains constant at the glass density for radii less than $8\,\mu$m, whereas lithic particles uniformly have densities similar to the glass density [*Cashman and Rust*, 2016]. For Eyjafjallajökull ash from the 2010 eruption, *Taddeucci et al.* [2011] reported the density of non-vesticular particles as $2.683\,\mathrm{g/cm^3}$ whilst *Bonadonna et al.* [2011] reported $2.738\,\mathrm{g/cm^3}$ as the glass density. The assumed density of $2.65\,\mathrm{g/cm^3}$ is likely to be a fairly good representation of the Eyjafjallajökull ash, although independent density measurements of VA7 and VA15 will be made in the future.

Figure 6.7 shows there is remarkably good agreement between the refractive index retrieved from the transmission measurements of the two Eyjafjallajökull volcanic ash samples, VA7 and VA15. Although a formal error propagation could not be performed in the prelimary refractive index retrievals, the differences in the retrieved refractive index between the two independent measurements of Eyjafjallajökull ash provide an indication of the uncertainty associated with the results. The mean absolute difference between the two complex refractive index retrievals indicate an uncertainty of 0.041 and 0.036 in the retrieved real and imaginary refractive indices, respectively, for $\lambda > 7\,\mu$m.

6.3 Application to satellite retrievals

The mean refractive index of VA7 and VA15 was used to analyse measurements of the 2010 Eyjafjallajökull eruption made by the MODIS instrument aboard NASA's Terra satellite. The retrievals using the VA7 & VA15 refractive index were compared to retrievals performed assuming the refractive index of pumice measured

by *Volz* [1973]. The calculations were run by Greg McGarragh (University of Oxford) and used the ORAC retrieval scheme, detailed in *Grainger et al.* [2013] and *Kokhanovsky and de Leeuw* [2009]. The aerosol size distribution was assumed to be log-normal and the width of the distribution was fixed at $S = 2.0$. This section covers analysis of a particular scene, but eight other scenes were analysed with similar results. The scene presented here was captured at 11:55 am on 6$^{\text{th}}$ May 2010. The brightness temperature difference between the 11 and 12 μm channels, shown in Fig. 6.8, was used to test which pixels to apply the retrieval to. The plume outline is clearly distinguishable in Fig. 6.8. Retrievals were performed for brightness temperature differences meeting the criterion $T_{11} - T_{12} < -0.5$ K. Furthermore, retrieval results were plotted only for pixels with $T_{11} - T_{12} < -0.5$ K and where the cost (χ^2) between the measurements and the forward model fulfilled $\chi^2 < 50$.

Figure 6.8: Brightness temperature difference between the 11 and 12 μm channels measured by the MODIS instrument aboard NASA's Terra satellite at 11:55 am on 6$^{\text{th}}$ May 2010. The Eyjafjallajökull volcanic plume is clearly distinguished.

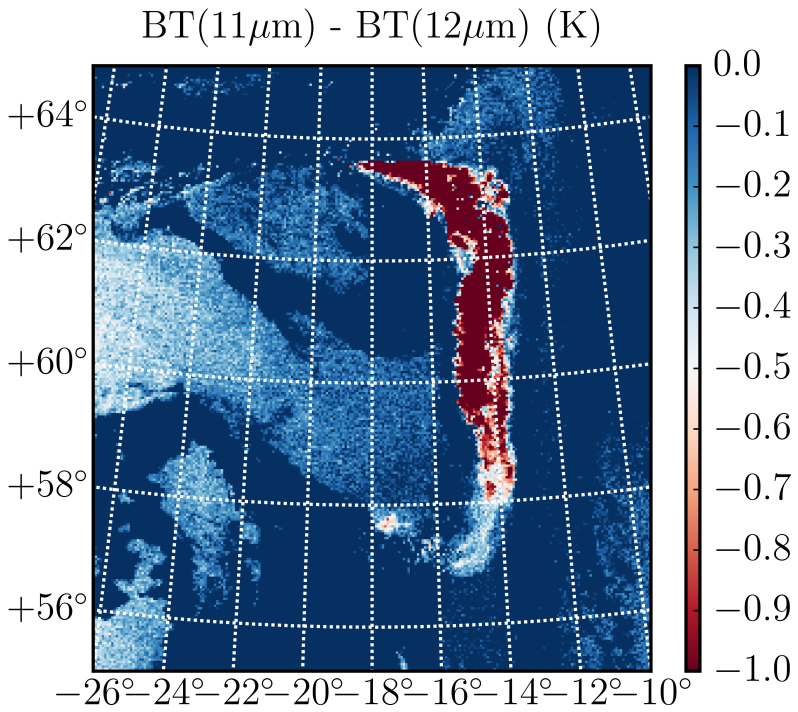

The retrieval results for optical path, effective radius, plume top pressure and the retrieval cost against the measurements are shown in Figs. 6.9, 6.10, 6.11 and 6.12, respectively. Firstly, it is clear that the number of pixels meeting the cost criterion is larger for VA7 & VA15. Using the new refractive index of VA7 & VA15 appears to be more sensitive to ash even in the presence of cloud, and produces

lower cost in regions where both cloud and volcanic ash are present (G. McGarragh, personal communication). In each of the figures of retrieved quantities there are significant differences in the results assuming *Volz* [1973] compared to using the new refractive index of VA7 & VA15.

Comparing the plume optical path shown in Fig. 6.9, the value of τ retrieved assuming *Volz* [1973] is significantly higher than for VA7 & VA15. Proximal to the source, the optical path for *Volz* [1973] is ~ 5, whereas for VA7 & VA15 the value is 2.5 – 3.5 and appears to decrease more gradually with distance from the source and towards the edge of the plume. The regions of high optical depth towards the edges of the plume for VA7 & VA15 are where there is also cloud present.

There are also significant differences in the retrieved effective radius, r_{e}, of the plume, shown in Fig. 6.10. The effective radius retrieved assuming VA7 & VA15 is higher at 2.5 – $2.0\,\mu$m proximal to the volcanic source and decreases gradually towards values less than $0.5\,\mu$m towards the edges of the plume. This is as expected: larger particles have higher settling velocities and are deposited closer to the source. The effective radius retrieved assuming *Volz* [1973] is lower at 1.5 – 0.5 proximal to the source, and the pattern of effective radius decreasing with distance from the source is less clear.

Figure 6.11 shows the retrieved cloud top pressure. For VA7 & VA15, there is a clear pattern of cloud top pressure increasing with distance from the volcanic vent; close to the volcanic source the cloud top pressure is $\sim 350\,$hPa increasing to $\sim 750\,$hPa at the plume edges. The cloud top pressure for *Volz* [1973] is lower than VA7 & VA15, reaching values approaching $100\,$hPa in some pixels.

Figure 6.12 shows the cost (χ^2) between the measurements and the forward model. The VA7 & VA15 refractive index allows a larger portion of the plume to be analysed; a larger number of pixels met the cost criterion. However, over the rest of the plume the cost is similar to *Volz* [1973], although VA7 & VA15 produces a region of higher cost proximal to the volcanic source. The streaks of higher cost passing through the plume for VA7 & VA15 are likely to be from thin ice cloud over the volcanic plume (G. McGarragh, personal communication). These streaks are less visible for *Volz* [1973].

Figure 6.9: Optical path retrieved using ORAC from MODIS data assuming the refractive index measured by *Volz* [1973] for pumice (top) and the mean refractive index of VA7 and VA15 (bottom). The retrieval was performed only on pixels with $T_{11} - T_{12} < -0.5$ and was plotted where $\chi^2 < 50$.

Volz [1973]

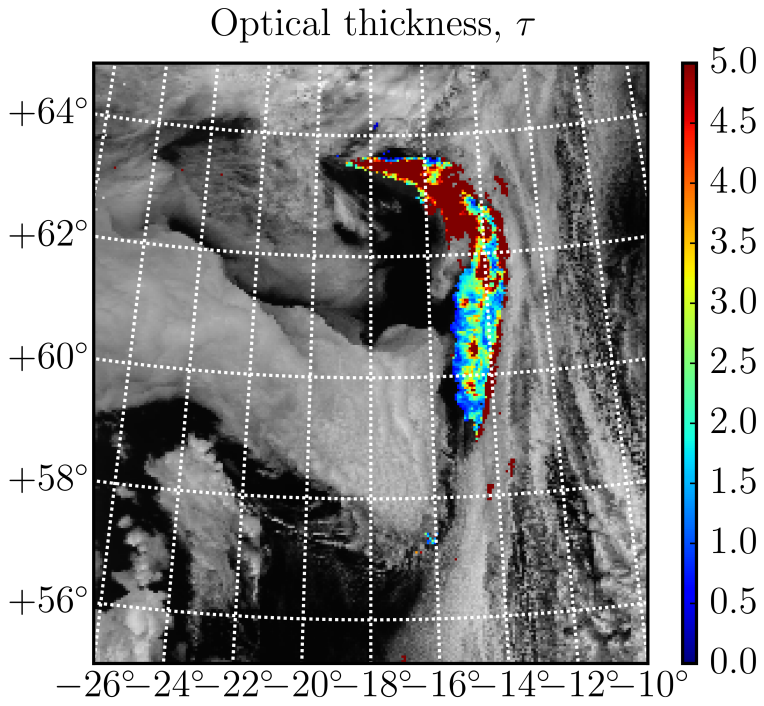

VA7 & VA15

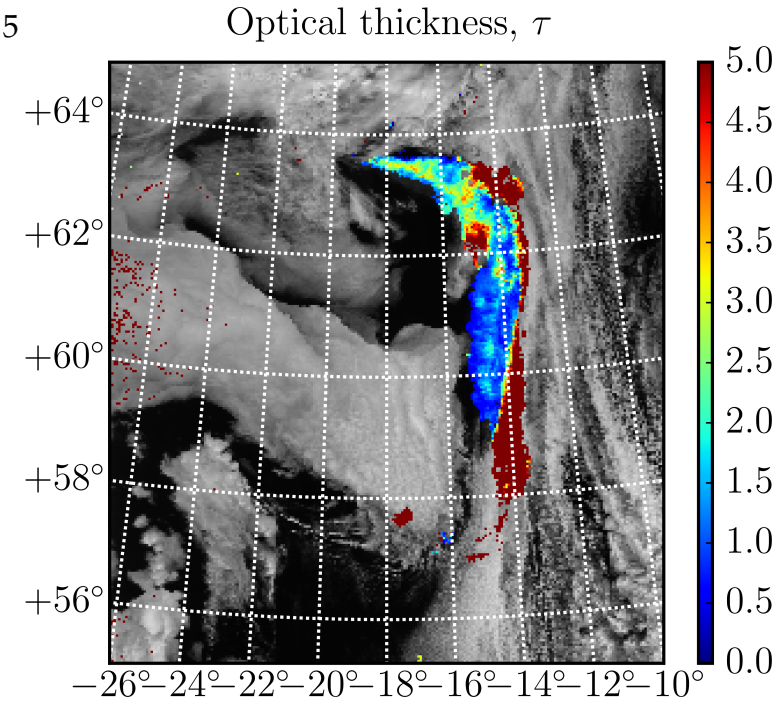

Figure 6.10: Effective radius retrieved using ORAC from MODIS data assuming the refractive index measured by *Volz* [1973] for pumice (top) and the mean refractive index of VA7 and VA15 (bottom). The retrieval was performed only on pixels with $T_{11} - T_{12} < -0.5$ and was plotted where $\chi^2 < 50$.

Volz [1973]

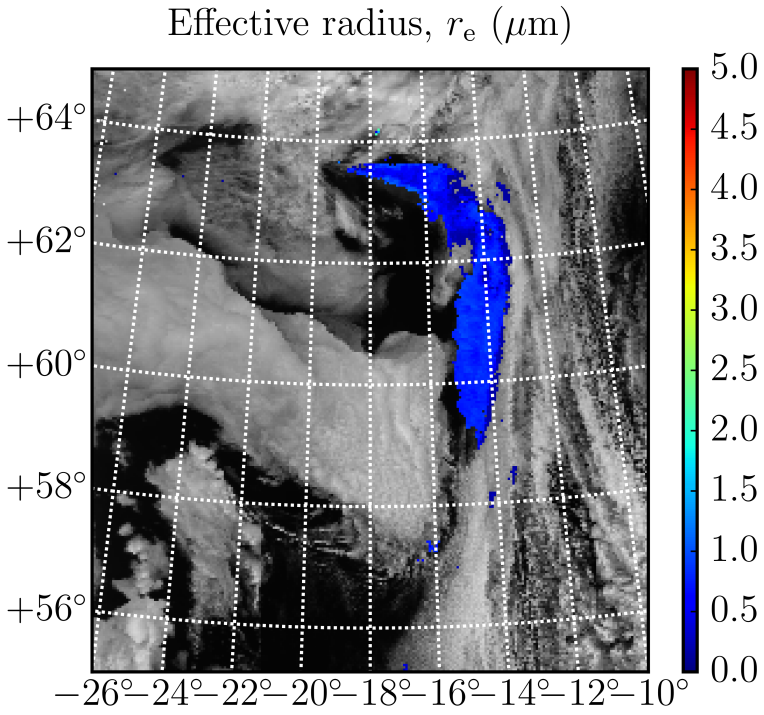

VA7 & VA15

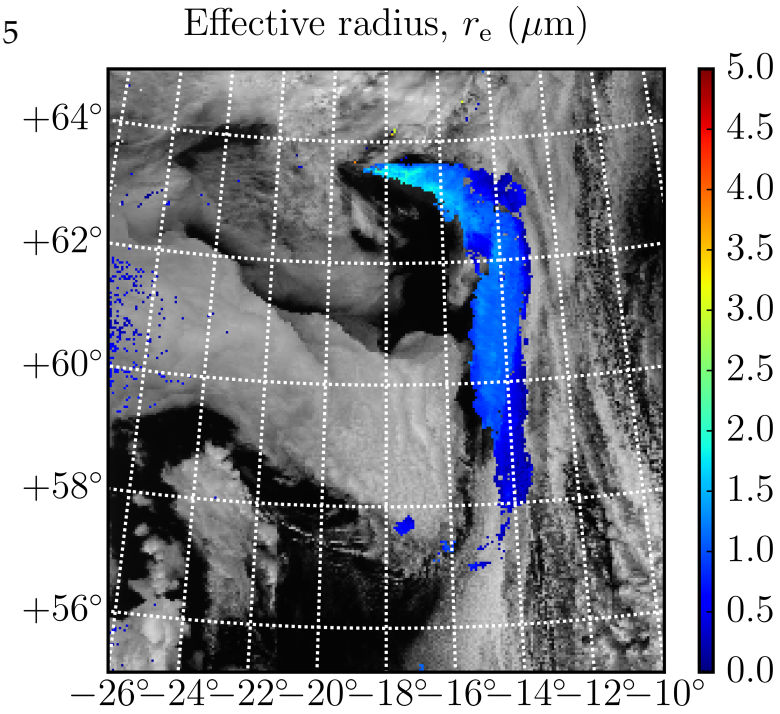

Figure 6.11: Plume top pressure retrieved using ORAC assuming the refractive index measured by *Volz* [1973] for pumice (top) and the mean refractive index of VA7 and VA15 (bottom). The retrieval was performed only on pixels with $T_{11} - T_{12} < -0.5$ and was plotted where $\chi^2 < 50$.

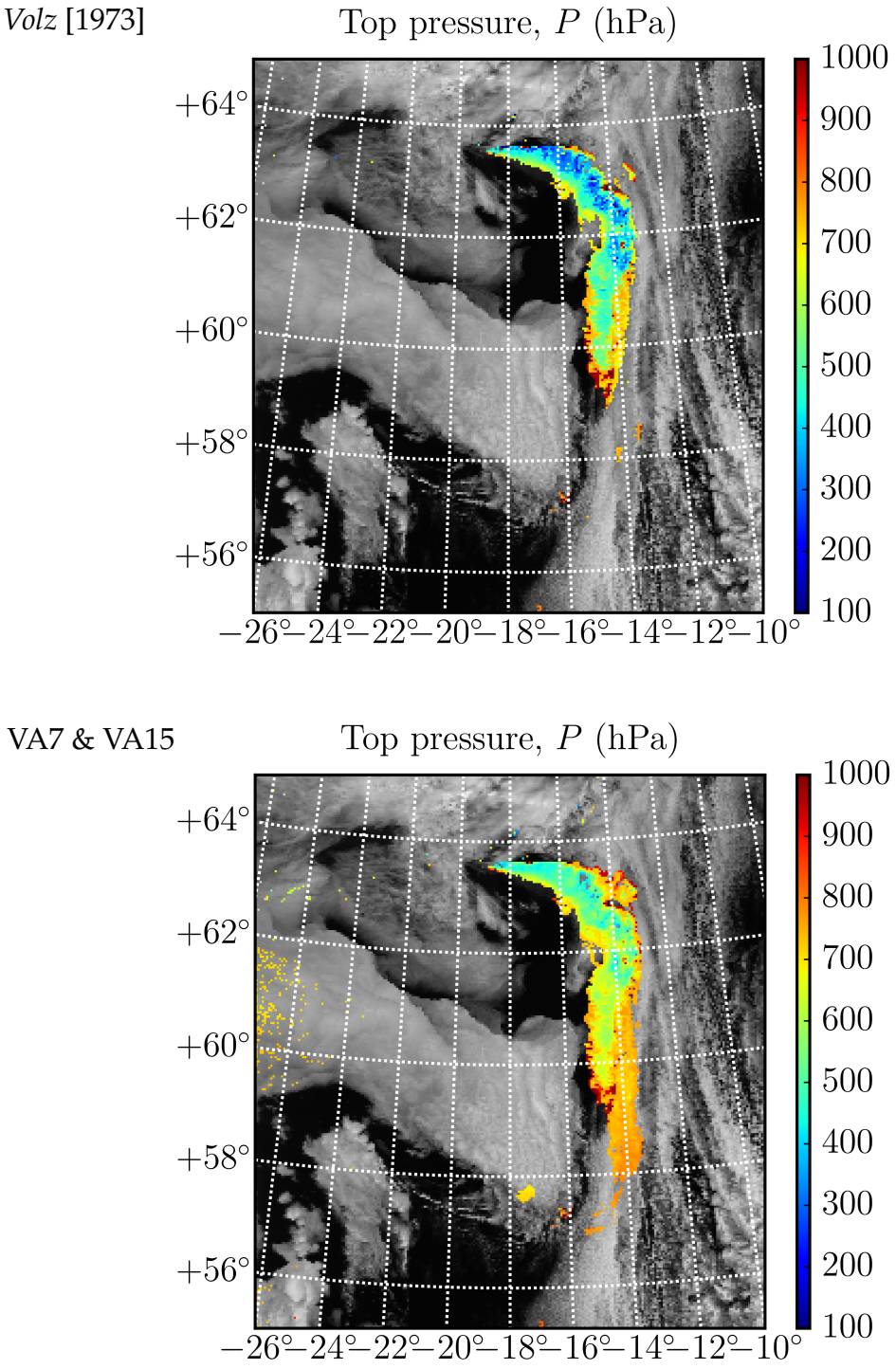

Figure 6.12: Cost between the measurements and the forward model, assuming the refractive index measured by *Volz* [1973] for pumice (top) and the mean refractive index of VA7 and VA15 (bottom).

Volz [1973]

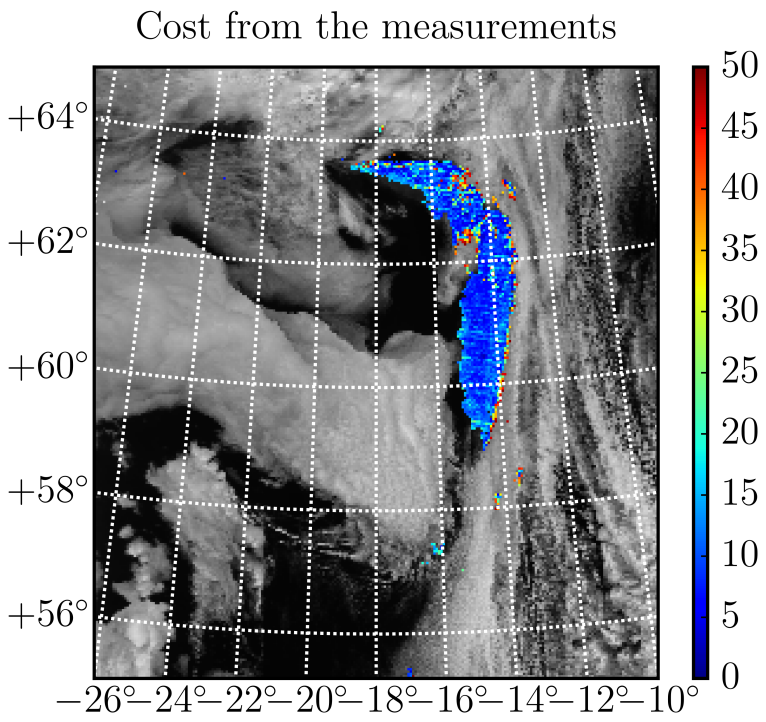

VA7 & VA15

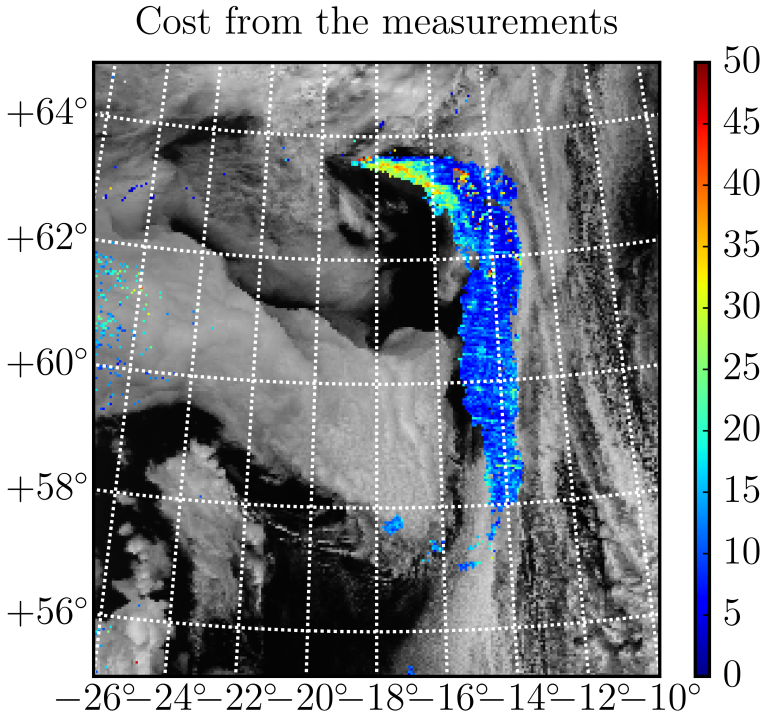

6.4 Chapter summary and conclusions

This chapter presents the spectral MEC results for nine volcanic ash samples. The in-cell size distributions of the samples, and other in-cell parameters such as the relative humidity, were also presented. The two separate measurements of VA4 demonstrate that the technique had excellent repeatability. There was considerable variation in the MEC of the different volcanic ashes, highlighting the importance of eruption-specific measurements of optical properties. Forward modelled mass extinction at visible wavelengths, assuming the complex refractive index values measured for the samples using the Becke and attenuation methods, matched the measured values remarkably well and the small differences in some cases are likely a result of uncertainty in the in-cell size distribution (deriving from uncertainty in the assumed density and dynamic shape factor of particles). Non-spherical scattering effects may also play a role.

Preliminary complex refractive index retrievals were performed for two quartz samples (one crystalline and one amorphous) from the measured spectral extinction using the CDHO model. The shape of the retrieved complex refractive index curves closely resembled literature values for crystalline quartz and amorphous quartz. The importance of having independent density measurements for the samples was highlighted by the change in the retrieved refractive index for amorphous quartz if the incorrect higher density of alpha-quartz is assumed. Reducing the assumed density by 17 % to the correct value for amorphous quartz resulted in a significant change to the retrieved refractive index. The peaks in the features associated with symmetric and asymmetric stretching of Si—O—Si were shifted to slightly higher wavelengths compared to two literature values for the refractive indices. It was hypothesised that these shifts may relate to the ratio of Si to O atoms within the samples, as detailed in *Tomozeiu* [2011] where a shift to larger wavelengths is associated with a reduction in oxygen content, or because of other impurities.

The complex refractive indices of two samples from the 2010 eruption of Eyjafjallajökull were retrieved. The retrieved refractive indices for the two samples showed excellent agreement. Based on the two retrievals, the uncertainty in the complex refractive index was estimated as 0.041 and 0.036 for the real and imaginary parts, respectively, for $\lambda > 7\,\mu$m. The retrieved refractive indices for the Eyjafjallajökull ash were significantly different to literature measurements of generic volcanic materials.

The mean refractive index for the two Eyjafjallajökull samples, VA7 & VA15, was applied within the ORAC aerosol retrieval scheme to MODIS measurements of the 2010 eruption of Eyjafjallajökull. The retrieved quantities of optical depth, effective radius, and plume top pressure were compared to values retrieved assuming the complex refractive index of pumice measured by *Volz* [1973], and significant differences were seen. The brightness temperature method was used to test which pixels to apply the retrieval to, and results were plotted provided the cost was below 50. The new refractive indices were found to be more sensitive to ash in the presence of cloud and resulted in a much lower cost in these regions. The result for effective radius with VA7 & VA15 showed r_{e} decreased gradually with distance from the volcanic vent; this pattern was not present with *Volz* [1973]. Values of r_{e} were also significantly higher with VA7 & VA15 compared to *Volz* [1973]. Although the cost over the plume area was similar assuming the refractive index of *Volz* [1973] compared to the new refractive index of VA7 & VA15, having an eruption-specific measurement of the complex refractive index made significant changes to the retrieved plume properties of optical depth, effective radius, and plume altitude.

Chapter 7

Conclusions and future work

7.1 Conclusions

Eruption-specific measurements of the complex refractive index of volcanic ash are required for accurate remote sensing of volcanic plumes. Assuming the incorrect complex refractive index when interpreting satellite measurements results in significant errors in retrieved quantities such as the optical path, effective radius, and plume top altitude. Existing measurements of the complex refractive index of volcanic ash over the broad range of wavelengths used in satellite retrieval schemes, such as ORAC, are very limited. This thesis presents measurements of the complex refractive index, mass extinction coefficient, and composition of a wide range of volcanic ash samples. Three separate experimental techniques have been developed.

This thesis presents the mass extinction coefficients for suspended volcanic ash particles, over the spectral range 0.3 – $14\,\mu$m, from a wide range of volcanic sources. These measurements are the first of their kind. Previous studies have only determined the optical constants of generic volcanic materials and glasses; direct measurements of the volume and mass extinctions coefficients of volcanic ash particles have not been reported elsewhere. The results for the mass extinction coefficients, presented in Chapter 6, show considerable variation between the different samples, highlighting the importance of eruption-specific measurements. Along with the mass extinction coefficients, the in-cell size distributions and other in-cell parameters, including the effective radius and relative humidity, are presented. The two repeat measurements on VA4 demonstrate that the technique has excellent repeatability and accuracy.

Chapter 4 presents the theory required to interpret the aerosol cell extinction measurements and the sizing measurements which were performed simultan-

eously. Particular care is needed when interpreting sizing measurements returned by different instruments. For example, an SMPS measures the electrical mobility radius of particles whereas an APS measures the aerodynamic radius. Interpreting extinction measurements requires converting to the volume equivalent radius. Both the SMPS and the APS apply known equations for the drag force experienced by particles in a gas. The drag equations vary depending on the particle-gas flow regime, and therefore so do the radii conversion equations. The equations also depend on the dynamic shape factor and density of particles, and consequently any error in the assumed values for these quantities will result in error in the calculated in-cell size distribution.

Chapter 5 presents the apparatus and experimental method applied to measure the extinction of suspended volcanic ash particles and quartz calibration particles within the aerosol cell. The Wright dust feeder provided a near constant supply of dispersed aerosol to the cell, and an eight pass White cell was used within the aerosol cell for the FTS IR measurements to increase the sensitivity to low concentrations of particles. Two diffraction grating spectrometers were used covering UV, visible, and NIR wavelengths. Particle loss calculations were performed to take into account the size-selection of aerosol tubing passing from the cell to sizing instruments. The radii conversion equations were applied to the sizing instruments' data as well as known corrections for the efficiencies of instruments. These corrections made significant differences to the returned distributions. Calibration measurements were made using two quartz samples, and the measured extinction was compared to the modelled extinction assuming literature values for the complex refractive index of silicon dioxide. Various methods were investigated for combining data from the three sizing instruments, taking into account particle losses in aerosol tubing, to produce a best-estimate of the in-cell size distribution. It was found that combining data from the SMPS and OPC, assuming a dynamic shape factor of 1.36, and scaling the in-cell distribution by the measured filter deposit mass produced an in-cell size distribution that was able to accurately predict the measured extinction of quartz through the UV, visible, and IR. The ability to accurately forward model the measured extinction demonstrates the high level of accuracy of the measurements and the physical modelling of the system.

The spectral complex refractive index can be retrieved from measurements of the spectral extinction and size distribution. In Chapter 6, preliminary retrieval results are presented for the complex refractive index of two quartz samples (one crystalline and one amorphous) and two samples of Eyjafjallajökull ash from the

2010 eruption. The forward model used the classical damped harmonic oscillator model to represent the complex refractive index of samples in terms of a finite set of oscillator band parameters and Mie theory to determine the particle scattering and extinction. Previous studies using this approach showed a difficulty because there is redundancy in retrieving the relative permittivity in the small wavelength limit and the band strength parameters. To overcome this problem, reference values for the real refractive index of samples at a visible wavelength were used to constrain the value of the relative permittivity in the small wavelength limit. The retrieved complex refractive index of the two silicon oxide samples, SP15 and SP16, closely resembled literature curves for amorphous quartz and alpha-quartz. The IR features associated with symmetric and asymmetric stretching vibrations of Si—O—Si were shifted to slightly larger wavelengths compared to two literature values. It was hypothesised that these shifts are indicative of a reduced ratio of oxygen to silicon atoms within the samples, or other impurities. The features aligned in both the crystalline sample (SP15) and the amorphous sample (SP16), which was to be expected as both samples had the same natural origin. As expected, the amorphous sample showed smoothed and wider IR features compared to the narrow and high peaks seen in the IR refractive index of the crystalline sample.

The preliminary complex refractive index retrievals performed on the two Eyjafjallajökull volcanic ash samples, VA7 and VA15, showed excellent agreement. Based on the two measurements, for $\lambda > 7\,\mu$m the estimated uncertainty in the complex refractive index was 0.041 and 0.036 for the real and imaginary parts, respectively. The retrieved Eyjafjallajökull complex refractive index was significantly different to previous literature measurements of generic volcanic materials and glasses. The complex refractive index of Eyjafjallajökull ash, over a broad range of visible and IR wavelengths, has not been reported elsewhere.

The mean complex refractive index of the two Eyjafjallajökull ash samples, VA7 and VA15, was applied to satellite measurements of the 2010 Eyjafjallajökull eruption using the ORAC retrieval scheme. This is the first time that eruption-specific laboratory measurements of the spectral complex refractive index of volcanic ash have been applied to satellite measurements of the volcanic plume. In previous work the complex refractive index of generic volcanic rocks or glasses has been assumed. The retrieved quantities of optical depth, effective radius, and plume top pressure assuming the new refractive index of VA7 & VA15 were compared to values retrieved assuming the refractive index of pumice measured by *Volz* [1973], and significant differences were seen. The new refractive index of VA7 & VA15

was found to be more sensitive to ash even in the presence of thin cloud allowing a larger area of the plume to be analysed. The retrieval result with VA7 & VA15, for the plume scene analysed in Chapter 6, showed the expected pattern of effective radius decreasing gradually with distance from the volcanic vent; a pattern not visible when the refractive index of *Volz* [1973] was assumed. Although the cost between the ORAC forward model and the measurements was similar assuming the refractive index of VA7 & VA15 compared to the refractive index of *Volz* [1973], significant differences were seen in the retrieved optical depth, effective radius and plume top pressure (with some values differing by 100 % or more). These differences strongly validate the importance of the complex refractive index measurements presented in this thesis.

In addition to the spectral extinction measurements, two techniques were developed for measuring the refractive index of volcanic ash particles at visible wavelengths. These measurements were important to provide an independent reference value of the real refractive index needed to constrain the retrievals from the aerosol cell experiments. Furthermore, the sensitivity to complex refractive index from inverting extinction measurements reduces at shorter wavelengths and the sensitivity to errors in the calculated size distribution becomes more significant.

The Becke line method is a long-established technique allowing the relative real refractive index of two materials to be determined when viewed under an optical microscope in a sub-stage illumination set-up. A new and novel method for measuring the imaginary refractive index of individual particles has been developed, involving a relatively simple extension of the Becke line procedure and using analysis of CCD images of the particles to measure the attenuation of light within individual particles. In Chapter 2 the complex refractive index of volcanic ash samples at three discrete visible wavelengths (450, 546.7 and 650 nm) are presented, measured using the Becke line method for the real part and the attenuation technique for the imaginary part. The measurements are an improvement on previous applications of the Becke line method to volcanic ash, which used white light and therefore returned an averaged value for the real refractive index across visible wavelengths. Measurements of the imaginary refractive index of particles using an optical microscope have not been reported elsewhere. The accuracy of the techniques was validated using optical glass with precisely known optical properties.

X-ray fluorescence bulk compositional analysis was performed on the samples, and the results are presented in Chapter 2. It was found that the mass percentage

SiO_2 content of the samples was strongly correlated with both their real and imaginary refractive indices, at each of the three visible wavelengths measured using the Becke and attenuation methods. Furthermore, the ratio of non-bridging oxygen atoms to tetrahedral cations, calculated from the XRF bulk composition, was found to be an even stronger predictor of the real refractive index of samples in the visible. Previous work [*Kittleman*, 1963; *Kobayashi et al.*, 1976] has linked the SiO_2 content of volcanic samples to their refractive index determined using white light Becke measurements, but correlations with the imaginary refractive index and an investigation of correlations between complex refractive index and NBO/T have not been reported elsewhere.

In Chapter 3 a new technique for retrieving the real refractive index of aerosol particles suspended in a colloid was developed. Coherent reflectance measurements of the colloid were made in an internal reflection configuration over a range of incidence angles close to the critical angle. A coherent scattering model [*Barrera and García-Valenzuela*, 2003], valid for particles of any size but for low concentrations, was used to model the coherent reflectance from the system. A simple extension of the model, using successive applications of the composition law of amplitude, was presented to properly account for the modified particle size distribution at the interface between the glass optic and the colloid. This formulation is more straightforward and intuitive than previous treatments of the interface, presented in *García-Valenzuela et al.* [2005b]. A rigorous sensitivity analysis was performed to investigate how experimental uncertainties propagate to uncertainty in the retrieved real refractive index of particles. Coherent reflectance measurements were performed on spherical monodisperse polystyrene calibration particles, a polydisperse sand sample, and a polydisperse volcanic ash sample. Values for the retrieved real refractive index from these measurements agreed, within propagated uncertainties, with the known real refractive index of polystyrene and the real refractive index of the sand and ash sample measured using the Becke technique. Previous work has investigated the sensitivity of the reflectance and transmission of colloids to particle size [*García-Valenzuela et al.*, 2008], but the work presented in this thesis and *Reed et al.* [2016] is the first investigation of the accuracy of retrieving the real refractive index of scatterers from colloidal reflectance.

7.2 Future work

It would be useful to refine the preliminary complex refractive index retrievals from the aerosol cell extinction measurements, removing bands with zero or negligible strength parameters, allowing a rigorous propagation of measurement errors to uncertainty associated with the retrieved spectral complex refractive index. Refractive index retrievals could then be applied to each of the volcanic ash extinction measurements, allowing the complex refractive indices to be compared.

It would be useful to investigate the application of the Kramers-Kronig relation [*de L. Kronig*, 1926], relating the real and imaginary parts of the complex refractive index, to the retrieval problem, thereby no longer needing the assumption of a particular model describing the radiation-matter interaction. In previous work, the problem was under-constrained because the size distribution of particles was assumed to be log-normal and the log-normal parameters were retrieved quantities. The CDHO model was required because it allowed the complex refractive index of the samples to be represented by a set of band parameters, rather than a value for the real and imaginary refractive index at each measured wavelength. However, in the new work presented in this thesis the size-distribution has been measured. The Kramers-Kronig relation allows the spectral real refractive index to be calculated from the spectral imaginary refractive index (and vice versa), effectively allowing the number of retrieved quantities to be halved. When the size distribution is known, the problem then becomes well-constrained providing the Kramers-Kronig relation is applied. This approach would have the advantage of not making any assumptions about the light-matter interaction (for example, the CDHO model assumes the interaction of light with electrons is described by a damped harmonic oscillation).

The complex refractive indices of the ashes could be used to analyse satellite data specific to their source eruption. This is likely to significantly improve the accuracy of retrieved parameters such as optical path and effective radius. Furthermore, it may be useful to directly apply the MEC measurements, to retrieve properties such as the total column mass of ash from satellite radiance measurements. This may provide a more straightforward approach compared to using complex refractive indices within the detailed radiative transfer calculations performed by the ORAC retrieval scheme.

As detailed in Chapter 4, corrections to the sizing data depended on the density and the dynamic shape factor of particles. Furthermore, the calculated in-cell

size distributions were scaled to match the measured filter holder mass deposit, requiring an assumption about the density of particles. The importance of density assumptions was highlighted by the change in the retrieved complex refractive index of the amorphous quartz sample, presented in Chapter 6, when the incorrect density was assumed compared to a more accurate value. In future, it would be useful to perform density measurements of each of the samples using a gas pycnometer. Additionally, the filter samples taken during each of the aerosol runs could be analysed using an SEM. The analysis of the SEM images would provide an independent measurement of the particle size distribution. The technique was applied recently by *Smith et al.* [2015] to black carbon particles. SEM image analysis can also provide information about the sphericity of particles [*Riley et al.*, 2003], and formulae have been developed for the drag force on volcanic ash particles as a function of their sphericity [*Ganser*, 1993; *Alfano et al.*, 2011]. This means measurements of sphericity from SEM image analysis could be used to correct the SMPS size distribution data.

The work presented in Chapter 2 showed there is a strong correlation between the SiO_2 content of volcanic ash and both its real and imaginary refractive index at visible wavelengths. Furthermore, the ratio of NBO/T was found to be even more strongly correlated with real refractive index in the visible. It would be useful to analyse correlations between composition and compositional parameters such as NBO/T over a much broader set of wavelengths, including the IR. This analysis could be performed once the complete set of complex refractive indices of the volcanic samples (of which MEC and sizing measurements are presented in Chapter 6) has been completed.

In Chapter 3 the accuracy of retrieving the real refractive index of scatterers, from colloidal reflectance measurements close to the critical angle, was assessed. The coherent scattering model of *Barrera and García-Valenzuela* [2003] was used to model the coherent reflectance of the system; the model is valid for particles of any size but for dilute concentrations. Recently, *Morales-Luna et al.* [2016] compared the CSM and other similar models to experimental data to assess the range of validity of the models, without performing retrievals. The CSM was in good agreement with all parameters evaluated (including values similar to those presented in Chapter 3), however it was argued that the "heuristic approximation" model outlined in the paper was slightly better at higher concentrations. As future work, it would be useful to compare these models with more complex multiple scattering models capable of handling systems with higher concentrations of particles:

a prime candidate would be the multiple scattering theory for discrete scatterers under the so called "quasi-crystalline with coherent potential" approximation, outlined in *Tsang and Kong* [2001]. Experimental colloidal reflectance data for higher particle densities, using the methodology detailed in Chapter 3, could be compared to the model presented in *Tsang and Kong* [2001], and the sensitivity of the colloidal reflectance to particle size and refractive index could be assessed.

Appendix A

Definitions and derivations

A.1 The Pearson product moment correlation coefficient

The Pearson product-moment correlation (PPMC) coefficient for a set of n measurements of two quantities X and Y with expected values μ_X and μ_Y and standard deviations σ_X and σ_Y is defined as:

$$\mathrm{corr(X,Y)} = \frac{\sum_{\mathrm{i}=1}^{\mathrm{N}}(\mathrm{x_i}-\mu_\mathrm{X})(\mathrm{y_i}-\mu_\mathrm{Y})}{\sigma_\mathrm{X}\sigma_\mathrm{Y}} \tag{A.1}$$

The PPMC value gives a measure of the strength of the linear relationship between the two quantities, X and Y. It has a range of values $-1 \geq \mathrm{corr(X,Y)} \leq 1$. A value of 1 indicates a perfect linear relationship; -1 indicates a perfect inverse linear relationship; whereas a value of 0 indicates no correlation.

A.2 Relative humidity and aerosol scattering

Relative humidity, RH, is defined as the ratio of the partial pressure of water vapour, traditionally denoted by the symbol e, to the saturated water vapour pressure, e_s:

$$\mathrm{RH} = \frac{e}{e_\mathrm{s}} \tag{A.2}$$

Since aerosols can take up water altering their composition and size, their scattering properties are affected by the relative humidity with the magnitude of the effect tending to be greater for more hygroscopic aerosols. The RH-dependency of

aerosol scattering is characterised by the scattering enhancement factor, $f\left(\mathrm{RH},\lambda\right)$, defined as:

$$f\left(\mathrm{RH},\lambda\right)=\frac{\sigma^{\mathrm{sca}}\left(\mathrm{RH},\lambda\right)}{\sigma^{\mathrm{sca}}\left(\mathrm{RH}_{\mathrm{dry}},\lambda\right)} \tag{A.3}$$

where $\sigma^{\mathrm{sca}}\left(\mathrm{RH},\lambda\right)$ is the scattering cross-section at some relative humidity RH, and $\sigma^{\mathrm{sca}}\left(\mathrm{RH}_{\mathrm{dry}},\lambda\right)$ is the scattering cross-section of the aerosol in dry air.

A.3 The Twomey effect

The Twomey effect [*Twomey*, 1977] describes how cloud condensation nuclei affect the reflection of solar radiation by clouds. The effective radius, r_{e}, is defined as the ratio of the third distribution moment, m_3 to the second, m_2:

$$r_{\mathrm{e}}=\frac{m_3}{m_2}=\frac{\int r^3N\left(r\right)dr}{\int r^2N\left(r\right)dr} \tag{A.4}$$

The mass of aerosol per unit volume, MPV, is given by:

$$\mathrm{MPV}=\frac{4}{3}\pi\rho_{\mathrm{p}}\int r^3N\left(r\right)dr, \tag{A.5}$$

and the volume extinction coefficient of the aerosol is given by:

$$\beta^{\mathrm{ext}}=\int\pi r^2Q^{\mathrm{ext}}\left(r,m,\lambda\right)N\left(r\right)dr. \tag{A.6}$$

where Q^{ext} is the extinction efficiency and is in general a function of particle radius, complex refractive index and wavelength. However, for cloud water droplets illuminated by solar radiation, the extinction efficiency is roughly constant at $Q^{\mathrm{ext}}\approx 2$. Under this approximation, combining Eqs. (A.4), (A.5) and (A.6) yields:

$$\beta^{\mathrm{ext}}\approx\frac{3}{2}\frac{MPV}{r_{\mathrm{e}}\rho_{\mathrm{p}}}, \tag{A.7}$$

i.e. for a given mass of aerosol, the volume extinction coeficient is inversely proportional to the effective radius of particles.

Bibliography

Agarwal, A., and M. Tomozawa, Correlation of silica glass properties with the infrared spectra, *Journal of Non-Crystalline Solids*, *209*, 166 – 174, doi:10.1016/S0022-3093(96)00542-X, 1997.

Albrecht, B. A., Aerosols, cloud microphysics, and fractional cloudiness, *Science*, *245*, 1989.

Alexander, J. M., D. M. Bell, D. Imre, P. D. Kleiber, V. H. Grassian, and A. Zelenyuk, Measurement of size-dependent dynamic shape factors of quartz particles in two flow regimes, *Aerosol Science and Technology*, *50*(8), 870–879, doi:10.1080/02786826.2016.1200006, 2016.

Alfano, F., C. Bonadonna, P. Delmelle, and L. Costantini, Insights on tephra settling velocity from morphological observations, *Journal of Volcanology and Geothermal Research*, *208*, 86 – 98, doi:10.1016/j.jvolgeores.2011.09.013, 2011.

Allen, M. D., and O. G. Raabe, Slip correction measurements of spherical solid aerosol particles in an improved millikan apparatus, *Aerosol Science and Technology*, *4*(3), 269–286, doi:10.1080/02786828508959055, 1985.

Andrews, D. G., *An introduction to Atmospheric Physics*, Cambridge University Press, 2000.

Bagheri, G., and C. Bonadonna, Chapter 2 - Aerodynamics of Volcanic Particles: Characterization of Size, Shape, and Settling Velocity, in *Volcanic Ash*, edited by S. Mackie, K. Cashman, H. Ricketts, A. Rust, and M. Watson, pp. 39 – 52, Elsevier, doi:http://dx.doi.org/10.1016/B978-0-08-100405-0.00005-7, 2016.

Ball, J. G. C., B. E. Reed, R. G. Grainger, D. M. Peters, T. A. Mather, and D. M. Pyle, Measurements of the complex refractive index of volcanic ash at 450, 546.7 and 650 nm, *J. Geophys. Res. Atmos.*, *120*, 7747–7757, 2015.

Banwell, C. N., *Fundamentals of Molecular Spectroscopy*, McGraw-Hill, 1983.

Barrera, R. G., and A. García-Valenzuela, Coherent reflectance in a system of random mie scatterers and its relation to the effective-medium approach, *J. Opt. Soc. Am. A*, *20*(2), 296–311, doi:10.1364/JOSAA.20.000296, 2003.

Barrera, R. G., A. Reyes-Coronado, and A. García-Valenzuela, Nonlocal nature of the electrodynamic response of colloidal systems, *Phys. Rev. B*, *75*, 184,202, doi:10.1103/PhysRevB.75.184202, 2007.

Becke, F. J. K., Beziehungen zwischen Dynamometamorphose und Moldkularcolumen., *Neues Jahrbuch für Mineralogie*, pp. 182–183, 1896.

Beckett, F. M., C. S. Witham, M. C. Hort, J. A. Stevenson, C. Bonadonna, and S. C. Millington, Sensitivity of dispersion model forecasts of volcanic ash clouds to the physical characteristics of the particles, *Journal of Geophysical Research: Atmospheres*, *120*(22), 11,636–11,652, doi:10.1002/2015JD023609, 2015JD023609, 2015.

Bertie, J. E., S. L. Zhang, and C. Keefe, Infrared intensities of liquids XVI. Accurate determination of molecular band intensities from infrared refractive index and dielectric constant spectra, *Journal of Molecular Structure*, *324*(1), 157 – 176, doi:10.1016/0022-2860(94)08237-5, 1994.

Bohren, C. F., and D. R. Huffman, *Absorption and Scattering of Light by Small Particles*, John Wiley & Sons, 1983.

Bonadonna, C., R. Genco, M. Gouhier, M. Pistolesi, R. Cioni, F. Alfano, A. Hoskuldsson, and M. Ripepe, Tephra sedimentation during the 2010 Eyjafjallajökull eruption (Iceland) from deposit, radar, and satellite observations, *Journal of Geophysical Research: Solid Earth*, *116*(B12), doi:10.1029/2011JB008462, b12202, 2011.

Boucher, O., et al., *Clouds and Aerosols*, book section 7, pp. 571–658, Cambridge University Press, Cambridge, United Kingdom and New York, NY, USA, doi:10.1017/CBO9781107415324.016, 2013.

Brown, R., C. Bonadonna, and A. Durant, A review of volcanic ash aggregation, *Physics and Chemistry of the Earth, Parts A/B/C*, *44 – 46*, 65 – 78, doi:10.1016/j.pce.2011.11.001, volcanic ash: an agent in Earth systems, 2012.

Buck, A. L., New equations for computing vapor pressure and enhancement factor, *Journal of Applied Meteorology*, *20*(12), 1527–1532, doi:10.1175/1520-0450(1981)020<1527:NEFCVP>2.0.CO;2, 1981.

Bursik, M. I., S. N. Carey, and R. S. J. Sparks, A gravity current model for the may 18, 1980 mount st. helens plume, *Geophysical Research Letters*, *19*(16), 1663–1666, doi:10.1029/92GL01639, 1992.

Büttner, R., P. Dellino, L. La Volpe, V. Lorenz, and B. Zimanowski, Thermohydraulic explosions in phreatomagmatic eruptions as evidenced by the comparison between pyroclasts and products from molten fuel coolant interaction experiments, *Journal of Geophysical Research: Solid Earth*, *107*(B11), ECV 5–1–ECV 5–14, doi:10.1029/2001JB000511, 2277, 2002.

CAA, Volcanic ash, a briefing from the Civil Aviation Authority, `https://www.caa.co.uk/docs/2011/VolcanicAshBriefing.pdf`, accessed Dec 2011, 2010.

Cartwright, J., Particle shape factors, *The Annals of Occupational Hygiene*, *5*, 163 – 171, doi:10.1093/annhyg/5.3.163, 1962.

Cashman, K., and A. Rust, Introduction, in *Volcanic Ash*, edited by S. Mackie, K. Cashman, H. Ricketts, A. Rust, and M. Watson, pp. 5 – 22, Elsevier, doi:http://dx.doi.org/10.1016/B978-0-08-100405-0.00002-1, 2016.

Cheng, Y. S., B. T. Chen, H. C. Yeh, I. A. Marshall, J. O. Mitchell, and W. D. Griffiths, Behavior of Compact Nonspherical Particles in the TSI Aerodynamic Particle Sizer Model APS33B: Ultra-Stokesian Drag Forces, *Aerosol Science and Technology*, pp. 255–267, 1993.

Chýlek, P., V. Srivastava, R. G. Pinnick, and R. T. Wang, Scattering of electromagnetic waves by composite spherical particles: experiment and effective medium approximations, *Appl. Opt.*, *27*(12), 2396–2404, doi:10.1364/AO.27.002396, 1988.

Corradini, S., C. Spinetti, E. Carboni, C. Tirelli, M. F. Buongiorno, S. Pugnaghi, and G. Gangale, Mt. Etna tropospheric ash retrieval and sensitivity analysis using moderate resolution imaging spectroradiometer measurements, *Journal of Applied Remote Sensing*, *2*, 2008.

Cunningham, E., On the velocity of steady fall of spherical particles through fluid medium, *Proceedings of the Royal Society of London A: Mathematical, Physical and Engineering Sciences*, *83*(563), 357–365, doi:10.1098/rspa.1910.0024, 1910.

Dagaa, R., S. R. Guevaraa, D. G. Poireb, and M. Arribérea, Characterization of tephras dispersed by the recent eruptions of volcanoes Calbuco (1961), Chaitén (2008) and Cordón Caulle Complex (1960 and 2011), in Northern Patagonia, *Journal of South American Earth Sciences*, *49*, 1–14, doi:10.1016/j.jsames.2013.10.006, 2014.

Daimon, M., and A. Masumura, Measurement of the refractive index of distilled water from the near-infrared region to the ultraviolet region, *Appl. Opt.*, *46*(18), 3811–3820, doi:10.1364/AO.46.003811, 2007.

Daines, M. J., and M. Pec, Chapter 2 — Migration of Melt, in *The Encyclopedia of Volcanoes (Second Edition)*, edited by H. Sigurdsson, second edition ed., pp. 49 – 64, Academic Press, Amsterdam, doi:http://dx.doi.org/10.1016/B978-0-12-385938-9.00002-X, 2015.

de L. Kronig, R., On the theory of dispersion of x-rays, *J. Opt. Soc. Am.*, *12*(6), 547–557, doi:10.1364/JOSA.12.000547, 1926.

DeCarlo, P. F., J. G. Slowik, D. R. Worsnop, P. Davidovits, and J. L. Jimenez, Particle morphology and density characterization by combined mobility and aerodynamic diameter measurements. Part 1: Theory, *Aerosol Science and Technology*, *38*, 1185–1205, doi:10.1080/027868290903907, 2004.

Delapasse, J., Mitigating effects of volcanic ash on air force weapon systems, TTCP Volcanic Ash Working Group Meeting, Fairbanks, Alaska, 2011.

Dellino, P., M. T. Gudmundsson, G. Larsen, D. Mele, J. A. Stevenson, T. Thordarson, and B. Zimanowski, Ash from the eyjafjallajökull eruption (iceland): Fragmentation processes and aerodynamic behavior, *Journal of Geophysical Research: Solid Earth*, *117*(B9), n/a–n/a, doi:10.1029/2011JB008726, b00C04, 2012.

Dick, W. D., P. J. Ziemann, and P. H. McMurry, Multiangle light-scattering measurements of refractive index of submicron atmospheric particles, *Aerosol Science and Technology*, *41*(5), 549–569, doi:10.1080/02786820701272012, 2007.

Dingwell, D. B., Volcanic dilemma–flow or blow?, *Science*, *273*(5278), 1054–1055, doi:10.1126/science.273.5278.1054, 1996.

Dudhia, A., Reference Forward Model, `http://www.atm.ox.ac.uk/RFM`.

Dunn, M. G., and D. P. Wade, Influence of volcanic ash clouds on gas turbine engines, in *roceedings of the first international symposium on volcanic ash and aviation safety, U.S. Geological Survey Bulletin B 2047*, edited by T. J. Casadevall, USGS Bulletin 2047, pp. 107–117, Washington, 1994.

Egan, W., T. Hilgeman, and K. Pang, Ultraviolet complex refractive-index of Martian dust — Laboratory measurements of terrestrial analogs, *Icarus*, *25*(2), 344–355, doi:10.1016/0019-1035(75)90029-9, 1975.

European Union, Volcano crisis report: Report on the actions undertaken in the context of the impact of the volcanic ash cloud crisis on the air transport industry, report, Eur. Comm., Brussels, 2010.

Felske, J. D., T. T. Charalampopoulos, and H. S. Hura, Determination of the refractive indices of soot particles from the reflectivities of compressed soot pellets, *Combustion Science and Technology*, *37*(5-6), 263–283, doi:10.1080/00102208408923757, 1984.

Fuchs, N. A., On the stationary charge distribution on aerosol particles in a bipolar ionic atmosphere, *Pure and Applied Geophysics*, *56*, 185–193, doi:10.1007/BF01993343, 1963.

Fuchs, N. A., The mechanics of aerosols, *Quarterly Journal of the Royal Meteorological Society*, *91*, 249, doi:10.1002/qj.49709138822, 1965.

Ganser, G. H., A rational approach to drag prediction of spherical and nonspherical particles, *Powder Technology*, *77*(2), 143 – 152, doi:http://dx.doi.org/10.1016/0032-5910(93)80051-B, 1993.

Gao, L., F. Lemarchand, and M. Lequime, Refractive index determination of sio2 layer in the uv/vis/nir range: spectrophotometric reverse engineering on single and bi-layer designs, *Journal of the European Optical Society - Rapid publications*, *8*(0), 2013.

García-Valenzuela, A., R. G. Barrera, C. Sánchez-Pérez, A. Reyes-Coronado, and E. R. Méndez, Coherent reflection of light from a turbid suspension of particles in an internal-reflection configuration: Theory versus experiment, *Opt. Express*, *13*(18), 6723–6737, doi:10.1364/OPEX.13.006723, 2005a.

García-Valenzuela, A., C. Sánchez-Pérez, R. G. Barrera, and A. Reyes-Coronado, Surface Effects on the Coherent Reflection of Light from a Polydisperse Colloid, in *Progress in Electromagnetics Research Symposium 2005*, pp. 650–653, PIERS Online, 2005b.

García-Valenzuela, A., R. G. Barrera, and E. Gutierrez-Reyes, Rigorous theoretical framework for particle sizing in turbid colloids using light refraction, *Opt. Express*, *16*(24), 19,741–19,756, doi:10.1364/OE.16.019741, 2008.

García-Valenzuela, A., C. Sánchez-Pérez, and E. Gutiérrez-Reyes, On the retrieval of particle size from the effective optical properties of colloids, *Physica B*, *405*, 3016–3021, 2010.

Gillespie, J. B., S. G. Jennings, and J. D. Lindberg, Use of an average complex refractive index in atmospheric propagation calculations, *Appl. Opt.*, *17*(7), 989–991, doi:10.1364/AO.17.000989, 1978.

Gonnermann, H. M., Magma fragmentation, *Annual Review of Earth and Planetary Sciences*, *43*(1), 431–458, doi:10.1146/annurev-earth-060614-105206, 2015.

Grainger, R. G., J. Lucas, G. E. Thomas, and G. B. L. Ewen, Calculation of mie derivatives, *Appl. Opt.*, *43*(28), 5386–5393, doi:10.1364/AO.43.005386, 2004.

Grainger, R. G., D. M. Peters, G. E. Thomas, A. J. A. Smith, R. Siddans, E. Carboni, and A. Dudhia, *Remote Sensing of Volcanoes and Volcanic Processes: Integrating Observation and Modelling*, vol. 380, chap. Measuring volcanic plume and ash properties from space, pp. 293–320, Geol. Soc. London Spec. Publ., doi:10.1144/SP380.7, 2013.

Grieken, R. E. V., and A. A. Markowicz, *Handbook of X-Ray Spectrometry*, vol. 29, Marcel Dekker Inc., New York, 2002.

Grossel, P., J. M. Vigoureux, and F. Baïda, Nonlocal approach to scattering in a one-dimensional problem, *Phys. Rev. A*, *50*, 3627–3637, doi:10.1103/PhysRevA.50.3627, 1994.

Gudmundsson, G., Respiratory health effects of volcanic ash with special reference to iceland. a review, *The Clinical Respiratory Journal*, *5*(1), 2–9, doi:10.1111/j.1752-699X.2010.00231.x, 2011.

Gudmundsson, M. T., et al., Ash generation and distribution from the April–May 2010 eruption of Eyjafjallajökull, Iceland, *Scientific Reports*, *2*(572), doi:0.1038/srep00572, 2012.

Guffanti, M., T. J. Casadevall, and K. Budding, Encounters of aircraft with volcanic ash clouds; A compilation of known incidents, 1953 – 2009: U.S. Geological Survey Data Series 545, 2010.

Gutiérrez-Reyes, E., A. García-Valenzuela, and R. G. Barrera, Overview of an effective-medium approach to the reflection and refraction of light at a turbid colloidal half-space, *Phys. Status Solidi B*, *249*(6), 1140–1147, 2012.

Haiyan, H., W. Chen, and L. Zhao, 2014 Asia-Pacific International Symposium on Aerospace Technology, APISAT 2014 September 24 – 26, 2014 Shanghai, China Review Volcanic Ash and its Influence on Aircraft Engine Components, *Procedia Engineering*, *99*, 795 – 803, doi:10.1016/j.proeng.2014.12.604, 2015.

Han, Y., D. Lü, R. Rao, and Y. Wang, Determination of the complex refractive indices of aerosol from aerodynamic particle size spectrometer and integrating nephelometer measurements, *Appl. Opt.*, *48*(21), 4108–4117, doi:10.1364/AO.48.004108, 2009.

Hanstrum, B. N., and A. S. Watson, A case study of two eruptions of Mount Galunggung and an investigation of volcanic eruption cloud characteristics using remote sensing techniques, *Aust. Met. Mag.*, p. 131177, 1983.

Harbin, M., S. Swanson, C. Nye, and T. Miller, Preliminary petrology and chemistry of proximal eruptive products; 1992 eruptions of Crater Peak, Mount Spurr Volcano, Alaska, in *The 1992 Eruptions of Crater Peak Vent, Mount Spurr Volcano, Alaska, U.S.*, edited by T. Keith, pp. 139–148, Geol. Surv. Prof. Pap., Geol. Surv., Reston, Va, 1995.

Haynes, W. M., *CRC handbook of chemistry and physics: A ready-reference book of chemical and physical data*, CRC Press, Boca Raton, 2009.

Hecht, E., *Optics*, 4th ed., Addison-Wesley, 1998.

Heiken, G., Morphology and petrography of volcanic ashes, *Geol. Soc. Am. Bull.*, pp. 1961 – 1987, 1972.

Hinds, W., *Aerosol technology: properties, behavior, and measurement of airborne particles*, Wiley-Interscience, Wiley, 1999.

Hreinsdóttir, S., et al., Volcanic plume height correlated with magma-pressure change at Grímsvötn Volcano, Iceland, *Nature Geoscience*, *7*, 214–218, doi:10.1038/NGEO2044, 2014.

IPCC, *Climate Change 2013: The Physical Science Basis. Contribution of Working Group I to the Fifth Assessment Report of the Intergovernmental Panel on Climate Change*, 1535 pp., Cambridge University Press, Cambridge, United Kingdom and New York, NY, USA, doi:10.1017/CBO9781107415324, 2013.

Ishimoto, H., K. Masuda, K. Fukui, T. Shimbori, T. Inazawa, H. Tuchiyama, K. Ishii, and T. Sakurai, Estimation of the refractive index of volcanic ash from satellite infrared sounder data, *Remote Sensing of Environment*, *174*, 165 – 180, doi:10.1016/j.rse.2015.12.009, 2016.

Johnson, B., et al., In situ observations of volcanic ash clouds from the FAAM aircraft during the eruption of Eyjafjallajökull in 2010, *Journal of Geophysical Research: Atmospheres*, *117*(D20), n/a–n/a, doi:10.1029/2011JD016760, d00U24, 2012.

Kasarova, S. N., N. G. Sultanova, C. D. Ivanov, and I. D. Nikolov, Analysis of the dispersion of optical plastic materials, *Opt. Mater.*, *29*, 1481–1490, doi:10.1016/j.optmat.2006.07.010, 2007.

King, P. L., P. F. McMillan, and G. M. Moore, *Molecules to Planets: Infrared Spectroscopy in Geochemistry, Exploration Geochemistry and Remote Sensing*, chap. Infrared spectroscopy of silicate glasses with application to natural systems, Mineral Association of Canada, 2004.

Kischkat, J., et al., Mid-infrared optical properties of thin films of aluminum oxide, titanium dioxide, silicon dioxide, aluminum nitride, and silicon nitride, *Appl. Opt.*, *51*(28), 6789–6798, doi:10.1364/AO.51.006789, 2012.

Kitamura, R., L. Pilon, and M. Jonasz, Optical constants of silica glass from extreme ultraviolet to far infrared at near room temperature, *Appl. Opt.*, *46*(33), 8118–8133, doi:10.1364/AO.46.008118, 2007.

Kittleman, L., Glass-bead silica determination for a suite of volcanic rocks from the Owyee Plateau, Oregon, *Geol. Soc. Am. Bull.*, *73*, 1405–1410, 1963.

Kobayashi, S., S. Shoji, I. Yamada, and J. unIchi Masui, Chemical and mineralogical studies on volcanic ashes, *Soil Science and Plant Nutrition*, *22*(1), 7–13, doi:10.1080/00380768.1976.10432962, 1976.

Kokhanovsky, A. A., and G. de Leeuw, *Satellite Aerosol Remote Sensing Over Land*, Springer, 2009.

Kotrappa, P., Shape factors for quartz aerosol in respirable size range, *Journal of Aerosol Science*, *2*(3), 353 – 359, doi:http://dx.doi.org/10.1016/0021-8502(71)90060-7, 1971.

Krotkov, N. A., D. E. Flittner, A. J. Krueger, A. Kostinski, C. Riley, W. Rose, and O. Torres, Effect of particle non-sphericity on satellite monitoring of drifting volcanic ash clouds, *J. Quant. Spectrosc. Radiat. Transfer*, *63*(2-6), 613–630, doi:10.1016/S0022-4073(99)00041-2, 1999.

Kuga, Y., D. Rice, and R. D. West, Propagation constant and the velocity of the coherent wave in a dense strongly scattering medium, *IEEE Transactions on Antennas and Propagation*, *44*, 326–332, 1996.

LaFemina, P. C., Chapter 3 - plate tectonics and volcanism, in *The Encyclopedia of Volcanoes (Second Edition)*, edited by H. Sigurdsson, second edition ed., pp. 65 – 92, Academic Press, Amsterdam, doi:http://dx.doi.org/10.1016/B978-0-12-385938-9.00003-1, 2015.

Larsen, J. F., C. J. Nye, M. L. Coombs, M. Tilman, P. Izbekov, and C. Cameron, Petrology and geochemistry of the 2006 eruption of Augustine Volcano, in *The 2006 Eruption of Augustine Volcano, Alaska, U.S.*, edited by J. A. Power, M. L. Coombs, and J. T. Freymueller, chap. 15, pp. 335–382, Geol. Surv. Prof. Pap., Geol. Surv., Reston, Va, 2010.

Lean, K., Empirical methods for detecting atmospheric aerosol events from satellite measurements, *Tech. rep.*, Department of Physics, University of Oxford, 2009.

Lindberg, J. D., and J. B. Gillespie, Relationship between particle size and imaginary refractive index in atmospheric dust, *Appl. Opt.*, *16*(10), 2628–2630, doi:10.1364/AO.16.002628, 1977.

Lindberg, J. D., R. E. Douglass, and D. M. Garvey, Carbon and the optical properties of atmospheric dust, *Appl. Opt.*, *32*(30), 6077–6081, doi:10.1364/AO.32.006077, 1993.

Liu, E., K. Cashman, and A. Rust, Optimising shape analysis to quantify volcanic ash morphology, *GeoResJ*, *8*, 14 – 30, doi:10.1016/j.grj.2015.09.001, 2015a.

Liu, E., K. Cashman, A. Rust, and S. Gislason, The role of bubbles in generating fine ash during hydromagmatic eruptions, *Geology*, *43*, 239–242, 2015b.

Loiko, V. A., V. P. Dick, and A. P. Ivanov, Features in coherent transmittance of a monolayer of particles, *Journal of the Optical Society of America*, *A 17*, 2040–2045, 2000.

Longchamp, C., C. Bonadonna, O. Bachmann, and A. Skopelitis, Characterization of tephra deposits with limited exposure: the example of the two largest explosive eruptions at Nisyros volcano (Greece), *Bulletin of Volcanology*, *73*(9), 1337–1352, doi:10.1007/s00445-011-0469-9, 2011.

Lvovsky, A. I., *Fresnel Equations*, chap. 63, pp. 1–6, doi:10.1081/E-EOE-120047133, 2013.

Maitre, R. W. L., A. Streckeisen, B. Zanettin, M. J. L. Bas, B. Bonin, and P. Bateman (Eds.), *Igneous Rocks: A Classification and Glossary of Terms*, second ed., Cambridge University Press, cambridge Books Online, 2002.

Martins, J. V., P. Artaxo, Y. J. Kaufman, A. D. Castanho, and L. A. Remer, Spectral absorption properties of aerosol particles from $350 - 2500\,\mathrm{nm}$, *Geophysical Research Letters*, *36*(13), doi:10.1029/2009GL037435, l13810, 2009.

Massol, H., and C. Jaupart, The generation of gas overpressure in volcanic eruptions, *Earth and Planetary Science Letters*, *166*, 57 – 70, doi:10.1016/S0012-821X(98)00277-5, 1999.

Mather, T. A., Volcanism and the atmosphere: the potential role of the atmosphere in unlocking the reactivity of volcanic emissions, *Philosophical Transactions of the Royal Society of London A: Mathematical, Physical and Engineering Sciences*, *366*(1885), 4581–4595, doi:10.1098/rsta.2008.0152, 2008.

Mishchenko, M. I., and L. D. Travis, Capabilities and limitations of a current FORTRAN implementation of the t-matrix method for randomly oriented, rotationally symmetric scatterers, *J. Quant. Spectrosc. Radiat. Transfer*, *60*, 309–324, doi:10.1016/S0022-4073(98)00008-9, 1998.

Mishchenko, M. I., J. W. Hovenier, and L. D. Travis (Eds.), *Light Scattering by Nonspherical Particles: Theory, Measurements and Applications*, Academic Press, 2000.

Morales-Luna, G., H. Contreras-Tello, A. García-Valenzuela, and R. G. Barrera, Experimental Test of Reflectivity Formulas for Turbid Colloids: Beyond the Fresnel Reflection Amplitudes, *The Journal of Physical Chemistry B*, *120*(3), 583–595, doi:10.1021/acs.jpcb.5b10814, pMID: 26727494, 2016.

Mukherjee, G. D., S. N. Vaidya, and V. Sugandhi, Direct observation of amorphous to amorphous apparently first-order phase transition in fused quartz, *Phys. Rev. Lett.*, *87*, 195,501, doi:10.1103/PhysRevLett.87.195501, 2001.

Munk, P., Ein Beitrag zur Optik der Farbanstriche Kubelka, *Z. Tech. Phys. (Leipzig)*, *13*, 593–601, 1931.

Mysen, B. O., The structure of silicate melts, *Annual Review of Earth and Planetary Sciences*, *11*, 1983.

National Oceanic and Atmospheric Administration, National Aeronautics, and Space Adminsitration and United States Airforce, *U.S. Standard Atmosphere*, U.S. Government Printing Office, Washington, D.C., 1976.

Newhall, C. G., and S. Self, The volcanic explosivity index (vei) an estimate of explosive magnitude for historical volcanism, *Journal of Geophysical Research: Oceans*, *87*(C2), 1231–1238, doi:10.1029/JC087iC02p01231, 1982.

Niskanen, I., and J. R. K. Erik Peiponen, Determination of the refractive index of microparticles by utilizing light dispersion properties of the particle and an immersion liquid, *Talanta*, *115*, 68–73, 2013.

Norton, R. H., and R. Beer, New apodizing functions for fourier spectrometry, *Journal of the Optical Society of America*, pp. 259–264, doi:10.1364/JOSA.66.000259, 1975.

Novatski, A., A. Steimacher, A. N. Medina, A. C. Bento, M. L. Baesso, L. H. C. Andrade, S. M. Lima, Y. Guyot, and G. Boulon, Relations among nonbridging oxygen, optical properties, optical basicity, and color center formation in CaO–MgO aluminosilicate glasses, *Journal of Applied Physics*, *104*(9), 094910, doi:http://dx.doi.org/10.1063/1.3010306, 2008.

Oxford Economics, The economic impacts of air travel restrictions due to volcanic ash, report, Abbey House, Oxford, UK, 12 pp., 2010.

Parker, D. E., H. Wilson, P. D. Jones, J. R. Christy, and C. K. Folland, The impact of mount pinatubo on world-wide temperatures, *Int. J. Climatol.*, doi:10.1002/(SICI)1097-0088(199605)16:5<487::AID-JOC39>3.0.CO;2-J, 1996.

Patterson, E. M., Measurements of the imaginary part of the refractive index between 300 and 700 nanometers for Mount St. Helens ash, *Science*, *211*(4484), 836–838, doi:10.1126/science.211.4484.836, 1981.

Patterson, E. M., Optical absorption coefficients of soil-aerosol particles and volcanic ash between 1 and 16 μm, *Proceedings of the Second Conference on Atmospheric Radiation*, pp. 177–180, 1994.

Patterson, E. M., C. O. Pollard, and I. Galindo, Optical-properties of the ashes from El Chichon volcano, *Geophys. Res. Lett.*, *10*(4), 317–320, doi:10.1029/GL010i004p00317, 1983.

Pollack, J. B., O. B. Toon, and B. N. Khare, Optical properties of some terrestrial rocks and glasses, *Icarus*, *19*(3), 372–389, doi:10.1016/0019-1035(73)90115-2, 1973.

Prata, A. J., Infrared radiative transfer calculations for volcanic ash clouds, *Geophysical Research Letters*, *16*, 1293–1296, 1989a.

Prata, A. J., Observations of volcanic ash clouds in the 10-12 μm window using AVHRR/2 data, *International Journal of Remote Sensing*, *10*, 751–761, 1989b.

Prata, A. J., and I. F. Grant, Retrieval of microphysical and morphological properties of volcanic ash plumes from satellite data: Application to Mt Ruapehu, New Zealand, *Quarterly Journal of the Royal Meteorological Society*, *127*, 2153–2179, 2001.

Prata, A. J., and A. T. Prata, Eyjafjallajökull volcanic ash concentrations determined using Spin Enhanced Visible and Infrared Imager measurements, *Journal of Geophysical Research: Atmospheres*, *117*(D20), n/a–n/a, doi:10.1029/2011JD016800, d00U23, 2012.

Przedpelski, Z. J., and T. J. Casadevall, Impact of volcanic ash from 15 December 1989 Redoubt volcano eruption on GE CF6–80C2 Turbofan engines, in *Proceedings of the first international symposium on volcanic ash and aviation safety, U.S. Geological Survey Bulletin B 2047*, edited by T. J. Casadevall, pp. 129–135, 1994.

Pyle, D. M., Chapter 13 - Sizes of volcanic eruptions, in *The Encyclopedia of Volcanoes (Second Edition)*, edited by H. Sigurdsson, second edition ed., pp. 257 – 264, Academic Press, Amsterdam, doi:10.1016/B978-0-12-385938-9.00013-4, 2015.

Reed, B. E., R. G. Grainger, D. M. Peters, and A. J. A. Smith, Retrieving the real refractive index of mono- and polydisperse colloids from reflectance near the critical angle, *Opt. Express*, *24*(3), 1953–1972, doi:10.1364/OE.24.001953, 2016.

Reubi, O., and J. Blundy, A dearth of intermediate melts at subduction zone volcanoes and the petrogenesis of arc andesites, *Nature*, *461*(7268), 1269–1273, 2009.

Riley, C. M., W. I. Rose, and G. J. S. Bluth, Quantitative shape measurements of distal volcanic ash, *Journal of Geophysical Research: Solid Earth*, *108*(B10), n/a–n/a, doi:10.1029/2001JB000818, 2504, 2003.

Riley, K. F., M. P. Hobson, and S. J. Bence, *Mathematical Methods for Physics and Engineering*, Cambridge University Press, 2008.

Ripepe, M., C. Bonadonna, A. Folch, D. D. Donne, G. Lacanna, E. Marchetti, and A. Höskuldsson, Ash-plume dynamics and eruption source parameters by infrasound and thermal imagery: The 2010 Eyjafjallajökull eruption, *Earth and Planetary Science Letters*, *366*, 112 – 121, doi:10.1016/j.epsl.2013.02.005, 2013.

Rocha-Lima, A., J. V. Martins, L. A. Remer, N. A. Krotkov, M. H. Tabacniks, Y. Ben-Ami, and P. Artaxo, Optical, microphysical and compositional properties of the eyjafjallajökull volcanic ash, *Atmospheric Chemistry and Physics*, *14*(19), 10,649–10,661, doi:10.5194/acp-14-10649-2014, 2014.

Rodgers, C. D., *Inverse Methods for Atmospheric Sounding: Theory and Practice*, World Scientific, 2000.

Rogak, S. N., R. C. Flagan, and H. V. Nguyen, The mobility and structure of aerosol agglomerates, *Aerosol Science and Technology*, *18*(1), 25–47, doi:10.1080/02786829308959582, 1993.

Rose, W., and A. Durant, Fine ash content of explosive eruptions, *Journal of Volcanology and Geothermal Research*, *186*, 32 – 39, doi:10.1016/j.jvolgeores.2009.01.010, Improved Prediction and Tracking of Volcanic Ash Clouds, 2009.

Rose, W., G. Bluth, and G. Ernst, Integrating retrievals of volcanic cloud characteristics from satellite remote sensors: a summary, *Philosophical Transactions of the Royal Society of London Series A - Mathematical Physical and Engineering Sciences*, *358*(1770), 1585–1606, 2000.

Rosenfeld, D., S. Sherwood, R. Wood, and L. Donner, Climate effects of aerosol-cloud interactions, *Science*, *343*(6169), 379–380, doi:10.1126/science.1247490, 2014.

Rousseau, R. M., Detection limit and estimate of uncertainty of analytical XRF results, *The Rigaku Journal*, *18*, 33–47, 2001.

Sánchez-Pérez, C., A. García-Valenzuela, R. Y. Sato-Berrú, J. O. Flores-Flores, and R. G. Barrera, Sizing colloidal particles from their contribution to the effective refractive index: Experimental results, *J. Phys. Conf. Ser.*, *274*, 2011.

Schmid, R., Descriptive nomenclature and classification of pyroclastic deposits and fragments: Recommendations of the iugs subcommission on the systematics of igneous rocks, *Geology*, *9*(1), 41–43, doi:10.1130/0091-7613(1981)9<41:DNACOP>2.0.CO;2, 1981.

Sigurdsson, H., Part I Origin and Transport of Magma, in *The Encyclopedia of Volcanoes*, edited by H. Sigurdsson, second ed., pp. 33 – 34, Academic Press, Amsterdam, doi:http://dx.doi.org/10.1016/B978-0-12-385938-9.02003-4, 2015.

Smith, A. J. A., D. M. Peters, R. McPheat, S. Lukanihins, and R. G. Grainger, Measuring black carbon spectral extinction in the visible and infrared, *Journal of Geophysical Research: Atmospheres*, *120*(18), 9670–9683, doi:10.1002/2015JD023564, 2015JD023564, 2015.

Sparks, R. S. J., L. Wilson, and H. Sigurdsson, The pyroclastic deposits of the 1875 eruption of Askja, Iceland, *Philosophical Transactions of the Royal Society of*

London A: Mathematical, Physical and Engineering Sciences, *299*(1447), 241–273, doi:10.1098/rsta.1981.0023, 1981.

Spitzer, W. G., and D. A. Kleinman, Infrared lattice bands of quartz, *Phys. Rev.*, *121*, 1324–1335, doi:10.1103/PhysRev.121.1324, 1961.

Stamnes, K., S.-C. Tsay, W. Wiscombe, and K. Jayaweera, A numerically stable algorithm for discrete-ordinate-method radiative transfer in multiple scattering and emitting layered media, *Applied Optics*, *27*(12), 2502–2509, doi:10.1364/AO.27.002502, 1988.

Stevenson, J. A., et al., Uk monitoring and deposition of tephra from the may 2011 eruption of grímsvötn, iceland, *Journal of Applied Volcanology*, *2*(1), 1–17, doi:10.1186/2191-5040-2-3, 2013.

Sumitra Optical glass Inc., Sumitra optical glass data sheet, `http://refractiveindex.info/`, 2012.

Taddeucci, J., P. Scarlato, C. Montanaro, C. Cimarelli, E. Del Bello, C. Freda, D. Andronico, M. Gudmundsson, and D. Dingwell, Aggregation-dominated ash settling from the Eyjafjallajökull volcanic cloud illuminated by field and laboratory high-speed imaging, *Geology*, *39*(9), 891–894, doi:10.1130/G32016.1, 2011.

Thomas, G. E., S. F. Bass, R. G. Grainger, and A. Lambert, Retrieval of aerosol refractive index from extinction spectra with a damped harmonic-oscillator band model, *Applied Optics*, *44*(7), 1332–1341, doi:10.1364/AO.44.001332, 2005.

Thornburg, J., S. J. Cooper, and D. Leith, Counting efficiency of the API aerosizer, *J. Aerosol Sci.*, *30*, 479–488, 1999.

Tomozeiu, N., *Optoelectronics — Materials and Techniques*, chap. Silicon Oxide (SiOx, 0<x<2): a Challenging Material for Optoelectronics, InTech, doi:10.5772/20156, 2011.

Toon, O. B., J. B. Pollack, and C. Sagan, Physical properties of the particles composing the Martian dust storm of 1971-1972, *Icarus*, *30*(4), 663–696, doi:10.1016/0019-1035(77)90088-4, 1977.

Tsang, L., and J. A. Kong, Multiple scattering of electromagnetic waves by random distribution of discrete scatterers with coherent potential and quantum mechanical formalism, *Journal of Applied Physics*, *51*, 3465–3485, 1980.

Tsang, L., and J. A. Kong, Effective propagation constants for coherent electromagnetic waves propagating in media embedded with dielectric scatters, *Journal of Applied Physics*, *53*, 7162, 1982.

Tsang, L., and J. A. Kong, *Scattering of electromagnetic waves: Advanced topics*, Wiley, New York, USA, 2001.

Twomey, S., The influence of pollution on the shortwave albedo of clouds, *Journal of Atmospheric Sciences*, 1977.

Vigoureux, J. M., Use of Einstein's addition law in studies of reflection by stratified planar structures, *J. Opt. Soc. Am. A*, *9*(8), 1313 – 1319, doi:10.1364/JOSAA.9.001313, 1992.

Vollmayr, K., W. Kob, and K. Binder, Cooling-rate effects in amorphous silica: A computer-simulation study, *Phys. Rev. B*, *54*, 15,808–15,827, doi:10.1103/PhysRevB.54.15808, 1996.

Volz, F. E., Infrared optical constants of ammonium sulfate, Sahara dust, volcanic pumice and flyash, *Appl. Optics*, *12*, 564–568, 1973.

von der Weiden, S.-L., F. Drewnick, and S. Borrmann, Particle Loss Calculator — a new software tool for the assessment of the performance of aerosol inlet systems, *Atmospheric Measurement Techniques*, *2*(2), 479–494, doi:10.5194/amt-2-479-2009, 2009.

Wallace, K., S. Snedigar, and C. Cameron, 'is ash falling?', an online ashfall reporting tool in support of improved ashfall warnings and investigations of ashfall processes, *Journal of Applied Volcanology*, *4*(1), 1–10, doi:10.1186/s13617-014-0022-6, 2015.

Wang, Y., et al., Atomistic insight into viscosity and density of silicate melts under pressure, *Nat. Commun.*, *5*, doi:10.1038/ncomms4241, 2014.

Watt, S. F. L., D. M. Pyle, T. A. Mather, R. S. Martin, and N. E. Matthews, Fallout and distribution of volcanic ash over Argentina following the May 2008 explosive eruption of Chaitén, Chile, *Journal of Geophysical Research: Solid Earth*, *114*(B4), n/a–n/a, doi:10.1029/2008JB006219, b04207, 2009.

Wemple, S. H., and M. DiDomenico, Behavior of the electronic dielectric constant in covalent and ionic materials, *Phys. Rev. B*, *3*, 1338–1351, doi:10.1103/PhysRevB.3.1338, 1971.

Wen, C. S., *The Fundametals of Aerosol Dynamics*, World Scientific, P O Box 128, Farrer Road, Singapore 912805, 1996.

White, J. U., Long optical paths of large aperture, *Journal of the Optical Society of America*, *32*, 285–288, doi:10.1364/JOSA.32.000285, 1942.

Wright, H. M., K. V. Cashman, P. A. Mothes, M. L. Hall, A. G. Ruiz, and J. Le Pennec, Estimating rates of decompression from textures of erupted ash particles produced by 1999–2006 eruptions of tungurahua volcano, ecuador, *Geology*, *40*(7), 619–622, doi:10.1130/G32948.1, 2012.

Xiaoyan, M., Q. L. Jun, R. S. Brock, K. M. Jacobs, P. Yang, and X. Hu, Determination of complex refractive index of polystyrene microspheres from 370 to 1610 nm, *Phys. Med. Biol.*, *48*, 4165–4172, doi:10.1088/0031-9155/48/24/013, 2003.

Yuan, T., L. A. Remer, and H. Yu, Microphysical, macrophysical and radiative signatures of volcanic aerosols in trade wind cumulus observed by the A-Train, *Atmospheric Chemistry and Physics*, *11*(14), 7119–7132, doi:10.5194/acp-11-7119-2011, 2011.

Zacharias, M., T. Drüsedau, A. Panckow, H. Freistedt, and B. Garke, Physical properties of a-SiOx : H alloys prepared by DC magnetron sputtering with water vapour as oxygen source, *Journal of Non-Crystalline Solids*, *169*(1), 29 – 36, doi:10.1016/0022-3093(94)90221-6, 1994.

Zimanowski, B., K. Wohletz, P. Dellino, and R. B′uttner, The volcanic ash problem, *Journal of Volcanology and Geothermal Research*, *122*, 1–5, 2003.